

KWAME NKRUMAH UNIVERSITY OF SCIENCE AND TECHNOLOGY, KUMASI

COLLEGE OF SCIENCE

DEPARTMENT OF CHEMISTRY



**GREEN APPROACH TO METAL CHALCOGENIDE SEMICONDUCTOR  
NANOMATERIALS: SYNTHESSES AND CHARACTERIZATION OF CdS,  
PbS, ZnS, MnS AND  $Mn_xZn_{1-x}S$  NANOPARTICLES**

A THESIS SUBMITTED TO THE DEPARTMENT OF CHEMISTRY, KWAME NKRUMAH  
UNIVERSITY OF SCIENCE AND TECHNOLOGY, KUMASI, IN PARTIAL FULFILMENT  
OF THE REQUIREMENT FOR THE AWARD OF THE DEGREE OF  
DOCTOR OF PHILOSOPHY IN PHYSICAL CHEMISTRY

BY

MICHAEL BAAH MENSAH

(M.PHIL. PHYSICAL CHEMISTRY)

JULY, 2018

**DECLARATION**

I hereby declare that this submission is my own work and that, to the best of my knowledge and belief, it contains no material previously published or written by another person nor material which to a substantial extent has been accepted for the award of any other degree or diploma at Kwame Nkrumah University of Science and Technology, Kumasi or any other educational institution, except where due acknowledgment is made in the thesis.

**Michael Baah Mensah (9998713)** .....  
Signature Date  
Student Name & ID

Certified by:  
**Prof. Johannes A. M. Awudza** .....  
Signature Date  
Supervisor's Name

Certified by:  
**Dr. Osei Akoto** .....  
Signature Date  
Head of Department's Name

## ABSTRACT

Metal chalcogenide nanomaterials such as CdS, PbS, ZnS, MnS and  $Mn_xZn_{1-x}S$  are very useful compound semiconductors with potential applications in sensing, bioimaging, drug delivery, data storage and photovoltaic devices as well as in catalysis. However, the syntheses of good quality nanomaterials usually include toxic chemical reagents and therefore limit their application and adaptation to large scale production. Castor oil and single source precursors (SSPs) are suitable alternative green reagents for the syntheses of undoped and doped metal chalcogenide nanocrystals. In this thesis, green syntheses of (i) CdS nanoclusters and PbS nanorods/belts via thermal decomposition of xanthate complexes in castor oil, and (ii) ZnS, MnS and  $Mn_xZn_{1-x}S$  nanocrystals via the thermal decomposition of diricinoleate carboxylate and heterocyclic dithiocarbamate complexes in oleylamine are reported. The dopant (Mn) feed concentration was varied in the range  $0 \leq x \leq 0.1$ . The CdS displayed a band gap of 2.63 – 2.84 eV and a strong emission in the near-UV ( $\lambda_{max} = 393$  nm) region and formed small clusters of nanocrystals with average particle size of  $6.78 \pm 1.89$  nm. The PbS nanocrystals showed variety of morphologies. The average width and length of the PbS nanorods observed were  $22.2 (\pm 2.3)$  nm and  $225.9 (\pm 23.3)$  nm respectively. The activation energy obtained for the growth of ZnS nanoparticles in oleylamine was 53.41 kJ/mol. Powder-X-ray diffraction (p-XRD) patterns showed that the ZnS and  $Mn_xZn_{1-x}S$  nanocrystals synthesized by different precursor routes were sphalerite and the shift in the lattice parameter indicated distortion due to the incorporation of the Mn(II) into the ZnS. The MnS nanocrystals were pure alabandite. The p-XRD patterns of the nanocrystals synthesized by the dithiocarbamate route showed some wurtzitic characteristics of ZnS and  $Mn_xZn_{1-x}S$ . The band gap energy was found to decrease with increasing Mn(II) dopant concentration which indicated the introduction of trap states into the forbidden zone of the host ZnS. Luminescence was observed for  $Mn_xZn_{1-x}S$  (for  $x \leq$

0.01) nanocrystals at 587 – 599.7 nm characteristic of  $Mn^{4T_1} \leftarrow ^6A_1$  transition suggesting possible incorporation of the Mn(II) into the

ZnS host lattice. Electron paramagnetic resonance (EPR) studies confirmed the presence of Mn(II) ions dispersed at substitutionary sites for  $x \leq 0.01$   $Mn_xZn_{1-x}S$  nanocrystals. However, at high concentrations of Mn dopant ( $\geq 0.01$ ), the Mn(II) ions were found bound to the surface/interstitial sites in ZnS. Thus, useful morphologies and interesting properties of important metal chalcogenide semiconductors were achieved by the use of environmentally benign materials.

**Keywords:** Green nanochemistry, nanomaterial, metal chalcogenide, castor oil, single source precursor, carboxylate

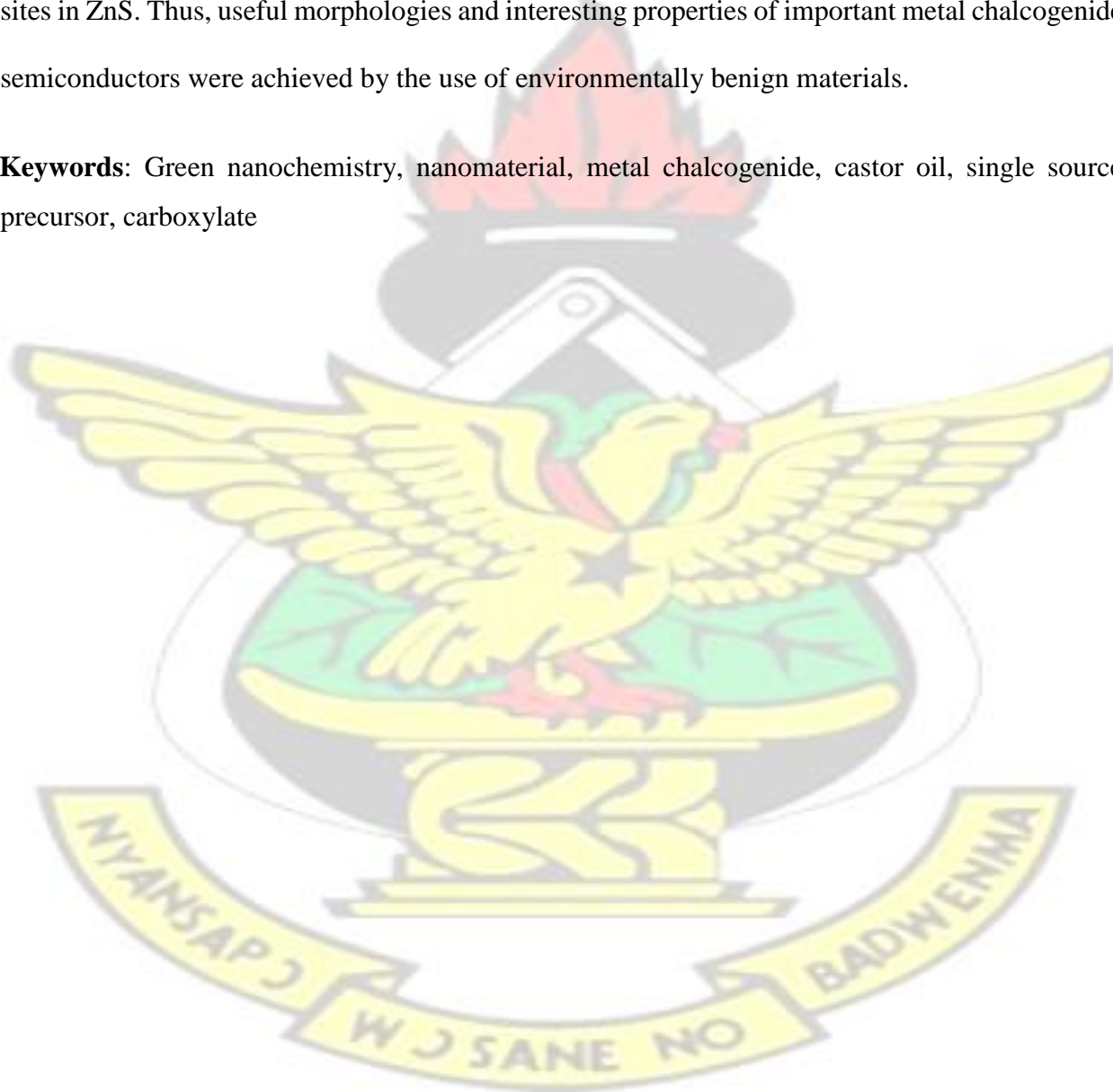


## TABLE OF CONTENTS

TITLE PAGE.....	i
DECLARATION.....	ii
ABSTRACT.....	iii
TABLE OF CONTENTS.....	v
LIST OF TABLES.....	ix
LIST OF FIGURES.....	x
LIST OF ABBREVIATIONS.....	xv
ACKNOWLEDGEMENT.....	xvii
DEDICATION.....	xix
<b>CHAPTER 1: GENERAL INTRODUCTION.....</b>	<b>1</b>
1.1 Background.....	1
1.2 Problem Statement and Justification.....	6
1.3 Objectives.....	10
1.3.1 Main objective	
1.3.2 Specific objectives	
1.4 Scope of Work.....	11
<b>CHAPTER 2: LITERATURE REVIEW.....</b>	<b>12</b>
2.1 Introduction to Nanotechnology.....	12
2.1.1 Nanoscience	
2.1.2 Nanomaterials	
2.1.3 Classification of nanomaterials	
2.1.4 Semiconductor nanomaterials	
2.1.5 Applications of nanomaterials	
2.1.5.1 Energy	
2.1.5.2 Healthcare	
2.1.5.3 Electronic devices	
2.1.5.4 Food	
2.1.5.5 Clothing	

2.1.5.6	Construction	
2.1.5.7	Environmental remediation	
2.2	Theories and Mechanisms of Nanocrystals Formation.....	25
2.2.1	Quantum confinement	
2.2.2	The LaMer model	
2.2.3	Derivation of nucleation rate equations	
2.2.4	Derivation of growth rate equations	
2.2.4.1	Ostwald ripening	
2.2.4.2	Oriented attachment	
2.3	Doping of Semiconductor Nanoparticles.....	42
2.3.1	Mechanisms of doping	
2.3.1.1	Self-purification model	
2.3.1.2	Trap model	
2.4	Size Controlled Colloidal Syntheses of Nanoparticles.....	46
2.4.1	Hot-injection and heat-up syntheses	
2.4.2	Other methods of syntheses	
2.5	Green Precursors for Syntheses of Metal Chalcogenide Nanoparticles.....	51
2.5.1	Vegetable oils	
2.5.2	Castor oil and ricinoleic acid	
2.5.2.1	Isolation of ricinoleic acid from castor oil	
2.5.2.2	Characteristics of ricinoleic acid compared to oleic acid	
2.5.3	Metal carboxylates	
2.5.4	Single source precursors (SSPs)	
2.5.4.1	Dithiocarbamates	
2.5.4.2	Decomposition mechanism of dithiocarbamates	
2.6	Metal Chalcogenide Nanoparticles.....	71
2.6.1	Zinc sulfide (ZnS)	
2.6.1.1	Crystal structure	
2.6.1.2	Polytypes	
2.6.1.3	Properties	
2.6.1.4	Synthesis of ZnS nanoparticles	
2.6.1.5	Growth kinetics of ZnS nanocrystals	
2.6.2	Manganese sulfide (MnS)	
2.6.3	Manganese-doped ZnS ( $Mn_xZn_{1-x}S$ )	
2.6.3.1	Application of ZnS and $Mn_xZn_{1-x}S$	
2.6.3.1.1	Electronic devices	
2.6.3.1.2	Solar cells	
2.6.3.1.3	Light-emitting diodes (LEDs)	
2.6.3.1.4	Bio-medical probes or sensors	
2.6.3.1.5	Chemical sensors	
2.6.3.1.6	Photocatalysis	
2.6.4	Cadmium sulfide (CdS) and lead sulfide (PbS)	

## CHAPTER 3: METHODOLOGY.....101

3.1	Materials.....	101
3.2	Methods of Synthesis.....	101
3.2.1	Synthesis of cadmium(II) ethyl xanthate (1)	
3.2.2	Synthesis of lead(II) ethyl xanthate (2)	
3.2.3	Syntheses of CdS and PbS nanoparticles	
3.2.4	Extraction of ricinoleic acid from castor oil	
3.2.5	Synthesis of zinc(II) diricinoleate complex, $[\text{Zn}(\text{Ra})_2]$ (3)	
3.2.6	Synthesis of manganese(II) diricinoleate complex, $[\text{Mn}(\text{Ra})_2]$ (4)	
3.2.7	Syntheses and growth kinetic study of ZnS nanoparticles from complex (3)	
3.2.8	Syntheses of MnS nanoparticles from complex (4)	
3.2.9	Syntheses of Mn-doped ZnS nanoparticles from complexes (3) and (4)	
3.2.10	Synthesis of ligand, sodium tetrahydroisoquinoline dithiocarbamate, $[\text{Na}(\text{S}_2\text{CN}(\text{thiq}))]$	
3.2.11	Synthesis of zinc(II) bis(tetrahydroisoquinolinyl dithiocarbamate), $[\text{Zn}(\text{S}_2\text{CN}(\text{thiq}))_2]$ (5)	
3.2.12	Synthesis of manganese (III) tris(tetrahydroisoquinolinyl dithiocarbamate), $[\text{Mn}(\text{S}_2\text{CN}(\text{thiq}))_3]$ (6)	
3.2.13	Syntheses of ZnS nanocrystals from complex (5)	
3.2.14	Syntheses of MnS nanocrystals from complex (6)	
3.2.15	Syntheses of Mn-doped ZnS nanocrystals from complexes (5) and (6)	
3.3	Characterization of complexes and nanoparticles	
3.3.1	Analyses of chemical structures of complexes	
3.3.2	Elemental and thermal analyses	
3.3.3	p-XRD analyses	
3.3.4	Optical analyses	
3.3.5	Analyses of morphology and elemental composition of nanoparticle	
3.4	Data analyses	

## CHAPTER 4: RESULTS AND DISCUSSIONS.....115

### 4.1 Syntheses of CdS Nanoclusters and PbS Nanobelts via Facile Thermolysis of Ethyl Xanthate Complexes in Castor oil.....115

#### 4.1.1 Introduction

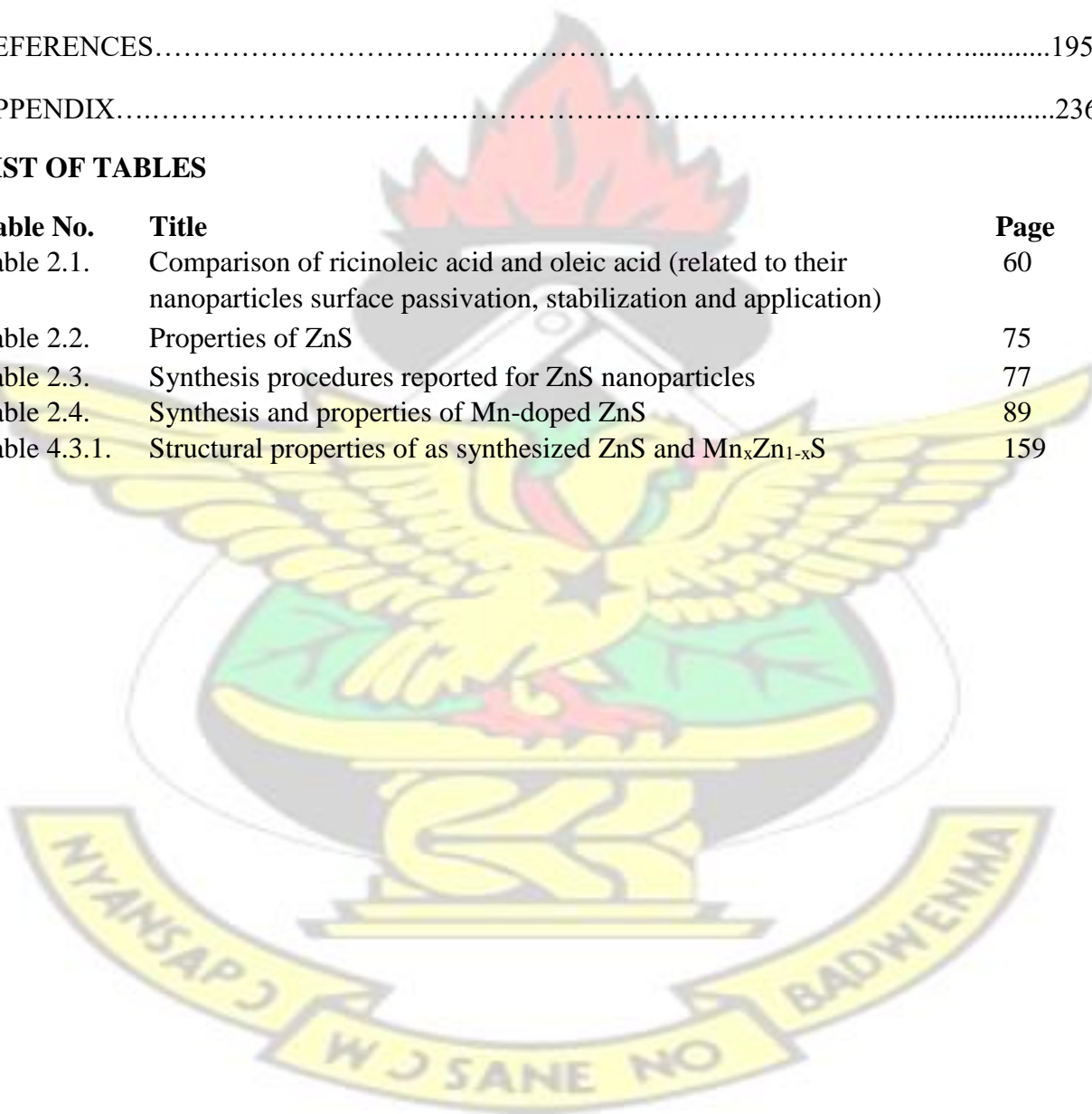
4.1.2	Results and discussions	
4.1.2.1	Analysis of castor oil	
4.1.2.2	Thermal analysis of ethyl xanthate of Cd and Pb complexes	
4.1.2.3	CdS nanoclusters	
4.1.2.3.1	p-XRD analysis of CdS	
4.1.2.3.2	Optical properties of CdS	
4.1.2.3.3	Morphology of CdS	
4.1.2.4	PbS nanobelts	
4.1.2.4.1	p-XRD analysis of PbS	

4.1.2.4.2	Morphology of PbS	
4.1.2.4.3	Optical properties of PbS	
4.1.3	Summary of main findings	
<b>4.2</b>	<b>Growth Kinetics of ZnS Nanoparticles Synthesized by the Thermal Decomposition of Zinc Diricinoleate Carboxylate in Oleylamine/ Dodecanethiol.....</b>	<b>132</b>
4.2.1	Introduction	
4.2.2	Results and discussions	
4.2.2.1	Analysis of isolated ricinoleic acid from castor oil	
4.2.2.2	Formation and thermal analysis of zinc diricinoleate carboxylate precursor	
4.2.2.3	Formation and growth of ZnS nanoparticles	
4.2.2.4	p-XRD measurement on ZnS nanoparticles	
4.2.2.5	Particle size determination of ZnS nanoparticles	
4.2.2.6	Effect of temperature on particle size	
4.2.2.7	Effect of reaction time on particle size	
4.2.2.8	Determination of activation energy of ZnS nanoparticles growth	
4.2.3	Summary of main findings	
<b>4.3</b>	<b>The Syntheses of Manganese doped Zinc Sulfide (<math>Mn_xZn_{1-x}S</math>) Nanocrystals by the Thermal Decomposition of Diricinoleate Carboxylates in Oleylamine/ Dodecanethiol.....</b>	<b>149</b>
4.3.1	Introduction	
4.3.2	Results and discussions	
4.3.2.1	Diricinoleate carboxylate complexes of Zn and Mn	
4.3.2.2	Syntheses and composition of Mn-doped ZnS nanocrystals	
4.3.2.3	XRD measurements on ZnS, MnS and $Mn_xZn_{1-x}S$ nanocrystals	
4.3.2.4	Morphology of undoped ZnS and Mn-doped ZnS nanocrystals	
4.3.2.5	Optical properties of undoped ZnS and Mn-doped ZnS nanocrystals	
4.3.3	Summary of main findings	
<b>4.4</b>	<b>The Syntheses of Manganese doped Zinc Sulfide (<math>Mn_xZn_{1-x}S</math>) Nanocrystals by the Thermal Decomposition of Heterocyclic Dithiocarbamate Single Source Precursors in Oleylamine.....</b>	<b>170</b>
4.4.1	Introduction	
4.4.2	Results and discussions	
4.4.2.1	Heterocyclic dithiocarbamate complexes of Zn and Mn	
4.4.2.2	Syntheses and composition of Mn-doped ZnS nanoparticles	
4.4.2.3	XRD measurements on ZnS, MnS and $Mn_xZn_{1-x}S$ nanocrystals	
4.4.2.4	Morphology of Mn-doped ZnS nanocrystals	
4.4.2.5	Optical properties of undoped ZnS and Mn-doped ZnS nanocrystals	4.4.3
	Summary of main findings	

<b>4.5</b>	<b>General Discussions.....</b>	<b>188</b>
4.5.1	CdS and PbS Nanocrystals	
4.5.2	ZnS and MnS Nanocrystals	
4.5.3	Mn-doped ZnS Nanocrystals	
<b>CHAPTER 5: CONCLUSIONS AND RECOMMENDATIONS.....</b>		<b>193</b>
5.1	Conclusions	
5.2	Recommendations	
REFERENCES.....		195
APPENDIX.....		236

### LIST OF TABLES

<b>Table No.</b>	<b>Title</b>	<b>Page</b>
Table 2.1.	Comparison of ricinoleic acid and oleic acid (related to their nanoparticles surface passivation, stabilization and application)	60
Table 2.2.	Properties of ZnS	75
Table 2.3.	Synthesis procedures reported for ZnS nanoparticles	77
Table 2.4.	Synthesis and properties of Mn-doped ZnS	89
Table 4.3.1.	Structural properties of as synthesized ZnS and $Mn_xZn_{1-x}S$	159



# KNUST

## LIST OF FIGURES

<b>Figure No.</b>	<b>Caption</b>	<b>Page</b>
Figure 1.1	Chemical structures of triricinolein and ricinoleic acid (major fatty acid in castor oil, (90 %))	4
Figure 1.2	Chemical structures of dithiocarbamate and xanthate single source precursors	5
Figure 2.1	Nanoscale in comparison to microscale and milliscale	14
Figure 2.2	Classification of nanomaterials	15
Figure 2.3	Flow chart of different semiconductor materials	16
Figure 2.4	A comparison of band gap energies of different types of materials: bulk semiconductor, semiconductor nanocrystals and molecular semiconductor	27
Figure 2.5	Idealized density of state for one band of 3, 2, 1 and 0 dimensional structures	28
Figure 2.6	Schematic diagram of the LaMer model indicating the different stages in size-controlled colloidal synthesis of nanocrystals	29
Figure 2.7	A plot of free energy of crystallization and radius of the crystallite particles	31
Figure 2.8	(a) Schematic diagram illustrating the monomer diffusion layer structure surrounding the surface of a nanocrystal, NC, (b) Crosssection of the surface of a NC and a plot of the monomer concentration as a function of distance $x$ . $C_b$ is bulk concentration of monomer, $C_s$ is concentration at the surface of the NC	34
Figure 2.9	Plots of nanocrystals growth rate (solid line) and particle size distribution functions (shaded area). The dashed line indicates the maximum growth rate and the arrows showing the time evolution. $S$ is saturation of the monomers (a) Size focusing leading the narrowing of the particle size distribution and (b) Ripening leading to the broadening of the particle size distribution	36

Figure 2.10	Scheme of growth of nanocrystals controlled by (a) Ostwald ripening and (b) Oriented attachment	40
Figure 2.11	Schematic sketch illustrating the ‘self-purification model’ in doping mechanism	45
Figure 2.12	Schematic sketch illustrating the ‘trap model’ in doping mechanism	46
Figure 2.13	Schematic diagram of set-up for hot-injection and heat-up syntheses	48
Figure 2.14	Castor plant (a) matured castor plant, (b) bunch of castor seeds, (c) dried castor seed pod, seed and oil	53
Figure 2.15	Chemical structures of fatty acids (percentage composition in bracket) found to be present in castor oil (a: ricinoleic acid, b: linoleic acid, c: oleic acid, d: palmitic acid, e: stearic acid, f: linolenic acid, g: behenic acid, h: arachinic acid (or eicosanoic acid), i: tricosanoic acid, j: eicosanoic acid, k: nervonic acid, l: lignoceric acid, m: 11,12-dihydroxy-9,13-octadecadienoic acid, n:	



	11,12-dihydroxy-9-octadecenoic acid, o: 11,12-dihydroxyoctadecanoic acid, p: dihydroxystearic acid)	55
Figure 2.16	Reaction scheme showing the isolation of ricinoleic acid from castor oil	57
Figure 2.17	Thioacids: (a) dithiocarbamate, (b) xanthate, (c) dithiolate, (d) dithiophosphate, (e) piperidine-dithiocarbamate, (f) tetrahydroisoquinoline-dithiocarbamate, (g) tetrahydroquinoline-dithiocarbamate	63
Figure 2.18	Reaction scheme showing the synthesis of metal-dithiocarbamates. The $n$ is the valence of the metal ion and X is the anion of the metal salt	65
Figure 2.19	Canonical structures of metal-dithiocarbamates	66
Figure 2.20	Mechanism of decomposition of metal-dithiocarbamates in primary alkylamines to yield desired metal sulfide nanoparticles	69
Figure 2.21	Zinc blende, wurtzite and rock salt crystal structures	72
Figure 2.22	Transition states in Mn-doped ZnS nanoparticles	86
Figure 2.23	Sketch of model hypothesizing the physical location of Mn ions in lattice of ZnS	87
Figure 2.24	Different models describing the local effect of Mn ions in ZnS host lattice	88
Figure 2.25	Mechanism of glucose phosphorescent sensor: (a) mechanism of quenching of phosphorescence by generation of $H_2O_2$ by enzymatic oxidation of glucose (b) quenching of room temperature phosphorescence by $H_2O_2$	97
Figure 3.1	Reaction scheme for syntheses of ethyl xanthate complexes (M = Cd or Pb)	102
Figure 3.2	Experimental set-up for colloidal syntheses of nanocrystals	104
Figure 3.3	Extraction of ricinoleic acid from castor oil for syntheses of diricinoleate carboxylates of zinc (3) and manganese (4)	105
Figure 3.4	Reaction scheme for syntheses of ligand $[Na(S_2CN(thiq))]$ , $[Zn(S_2CN(thiq))_2]$ (5) and $[Mn(S_2CN(thiq))_3]$ (6) complexes	109
Figure 4.1.1	$^1H$ NMR of castor oil	117
Figure 4.1.2	TGA curves of cadmium(II) ethyl xanthate (1) and lead(II) ethyl xanthate (2) (at 30 – 600 C under nitrogen, at heating rate of 10 C min <sup>-1</sup> )	118
Figure 4.1.3	p-XRD patterns of CdS nanocrystals synthesized by heating up cadmium ethyl xanthate in castor oil at 200 C and 280 C for 15 minutes	119
Figure 4.1.4	(a) UV-Vis spectra of CdS nanocrystals synthesized at 180, 200, 220, 240 and 280 °C by heating up cadmium ethyl xanthate in castor oil for 15 minutes, (b) Tauc plot showing estimation of band gap energy, and (c) Plot of band gap energy and particle size against reaction temperature	121
Figure 4.1.5	UV-Vis spectra of CdS nanocrystals synthesized at 200 C via heating up cadmium	121

	ethyl xanthate in castor oil at different (a) reaction time and (b) concentration of precursor	122
Figure 4.1.6	PL spectra of CdS nanocrystals synthesized at different temperatures via heating up cadmium ethyl xanthate in castor oil for 15 minutes	123
Figure 4.1.7	TEM images of CdS nanocrystals synthesized at 200 C via heating up cadmium ethyl xanthate in castor oil for 15 minutes, (a) micrograph at 100 nm magnifications, (b) micrograph at 50 nm magnifications, and (c) nanoparticles size distribution	125
Figure 4.1.8	XRD patterns of PbS nanoparticles synthesized by heating up lead(II) ethyl xanthate in castor oil at 140, 160 and 180 °C for 15 minutes	127
Figure 4.2.1	<sup>1</sup> H NMR of (a) ricinoleic acid isolated from castor oil and (b) standard ricinoleic acid bought from Sigma-Aldrich	133
Figure 4.2.2	TGA pattern of decomposition of [Zn(Ra) <sub>2</sub> ] carboxylate precursor	130
Figure 4.1.9	TEM images of PbS synthesized at (a) 140 C (showing nanoplates and rod) and (b) 200 °C (showing nanobelts) via heating up lead(II) ethyl xanthate in castor oil for 15 minutes	128
Figure 4.1.10	NIR spectra (a) and Tauc's plot (b) of PbS nanocrystals synthesized (at 30 – 600 C under nitrogen, at heating rate of 10 C min <sup>-1</sup> )	134
Figure 4.2.3	p-XRD pattern of ZnS nanoparticles obtained by decomposing zinc diricinoleate carboxylate complex in oleylamine/dodecanethiol solvent system at 300 C for 1 hour. The red lines are standard pattern sphalerite ZnS	136
Figure 4.2.4	Graphs showing (a) Absorption spectrum (The insert graph is the carboxylate complex in oleylamine/dodecanethiol at 300 C for 1 hour	138
Figure 4.2.5	Correlation between particle sizes of ZnS nanoparticles determined by XRD and UV-Vis methods	140
Figure 4.2.6	p-XRD patterns of ZnS nanoparticles obtained by decomposing diricinoleate carboxylate precursors in oleylamine/dodecanethiol at different temperatures for 1 hour. The blue lines are standard patterns for sphalerite ZnS	141
Figure 4.2.7	The effect of reaction time on (a) p-XRD pattern, (b) absorption spectra and (c) optical band gap energy of ZnS nanoparticles synthesized by colloidal thermolysis of zinc diricinoleate precursor in oleylamine/ dodecanethiol	143

Figure 4.2.8	Temporal evolution of the average particle size of ZnS nanoparticles at different temperatures	145
Figure 4.2.9	Arrhenius plot of $\ln(k)$ against the reciprocal temperature. The slope of the linear fit yields the activation energy (i.e. slope = $E_A/R$ ) for the coarsening of the ZnS nanoparticles in oleylamine.	147
Figure 4.3.1	FT-IR spectra of castor oil, ricinoleic acid and zinc diricinoleate Tauc's plot showing the optical band gap energy), (b) TEM image and (c) particles size distribution histogram of the ZnS nanoparticles obtained by decomposing zinc diricinoleate complex	151
Figure 4.3.2	Characteristic FT-IR spectra ( $\nu(\text{COO}^-) = 1300 - 1700 \text{ cm}^{-1}$ ) of (a) $[\text{Zn}(\text{Ra})_2]$ and (b) $[\text{Mn}(\text{Ra})_2]$ indicating a bidentate coordination mode in the carboxylate complexes, and (c) FT-IR of $[\text{Zn}(\text{Ra})_2]$ showing the effect of washing the complexes with acetone	152
Figure 4.3.3	Plot of Mn wt.% found in elemental analyses of $\text{Mn}_{1-x}\text{Zn}_x\text{S}$ ( $0 \leq x \leq 0.1$ ) nanocrystals produced by colloidal thermolysis at 300 C by (a) EDX and ICP-OES spectroscopies as a function of varying Mn wt.% in the colloidal thermolysis feed, (b) plot showing correlation of Mn wt.% determine by EDX and ICP-OES	155
	oleylamine/dodecanethiol at 300 C for 1 hour	156
Figure 4.3.5	Molecular structures of face-centered cubic ZnS (sphalerite) unit cell (a) in 3-dimensional and (b) in 2-dimensional crystal structures, and (c) rocksalt structure of MnS (alabandite). The violet, yellow and pink balls are zinc, sulfur and manganese atoms respectively	157
Figure 4.3.6	Lattice parameter measured by p-XRD against increasing Mn wt.% (measured) in ZnS. Bullet in red is the standard lattice parameter for ZnS (AMCSD 0000110)	160
Figure 4.3.7	TEM images of (a) undoped ZnS nanocrystals and its (b) particles size distribution histogram, (c) $\text{Mn}_{0.0386}\text{Zn}_{0.9614}\text{S}$ nanocrystals and its (d) particles size distribution histogram	161
Figure 4.3.8	(a) Absorption spectra of (i) ZnS, (ii) $\text{Mn}_{0.0084}\text{Zn}_{0.9916}\text{S}$ , (iii) $\text{Mn}_{0.0386}\text{Zn}_{0.9614}\text{S}$ , (iv) $\text{Mn}_{0.0594}\text{Zn}_{0.9406}\text{S}$ and (v) $\text{Mn}_{0.0721}\text{Zn}_{0.9279}\text{S}$ . (Insert is Tauc's plot used in estimating the band gap energy). (b) Plot showing changes in band gap energy with increasing Mn dopant concentration: band gap energies obtained in the present work (●) and literature (*)	163
Figure 4.3.9	(a) Molecular representation of unit cell crystal structure of sphalerite ZnS with one $\text{Zn}^{2+}$ replaced with $\text{Mn}^{2+}$ , (b) electronic configuration of $\text{Zn}^{2+}$ , $\text{Mn}^{2+}$ and $\text{S}^{2-}$ (c) band structure of $\text{Mn}_x\text{Zn}_{1-x}\text{S}$	164

Figure 4.3.10	PL spectra showing the luminescence of the $Mn_xZn_{1-x}S$ nanoparticles where x is equal to (a) 0.0084, (b) 0.0386, (c) 0.0594, (d) 0.0721	165
Figure 4.3.11	EPR spectra of (a) undoped ZnS, (b) 0.1 % (feed), (c) 0.32 %, (d) 0.84 % and (e) 7.21 % Mn-doped ZnS nanocrystals produced by thermolysis of diricinoleate carboxylates in	
Figure 4.3.4	p-XRD patterns of (a) ZnS, $Mn_xZn_{1-x}S$ where x is equal to (b) 0.0085, (c) 0.0386, (d) 0.0594, (e) 0.0721 and (f) MnS nanocrystals obtained by decomposing diricinoleate carboxylate precursors in	
	(5) and $[Mn(S_2CN(thiq))_3]$ (6) recorded from 30 °C to 600 °C under nitrogen gas, at heating rate of 10 °C min <sup>-1</sup>	173
Figure 4.4.3	Thermal decomposition of manganese (III) tris(tetrahydroisoquinolanyl dithiocarbamate), ( $[Mn(S_2CN(thiq))_3]$ )	174
Figure 4.4.4	Plot of wt.% Mn found in elemental analysis of $Mn_{1-x}Zn_xS$ ( $0 \leq x \leq 0.1$ ) nanoparticles produced by colloidal thermolysis of complexes (5) and (6) at 280 °C by (a) EDX or ICP-OES spectroscopies as a function of varying wt.% of Mn in the colloidal thermolysis feed, (b) plot showing comparison of wt.% of Mn determined by EDX and ICP-OES	176
Figure 4.4.5	p-XRD patterns of (a) ZnS and (b) MnS nanoparticles synthesized by thermal decomposition of heterocyclic dithiocarbamate complexes in oleylamine at 280 °C for 1 hour (the insert graph is a plot for estimation of the crystallite size). The red, blue and green lines are standard sphalerite ZnS, wurtzite ZnS and alabadite MnS respectively. w represent wurtzite	177
	oleylamine/dodecanethiol at 300 °C for 1 hour	167
Figure 4.4.1	Comparison of FT-IR spectra of the ligand $[Na(S_2CN(thiq))]$ and the complexes $[Zn(S_2CN(thiq))_2]$ (5) and $[Mn(S_2CN(thiq))_3]$ (6)	172
Figure 4.4.2	TGA of the ligand $[Na(S_2CN(thiq))]$ , complexes $[Zn(S_2CN(thiq))_2]$ wurtzite ZnS and alabadite MnS respectively	179
Figure 4.4.7	Lattice parameter measured by p-XRD as against increasing Mn wt.% concentration (measured) in $Mn_xZn_{1-x}S$ . Bullet in red is the standard lattice parameter for ZnS	180
Figure 4.4.8	TEM images of 0.76 % Mn-doped ZnS nanoparticles at different magnifications (a) 100 nm, (b) 50 nm and (c) 20 nm and (d) the particles size distribution histogram	181
Figure 4.4.9	Graphs showing (a) absorption spectra and band gap energies of Mn-doped ZnS nanoparticles (Insert graph is Tauc's plot), and (b) plot of the band gap energy against Mn wt.% concentration measured in the doped samples	183

Figure 4.4.10	Graphs showing (a) PL spectra of undoped ZnS and 0.76 % Mndoped ZnS and (b) EPR spectra of (i) 0.76 % and (ii) 6.98 % Mndoped ZnS nanoparticles	185
Figure 4.5.1	Comparison of p-XRD patterns of ZnS and MnS obtained by thermal decomposition of (a) bis(tetrahydroisoquinolinyldithiocarbamato) zinc, (b) zinc diricinoleate carboxylate, (c) bis(tetrahydroisoquinolinyldithiocarbamato) manganese and (d) manganese diricinoleate carboxylate in oleylamine. The red and blue lines in (a) and (b) are standard sphalerite ( <i>s</i> ) and wurtzite ( <i>w</i> ) phases of ZnS. The red lines in (c) and (d) are standard alabandite MnS	189
Figure 4.5.2	Plot of (a) lattice parameter obtained from p-XRD patterns of $Mn_xZn_{1-x}S$ nanocrystals, (b) Mn wt.% measured (by EDX) in $Mn_xZn_{1-x}S$ nanocrystals, against Mn wt.% in feed	191
Figure 4.5.3	Plot of optical band gap energies of $Mn_xZn_{1-x}S$ nanocrystals against Mn wt.% (feed)	192
Figure 4.4.6	p-XRD patterns for (a) ZnS, $Mn_xZn_{1-x}S$ where x is equal to (b) 0.0076, (c) 0.0158, (d) 0.0253, (e) 0.0321, (f) 0.0524, (g) 0.0698 and (h) MnS nanoparticles obtained by decomposing tetrahydroisoquinoline dithiocarbamate complexes in oleylamine at	

## LIST OF ABBREVIATIONS

p-XRD	Powder X-ray Diffraction
EPR	Electron Paramagnetic Resonance
TEM	Transmission Electron Microscope
HRTEM	High Resolution TEM
TOP	Tri-n-octylphosphine
TOPO	Tri-n-octylphosphine oxide
VOs	Vegetable oils
SSPs	Single Source Precursors
QDs	Quantum Dots
NP	Nanoparticles
Eg	Energy gap

NC	Nanocrystal
OR	Ostwald Ripening
OA	Oriented Attachment
AMCSD	American Mineralogist Crystal Structure Database
NMR	Nuclear Magnetic Resonance
MFASs	Metal Fatty Acid Salts
UV-Vis	Ultra-violet Visible
ICDD	International Centre for Diffraction Data
CO	Castor Oil
RA	Ricinoleic Acid
PL	Photoluminescence
FTIR	Fourier Transform Infra-Red
MS	Mass Spectroscopy
CHNS	Carbon Hydrogen Nitrogen Sulfur
TGA	Thermogravimetric Analysis
ICP-OES	Inductively Coupled Plasma-Optical Emission Spectroscopy
ESI	Electrospray Ionization
SEM	Scanning Electron Microscope
EDX	Energy Dispersive X-ray
NIR	Near Infra-Red
FWHM	Full Width Half Maximum

# KNUST

## **ACKNOWLEDGEMENTS**

I would like to first acknowledge the Leverhulme Trust - Royal Society Africa Awards and The Royal Society – Department for International Development (DFID) Africa Capacity Building Initiative Grant for their financial support.

Many thanks to my supervisor Prof. Johannes A. M. Awudza of the Department of Chemistry, KNUST, and his research collaborators, Prof. Paul O'Brien (CBE, FRS) of the School of Chemistry, University of Manchester, UK and Prof. Neerish Revaprasadu of the University of Zululand, South Africa for their support and mentoring throughout my research.

Thanks to Dr. Peter Matthews, Mr. Simon McAdams, Dr. Claire Lydon, Dr. Nicky Savjani, Dr. Paul McNaughter, Dr. David Lewis, Dr. Azad Malik and the entire Prof. Paul O'Brien's group at the University of Manchester, for their support and inspiration. I acknowledge the support and

encouragement of Prof. Imelda Bates, Dr. Stefanie Gregorius and the entire monitoring team from the Liverpool School of Tropical Medicine (Capacity Research Unit (Department of International Public Health)), UK. Many thanks to Miss. Adjoa Anyimadu, Miss. Natasha Bevan and Mr. Paul McDonald of the Royal Society, UK, for their effort in ensuring smooth running of the RS-DFID project in Africa.

I would like to thank the following for their immense technical and administrative support: Dr. Chris Wilkins, Dr. John Waters, Dr. John Warren, Dr. Gary Harrison, Dr. Inigo Vitorica Yrezabal, Dr. George Whitehead, Dr. Chris Muryn, Dr. Mark Vincent, Mr. Martin Jennings, Mr. Masqood, Dr. Mike Faulkner, Mrs. Christine Taylor, Mr. Gareth Smith, Miss Seena Patel all of the University of Manchester and Prof. Motaung Tshwafo, Dr. Sixberth Mlowe and Mr. Johannes Buthelezi of University of Zululand, South Africa.

I would like to acknowledge Dr. Nathaniel Owusu Boadi, my colleague Miss. Selina Ama Saah and all the lecturers of the Department of Chemistry, KNUST, for their significant contributions made to this work, not forgetting their advice and encouragement.

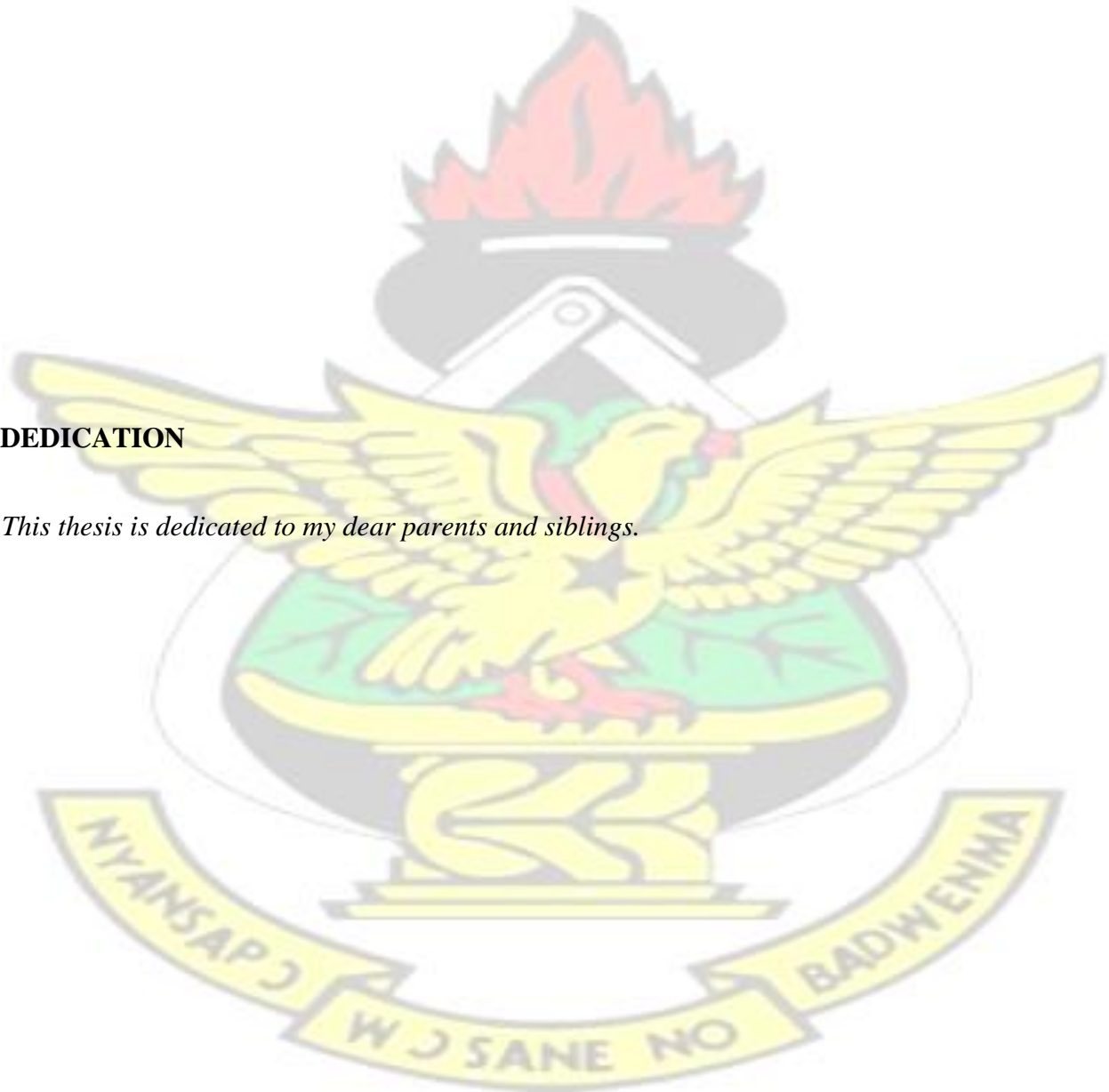
I would like to thank Mrs. Josephine Awudza (UK), the late Auntie Grace Antwi (UK), Prof. and Mrs. Opoku and family (South Africa) and everyone who in one way or the other made preparations for me in all my visits to Manchester and South Africa.

Finally, I would like to thank my family and Church for their prayers and love, and all friends at KNUST, for their continuing love and support. I am eternally grateful.

# KNUST

## DEDICATION

*This thesis is dedicated to my dear parents and siblings.*



## CHAPTER 1

### GENERAL INTRODUCTION

#### 1.1 Background

Metal chalcogenide nanomaterials are a technologically useful class of luminescent inorganic compound semiconductors with interesting size-dependent opto-electronic and surface properties (Jiang et al., 2014; Shen and Wang, 2012; Wu and Yan, 2013). The fascinating size-dependent properties of these materials emanate from quantum confinement effect, which is the systematic transformation of the density of electronic energy levels of nanocrystals as the particle size reduces (Alivisatos, 1996). Metal chalcogenides refer to compounds consisting of metal(s) (e.g. usually transition metals or post-transition metals) and chalcogen(s) (group VI of the Periodic Table: usually sulphur (S), selenium (Se) and tellurium (Te)).

Cadmium sulphide (CdS), lead sulphide (PbS), zinc sulphide (ZnS), manganese sulphide (MnS) and manganese-doped ZnS ( $\text{Mn}_x\text{Zn}_{1-x}\text{S}$ ) are important metal chalcogenide semiconductors which have significant impact on our daily lives as they have potential application in bioimaging, biomedical labeling, catalysis, sensing, photovoltaics, displays (e.g. light emitting diodes, LED), batteries, data storage and electronic devices (Peng et al., 2005; Lai et al., 2012; Donne et al., 2013; Ng et al., 2016; Zaera, 2012; Sitbon et al., 2014; Wu and Yan, 2013; Malik et al., 2010). Hot-injection (HI) and heat-up (HU) techniques are established procedures for synthesizing good

quality nanocrystals. The former technique involves the injection (using a syringe) of the dissolved precursor(s) into preheated solvent whilst the latter requires no injection (Kwon and Hyeon, 2009).

Murray and coworkers (1993) for the first time synthesized high quality luminescent cadmium chalcogenide (CdS, CdSe and CdTe) nanocrystals via pyrolysis of organometallic precursors by injecting into hot coordination solvents (i.e using the HI technique) at temperatures from 290 – 320 °C. They employed dimethylcadmium as metal source, bis(trimethylsilyl)sulphide, bis(trimethylsilyl)selenium and bis(tert-butyltrimethylsilyl)tellurium as the chalcogen precursors and tri-n-octylphosphine (TOP) and tri-n-octylphosphine oxide (TOPO) as coordinating solvents. They obtained good quality monodispersed nanocrystallites from 12 – 115 Å (in diameter) with consistent crystal structure and surface derivatization (Murray et al., 1993). Since then, these chemical reagents have been employed as key chemicals in the traditional syntheses of nanocrystals (Chang and Waclawik, 2014; Qu et al., 2001). However, the phosphine based solvents are extremely toxic, unstable, pyrophoric, explosive (at high temperatures) and expensive, and have potential negative impact on health and environment (Peng and Peng, 2001; Akhtar et al., 2010).

Consequently, many phosphine-free syntheses, which employ less toxic chemicals, have been reported as green approach to syntheses of metal chalcogenide nanomaterials (Malik et al., 2010; Sun et al., 2009; Qu et al., 2001; Pradhan et al., 2003; Sapra et al., 2006). Green chemistry principles embody the (i) design of less hazardous chemical synthesis, (ii) use of safer chemicals and solvents, (iii) use of renewable feedstocks and (iv) design of degradation (Alam et al., 2013). The green routes employed for nanomaterials syntheses include the use of environmentally benign (i) solvents such as vegetable oils, (ii) fatty acids, and (iii) single molecular precursors (or single

source precursors, SSPs) such as xanthates and dithiocarbamate inorganic complexes (Akhtar et al., 2010; Dickerson et al., 2005; Malik et al., 2010).

Metal oxides, sulphides and selenides have been prepared using vegetable oils and fatty acids as (i) both solvents and capping agents, (ii) co-solvents (mixture of solvents) and, (iii) metal fatty acid carboxylate salts (Akhtar et al., 2010; Liu et al., 2008; Pereira et al., 2012; Xiao et al., 2012). For biomedical applications (e.g. staining of proteins), nanoparticles should be biocompatible and easily functionalized or chemically modified on their surfaces in order to tailor their interaction with target biomolecules (Alam et al., 2013; Resch-Genger et al., 2008; Thanh and Green, 2010). Ligands used for nanoparticles surface functionalization must have minimal cytotoxicity and be specific to the targeted biomolecule. Vegetable oils and fatty acids meet these requirements (Thanh and Green, 2010).

Castor oil, olive oil, sunflower oil, almond oil, rapeseed oil, corn oil, palm oil and coconut oil have been applied as solvents in syntheses of metal, metal chalcogenide and upconversion nanoparticles as well as biodegradable nanocomposites (Kyobe et al., 2016; Pereira et al., 2012; Bastami and Entezari, 2010; Xiao et al., 2012; Mondal et al., 2012; Nyamen et al., 2014; He et al., 2014; Qu et al., 2001). Among the plant oils applied in nanomaterial syntheses, castor oil is non-edible, and provides versatile chemistry opportunities (because of its polyol functionality) (Vaisman et al., 2008; Lattuada and Hatton, 2007). The chemical structures of tricinolein (a major triglyceride in castor oil) and ricinoleic acid are shown in Figure 1.1.

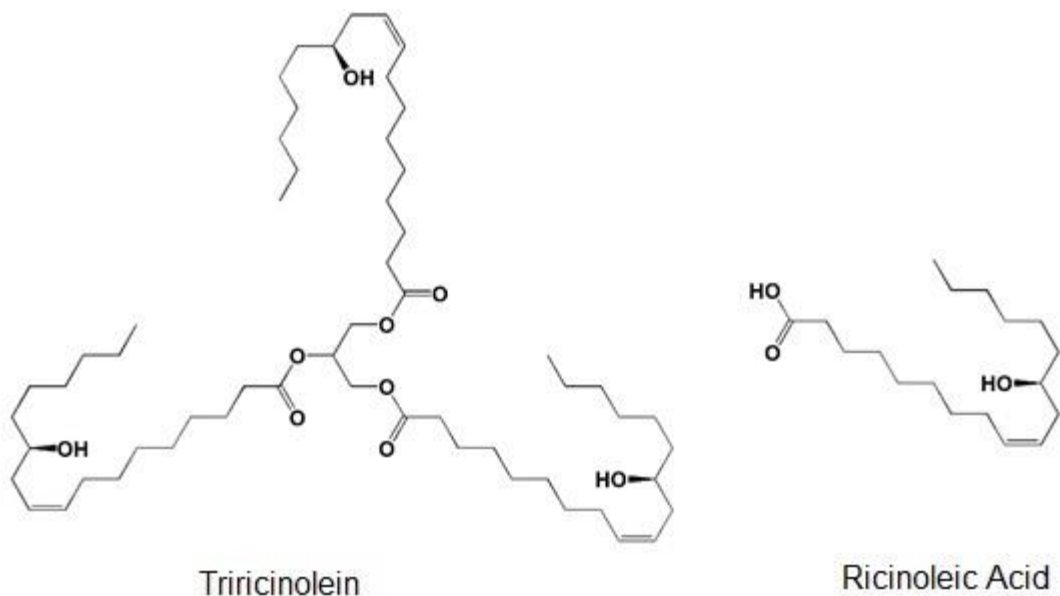


Figure 1.1: Chemical structures of triricinolein and ricinoleic acid (major fatty acid in castor oil, (90 %))

Fatty acids are extensively applied in nanomaterials syntheses as capping agents for nanoparticle surface modification (Chang and Waclawik, 2014). Another very useful and promising application of fatty acids is the formation of metal carboxylate complexes (Chen et al., 2009). Metal carboxylates or metal fatty acid salts are polyvalent metal soaps, prepared either by (i) metathesis of sodium or potassium fatty acid salt with metal salts in aqueous or polar solvents, (ii) dissolution or fusion of metal oxides (or hydroxides, oxy-hydroxides, hydrocarbonates, carbonates) in hot fatty acids and (iii) direct reaction of metals with hot fatty acids (Chen et al., 2009). The thermal decomposition of metal carboxylates in appropriate organic solvents such as alkylamines and alkylthiols has become an attractive green route to large scale production of metal chalcogenide nanoparticles (Choi et al., 2008; Cha et al., 2007; Pereira et al., 2012). This route yields very reproducible results and provides avenue for a wide range of naturally existing fatty acids such as

ricinoleic acid (derived from castor oil) to be employed (Srivastava et al., 2010; Kwon and Hyeon, 2008).

Apart from the use of vegetable oils, fatty acids and fatty acid metal carboxylates, O'Brien and coworkers over the years have championed the syntheses of nanoparticles by the thermal decomposition of SSPs in high boiling point organic solvents (Abdelhady et al., 2013; Byrom et al., 2000; Fan et al., 2007; Mlondo et al., 2009; Mlowe et al., 2014; Nair et al., 2002). This approach is less toxic compared to the chemical precursors employed by Murray et al., (1993). The SSPs route has been viewed to be innovative and facile route to the syntheses of good quality crystalline nanomaterials. A single molecular precursor (or SSP) contains all the required elements for synthesizing the semiconductor compound. Chemical structures of dithiocarbamate and xanthate SSPs are shown in Figure 1.2. SSPs have advantages such as (i) facile control over stoichiometry of the nanoparticles, (ii) low toxicity, (iii) easy to handle, and (iv) substituent groups in SSPs can serve as capping agents for controlling the size, shape and structure of nanoparticles (Fan et al., 2007).

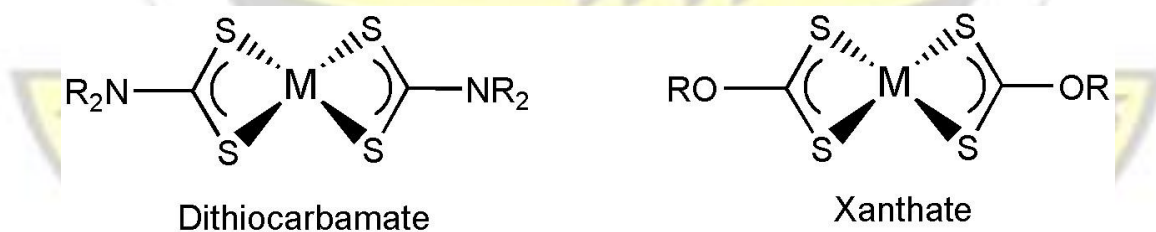


Figure 1.2: Chemical structures of dithiocarbamate and xanthate single source precursors

## 1.2 Problem Statement and Justification

The involvement of toxic chemicals in the traditional route to the syntheses of metal chalcogenide semiconductor nanoparticles hampers large-scale production and limits their application (Akhtar et al., 2010). The green routes on the other hand are adaptable to large-scale production and are considerably benign (Kim et al., 2011). However, the green routes are of recent interest and have received less research attention. The materials considered in this work for green synthesis of metal chalcogenide nanoparticles are castor oil, ricinoleic acid, xanthate and dithiocarbamate complexes.

### 1.2.1 Research Gaps

#### 1.2.1.1 Castor oil and ricinoleic acid

The application of castor oil and ricinoleic acid in the synthesis of metal chalcogenides is limited. Kyobe et al. (2016) synthesized CdS nanoparticles by reducing sulphur using sodium borohydride in deionized water and reacting with cadmium chloride under inert conditions at room temperature. The resultant CdS nanoparticles were stabilized by dispersing in castor oil or ricinoleic acid and then injecting into hot castor oil or ricinoleic acid at  $\geq 230$  °C. Their results showed that the near spherical castor oil capped cubic CdS nanoparticles were 4.64 nm in size compared to 5.56 nm for ricinoleic acid capped CdS nanoparticles. The author used similar approach to synthesize PbS, PbSe and PbTe (Kyobe et al., 2016). The nanoparticles obtained were less monodispersed. Shombe et al. (2015) synthesized 10 – 15 nm size spherical CdS nanoparticles by the thermal decomposition of pyridine and tetrahydroquinoline dithiocarbamate

complexes of Cd in castor oil and ricinoleic acid at 190 – 300 °C using the HI technique. Other researchers using laser ablation, sputtering and co-precipitation methods, have synthesized iron oxide and metallic (Ag and Au) nanoparticles by employing castor oil and ricinoleic acid as stabilizing/capping agents (Zamiri et al., 2011; Wender et al., 2010; Da Silva et al., 2008). From these works, the following research gaps have been identified:

1. Metal chalcogenide nanoparticles have not been synthesized using castor oil and the heatup method. The high viscosity of castor oil makes it unattractive for the traditional hotinjection technique due to the poor solubility of precursors in castor oil at room temperature. However, this problem of viscosity was not mentioned by Kyobe et al. (2016) and Shombe et al. (2015) when they employed the hot-injection method for the synthesis of CdS and PbS. Castor oil is a monohydroxy lipid and contains large amount (90 %) of ricinoleic acid (*12-hydroxy-9-cis-octadecenoic acid*) (Figure 1.1) (Vaisman et al. 2008). These properties make castor oil more suitable for applications requiring highly stable and polar organic solvent-nanoparticles colloidal dispersions (e.g. lubricants) (Lattuada and Hatton, 2007). The high viscosity is due to the formation of hydrogen bonding between the hydroxylated triglyceride molecules (Isbell, 2011). This increases the steric hindrance of the oil leading to the formation of weakly bound dimers and trimers of the original triglycerides, resulting in a very high viscosity of 260.4 cSt at 40 °C (Isbell, 2011). The heat-up method requires no injection of precursors and overcomes the problem of injecting highly viscous castor oil.
2. To obtain good quality nanocrystals, high temperature ( $\geq 250$  °C) organometallic synthesis is unavoidable (Lesnyak et al., 2012). Unfortunately, vegetable oils are unstable at elevated temperatures. Pereira et al. (2012) synthesized ZnO nanoparticles by

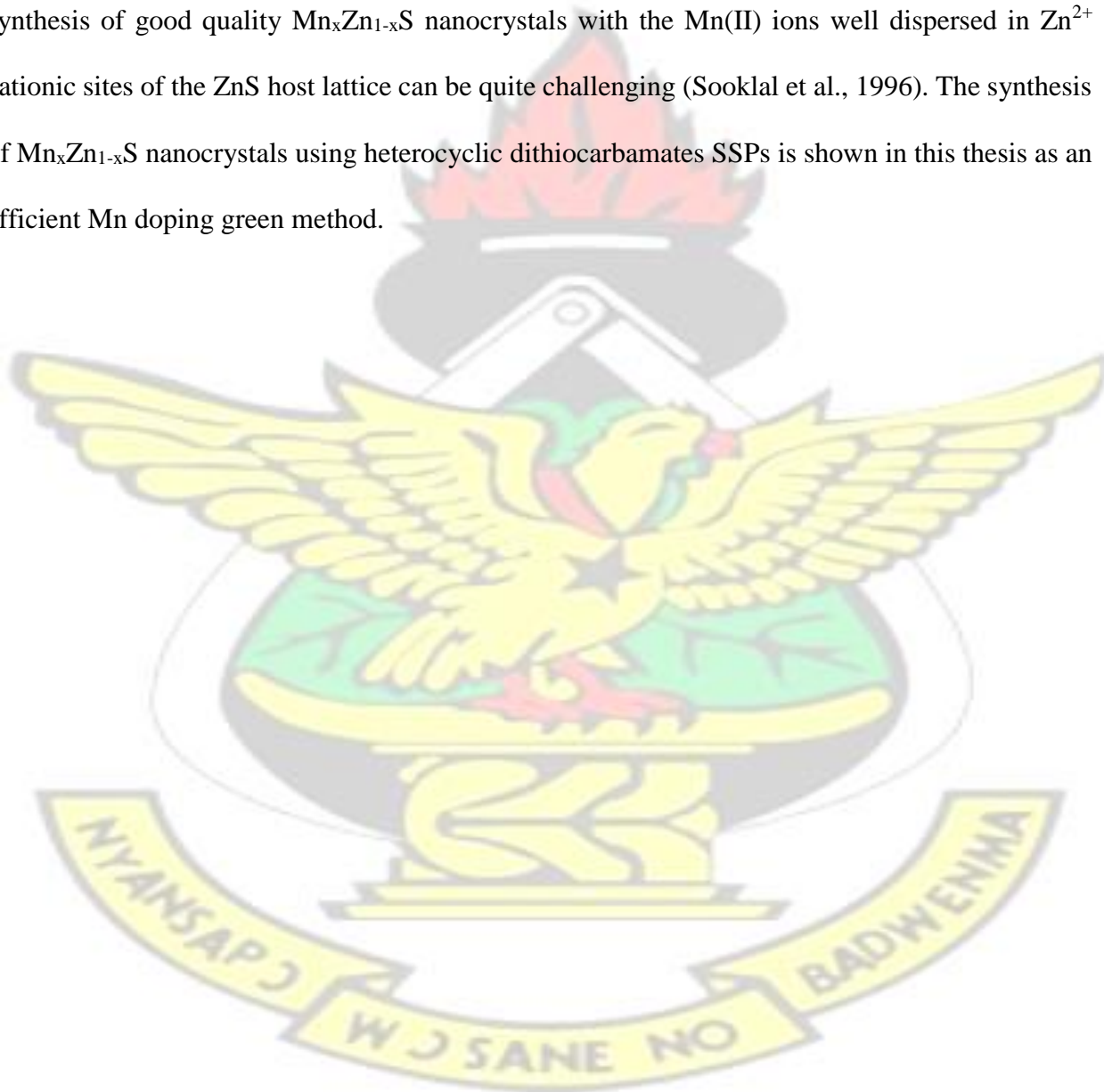
decomposing zinc oleate in sunflower oil at 250 – 310 °C. At 310 °C the sunflower oil was found to fully decompose (to esters, ketones, aldehydes, carbonates and fatty acids) and the formation of the ZnO nanoparticles was hindered. Castor oil is not suitable for high temperature synthesis due to the possible oxidation of the OH groups to ketones (Lattuada and Hatton, 2007). However, the only work that reports on thermal decomposition of SSPs in castor oil and ricinoleic acid employed dithiocarbamate complexes which have high decomposition temperatures above 250 °C. Thus, complexes such as xanthates with low decomposition temperatures ( $\leq 250$  °C) are more suitable precursors for the syntheses of chalcogenide nanoparticles in castor oil (McNaughton et al., 2016).

3. Ricinoleic acid has only been applied as solvent and capping agent in metal chalcogenide nanoparticles syntheses and not as a source of fatty acid carboxylate precursor/capping agent. The thermal decomposition of fatty acid carboxylate precursors in high boiling point organic solvent such as oleylamine yields more reproducible monodispersed crystalline nanoparticles compared to using vegetable oils as solvent (Choi et al., 2009). The fatty acid acts as both ligand (in the formation of the carboxylate complex) and capping agent for controlling the morphology and size of the nanoparticles. Ricinoleic acid metal carboxylate precursors are shown in this thesis as one of the potential applications of castor oil in the synthesis of monodispersed metal chalcogenide nanoparticles.

### **1.2.1.2 Single source precursors**

Single source precursors (SSPs) have been extensively employed in the synthesis of binary (e.g.

CdS, PbS, ZnS, CuS, MoS) and ternary (e.g. MnZnS, CdZnS, MnCdS) chalcogenide nanoparticles (Malik et al., 2010; McNaughter et al., 2016; Nair et al., 2002). Mn-doped ZnS ( $Mn_xZn_{1-x}S$ ) nanocrystals are ternary chalcogenide that comprise of relatively benign elements compared to the closely related Cd-doped nanocrystals (Ban et al., 2013; Srivastava et al., 2010; Yang et al., 2005).  $Mn_xZn_{1-x}S$  nanocrystals possess longer dopant emission and good photostability. However, the synthesis of good quality  $Mn_xZn_{1-x}S$  nanocrystals with the Mn(II) ions well dispersed in  $Zn^{2+}$  cationic sites of the ZnS host lattice can be quite challenging (Sooklal et al., 1996). The synthesis of  $Mn_xZn_{1-x}S$  nanocrystals using heterocyclic dithiocarbamates SSPs is shown in this thesis as an efficient Mn doping green method.



## 1.3 Objectives

### 1.3.1 Main objective

To synthesize CdS, PbS, ZnS, MnS and Mn-doped ZnS nanoparticles using single molecular precursors and diricinoleate carboxylate complexes.

### 1.3.2 Specific objectives

1. Syntheses of CdS and PbS nanoparticles via colloidal thermolysis of cadmium and lead xanthate complexes in castor oil
2. Study of growth kinetic of ZnS nanoparticles synthesized via colloidal thermolysis of zinc diricinoleate carboxylate precursor and dodecanethiol in oleylamine
3. The synthesis of Mn-doped ZnS nanoparticles via colloidal thermolysis of diricinoleate carboxylate complexes of zinc and manganese in oleylamine/ dodecanethiol. The effect of Mn doping is investigated.
4. The synthesis of Mn-doped ZnS nanoparticles via colloidal thermolysis of tetrahydroisoquinoline dithiocarbamate complexes of zinc and manganese in oleylamine. The effect of Mn doping is investigated.
5. Comparison of ZnS, MnS and Mn-doped ZnS nanocrystals synthesized using the diricinoleate carboxylate and heterocyclic dithiocarbamate routes

## 1.4 Scope of Work

Nanotechnology involves the (i) synthesis and characterization and (ii) potential applications of nanomaterials. This work is only limited to the syntheses and characterization of CdS, PbS, ZnS, MnS and Mn-doped ZnS nanoparticles.



## CHAPTER 2

## LITERATURE REVIEW

# KNUST

### 2.1 Introduction to Nanotechnology

Nanotechnology is an emerging multidisciplinary field which draws expertise from chemistry, physics, biology and engineering for developing new materials with nanometer dimensions which have potential fascinating modern applications in energy, medicine, pharmacy, environmental remediation, food and electronics (Duran and Marcato, 2013). The prefix „*nano*’ in the term „*nanotechnology*’ means a billionth (Poole and Owens, 2003). Though nanotechnology involves a wider scope of science and engineering, the term “nanotechnology” was first introduced by Norio Taniguchi (University of Tokyo) in 1974 to only describe the techniques used to precisely engineer materials whose particle sizes were within the nanometer dimension (Ramsden, 2005). According to Marbaniang and Donboklang, (2014):

*Nanotechnology is defined as the science and engineering involved in the design, synthesis, characterization, and application of materials and devices whose smallest functional organization, in at least one dimension, is on the nanometer scale or one billionth of a meter.*

### 2.1.1 Nanoscience

Nanotechnology strives on the shoulders of „*nanoscience*“. Nanoscience revolves around the science of objects with smallest dimensions ranging from a few nanometers to less than 100 nm where *quantum mechanical phenomenon* become evident, as it reflects in the properties of atoms and molecules which are largely hidden in the classical behaviour of macroscopic matter and structures (Whitesides, 2005). The intriguing behaviour of nano-sized matter was earlier predicted by renowned scientists such as Michael Faraday (in 1857) and Gustav Mie (in 1908) who tried to provide an explanation to why the size of metal particles affects the colours of windows of medieval cathedrals. Richard Feynman (Nobel Prize Winner in Physics in 1965) is also usually remembered by „nanoscientists“ due to his visionary lecture titled “*There is Plenty of Room at the Bottom*” which suggested the possibility of nanosize matter (Poole and Owens, 2003). Although early scientists had nanoscience in mind, it was not well known. But now nanoscience has become a subject of much interest and has received considerable research efforts and thus, useful technologies have been developed based on the inventions (Hobson, 2009).

### 2.1.2 Nanomaterials

The word „*nanomaterials*“ is used to refer to materials having sizes in the nanometer range. To easily understand the nano-dimension of materials discussed here, one has to know that the size of an atom is of the order of  $1 \text{ \AA}$  (0.1 nm) in size and thus, a nano-sized object with 10 nm size would be similitude to a molecule made up of 100 atoms covalently bonded together (Ramsden, 2005). Nanoscale in comparison to microscale and milliscale is shown in Figure 2.1.

Nanostructured materials though not new, have recently received tremendous attention. Examples of materials with nanometer dimensions are proteins, enzymes and DNA on which life strives and also nanosized particles (sources including fire and volcanic eruptions) which already exist naturally in the atmosphere (Albrecht et al., 2006; Dowling, 2004). It is often reported that in the fourth-century A.D. Roman glassmakers were fabricating glasses containing metallic nanomaterials of which the Lycurgus cup residing in the British Museum in London is a perfect example of such artifact. Also the beautiful colours shown by windows of medieval cathedrals are as a result of metallic nanomaterials inculcated in the glass fabrication (Poole and Owens, 2003).

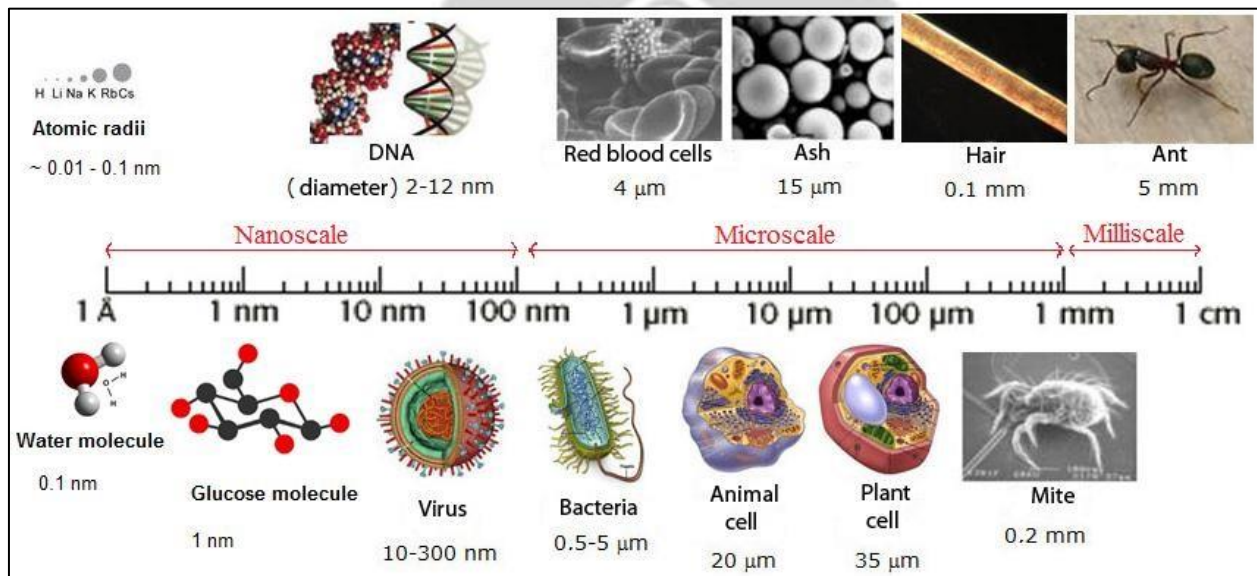


Figure 2.1: Nanoscale in comparison to microscale and milliscale

### 2.1.3 Classification of nanomaterials

Nanomaterials are classified according to the number of dimensions which falls in the nanoscale (1-100 nm) (Figure 2.2) (Purbia and Paria, 2015). Bulk materials have all three dimensions exceeding 100 nm and are classified as three dimensional (3d). Nanomaterials having only one dimension less than 100 nm are classified as two dimensional (2d). Typical examples of 2d nanomaterials are nanobelts and nanoplates. Nanomaterials with two of the dimensions less than 100 nm are classified as one dimensional (1d). Examples of 1d nanomaterial are nanowires and nanorods. Nanomaterials with all the three dimensions less than 100 nm are called nanoparticles and are classified as zero dimensional (0d). Examples of 0d nanomaterials are quantum dots and nanocrystals. The syntheses and applications of 0d nanomaterials have been explored extensively because of their interesting properties due to strong quantum confinement effect.

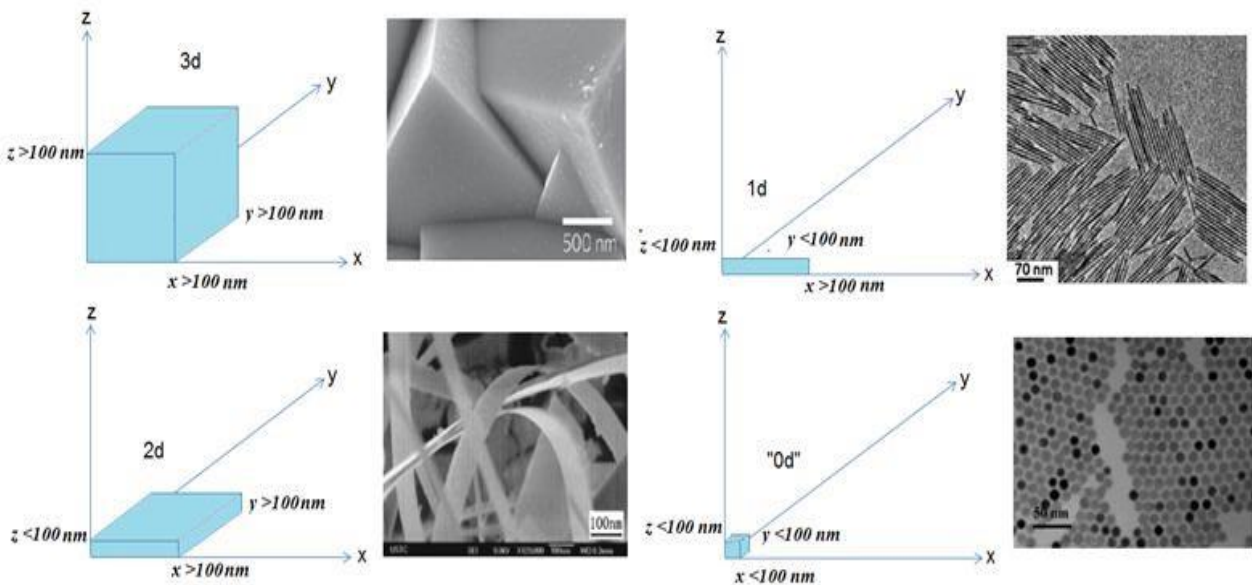


Figure 2.2: Classification of nanomaterials

### 2.1.4 Semiconductor nanomaterials

Semiconductors are materials that have electrical conductivities which fall between metals and insulators. They are classified into two main groups; namely elemental semiconductors (group IV elements) and compound semiconductors. Examples of semiconductors are shown in Figure 2.3.

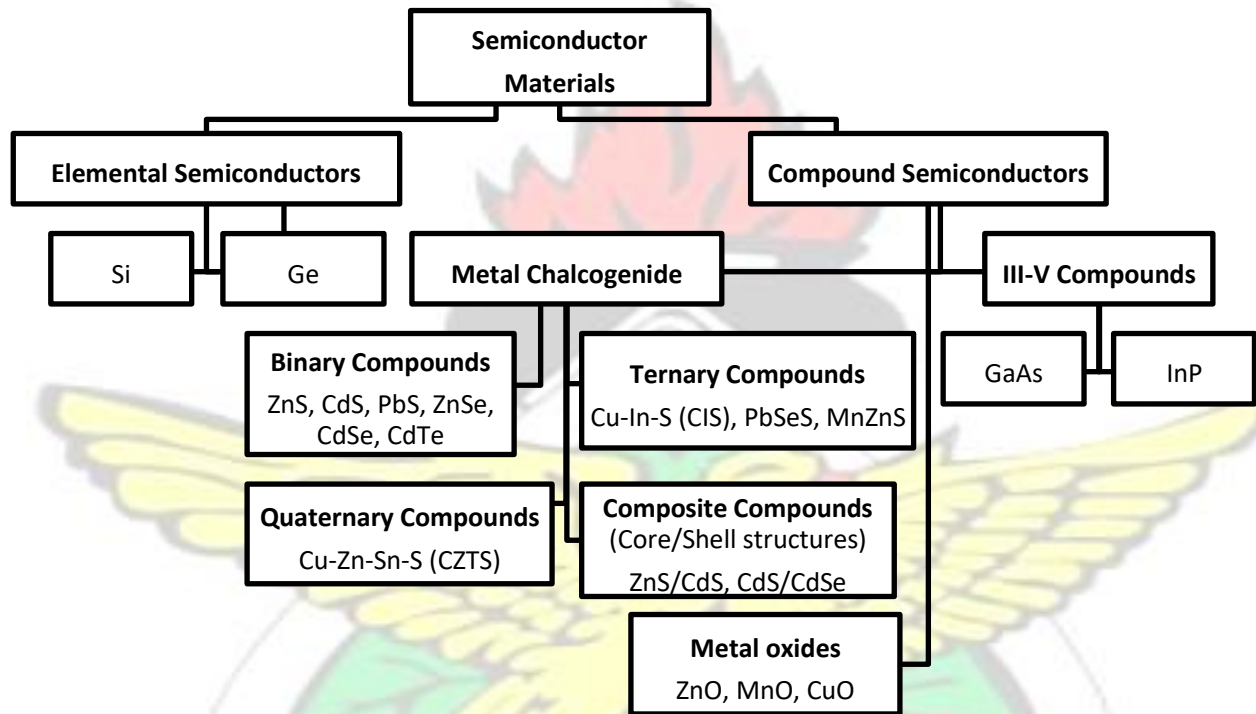


Figure 2.3: Flow chart of different semiconductor materials (source: Poole and Owens, 2003)

The compound semiconductors are technologically very important because of the sheer range of compounds available. Also, compound semiconductors offer the opportunity to synthesize ternary, quaternary and even higher orders of semiconductors by simply alloying the binary compounds together (Poole and Owens, 2003). Semiconductor nanomaterials are found to exhibit interesting optical, electrical and magnetic properties and have been the focus for much

technological advancement. Among the compound semiconductors, the metal chalcogenide nanomaterials (especially II-VI compounds) have been widely studied for applications in solar cells, batteries, photo-catalysis, sensors, light emitting diodes (LEDs) and luminescence devices. The group VI elements (O, S, Se, Te) on the Periodic Table are known as chalcogens, and the term „chalcogenide“ is usually referred to chemical compounds containing at least one of S, Se or Te anion and an electropositive element (e.g. Cd, Zn, Mn, Fe, Pb). The metal oxides are barely considered as chalcogenides.

## **2.1.5 Applications of nanomaterials**

### **2.1.5.1 Energy**

Energy is a vital component of society. Majority of social activities strive on energy: transportation, industry, communication, entertainment, lighting, law enforcement, and education. Energy makes these activities easier, faster, smarter and efficient. Sustainable source of energy is therefore critical to the economy of every nation. Solar energy is seen as one of the most sustainable and abundant source of energy available especially in Africa. Power consumption globally stands approximately at 14 terawatts (TW) ( $14 \times 10^{12} \text{ Js}^{-1}$ ) and is likely to increase to about 25 – 30 TW by 2050 (Baxter et al., 2009). More than 80 % of this power is generated from petroleum, coal and natural gas and less than 1 % from solar, geothermal, wind and biofuels. The earth's surface receives much solar energy (just within 1.5 hours) more than enough to cover the annual power consumption worldwide. That is, given solar cells with 10 % efficiency and land coverage of 1% of the earth's landmass, about 15 TW electrical power could be produced (Baxter et al., 2009). Irrespective of the massive efforts by scientists, engineers and governments to

harness this vast solar energy, photovoltaic (PV) or solar cells efficiencies and prices are still hurdles. Apart from using solar cells to convert solar energy to electricity, solar energy is also used to split water to produce hydrogen fuel which could be used in fuel cells to generate electricity.

Nanomaterials including photo-nanocatalysts (e.g. ZnS, CdS, TiO<sub>2</sub>) and carbon nanotubes (as H<sub>2</sub> storage material) have been instrumental in developing this new and green sources of energy. The application of nanomaterials in lithium rechargeable batteries has drastically improved their efficiency. It is interesting to know that Sony Corporation has commercialized a tin-based anode nanobattery (trade name Nexelion) which demonstrates for the first time a nanoalloy replacing a graphite electrode. Similarly, Toshiba Corporation has also come out with a nano-battery able to be recharged by 80 % within a minute, drastically reducing recharge times. These impressive achievements in electricity generation and storage were made possible with the advent of nanotechnology (Serrano et al., 2009).

#### **2.1.5.2 Healthcare**

A major impact of nanotechnology on medicine is in the area of molecular imaging (MI) and drug delivery (Neves et al., 2010; Zrazhevskiy et al., 2010). MI involves visualization, characterization and quantification of biological processes at the cellular and subcellular levels within living organisms (Massoud and Gambhir, 2003). The advent of biological imaging probes (BIPs) based on quantum dots (QDs) semiconductor nanomaterials has brought profound understanding to physiological and pathological processes such as the evaluation of phenotypes of healthy cells and detection of molecular signature of diseases (Rowland et al., 2015; Zrazhevskiy et al., 2010). In

recent biomedical research, QDs are used as fluorophores in place of the conventional organic pigments which suffer quick photobleaching, spectral overlaps and also requires specific wavelength of excitation. In addition, since the nanometer size and large surface area of QDs are comparable to proteins and small viruses, they are suitable for carrying multiple biomolecules that are involved in the maintenance and metabolic processes in living organisms (Zrazhevskiy et al., 2010; Marbaniang and Donboklang, 2014).

Also, the introduction of magnetic nanoparticles (MNP) as contrast agents in magnetic resonance imaging (MRI) has improved the quality of MRI images. The magnetic property of the MNP allows them to be efficiently separated from complex solutions (e.g. blood) by the magnetic field (Zrazhevskiy et al., 2010). Thus, the MRI image contrast is enhanced by the high longitudinal and transverse relaxivities properties of the MNP (Iv et al., 2015). MRI contrast agents based on iron oxide MNP are recently under clinical trial for visualization of tumors and treatment of iron deficiency anemia (Miller et al., 2015; Iv et al., 2015; German et al., 2015). Ferumoxytol, ferumoxtran-10 and ferucarbotran C are the common MNP under trial as contrast agents, however, only Ferumoxytol has received the approval by the U.S. Food and Drug Administration and some part of Europe for clinical use (Miller et al., 2015; Iv et al., 2015).

Another impact of nanotechnology is in the area of drug delivery. Interestingly, HIV therapies are being improved using nano-drug delivery systems such as polymeric nanoparticles, solid lipid nanoparticles, liposomes, dendrimas, metal nanoparticles and nanoemulsions to curtail inherent problems related to antiretroviral therapy (Neves et al., 2010). Nano-drug delivery systems have also received application in cancer therapy. Compared to the unconjugated cancer therapeutics, nano-systems with sizes less than 100 nm are found to efficiently accumulate within tumors at

higher concentrations and thus yield lower dose-limiting adverse side effects and higher therapeutic efficacies (Stegh, 2012).

Apart from MI and drug delivery, biomarker mapping, detection and diagnosis, gene delivery and targeted therapy are other clinical practices where nanomaterials are being applied (Sanna et al., 2014). The impact of nanotechnology on healthcare cannot be underestimated; however, biomedical research on nanotherapeutics still struggles with problems related to biocompatibility and toxicity of some nanomaterials to living systems.

### **2.1.5.3 Electronic devices**

Computers, phones, flat screen displays, television, radio, security sensors, cameras and household appliances are electronic and optoelectronic devices which cannot be done away with in this our modern society. These devices have profoundly changed the way social activities are done. P-n junctions (e.g. in transistors and diodes) are the basic functional elements or components in these electronic devices and their fabrications are of major concern to chemists and materials scientists (Baugher et al., 2014). Nanotechnology presents a new dimension to the design and fabrication of nanodevices with superior electronic performance. Interestingly, the latest approach to fabrication of electronics (e.g. circuits) is approaching the atomic level, i.e. molecular electronics (Li et al., 2006).

The chemical composition, structure, size, morphology and doping of semiconductor materials are central to the design of p-n junctions. Nanowires based p-n junctions have been developed by Li et al., (2006) using chemical synthetic techniques providing an alternative to the traditional

lithography technique. Also two-dimensional semiconductor nanomaterials have recently attracted much interest as emerging new class of materials possessing wide range of electrical properties suitable for innovative practical applications in electronic device fabrication (Lopezsanchez et al., 2013). Nanotechnology, thus, serves as a tool for discovering new semiconductor materials and approach for fabrication of electronic and optoelectronic devices which are used in almost every social activity.

#### **2.1.5.4 Food**

Nanotechnology holds many benefits to the food industries, consumers and government. Nanotechnology has been applied to food production, food packaging, food processing, food safety, nutrients delivery systems and food analysis, sensing or detection (Duran and Marcato, 2013; Gergely et al., 2010). The advantages are (i) increase of shelf life of packaged food, (ii) protection of food against pathogens, (iii) food quality, alteration or spoilage monitoring, (iv) enhancement of food nutrients and flavours, and (v) ability to incorporate important functionalities (such as antimicrobial, antioxidant and scavenger) (Sekhon, 2010; Duran and Marcato, 2013). Nanocomposite materials with improved mechanical property, reduced weight, and increase heat resistance have been developed for packaging of food. These nanocomposites have improved barrier against oxygen, carbon dioxide, ultraviolet radiation, moisture and volatiles of food packaged materials which lead to food spoilage. Antimicrobial packaging materials have been reported and are found to prolong shelf life of food. They are made by compositing polymers and nanoparticles possessing antibacterial and antifungal properties such as silver and zinc oxide nanoparticles (Duran and Marcato, 2013).

Nanosensors constitute an important area of nanotechnology that has been extensively applied to detect and quantify minute concentrations of toxic compounds and pathogens which are nondestructive. Pest control is one of the major factors which affect agricultural yields and pesticides are usually applied in high concentrations to control pest which end up in food, posing health related problems. The use of nanoparticles for encapsulation and safe delivery or controlled release of pesticides have been reported (Pérez-de-Luque and Rubiales, 2009). Also the detection of pesticide 2, 4-dichlorophenoxyacetic acid using CdTe quantum dots has been reported. Organophosphate pesticides have also been detected in water, fruit and plants using nanosensors. The sensitivity of these nanosensors is enhanced using metal and semiconductor nanoparticles with excellent optical and electrical properties to increase the sensitive transducer signals (Duran and Marcato, 2013). Though the application of nanotechnology in the food industries provide interesting results, however, this area of study is still young and requires thorough health related assessment before releasing products to the market.

#### **2.1.5.5 Clothing**

Nanotechnology can be used to develop textiles with desired characteristics such as high tensile strength, unique surface characteristics, durability, water repellency, fire retardancy, antimicrobial and sensing properties (Sawhney et al., 2008). The extraordinary physical, chemical, mechanical and electrical properties of nanomaterials make them attractive raw material for the clothing industry.

Nanofibres can be spun into mats and yarns and used as nonwoven clothing. Nanofibres endowed with catalytic ability are active against microorganisms and fine particulate matter and they serve

as better protective clothing to the conventional ones. Nanofibres for selective gas permeation ability have been developed as breathing, chemical and biological protective clothing (Thilagavathi et al., 2008). These nanofibres are also embedded with biological and chemical sensors. Integration of nano-sized antimicrobials into textiles leads to improved wound dressing and ultra-violet light protection (Parthasarathi and Thilagavathi, 2011; Sawhney et al., 2008).

Smart uniforms have been developed to be protective against bullets, bioagents and chemical agents for soldiers. These uniforms also have fire-retardant ability. Fire-retardant fabrics are composites of nano-sized clay particles finely dispersed in suitable polymer matrices. They are developed for their stiffness, toughness, tensile strength, thermal stability, gas-barrier properties and their flame retardant property (Thilagavathi et al., 2008).

Interestingly, self-cleaning clothing and next generation textiles have also been reported. The self-cleaning ability is due to the incorporated  $\text{TiO}_2$  nanoparticles which have the ability to oxidize dirt and other contaminants (Thilagavathi et al., 2008). Next generation textiles are sensor and energy-storage fabrics. They are made to convert exerted mechanical force into electrical signals and therefore can be used for monitoring body functions such as heart rhythm and pulse if they are worn next to the skin. These products appear extremely innovative, however, they are not on the market yet for reasons such as unknown health risks (Sawhney et al., 2008).

#### **2.1.5.6 Construction**

Nanotechnology application in the construction industry is in the area of concrete, structural composites, coatings and nanosensors. Nanotechnology offers the opportunity to study the

properties of cementitious materials at the micro and nano-scale. Major reactions such as hydration, alkali-silicate reactions and fly ash have been studied at the nano-scale. Addition of nanomaterials such as nano-SiO<sub>2</sub> and carbon nanotube into cement improves the compressive and flexural strength of the concrete (Rana et al., 2009). Steel is a major structural material. Doping of steel with copper nanoparticles leads to improved steel with higher corrosion resistance and weld ability. Incorporation of TiO<sub>2</sub> nanoparticles into coatings imparts its sterilizing and antifouling properties to materials such as glazing. TiO<sub>2</sub> break down and disintegrate organic dirt via catalytic reaction. Since TiO<sub>2</sub> is hydrophilic, it absorbs water uniformly over the surface and thus, washes away dirty (i.e. self-cleaning) (Pacheco-Torgal and Jalali, 2010; Rana et al., 2009). Other special coatings developed have properties such as antibacterial, thermal control, energy saving and anti-reflection (Pacheco-Torgal and Jalali, 2010; Rana et al., 2009). Nanosensor systems are also now embedded in construction to monitor environmental conditions and materials/structure performance (Rana et al., 2009).

#### **2.1.5.7 Environmental remediation**

The application of nanotechnology in environmental remediation lies in the large surface area of nanoparticles. Nanoparticles are applied as photo-catalyst for degradation of various organic dyes, and also as adsorbent material for chemisorption of toxic chemicals such as heavy metals. Some nanoparticles have anti-fungal and anti-bacterial properties which enable them to be used in water treatment. However, the application of nanotechnology has the risk of releasing toxic chemicals such as Cd and Pb nanomaterials into the environment (Hannah and Thompson, 2008).

## 2.2 Theories and Mechanisms of Nanocrystals Formation

Semiconductor nanomaterials exhibit fascinating size-dependent properties. This size effect greatly influences the optical, electrical, magnetic and thermal properties of the semiconductor.

A facile control or tuning of the particle size leads to effective manipulation of these properties.

The size-dependent properties are due to quantum confinement effect. The most emphasized size-dependent feature of semiconductor nanoparticles is the band gap energy. Extinction coefficient is also a size-dependent property. Extinction coefficient determines the extent of light absorption and the concentration of the semiconductor nanocrystals colloids, but it is less emphasized because of the experimental bottlenecks associated with its determination (Yu et al., 2003).

Apart from the particle size effect, the composition, shape, structure, doping and surface chemistry of the semiconductor nanoparticles also have major influence on the properties (Dushkin et al., 2000). Nanoparticles with different morphologies such as quantum dots, nanocrystals, nanowires, nanorods, nanotetrapods and nanoribbons with interesting optoelectronic properties have been synthesized via chemical methods (Yang and Zhang, 2004; Huang et al., 2012; Kar and Chaudhuri, 2005; Kaur et al., 2016). Nanoparticles by virtue of their nanometer size have larger number of atoms at the surface than the interior and thus, have higher surface to volume ratio. Surface atoms are less coordinated resulting in defects in the nanoparticles. Smaller nanoparticles have major defects. These defects are unsaturated dangling bonds which create trap states (or electronic states) within the forbidden region between the electronic band gaps of the bulk material (Chang and Waclawik, 2014). These trap states trap electrons or holes and thereby substantially alter the optical, electronic, magnetic and thermal properties of the semiconductor. The surface

atoms also contribute to the surface free energy and causes changes in the thermodynamic properties such as melting point and phase transition (Alivisatos, 1996).

### 2.2.1 Quantum confinement

Classical mechanics theories failed on the grounds of size. The German physicist Max Planck (in 1900) came out with the theory of quantization of energy which placed a limit on energy to discrete values bringing about the so-called *quantum mechanics*. The effect of particle size has been very interesting in the development of science. Density of states is a function of size (Alivisatos, 1996). Irrespective of the large surface energy of nanocrystals, the optical and electrical properties are strongly size dependent. This size dependent effect is a reflection of the systematic transformation of the density of electronic energy levels of nanocrystals as the particle size reduces. This phenomenon is known as *quantum size effect*. The band structure of semiconductor nanocrystals lies between the discrete density of state of molecules and the continuous band of the bulk semiconductor (Alivisatos, 1996). The band structure of a semiconductor nanocrystal in relation to the bulk and molecular counterparts is shown in Figure

2.4.

The band gap energies of nanocrystals are larger than that of the bulk material and smaller than the highest occupied molecular orbital/ lowest unoccupied molecular orbital (HOMO/LUMO) energy gap of the molecular semiconductor (Chang and Waclawik, 2014). The band gap energy refers to the energy difference (in electron volts, eV) between the top of the valence band (VB) and the bottom of the conduction band (CB) and is the major determinant of the electrical

conductivity of solids. The band gap energy is therefore the minimum amount of energy required to excite an electron from VB to CB.

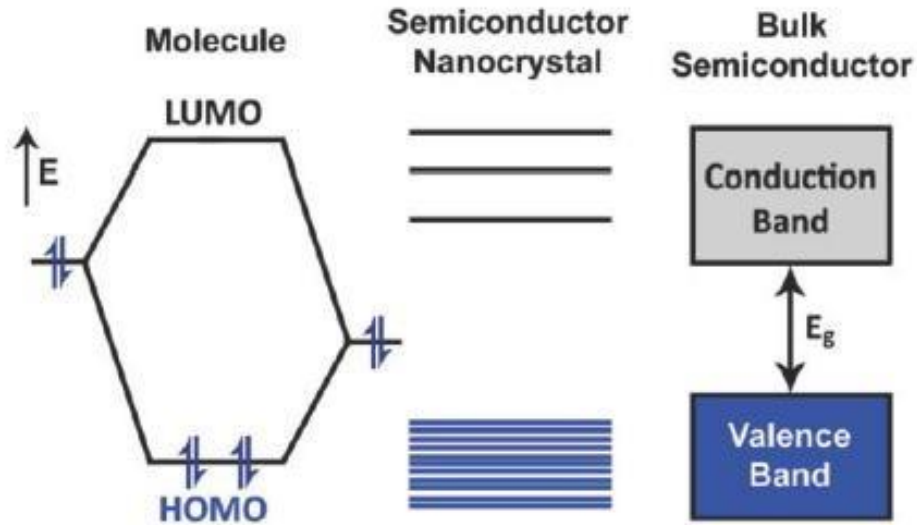


Figure 2.4: A comparison of band gap energies of different types of materials: bulk semiconductor, semiconductor nanocrystals and molecular semiconductor.  $E_g$  is band gap energy (Smith and Nie, 2010; Chang and Waclawik, 2014).

Idealized density of state for band structures of semiconductors with 3, 2, 1 and 0 dimensional structures are shown in Figure 2.5. As the size of a particle reduces, the electronic excitation shifts to higher energy and there is concentration of oscillator strength in few transitions (Alivisatos, 1996). This blue shift (shift to higher energy) is termed as *quantum confinement effect* which occurs when one dimension of the semiconductor become smaller than the Bohr exciton radius (usually between 1-10 nm) of the bulk material leading to modification of the energy levels (Chang and Waclawik, 2014).

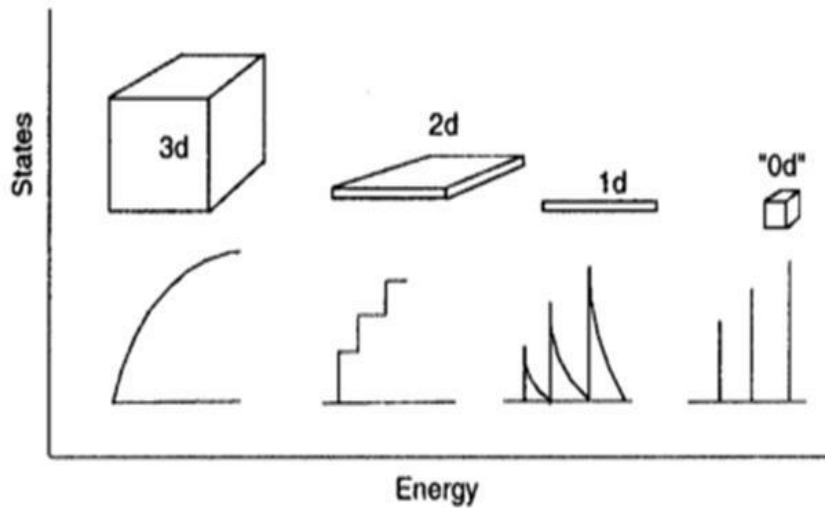


Figure 2.5: Idealized density of state for one band of 3, 2, 1 and 0 dimensional structures

In an idealized density of states, a 3-dimensional structure (e.g. bulk semiconductor) energy levels are continuous and as the material is reduced to a 0-dimensional structure or a molecule (e.g. quantum dot semiconductor) the energy levels become discrete. Energy levels for 2 and 1 dimensional structures are thought to fall between that of 3d and 0d (Alivisatos, 1996). This is similitude to the particle in a box model where the energy of the particle in a 1-dimensional box is quantized by virtue of satisfying the boundary conditions.

### 2.2.2 The LaMer model

The synthesis of semiconductor nanocrystals has been extensively explored using different physical, chemical and biological methods to control the size, shape, structure, composition and surface chemistry of nanocrystals. Size-controlled colloidal synthesis has been the fundamental technique used for manipulating the opto-electronic properties of semiconductors. The LaMer

model illustrates the two main stages in a size-controlled colloidal synthesis, namely (i) nucleation and (ii) crystal growth stages of the nanocrystals in solution (Figure 2.6) (Chang and Waclawik, 2014).

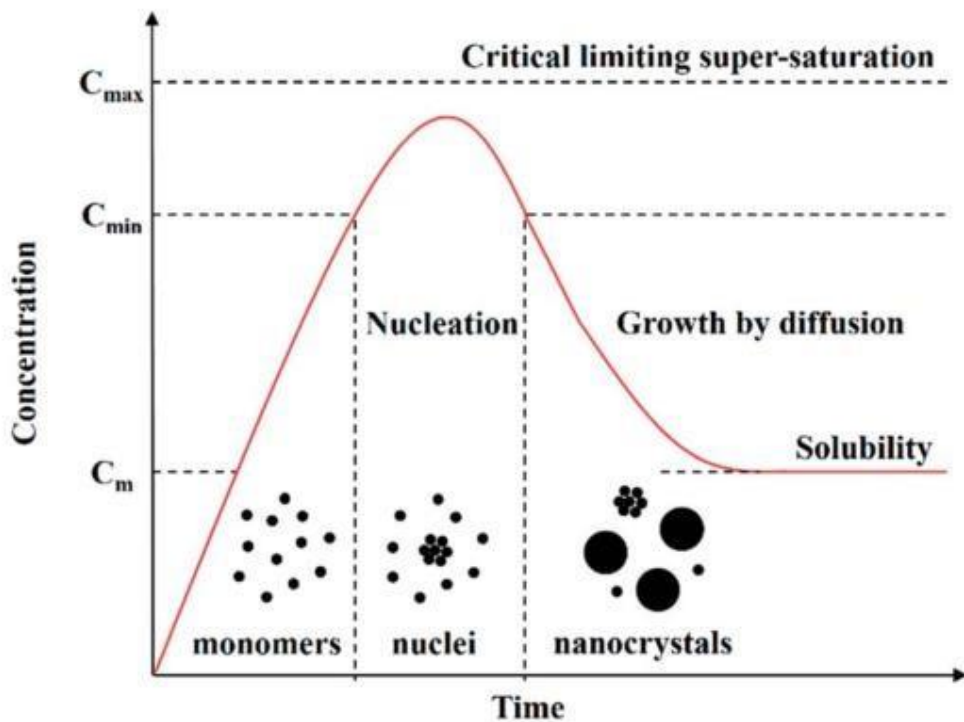


Figure 2.6: Schematic diagram of the LaMer model indicating the different stages in sizecontrolled colloidal synthesis of nanocrystals (Source: Chang and Waclawik, 2014).

In size-controlled synthesis, chemical reagents or molecules are reacted or decomposed in suitable organic solvents to generate monomers. A monomer in this regard is defined as the basic building unit of a crystal that can be solvated in solution and precipitated into a crystal. As the reaction solvent becomes supersaturated with monomer species, nucleation *burst* up to form nuclei by agglomeration and self-nucleation of monomers. The formed nuclei grow into nanocrystals.

During the growth stage, there is always the likelihood that nucleation also occurs simultaneously, which affects the final nanocrystal size and size distribution. The kinetics of the nucleation and growth is reported to be highly correlated to the particle size distribution (Chang and Waclawik, 2014).

### 2.2.3 Derivation of nucleation rate equations

The nucleation reaction is a phase transition process describing the precipitation of the monomers from solution to crystals. The rate of nucleation can be written in the Arrhenius form as in equation (2.1):

$$\frac{dN}{dt} = Ae^{\left[\frac{-\Delta G_N}{kT}\right]} \quad (2.1)$$

where  $N$ ,  $t$ ,  $A$ ,  $k$ ,  $T$  and  $\Delta G_N$  are number of nuclei, time, pre-exponential factor, Boltzmann's constant and free energy of nucleation respectively (Kwon and Hyeon, 2011; Kwon and Hyeon, 2009). The change in free energy,  $\Delta G$  when a nucleus with radius  $r$  is formed from solution, is expressed thermodynamically as:

$$\Delta G = 4\pi r^2 \gamma + \frac{4}{3}\pi r^3 \Delta G_v \quad (2.2)$$

where  $\gamma$  and  $\Delta G_v$  are the surface free energy per unit area, and the free energy per unit volume of crystal, respectively. The first and second terms in equation 2.2 are the various contributions from the surface and volume (Figure 2.7). The first term is always positive because it is related to the formation of an interface between the monomer and crystal which leads to an increase in free energy.

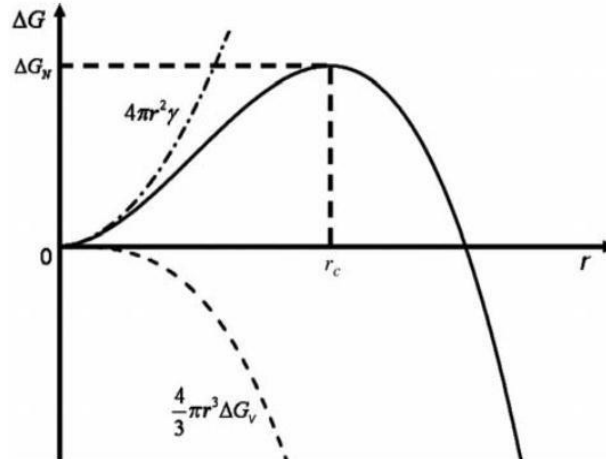


Figure 2.7: A plot of free energy of crystallization and radius of the crystallite particles (Source: Kwon and Hyeon, 2011)

The second term is always negative because it is related to the formation of crystal which leads to decrease in free energy. These tendencies occur when the supersaturation of the solution,  $S$ , i.e. the driving force is greater than 1. The  $S$  is derived from the expression for  $\Delta G_v$  which is the difference between the free energy of monomer in crystal and solution:

$$\Delta G_v = RT \frac{(\ln C_o - \ln C)}{V_m} = \frac{-RT \ln S}{V_m} \quad (2.3)$$

Note that

$$\ln C_o - \ln C = -\ln \frac{C}{C_o} = -\ln S \quad (2.3.1)$$

where  $C_o$  is the equilibrium monomer concentration in bulk crystal,  $C$  is monomer concentration in solution;  $V_m$  is the molar volume of monomer in crystal, and  $R$  and  $T$  are gas constant and temperature respectively. The  $S$  is expressed as the ratio of  $C$  to  $C_o$ . From Figure 2.7,  $r_c$  is defined as the minimum radius of a nucleus that can exist in solution. When the radius of a nucleus is

smaller than  $r_c$ , i.e.  $r < r_c$ , the nucleus spontaneously dissolves in solution in order to decrease free energy. When the radius of the nucleus is larger than  $r_c$ , i.e.  $r > r_c$ , the growth of the nucleus is thermodynamically favoured. The  $r_c$  can be determined by assuming that  $d\Delta G/dr = 0$  at  $r = r_c$ , then  $r_c$  is expressed as:

$$r_c = \frac{-2\gamma}{\Delta G_v} \quad (2.4)$$

Inserting equation 2.4 into equation 2.2, results

$$\Delta G_N = 4\pi\gamma \left(\frac{-2\gamma}{\Delta G_v}\right)^2 + \frac{4}{3}\pi\Delta G_v \left(\frac{-2\gamma}{\Delta G_v}\right)^3 = \frac{16\pi\gamma^3}{(\Delta G_v)^2} - \frac{32\pi\gamma^3}{3(\Delta G_v)^2} = \frac{16\pi\gamma^3}{(\Delta G_v)^2} \left(\frac{1}{3}\right) \quad (2.4.1)$$

Thus

$$\Delta G_N = \frac{16}{3} \frac{\pi\gamma^3}{(\Delta G_v)^2} \quad (2.5)$$

Inserting the expression for  $\Delta G_v$  (equation 2.3) into equation 2.5, results

$$\Delta G_N = \frac{16}{3} \frac{\pi\gamma^3}{\left(\frac{-RT\ln S}{V_m}\right)^2} = \frac{16}{3} \frac{\pi\gamma^3 V_m}{(-RT\ln S)^2} \quad (2.6)$$

Inserting expression for  $\Delta G_N$  into equation 2.1, the rate of nucleation is then obtained as

$$\frac{dN}{dt} = Ae \left[ \frac{16\pi\gamma^3 V_m^2}{3k^3 N_A^2 (\ln S)^2} \right] \quad (2.7)$$

Note that  $R = kN_A$ , where  $N_A$  is Avogadro's number.

## 2.2.4 Derivation of growth rate equations

The derivation of the growth rate equations is well reported by Park et al., (2007), Rempel et al., (2009), Thanh et al., (2013), Chang and Waclawik, (2014), and Ribeiro et al., (2005). The nanocrystals growth stage is understood by two different mechanisms; diffusion-controlled growth and reaction-controlled growth. The diffusion-controlled growth follows the Fick's first law of diffusion, that is, the nanocrystal grows as a result of diffusion of monomers along a concentration gradient. The rate of growth ( $dr/dt$ ) of the nanocrystal volume is proportional to the flux of monomers ( $J$ ) diffusing through the solvent medium onto the surface of the nanocrystal (assumed spherical).

$$J = \frac{4\pi r^2}{V_m} \frac{dr}{dt} \quad (2.8)$$

The flux of monomers can be obtained using the Fick's law

$$J = 4\pi x^2 D \frac{dC}{dx} \quad (2.9)$$

where  $D$  is the coefficient of diffusion,  $C$  is monomer concentration and  $x$  ( $\geq r$ ) is distance from the centre of the spherical nanocrystal. The amount of monomer,  $M$  required to increase the radius,  $r$  of a nanocrystal to  $r+\delta$  is proportional to the surface area of the nanocrystal (Figure 2.8), that is  $M \propto r^2$

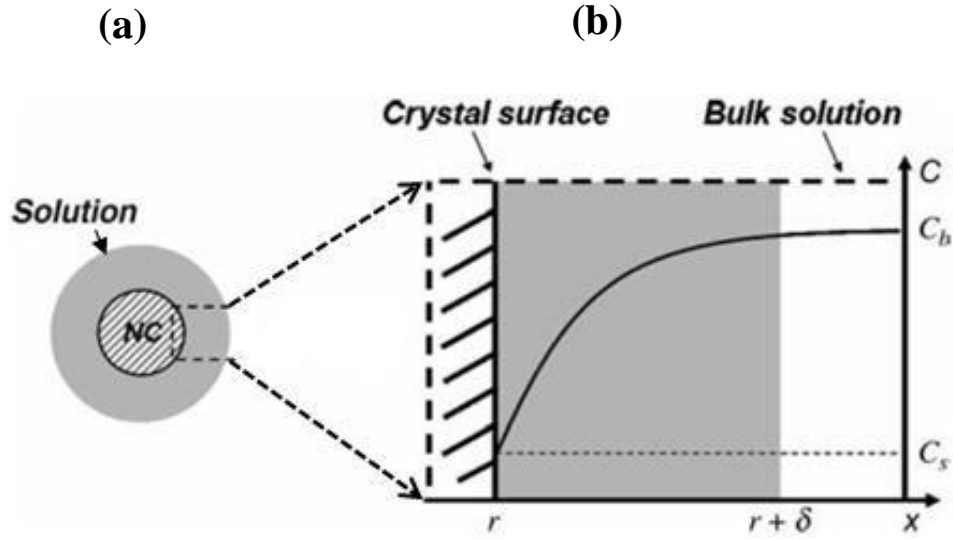


Figure 2.8: (a) Schematic diagram illustrating the monomer diffusion layer structure surrounding the surface of a nanocrystal,  $NC$ , (b) Cross-section of the surface of a  $NC$  and a plot of the monomer concentration as a function of distance  $x$ .  $C_b$  is bulk concentration of monomer,  $C_s$  is concentration at the surface of the  $NC$  (Source: Chang and Waclawik, 2014)

In the diffusion controlled model, the  $J$  is assumed constant for  $x$  and therefore, the integration of  $r$  to  $r+\delta$  with respect to  $x$  results

$$J = 4\pi D \frac{r(r+\delta)}{\delta} [C(r+\delta) - C_s] \quad (2.10)$$

When  $r \ll \delta$ , that is at sufficiently large values of  $\delta$ , the equation 2.10 reduces to

$$J = 4\pi r D (C_b - C_s) \quad (2.11)$$

Combining equations 2.8 and 2.11,

$$\frac{4\pi r^2}{V_m} \frac{dr}{dt} = 4\pi r D (C_b - C_s) \quad (2.11.1)$$

$$\frac{dr}{dt} = \frac{V_m \cdot 4\pi r D (C_b - C_s)}{4\pi r^2} = \frac{V_m D}{r} (C_b - C_s) \quad (2.12)$$

What equation 2.12 implies is that, the growth rate has an inverse relation with the radius of the nanocrystal assuming the  $C_s$  and  $C_b$  are constant. In simple terms, the growth rate reduces as the radius of the nanocrystal increases. Intuitively, the number of monomers that diffused to the surface of the nanoparticles increases to the second order of the radius and to the volume of the nanoparticle, a third order of the radius.

At high supersaturation, the crystals grow in solution until the concentration of the monomers drop. In this growth mode, the larger crystallite particles get limited supply of monomers and grow quite slowly whilst the smaller particles grow rapidly due to large supply of monomers diffusing onto the surface. This process occurs within few minutes and is termed as *size focusing* which leads to the narrowing of the particle size distribution (Figure 2.9(a)). Considering an ensemble of nanoparticles, the variance always decreases regardless of the starting size distribution provided all the particles are growing and there are no additional nucleation processes occurring. This is an ideal condition for size focusing. However, this does not happen in reality and the model made no provision for reaction kinetics and its dependence on the nanoparticle size (Park et al., 2007).

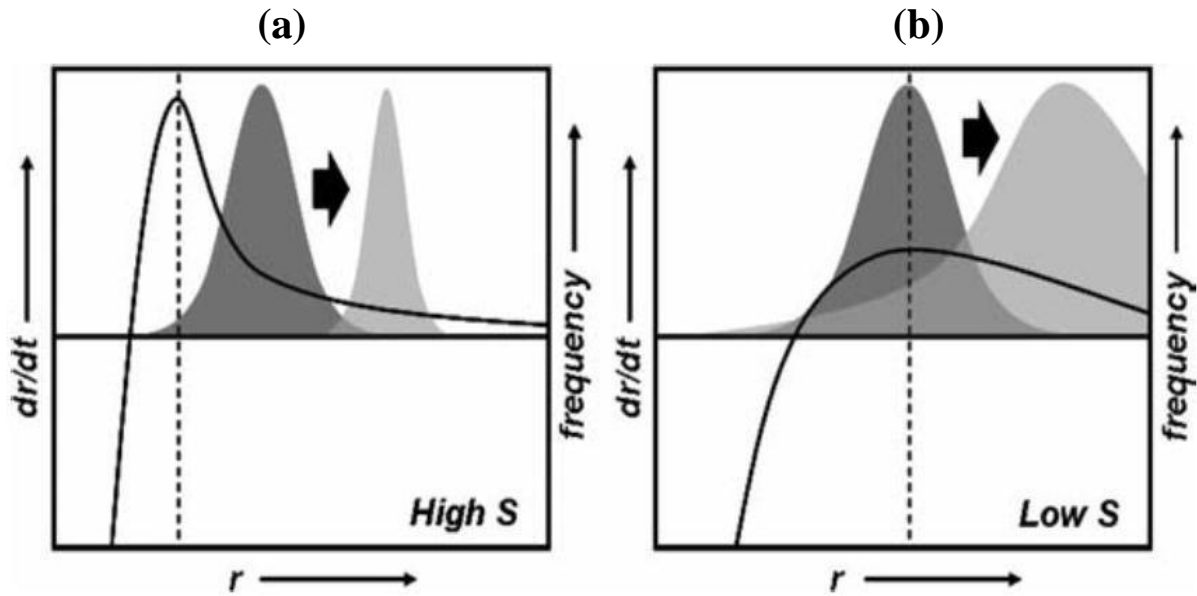


Figure 2.9: Plots of nanocrystals growth rate (solid line) and particle size distribution functions (shaded area). The dashed line indicates the maximum growth rate and the arrows showing the time evolution.  $S$  is saturation of the monomers (a) *Size focusing* leading to the narrowing of the particle size distribution and (b) *Ripening* leading to the broadening of the particle size distribution (Source: Kwon and Hyeon, 2009)

It is interesting to note that crystallization proceeds by either precipitation or dissolution, which are two opposing processes, equation (2.13).



$M^s$ ,  $M^c$ ,  $k_p$  and  $k_d$  are monomers in solution, monomers in crystal, reaction rate constants for precipitation and dissolution, respectively. The precipitation process is assumed to be a first-order reaction with respect to the  $C_s$  and the dissolution process is independent of  $C_s$ . At equilibrium,

$$C_{s,eq} = \frac{k_d}{k_p} \quad (2.14)$$

Considering a spherical nanocrystal with radius  $r$ , surface area  $A$ , and chemical potential ( $\mu(r)$ ), the change in chemical potential with respect to that of the bulk crystal ( $\mu^o$ ) is given as

$$\Delta\mu = \mu(r) - \mu^o = \gamma \frac{dA}{dn} \quad (2.15)$$

Equation 2.15 can be rewritten as the Gibbs-Thomson relation (because  $dA = 8\pi r dr$  and  $dn = 4\pi r^2 dr/V_m$ )

$$\Delta\mu = \frac{2\gamma V_m}{r} \quad (2.16)$$

Employing the activated complex theory, the variation of  $k_p$  and  $k_d$  with  $\Delta\mu$  can be obtained as

$$k_p = k_p^o e^{-\alpha \frac{\Delta\mu}{RT}} = k_p^o e^{-\alpha \frac{2\gamma V_m}{rRT}} \quad (2.17)$$

$$k_d = k_d^o e^{(1-\alpha) \frac{\Delta\mu}{RT}} = k_d^o e^{(1-\alpha) \frac{2\gamma V_m}{rRT}} \quad (2.18)$$

where  $\alpha$  is the transfer coefficient and  $k_p^o$  and  $k_d^o$  are the rate constants for the bulk crystal (when  $r=\infty$ ).

Equations 2.17 and 2.18 explain qualitatively that smaller crystals easily dissolve in solution and their growth is hindered due to their higher chemical potential. In the diffusion-controlled growth mode, the precipitation process dominants which imply that smaller crystals grow faster favouring focusing of the size distribution. However, in the instant where the driving force for precipitation diminish or become less effective (as explained by equations 2.17 and 2.18), some crystallite

particles dissolve into solution while others continue growing which leads to the *broadening* or *defocusing* of the particle size distribution. This process is termed as *ripening* (Figure 2.9(b)) and is no longer controlled by monomer diffusion (Kwon and Hyeon, 2009).

To combine these two opposing mechanisms, the assertion that the flux of monomer (J) in the diffusion controlled growth must be modified. Considering a particle with a radius r, the fluxes of monomers toward the surface by precipitation and dissolution are given as

$$J_p = 4\pi r^2 k_p^o C_s e^{\left[-\alpha \frac{2\gamma V_m}{rRT}\right]} \quad (2.19)$$

$$J_d = -4\pi r^2 k_d^o e^{\left[(1-\alpha) \frac{2\gamma V_m}{rRT}\right]} \quad (2.20)$$

Combining the equations (2.19) and (2.20), the net flux J is obtained

$$J = J_p + J_d = 4\pi r^2 k_p^o C_s e^{\left[-\alpha \frac{2\gamma V_m}{rRT}\right]} - 4\pi r^2 k_d^o e^{\left[(1-\alpha) \frac{2\gamma V_m}{rRT}\right]} \quad (2.21)$$

By equating equations 2.11 and 2.21, an expression for  $C_s$  is obtained as

$$C_s = \frac{k_d^o r e^{\left[(1-\alpha) \frac{2\gamma V_m}{rRT}\right]} + D C_b}{k_p^o C_s e^{\left[-\alpha \frac{2\gamma V_m}{rRT}\right]} + D} \quad (2.22)$$

Substituting equation 2.22 into equation 2.12 and using equation 2.14 results

$$\frac{dr}{dt} = V_m D C_{s,eq}^o \left[ \frac{s - e^{\left[\frac{2\gamma V_m}{rRT}\right]}}{r + \frac{D}{k_p^o} e^{\left[\alpha \frac{2\gamma V_m}{rRT}\right]}} \right] \quad (2.23)$$

$C_{s,eq}^o$  is the equilibrium surface concentration of the bulk crystal and S is the degree of supersaturation determined by the ratio of  $C_b/C_{s,eq}^o$ . Simplifying equation 2.23 gives

$$\frac{1}{r^*} \frac{dr^*}{d\tau} = \frac{s - e^{[r^*]}}{r^* + Ke^{[r^*]}} \quad (2.24)$$

where (in normalized to dimensionless forms)

$$r^* = \frac{RT}{2\gamma V_m} r \quad (2.25)$$

$$\tau = \frac{R^2 T^2 D C_{S,eq}}{4\gamma^2 V_m} t \quad (2.26)$$

$$K = \frac{RT}{2\gamma V_m} \frac{D}{k_p^0} \quad (2.27)$$

In equation 2.24, the mass transport and the reaction kinetics (related to the Gibbs-Thomson effect) are accounted for. From equation 2.27, it can be inferred that K (also known as the Damkohler number) represents the ratio of the rate of diffusion to the rate of the precipitation reaction (Thanh et al., 2013). When the value of K is very low, the crystal growth is controlled by the diffusion rate, i.e. focusing of the particles size distribution. When the value of K is very large, the crystal growth is controlled by the reaction rate, hence the term reaction controlled growth which leads to defocusing or ripening of the particles size distribution.

#### 2.2.4.1 Ostwald ripening

Ostwald ripening (OR) is a classical growth kinetics model which describes the coarsening of crystals where larger particles continue to grow at the expense of smaller particles (illustrated in Figure 2.10).

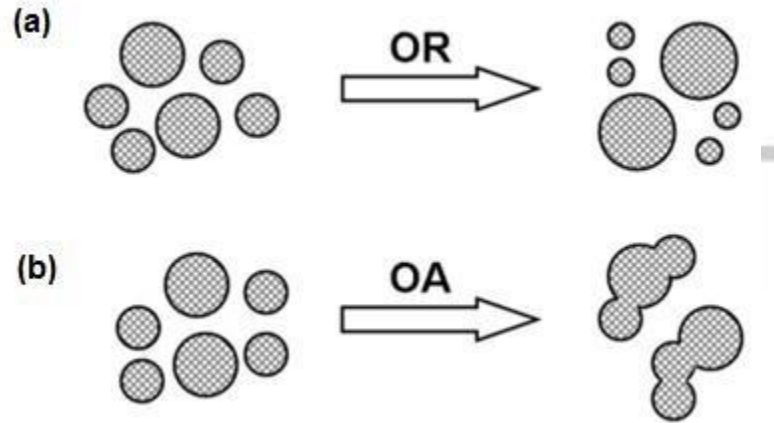


Figure 2.10: Scheme of growth of nanocrystals controlled by (a) Ostwald ripening and (b) Oriented attachment

The reason for OR is explained by the Gibbs-Thomson equation, where the solute concentration at the surface of the larger particles is lower than that of the smaller particles. Hence, solute ions flow from the surface of the small particles to the surface of the larger particle as a result of concentration gradient. This coarsening process is controlled by diffusion. The kinetic model for OR is known as the Lifshitz and Slyozov and Wagner (LSW) model which is based on the Gibbs-Thomson equation (Zhang et al., 2010; Thanh et al., 2013). The general kinetic equation is written as

$$D - D_2 = k(t - t_2)^{1/n} \quad (2.28)$$

where  $D$ , and  $D_2$  are the mean particle sizes at time  $t$  and  $t_2$ ,  $k$ , the temperature-dependent material constant and  $n$ , the exponent relevant to the coarsening process ( $n$  has value between 2 and 4, depending on how the ripening was controlled (by surface diffusion at the solid/liquid interface,  $n = 2$ , by volume diffusion in the liquid medium,  $n = 3$  and by dissolution kinetics,  $n = 4$ ) (Huang et al., 2003; Tiemann et al., 2008).

#### 2.2.4.2 Oriented attachment

Oriented attachment (OA) is a non-classical mechanism discovered by Penn and Banfield in 1999. This mechanism describes the spontaneous self-organization or coalescence of adjacent particles that share common crystallographic orientation (shown in Figure 2.10). This, however, results in nanoparticles with irregular shapes which are formed by consumption of primary nanoparticles as „building blocks“. The process is size dependent. This model has been proven experimentally in many different nanoparticles systems (Thanh et al., 2013; Zhang et al., 2010).

The kinetic equation that govern OA mechanism is

$$D = \frac{D_o(\sqrt[3]{2k_1t+1})}{(k_1t+1)} \quad (2.29)$$

where  $D$ ,  $D_o$ ,  $k_1$  and  $t$  are the particle diameter at any time, initial particle diameter, rate constant and time respectively.

Other mechanisms include the Finke-Watzky two-step mechanism (assumes that the nucleation and growth processes occur spontaneously) and intraparticle ripening described by Peng (which involves the diffusion of monomers to the surface of nanomaterial so as to change the shape of the particle with time) (Thanh et al., 2013).

### 2.3 Doping of Semiconductor Nanoparticles

Doping is another convenient way of tuning the optical, electrical and magnetic properties of a material. It is a well-known semiconductor processing technique whereby atoms or ions of a particular element are incorporated or introduced as impurity into host lattices to yield desirable properties and functions. Doped nanoparticles combine the size and dopant effects and thus are potentially considered as a new class of luminescent materials (Bol and Meijerink, 2000). Undoped quantum dots possess tunable emission colours, broad and strong absorption, low scattering and good stability but suffers from self-quenching as a result of intra-molecular ground-state dimer complex or transfer of energy between adjacent quantum dots (Beaulac et al., 2008; Bwatanglang et al., 2016). However, doped quantum dots overcome this problem because of the large Stokes shift they possess which makes them better candidates for biological applications. The large Stokes shift results from the low emission energy band gap relative to the high band gap energy of the host material (Wu and Yan, 2013).

Doping semiconductors with magnetic ions yields materials known as diluted magnetic semiconductors which have potential application in future spin-based electronics (Bryan and Gamelin, 2005). Another class of dopants is the luminescence activators. This class of dopants has luminescent properties and is potential candidate for optical imaging applications. A third class of dopants is the electronic dopants. These dopants introduce carriers by acting as either shallow donors or acceptors within the host semiconductor band structure and hold the promise as the future nanotechnology self-assembled device structures. A dopant occupying a substitutionary position and has one valence electron more than its host material, upon thermal ionization, donates its electron to the semiconductor (i.e. *n*-type doping). In the same way, if the

dopant has one electron less, or has a hole to provide to the host semiconductor, then the type of doping is termed as *p*-type doping (Bryan and Gamelin, 2005). These are common doping strategies for doping bulk semiconductors.

Transition metal ions with open d-shell electronic configurations have largely been used as dopant materials because they possess unique properties such as magnetic ground states and lowenergy excited states which are suitable for altering the properties of the host semiconductor material (Bryan and Gamelin, 2005). Transition metals such as Mn, Cu, Ni, Cr, Fe and Co have received attention as dopant materials (Jana et al., 2011; Pradhan and Sarma, 2011; Srivastava et al., 2010; Shamsipur and Reza, 2014; Reddy et al., 2012; Murugadoss, 2012). Rare earth (RE) metals ions,  $\text{Eu}^{3+}$ ,  $\text{Tb}^{3+}$ ,  $\text{Er}^{3+}$ ,  $\text{Sm}^{3+}$  and  $\text{Pr}^{3+}$  have also been reported as dopant materials and some  $4f^n - 4f^n$  transition-related emissions have been observed (Bol et al., 2002). The II-VI semiconductors are attractive materials and are widely used as host lattices. CdS, CdSe, ZnS and ZnSe nanoparticles have been doped with both transition and RE metal ions. However, doping with RE is hampered by the dissimilar chemical properties (e.g. ionic radius, valence state) between the RE and II-VI semiconductor hosts ions such as  $\text{Zn}^{2+}$  and  $\text{Cd}^{2+}$  (Yang et al., 2005). The most studied doped semiconductor nanomaterial is Mn-doped ZnS nanoparticles because they have low cytotoxicity and longer dopant emission lifetime.

Despite the huge advancement made in the synthesis of nanocrystalline materials, the synthesis of doped nanoparticles faces serious challenges. In a particular synthesis, the dopant and host precursors are reacted in appropriate solvent and allowed to age, similar to the synthesis of undoped nanoparticles. The dopant metal ion in an ideal case is expected to diffuse into the host lattice to occupy some of the tetrahedral positions or substitute some host metal ions.

Unfortunately in practice, not all the dopant ions diffuse into the host crystal lattice, rather some remain on the surfaces of the host or occupy interstitial positions in the host resulting in low emission intensities. To date, analytical techniques to diagnose whether the dopants atoms are incorporated in the lattice or on the surface are very few. For magnetic dopants, electron paramagnetic resonance (EPR) and magnetic circular dichroism (MCD) are some powerful techniques reported for revealing or identifying the position of magnetic metal ions in the host. These techniques measure the spin interactions related to the local environment of the dopant (Norris et al., 2008).

### **2.3.1 Mechanisms of doping**

#### **2.3.1.1 Self-purification model**

Doping mechanism is better explained by the „self-purification“ model which is based on the low solubility of the dopant or impurity in the host material (Norris et al., 2008). This model asserts that nanoparticles are hard to dope for thermodynamic reasons and therefore impurities are expelled (Figure 2.11). It is assumed that the nanoparticle is in thermal equilibrium with its environment (which includes the reservoir of semiconductor and the impurity or dopant) and to minimize the Gibbs free energy of such system, factors such as impurity formation energy, solubility limit and impurity size become relevant. This concept of thermal equilibrium only holds if there is the possibility for free ions including the impurity to diffuse easily to and from the nanoparticle and its environment. Facile diffusion of dopants into lattices usually occurs at very high temperatures (>1000 °C). Unfortunately, for colloidal synthesis of nanoparticles, the temperatures (>350 °C) used do not favour facile dopant diffusion into the host, though the rate

of diffusion might differ for different dopant material. Diffusion of  $Mn^{2+}$  into the inside of II-VI semiconductors is said to be negligible but faster at the surface (Norris et al., 2008; Erwin et al., 2005).

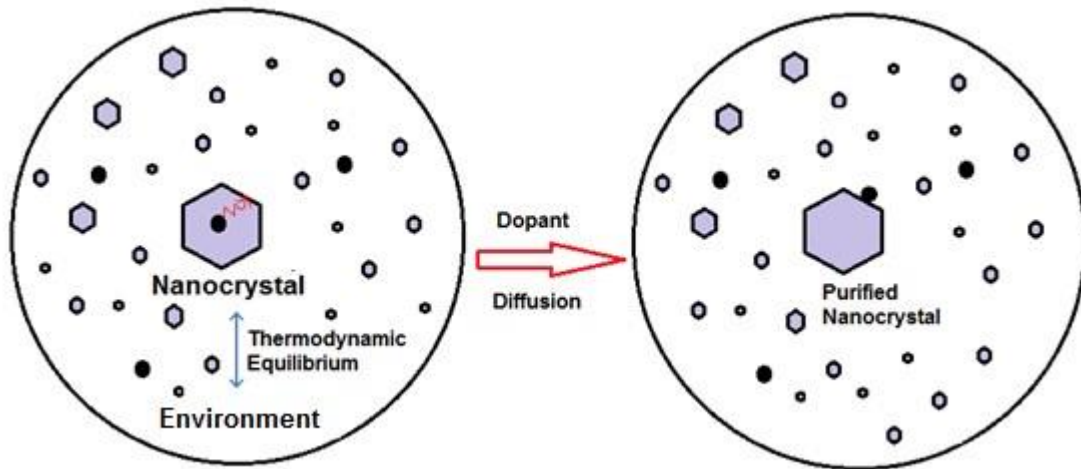


Figure 2.11: Schematic sketch illustrating the „self-purification model“ in doping mechanism

### 2.3.1.2 Trap model

In the absence of thermodynamic equilibrium, kinetic factor such as activation energy barrier controls the doping. This is explained by the „Trap model“ (Figure 2.12). In this model, the dopant must adsorb to the surface of the host nanocrystals and another layer of the host cover or „trap“ the dopant material (Norris et al., 2008). This implies that the surface characteristics of the host nanocrystal such as the crystal structure and shape are critical for binding or *trapping* the dopant ion. However, in colloidal syntheses of nanoparticles, surfactants or capping agents are used which bind to the surface of the nanoparticles to control their structure and shape and also to induce solubility (Chang and Waclawik, 2014). Thus, capping agents that bind strongly to surfaces of

nanoparticles are not favourable for doping compared to those that bind weakly, according to the trap model (Norris et al., 2008). It is worth noting that the „self-purification“ and „trap“ models are still under empirical investigations but are attractive for understanding the mechanism of doping of nanocrystals.

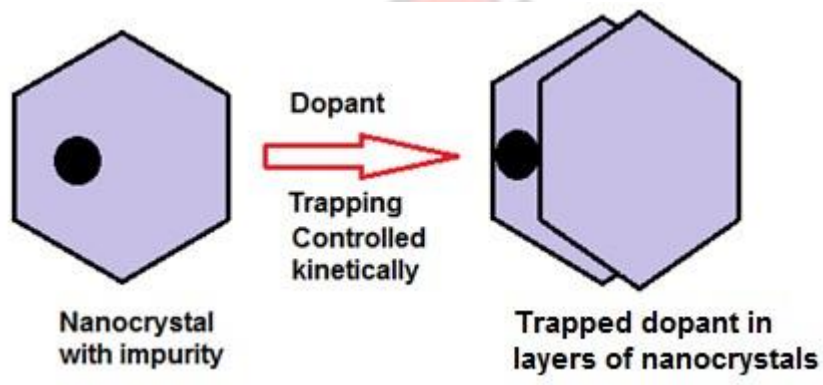


Figure 2.12: Schematic sketch illustrating the „trap model“ in doping mechanism

## 2.4 Size Controlled Colloidal Syntheses of Nanoparticles

Size controlled synthesis is one of the hottest areas of current research that have attracted much attention since the advent of nanochemistry. The size of the nanoparticles can be tuned by varying the experimental conditions. The synthesis parameters for a size controlled colloidal synthesis of nanoparticles are (i) reactivity of precursors, (ii) type of solvent and capping agent, (iii) reaction temperature and time and (iv) synthesis technique. In a typical synthesis, the precursors (which consist of the compound semiconductor elements) are thermolyzed or reacted in a suitable solvent in the presence of a capping agent at appropriate temperature and time to generate the nuclei which grow into the nanoparticles.

### 2.4.1 Hot-injection and heat-up syntheses

The two common techniques for controlling the size of nanoparticles are the hot-injection and heat-up methods (Figure 2.13). The hot-injection is the earliest method designed for the synthesis of uniform nanoparticles. It involves the injection of the precursors dissolved in a minimum amount of solvent into a preheated hot solvent. Upon injection, the precursors decompose or react to yield the nanoparticles. The hot-injection method has the advantage of yielding monodispersed nanoparticles but is less reproducible. Unlike this method, the heat-up route requires no injection of the precursors; rather, all the reagents required for the synthesis are loaded into the reaction vessel at room temperature and heated up to the required temperature and allowed to age for appropriate period. This route is more suitable for large scale production of nanoparticles and is more reproducible compared to hot-injection. However, only precursors which become reactive

at higher temperatures are more favourable for heat-up synthesis than lower temperature reactive precursors.

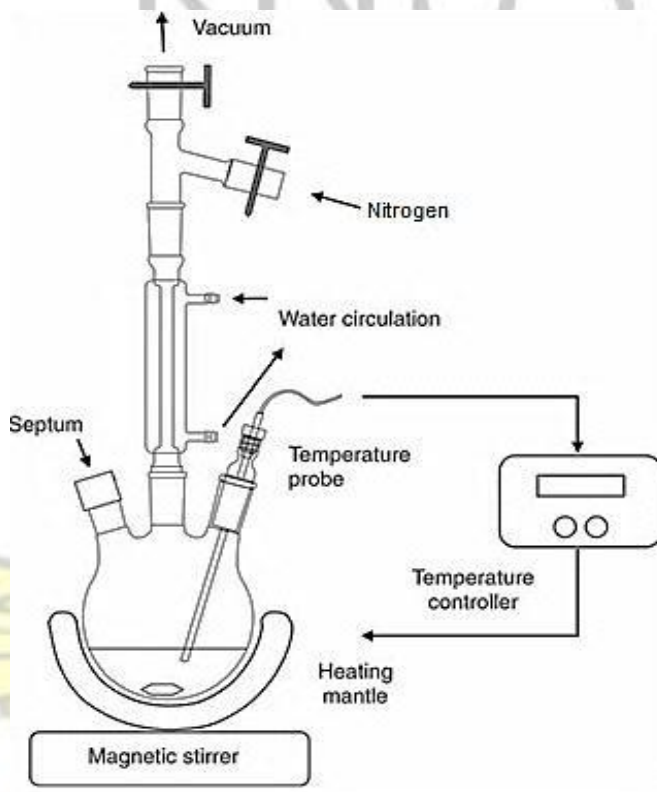


Figure 2.13: Schematic diagram of set-up for hot-injection and heat-up syntheses

Theoretically, the difference between the hot injection and heat-up methods lies in the procedure used to control the size and size distribution of the nanoparticles. The hot injection route involves two major steps in controlling the distribution of nanoparticles; namely nucleation and crystal growth according to the LaMer model (Chang and Waclawik, 2014; Kwon and Hyeon, 2011). The sudden induction of burst nucleation due to high supersaturation introduced by the swift injection of precursors in hot solvent helps to initiate homogeneous nucleation leading to fairly uniform

nanoparticles growth; thereby effectively controlling the size distribution. Similarly, the heat-up method also follows in two major steps which are the decomposition of the precursor and growth of the nanoparticles. The nanoparticles size distribution is controlled by the high energy barrier required for the induction of homogeneous nucleation. The nucleation is delayed until a large amount of monomers are accumulated by the decomposition of the precursor to reach a high supersaturation level where burst nucleation eventually evolves to initiate the nanoparticles growth stage. Thus, factors associated to size focusing such as no subsequent nucleation and high supersaturation level are fulfilled for narrowing of the nanoparticles size distribution (Kwon and Hyeon, 2011). However, in both methods there is the likelihood of nucleation occurring along the growth stage which may result in size broadening or defocusing.

#### **2.4.2 Other methods of syntheses**

Other methods for nanoparticles synthesis include solvothermal, microwave assisted synthesis, reverse micelles, co-precipitation and melt reactions (Biswas et al., 2005; Zhu et al., 2014; Smith et al., 2000; Peng et al., 2005; Lewis et al., 2014; McNaughter et al., 2016). In a solvothermal reaction, the reagents including the precursors and capping agents are put in a suitable solvent in a Teflon-lined stainless steel autoclave reactor and then autoclaved for an appropriate time, temperature and pressure. When the source of heating is changed to a microwave then that becomes the microwave assisted synthesis. The co-precipitation method is based on the precipitation of ions in aqueous solution. The pH of the solution is critical to the precipitation to form the desired nanomaterial. Co-precipitation method is cheap compared to the other conventional methods; however, it yields less crystalline nanoparticles with more defects (Wu and

Yan, 2013). The melt reaction method has currently received attention because it has an advantage of obviating the solvent in the synthesis (McNaughter et al., 2016). Melt reaction is a solid state reaction where the precursors are placed in a ceramic boat or crucible and heated in a furnace for a required time and temperature. The disadvantages of these methods are that they yield less uniform nanoparticles and are not reproducible compared to the hot-injection and heatup methods.



## 2.5 Green Precursors for Syntheses of Metal Chalcogenide Nanoparticles

Precursors are starting materials for synthesis. In the synthesis of metal chalcogenide nanoparticles, two different precursor routes are known; (i) dual source and (ii) single source precursor (SSP). In the dual source route, two separate chemical compounds are reacted together to yield the metal chalcogenide nanoparticles. The two chemical compounds are the metal ion containing compound (which are usually metal salts) and the chalcogen (S, Se, Te) containing compound. This route was first reported by Murray and coworkers (1993) for synthesizing CdS, CdSe and CdTe nanocrystals. In their synthesis, the Cd and chalcogen precursors used were dimethylcadmium, bis(trimethylsilyl)sulphide, bis(trimethylsilyl)selenium and bis(tertbutyldimethylsilyl)tellurium. The solvents used were tri-n-octylphosphine (TOP) and tri-n-octylphosphine oxide (TOPO). This route is the traditional method for synthesizing high quality monodispersed nanoparticles; however, it has intrinsic problems related to toxicity of chemicals used and poor control over stoichiometry of the final product. Thus, current research has focused on finding alternative greener precursors and solvents for synthesis of good quality nanoparticles.

### 2.5.1 Vegetable oils

Vegetable oils (VOs) have attracted attention as alternative green coordinating solvents due to their abundance and low-toxicity as compared to typical solvents such as trioctylphosphine oxide. VOs consist of triacylglycerides of long chain aliphatic fatty acids which are effective for tuning the size and morphology of nanoparticles. They also make nanoparticles biocompatible and ensure their dispersion in nonpolar solvents. Notable examples of VOs used as solvent for syntheses of

metal chalcogenide nanoparticles are olive oil, sunflower oil and castor oil (Mondal et al., 2012; Pereira et al., 2012; Shombe et al., 2015).

The underlying difficulty in using VOs as solvents is their high viscosity which makes them unattractive to the traditional hot injection technique due to the poor solubility of the precursors in VOs at room temperature. Co-solvents are usually used in addition to VOs to reduce the viscosity, especially in the hot injection method. In this approach, the dual or single source precursors are injected into a coordinating solvent. Akhtar et al., (2010) synthesized PbS nanoparticles by injecting a solution of trimethylsilyl sulphide dissolved in a mixture of olive oil and octadecene (4:1 v/v) into a hot solution of PbO dissolved in a mixture of olive oil, oleic acid and octadecene (12.5:1:1 v/v). The octadecene was added to reduce the viscosity of the olive oil in order to induce uniform nucleation of nanoparticles whilst the oleic acid was to dissolve the PbO. Employing a similar procedure, Nyamen et al., (2014) produced CdS and PbS nanoparticles by injecting a solution of heterocyclic dithiocarbamate complexes of Cd and Pb in trioctylphosphine (TOP) into hot olive oil. However, the heat-up method requires no injection and viscous liquids such as VOs could be used without co-solvents.

### **2.5.2 Castor oil and ricinoleic acid**

Castor oil (CO) has been viewed as one of the most probable sources of plant oils suitable as solvent and/or capping agent for synthesis of metal and metal chalcogenide nanoparticles (Kyobe et al., 2016; Kumari and Philip, 2013). CO (also called *Oleum Palmae Christi*) is a hydroxylated lipid obtained from the seed of castor plant, *Ricinus Communis Linne* of the family

Euphorbiaceae and a native of tropical Asia and Africa (Mutlu and Meier, 2010; Tunaru et al., 2012). Pictures of castor plant, seeds and the oil are shown in Figure 2.14. CO is considered as a very important bio-resource material for wide variety of applications (Mubofu, 2016).



Figure 2.14: Castor plant (a) matured castor plant, (b) bunch of castor seeds, (c) dried castor seed pod, seed and oil

The triglycerides of CO consist of fatty acids (FAs) of which about 90 % are ricinoleic acid (RA), a hydroxylated, monounsaturated 18-carbon carboxylic acid. CO is the only pure source of RA (Da Silva et al., 2008; Concei et al., 2007; Ogunniyi, 2006).

RA is a multi-functional compound, possessing carboxylic acid, a double bond (between C9 and C10) and secondary alcohol or hydroxyl (at C12) functional groups. The hydroxyl group is beta to the double bond and protects it from peroxides formation (Vaisman et al., 2008). These functional groups make CO (and its derivatives) completely soluble in all alcohols and present viscosities that are up to about sevenfold higher than those of other vegetable oils (Meneghetti et al., 2006). CO is prone to reactions such as amidation, saponification, reduction, esterification,

alcoholysis, hydrolysis, dehydration, caustic fusion, sulfonation, pyrolysis, oxidation, polymerization, halogenation, epoxidation, hydrogenation and olefin metathesis (Kulkarni and Sawant, 2003; Mubofu, 2016; Xia and Larock, 2010). Thus, CO is applicable as valuable raw material in industries for production of coatings, biopolymers, paints, adhesives, cosmetics, lubricants, hydraulic fluids, inks, linoleum and chemicals including sebacic acid and undecylenic acid used in the production of plasticizers and nylon (Hablott et al., 2008; Meneghetti et al., 2006; Xia and Larock, 2010).

The properties of castor oil which makes it appropriate as solvent for nanoparticles syntheses are (i) non-toxicity, (ii) high boiling temperature of 313 °C, (iii) it is colourless to pale yellow liquid, (iv) has mild or no odour or taste and (v) it is a clear liquid at room temperature and shows no solid fat at 0 °C (Salimon et al., 2010; Chakrabarti and Ahmad, 2008). The alkyl groups impose steric effect which controls the growth, crystal structure, morphology and surface characteristics of the nanoparticles (Green, 2010; Thanh and Green, 2010). However, castor oil is not suitable for high temperature synthesis due to possible oxidation of the OH groups to ketones (Lattuada and Hatton, 2007).

The uniqueness of castor oil compared to other vegetable oils lies in its fatty acid composition. The fatty acids found to be present in castor oil are ricinoleic acid, linoleic acid, oleic acid, stearic acid and linolenic acid (Figure 2.15). About 84 to 90 % of the FAs are RA and 10 – 16 % consists of the other fatty acids (Schneider et al., 2004; Salimon et al., 2010; Jafari et al., 2013; Vaisman et al., 2008; Chakrabarti and Ahmad, 2008). Da Silva et al., (2011) also showed castor oil composition as 89.5 % ricinoleic acid, 3.7 % linoleic acid, 3.0 % oleic acid, 1.6 % palmitic acid, 0.9 % stearic acid, 0.6 % behenic acid, 0.4 % linolenic acid and 0.3 % arachinic acid.

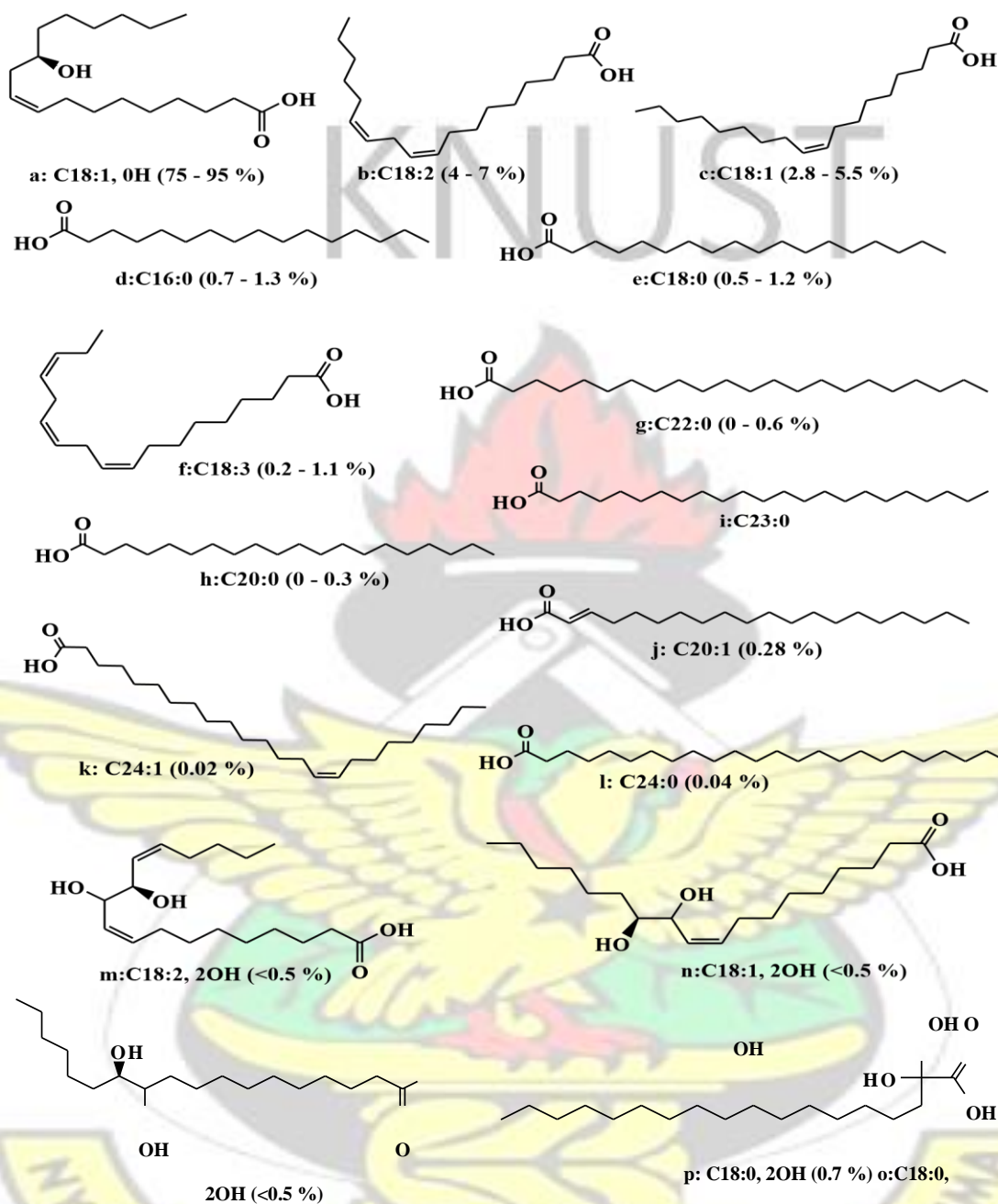


Figure 2.15: Chemical structures of FAs (percentage composition in bracket) found to be present in CO (**a**: ricinoleic acid, **b**: linoleic acid, **c**: oleic acid, **d**: palmitic acid, **e**: stearic acid, **f**: linolenic acid, **g**: behenic acid, **h**: arachidic acid (or eicosanoic acid), **i**: tricosanoic acid, **j**: eicosenoic acid, **k**: nervonic acid, **l**: lignoceric acid, **m**: 11,12-dihydroxy-9,13-octadecadienoic acid, **n**: 11,12-dihydroxy-9-octadecenoic acid, **o**: 11,12-dihydroxyoctadecanoic acid, **p**: dihydroxystearic acid)

Although castor oil is known to contain ricinoleic acid which is a monohydroxy fatty acid, Lin

(2009) has identified three new dihydroxy fatty acids in castor oil which they proposed to be 11, 12-dihydroxy-9-octadecenoic acid; 11, 12-dihydroxy-9,13-octadecadienoic acid; and 11, 12-dihydroxyoctadecanoic acid (Figure 2.15). Also, tricosanoic acid which is an odd-numbered long

FA, C23:0 has been identified to be present in castor oil by the same group (Lin and Chen, 2012).

Remarkably, Hosamani et al., (2004) also reported *Alternanthera triandra*, Lam Syn. *Alternanthera sessilis* (Linn) R. Br. seed oil as another source of ricinoleic acid (contains about 22.1 % of RA). However, in spite of the possibility that other seed oils may contain ricinoleic acid, castor oil remains the only reported rich source of ricinoleic acid so far.

#### **2.5.2.1 Isolation of ricinoleic acid from castor oil**

Several methods including chemical and biochemical pathways have been used to isolate ricinoleic acid from castor oil. The isolation occurs by hydroxylation of the ester linkages in the triglyceride molecules to yield ricinoleic acid and glycerol (Figure 2.16). The salt-solubility-based fractionation method reported by Vaisman et al., (2008) is an example of a chemical method for isolating ricinoleic acid from castor oil. In this method, castor oil is hydrolyzed by refluxing with ethanol solution of KOH for 1 hour and the ethanol evaporated to yield potassium salt of the FAs. The fatty acids are liberated by dissolving in deionized water and acidifying with concentrated HCl. The fatty acids are then extracted with ethylacetate and dried over MgSO<sub>4</sub>. Clarification of the FAs is done by mixing with n-hexane (1:5 w/v) and keeping at -4 °C for 72 h in darkness. Chromatographic analysis of the resultant fatty acids revealed the purity to be within

87.50 – 88.10 % ricinoleic acid and 12.5 – 11.9 % palmitic acid, stearic acid, oleic acid, vaccenic acid, linoleic acid and linolenic acid. Solid residues found after clarification was identified to be 9, 10-dihydroxystearic acid (Vaisman et al., 2008).

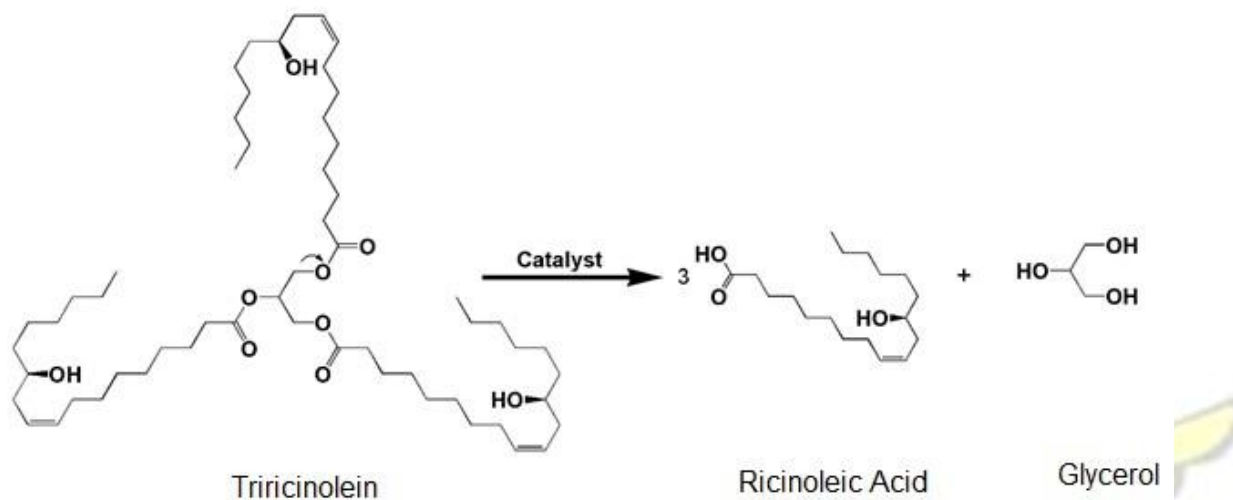


Figure 2.16: Reaction scheme showing the isolation of ricinoleic acid from triricinolein (the major triglyceride in castor oil)

Biocatalysts such as lipase (triacylglycerol acylhydrolase, EC 3.1.1.3) enzymes have been used to isolate ricinoleic acid from castor oil. Foglia et al., (2000) employed *C. rugosa*, *P. cepacia* and *G. candidum* lipases for hydrolysis of castor oil. In a typical reaction, tubes containing 100 mg oil, 0.6 mL of 0.5 M phosphate buffer (pH 7), about 2 – 5 mg of free lipase, were stirred at 500 rpm at 30 °C for 1 – 4 hours. The extent of hydrolysis was determined by means of titrating the hydrolysis mixture (in 20 mL of diethyl ether/ethanol/water (3:3:2)) to pH 12 with 0.1 N NaOH solution. The *P. cepacia* lipase was found to be effective in hydrolyzing castor oil to ricinoleic acid to the tune of 27 % compared to 13 % recorded for *C. rugosa* and *G. candidum*. Ozcan and

Sagioglu, (2009) also implored immobilized *Candida rugosa*, *porcine pancreatic* and *castor bean* lipases for lipolysis of castor oil and obtained yield of ricinoleic acid to be within 20 – 40 % taking into consideration a number of parameters such as pH, temperature, amount of substrate and enzyme. Interestingly, Piazza and Farrell, (1991) used lipase from ground oat (*Avena Sativa L.*) to hydrolyze castor oil and obtained approximately 90 % yield of ricinoleic acid.

Eco-friendly approach by the use of microwave assisted extraction of ricinoleic acid from castor oil has also been reported by Karpakavalli et al., (2012). In their approach, a 250 mL beaker containing 5 g of castor oil and a solution of ethanolic KOH with some few pieces of ice, was covered and kept in a household microwave oven. The microwave oven was modified to contain a magnetic stirrer and water condenser. Heating continuously the reaction system with the microwave oven at 160 W intensity for 19 minutes, 89 % yield of ricinoleic acid was obtained. This microwave assisted technique was found to be efficient compared to conventionally heating the hydrolysis system. All the above approaches for isolation of ricinoleic acid from castor oil, show good yield but only differs in the use of different catalyst and source of heat.

#### **2.5.2.2 Characteristics of ricinoleic acid compared to oleic acid**

Fatty acids are Lewis acids and have been extensively applied as capping agents and surfactants in the syntheses of nanoparticles. Oleic acid is known as a standard fatty acid, the double bond and alkyl chain forming a „*kink*“ imparts colloidal stability (Lattuada and Hatton, 2007). In Table 2.1 ricinoleic acid is compared with oleic acid (see also Figure 2.15).

Oleic acid is found to be efficient in stabilizing magnetic nanoparticles than stearic acid which has no '*kink*' in its chemical structure (Green, 2010). A more closely related fatty acid to oleic acid is

ricinoleic acid. Ricinoleic acid is isostructural with oleic acid and has also received considerable attention for stabilizing and capping of magnetic and luminescent nanoparticles (Jacintho et al., 2009; Kyobe et al., 2016; Furlan et al., 2010; Gyergyek et al., 2011).

One interesting difference between ricinoleic acid and oleic acid is that the former has an OH in its carbon chain which is susceptible to reactions such as acetylation and polymerization. This provides avenue for small ricinoleic acid capped nanoparticles to be coated with polymers for specific applications such as drug delivery. It also provides avenue for further chemical functionalization or modification of nanoparticles to improve on their dispersion or solubility in varying solvent media.



Table 2.1: Comparison of ricinoleic acid and oleic acid (related to their nanoparticles surface passivation, stabilization and application)

No.	Oleic acid	Ricinoleic acid
-----	------------	-----------------

1. It is a C18 FA with one double bond between C9 and C10	It is isostructural with oleic acid but has hydroxyl group at C12 in the C18 tail
2. The double bond in the middle of its carbon chain forms a 'kink' believed to be effective at nanoparticles stabilization	<p>Has similar 'kink' for nanoparticles stabilization. Provides a functional group (OH) in addition to the steric repulsion.</p> <ul style="list-style-type: none"> <li>• The OH can be acetylated under mild conditions</li> <li>• The OH has low affinity for iron oxide surfaces</li> <li>• The OH could initiate ring opening polymerization reactions</li> </ul>
3. Only colloidal suspensions in non-polar organic media can be prepared (Oleic acid coated nanoparticles cannot be dispersed in organic media with a dielectric constant larger than 5)	Colloidal suspensions in more polar organic media can be prepared
4. Suitable for capping of mono-dispersed nanoparticles synthesized at very high temperatures	Not suitable for high temperature synthesis due to possible oxidation of the OH groups to ketones

In addition, applications requiring highly polar organic solvents, ricinoleic acid is most preferred over oleic acid. Unfortunately, due to the possibility of oxidation of the OH functional group to ketones, ricinoleic acid is less preferred to oleic acid in high temperature organometallic synthesis of monodispersed nanoparticles. However, oleic acid can be replaced with ricinoleic acid in a ligand exchange process (Lattuada and Hatton, 2007).

### 2.5.3 Metal carboxylates

Metal carboxylates or metal fatty acid salts (MFASs) are polyvalent metal soaps, prepared either by (i) metathesis of sodium or potassium fatty acid salt with metal salts in aqueous or polar solvents, (ii) dissolution or fusion of metal oxides (or hydroxides, oxy-hydroxides, hydrocarbonates, carbonates) in hot fatty acids and (iii) direct reaction of metal with hot fatty acids (Chen et al., 2009). MFASs have become attractive as precursors for ultra-large scale synthesis of metal oxide and metal chalcogenide nanoparticles because they (i) are environmentally benign and (ii) yield very reproducible results. Pereira et al. (2012) combined MFASs (iron and zinc oleates) single source precursors and sunflower oil (as solvent) for the synthesis of iron oxide and zinc oxide nanoparticles (at 200 – 250 °C). Iron oxide and zinc oxide nanoparticles with average diameters of 7 nm and 3 nm and spheroidal in shape were obtained respectively. Whilst this route is considered green, the sunflower oil was prone to autoxidation via the double bonds in the oil at elevated temperatures (such as 310 °C). Decomposition products such as ketones, esters, aldehydes, carbonates and carboxylic acids were identified. Factors such as temperature, UV light and metal ion complexes (iron and tin) were suggested to have accelerated the autoxidation process. Thus, choosing the right organic solvent (with suitable boiling point) to decompose MFASs is crucial to obtaining monodispersed nanoparticles.

Chen et al., (2009) decomposed iron-oleate complex in five different organic solvent (oleylalcohol, benzyl ether, octadecene or tri-octylamine)/ oleic acid mixtures. Typically, the MFASs and the solvent mixture were placed in a flask and refluxed at the boiling point of the respective organic solvents for an hour to decompose the precursor. The outcome was monodispersed spherical iron oxide nanoparticles with sizes between 4.5 and 20.4 nm. The sizes

were found to be dependent on both the boiling point of the organic solvent and the amount of oleic acid. The oleic acid was found to control the decomposition of the MFASs and growth of the nanoparticles. In contrast, Cha et al., (2007) decomposed iron-oleate complexes in the absence of an organic solvent (i.e. solventless method) and obtained similar monodispersed iron oxide nanoparticles. By varying the annealing time and vacuum pressure, different shapes (spherical, regular triangular, short rod, diamond and long rod shape) with mean size of 10.6 nm of iron oxide resulted. The decomposition of MFASs follows equations (2.30) and (2.31).



MFASs thermally decompose through the formation of free radicals which combine, disintegrate into smaller molecules or react with other metal carboxylates to propagate to decompose metal carboxylates in MFASs (Cha et al., 2007).

Choi et al., (2009) synthesized Cu<sub>2</sub>S, MnS, PbS, CdS and ZnS nanocrystals by the solution-phase thermolysis of metal-oleate complexes in alkanethiol. This method was considered simple and general for the synthesis of metal chalcogenides. Specifically, the metal-oleate precursors were dissolved in solvent mixtures of oleylamine and docanethiol. The resultant mixtures were then heated to the required temperatures and kept for a period. The reaction temperature, time and the molar ratio of the two solvents were varied in order to tune the sizes of the nanoparticles. The nanoparticles sizes were uniform and had average particle sizes of 18, 11, 47, 10 and 10 nm for Cu<sub>2</sub>S, MnS, PbS, CdS and ZnS nanocrystals respectively. Similarly, Patel et al., (2012) obtained uniform sized CdS, ZnS and PbS nanoparticles by sulphurization of metal-oleate precursors with thioacetamide at 140 °C. Thermogravimetric and infrared studies indicated that the fatty acids

were strongly coordinated or attached (symmetrically) to the surface of the nanocrystals via the carboxylate functional group.

Metal-oleate complexes have been extensively explored for synthesis of metal chalcogenide nanocrystals, however, metal-ricinoleate complexes (prepared by reacting ricinoleic acid with metal salts) has not been explored though RA is isostructural with oleic acid.

#### 2.5.4 Single source precursors (SSPs)

The SSPs route has been suggested and championed by O'Brien and coworkers, as a greener alternative route to the dual source (Malik et al., 2010). SSP is a molecular compound or complex which contains the requisite elements for synthesizing the semiconductor nanomaterial. The thioacid (sulphur donor ligands) complexes are of much interest for synthesis of metal chalcogenide nanoparticles (Figure 2.17).

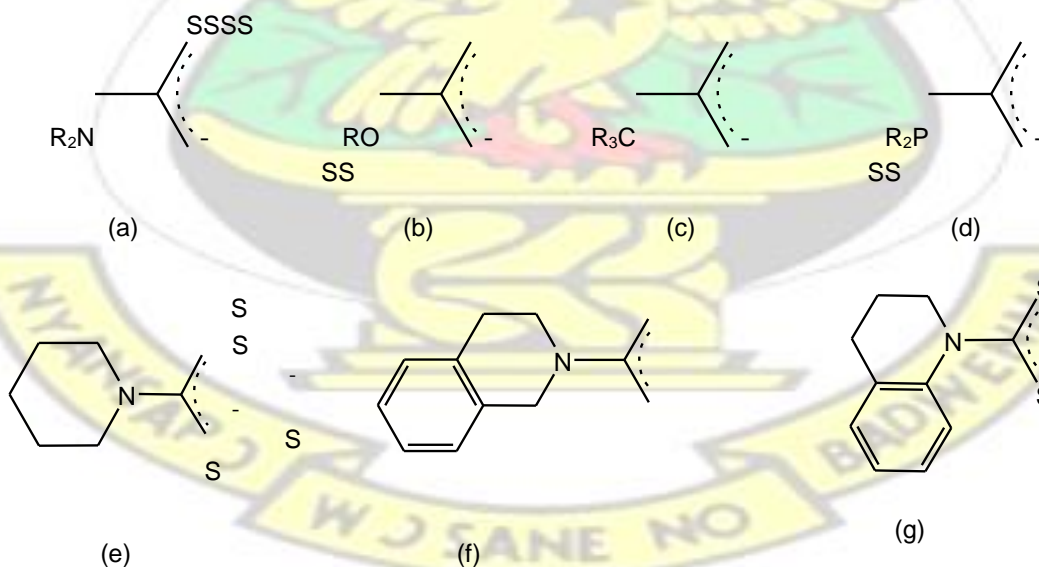


Figure 2.17: Thioacids: (a) dithiocarbamate, (b) xanthate, (c) dithiolate, (d) dithiophosphate, (e) piperidine-dithiocarbamate, (f) tetrahydroisoquinoline-dithiocarbamate, (g) tetrahydroquinolinedithiocarbamate

The structures (a) – (d) are the different types of thioacids whilst the (e) – (g) are dithiocarbamates where the R group is substituted with a heterocyclic substituent group (or are heterocyclic dithiocarbamates). Thioacid complexes have been investigated for their antifungal, antiviral and anticancer properties and also as vulcanization accelerators (Singhal et al., 2004; Garg et al., 1994; Sharma, 1986; Halls, 1969).

SSPs are advantageous because they (i) provide facile control over stoichiometry of the nanoparticles, (ii) are less toxic and easy to handle, (iii) are attractive for a wide range of interesting syntheses techniques, (iv) have substituent groups which serve as capping agents for controlling the size, shape and structure of nanoparticles, and (v) provide easy route for doping semiconductor nanoparticles (Afzaal et al., 2007). They have been reported for syntheses of good quality PbS, CdS, and ZnS nanoparticles using different single SSPs (Pickett and O'Brien, 2001, McNaughton et al., 2016, Boadi et al., 2012, Mlowe et al., 2014, Nyamen et al., 2013). Though there are reasonable amount of work done on this route, however, the mechanism of decomposition of SSPs in solvents is complex and the understanding of the role of solvent in the decomposition still lacking.

#### 2.5.4.1 Dithiocarbamates

Dithiocarbamates are very important source of SSPs. Of all the thioacids, dithiocarbamates have strong metal binding properties and have been considered the most versatile ligand (Sharma, 1986). The synthesis of metal-dithiocarbamates follows the scheme shown in Figure 2.18. Early

studies on organosulphur chemistry led to the discovery of dithiocarbamates. The exothermic reaction between carbon disulphide and either ammonia or a primary or secondary amine in the presence of a base yields dithiocarbamates (Halls, 1969). The low electronegativity of the sulphur atom (compared to oxygen) decreases the ionic character of dithiocarbamates and thereby alters the relative stability of the various bonds. It also reduces the significance of hydrogen bonding in the dithiocarbamate. Sulphur has the ability to form double bonds due to the presence of vacant  $d\pi$  orbitals (Sharma, 1986).

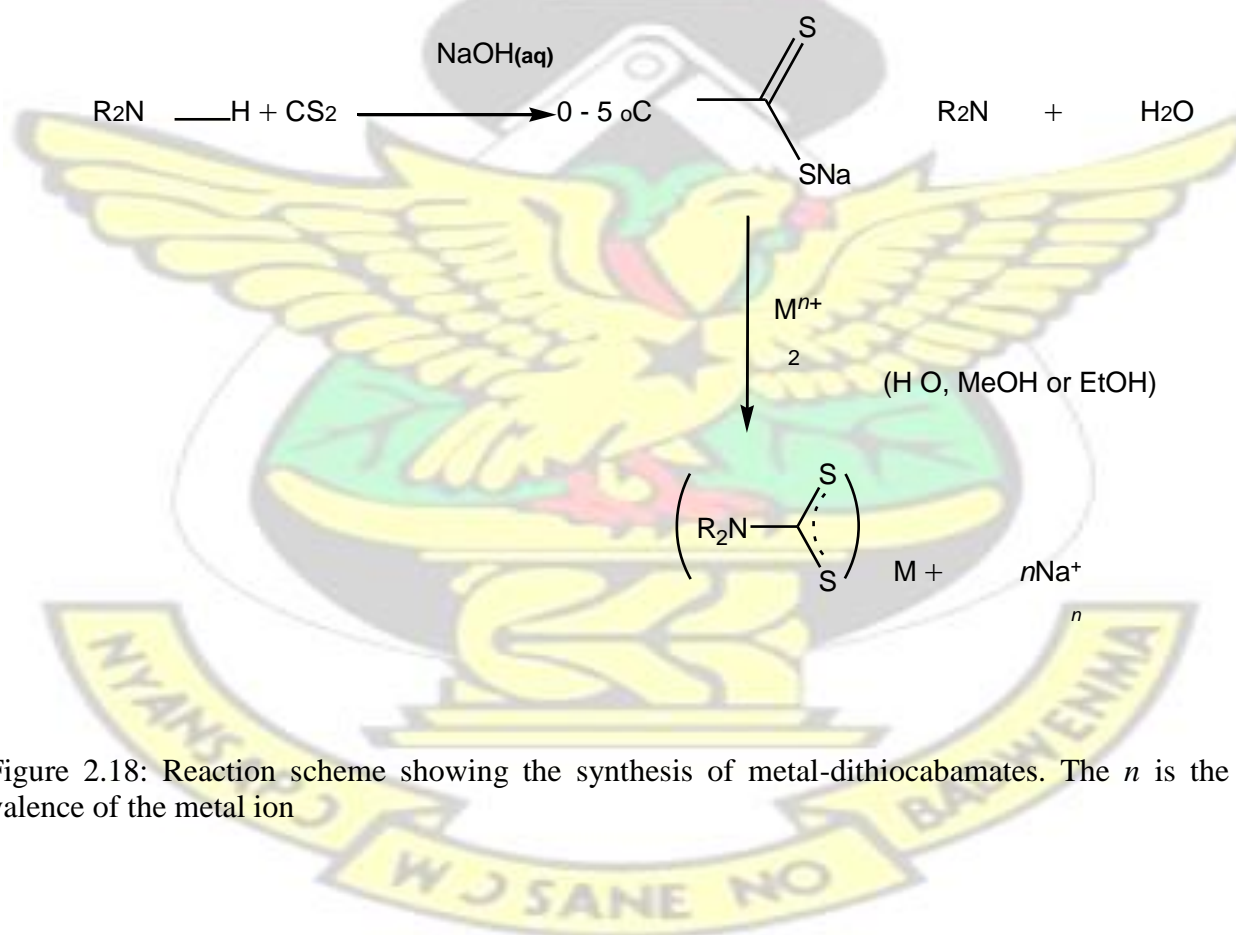


Figure 2.18: Reaction scheme showing the synthesis of metal-dithiocarbamates. The  $n$  is the valence of the metal ion

The structure of metal-dithiocarbamates ( $\text{M}(\text{R}_2\text{NCS}_2)_n$ ) can be written in different canonical forms as shown in Figure 2.19 (Sharma, 1986).

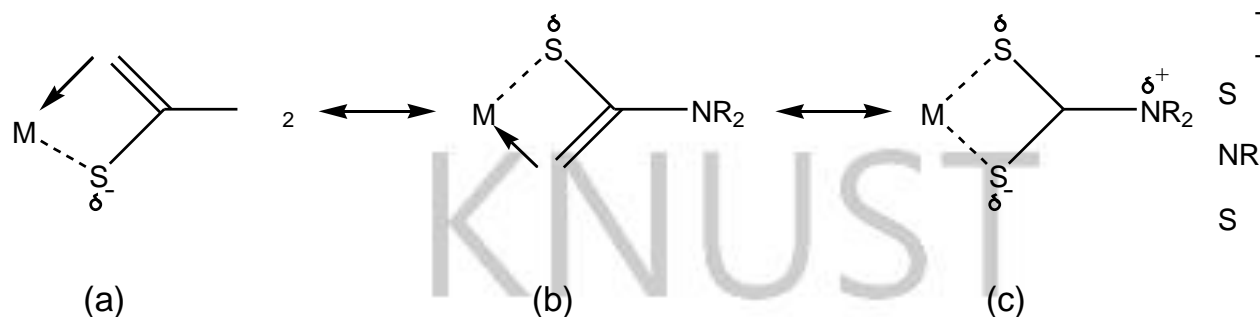


Figure 2.19: Canonical structures of metal-dithiocarbamates

The canonical form (c) is said to arise from the mesomeric electron releasing tendency of the  $R_2N$  group. The drift of electrons to the sulphur atoms increases the electron donor capacity and thus the dithiocarbamates form strong complexes with heavy metals with a reduced tendency to deactivate, pi-bond formation from metal to sulphur atom. Dithiocarbamates can also stabilize transition metals with high oxidation states. The strong metal binding of dithiocarbamates is demonstrated in their water insolubility; however, those with alkali and alkaline earth metals are soluble in water (Sharma, 1986; Hassan and Zayed, 2014). Dithiocarbamates are soluble in nonpolar organic solvents (Sharma, 1986).

Dithiocarbamates act as monodentate, bidentate and bidentate bridging ligand of metal complexes (Onwudiwe and Ajibade, 2010). Monodentate and bidentate formation in dithiocarbamate can be distinguished using infrared (IR) technique. The  $\nu(C-S)$  stretching frequency appears in the region  $980-1050\text{ cm}^{-1}$  of the IR spectra of dithiocarbamates. One strong bend in the region gives indication of the formation of a bidentate whilst a doublet indicates the presence of  $\nu(C-S)$  and  $\nu(C=S)$ , supporting a monodentate formation. Another significant band is the  $\nu(C^N)$  (also known as *thioureide*) which appears at about  $1500\text{ cm}^{-1}$ . The

appearance of this band gives indication of the double character in the  $S_2CNR_2$  bond (Sharma, 1986; Halls, 1969).

KNUST

#### 2.5.4.2 Decomposition mechanism of dithiocarbamates

Early studies suggest the decomposition of metal-dithiocarbamates via a thiocyanide intermediate which further decomposes to sulphides and finally oxidized to metal or metal oxide (Sharma, 1986). The stability of dithiocarbamates is pH dependent. Joris et al., (1969) explained this instability to be as a result of an intramolecular hydrogen bonding that forms between the sulphur and nitrogen atom when the sulphur atom is protonated. Thus, a high internal energy resulting from the hydrogen bonding is introduced into the dithiocarbamates which is responsible to the instability.

Recently, dithiocarbamates have received considerable attention as SSPs for the synthesis of good quality semiconductor nanomaterials (Nyamen et al., 2014; Mthethwa et al., 2009; Srinivasan and Thirumaran, 2014). The chemical structure, strong metal binding ability, stability, decomposition and ease of substituting of the R group bring on board interesting chemistries that can be explored in nanomaterials synthesis. The R group (substituents) attached to the nitrogen in dithiocarbamates significantly influence the thermal stability of the complex and also serves as a capping agent for the nanomaterials during synthesis (Srinivasan et al., 2012). Heterocyclic dithiocarbamates (Figure 2.17 (e) – (g)) are a class of dithiocarbamates with superior stability and self-capping ability. It has been reported that the heterocycle attached to the amine influences the behaviour of

the dithiocarbamate through variation in the electron-releasing ability of the amine (Forghieri et al., 1988; Fabretti et al., 1983).

The decomposition of SSPs in suitable solvents yields good quality nanoparticles. Nyamen et al., (2011) prepared CdS nanorods by decomposing cadmium piperidine dithiocarbamate and cadmium tetrahydroquinoline dithiocarbamate complexes in hexadecylamine or tri-n-octylphosphine oxide. Similarly, the synthesis of ZnS nanoparticles has been reported by Srinivasan and Thirumaran, (2014) in which they decomposed pyridine adducts of zinc dithiocarbamates in triethylenetetraamine. The nature of the solvent plays significant role in the decomposition of the precursor to the desired nanomaterial. Early studies focused on understanding the mechanism of decomposition of dithiocarbamates in aqueous systems, however, synthesis of nanomaterials in aqueous medium yield less crystalline nanomaterials (Humeres et al., 1999). In contrast, the syntheses of nanomaterials in organic solvents such as alkylamines yield high crystalline nanomaterials. Thus, the advent of size-controlled colloidal synthesis of nanomaterial has sprung much interest into understanding the decomposition of dithiocarbamates in organic solvents.

Decomposition of dithiocarbamates in some alkylamines has been reported (Figure 2.20). With the help of NMR spectroscopy, LC-MS, XRD and TEM, Jung et al., (2010) studied the decomposition of zinc alkyldithiocarbamates in the presence of alkylamines. Their analysis showed that the amine (solvent) coordinates with the central metal and this metal-coordinated amine initiates a nucleophilic attack on the most electron-deficient thiocarbonyl carbon of the alkyldithiocarbamate ligand which leads to the decomposition to generate thiourea, hydrogen sulphide and the desired metal sulphide nanoparticles.

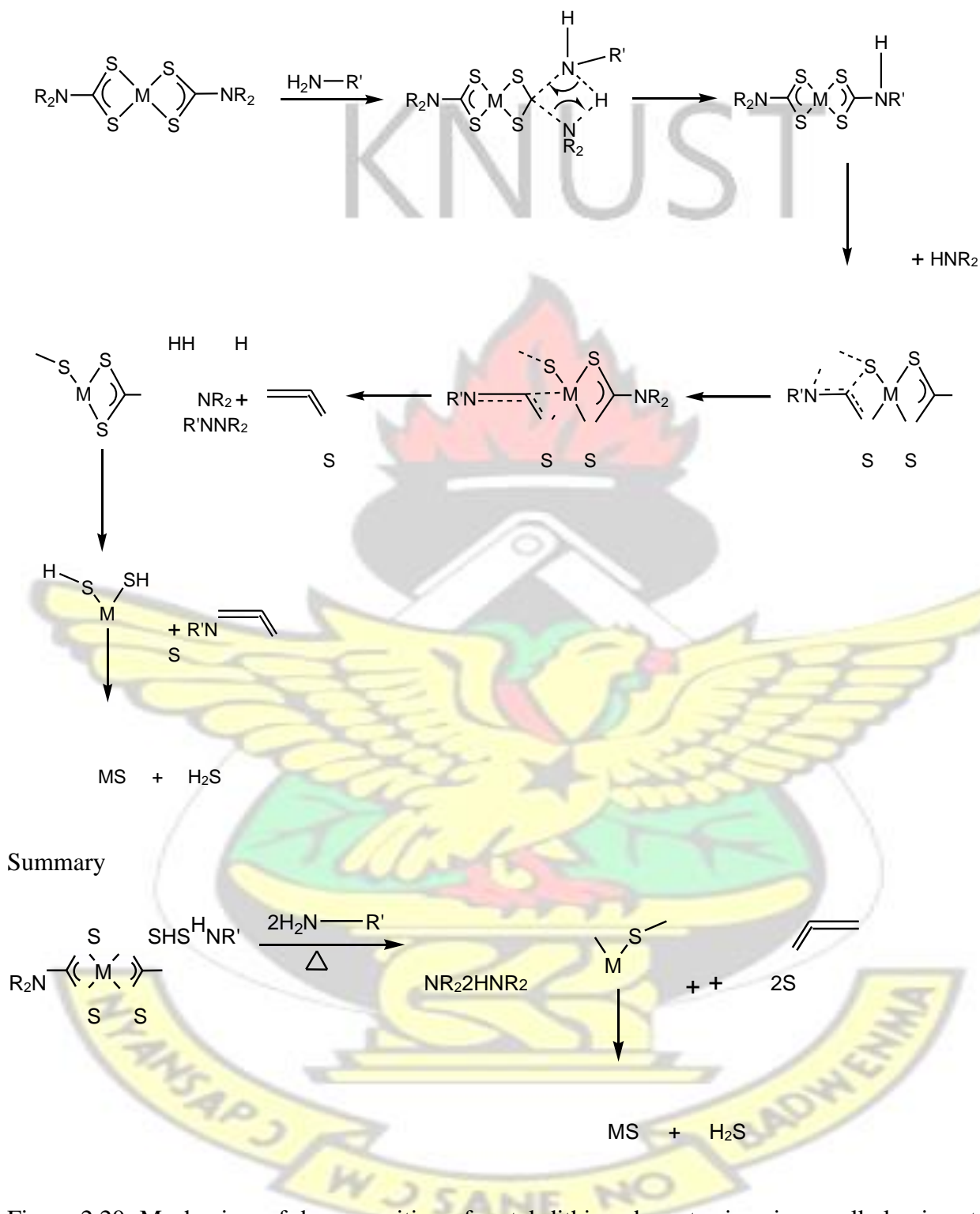


Figure 2.20: Mechanism of decomposition of metal-dithiocarbamates in primary alkylamines to yield desired metal sulphide nanoparticles

They also added that excess of alkylamine in the reaction system promoted the possibility of replacing the secondary amine group on the dithiocarbamates with the alkylamine which is similitude to trans-amidation reactions. Hollingsworth et al., (2014), using experimental and computational modeling (using DFT), also found that the decomposition of nickelalkyldithiocarbamates in primary amines proceed via (i) formation of adduct of nickelalkyldithiocarbamate with the primary amine (this occurs when the complex dissolves in the amine), (ii) replacement of the secondary amine on the dithiocarbamate with the primary amine (amide-exchange), (iii) nucleophilic attack of the primary amine at the backbone carbon of the dithiocarbamate (iv) formation of dithiocarbamate species which loses isothiocyanates as the proton on the nitrogen migrate to the sulphur atom, and finally (v) formation of the desired nickel sulphide nanoparticles.

From the mechanisms discussed above, it is evident that the formation of metal sulphides from decomposition of dithiocarbamates in primary amines proceeds through the formation of primary amine-dithiocarbamates intermediate (serving as the rate determining step) which eventually decomposes to metal sulphides. Islam et al., (2013), using *in situ* XAS technique found two different mechanistic pathways for decomposition of nickel and iron dithiocarbamate complexes in oleylamine. It is worth noting that these proposed mechanisms are only limited to the metaldithiocarbamate complexes studied and therefore in-depth decomposition studies of other metaldithiocarbamate systems in different environments is required to come out with conclusive decomposition mechanism.

## 2.6 Metal Chalcogenide Nanoparticles

### 2.6.1 Zinc sulphide (ZnS)

Zinc sulphide (ZnS) is a direct wide bandgap (II–VI) semiconductor compound, which has excellent optical properties in the infrared (IR) and the far-IR region (Afzaal et al., 2007; Han et al., 2006). It shows photoluminescence in the ultraviolet (UV) region, and also possesses other important luminescence properties (such as electroluminescence, mechanoluminescence, acausticluminescence and thermal luminescence) (Jassby et al., 2011; Zhu et al., 2003). Thus, ZnS is a very promising metal chalcogenide material which has immensely attracted attention as valuable transparent semiconductor for applications in photovoltaics, photocatalysis, ultra-violet light emitters, diodes, sensors (ultraviolet light sensors, gas sensors, biosensors), lasers, fluorescence probes, biomedical imaging, flat screen displays, spin-tropics (related to storage devices) and other electronic devices (He et al., 2016; Hu et al., 2005; Ng et al., 2016; Khalkhali et al., 2016; Kaur et al., 2016). ZnS is white- to slightly yellowish material and it is most considered alternative to cadmium (Cd) containing semiconductor chalcogenides (such as CdS, CdSe, CdTe) because it is nontoxic and more suitable for biological applications (Fang et al., 2009; Khalkhali et al., 2016).

### 2.6.1.1 Crystal structure

At room temperature, bulk ZnS crystallizes in a cubic zinc blende (space group  $F43m$ ) structure (Sphalerite) and transforms at elevated temperatures (usually above 1020 °C depending on the sulphur reactivity) to hexagonal wurtzite (space group  $P6_3mc$ ) structure (Figure 2.21) (Zhang and Banfield, 2009; Khalkhali et al., 2016; Afzaal et al., 2007).

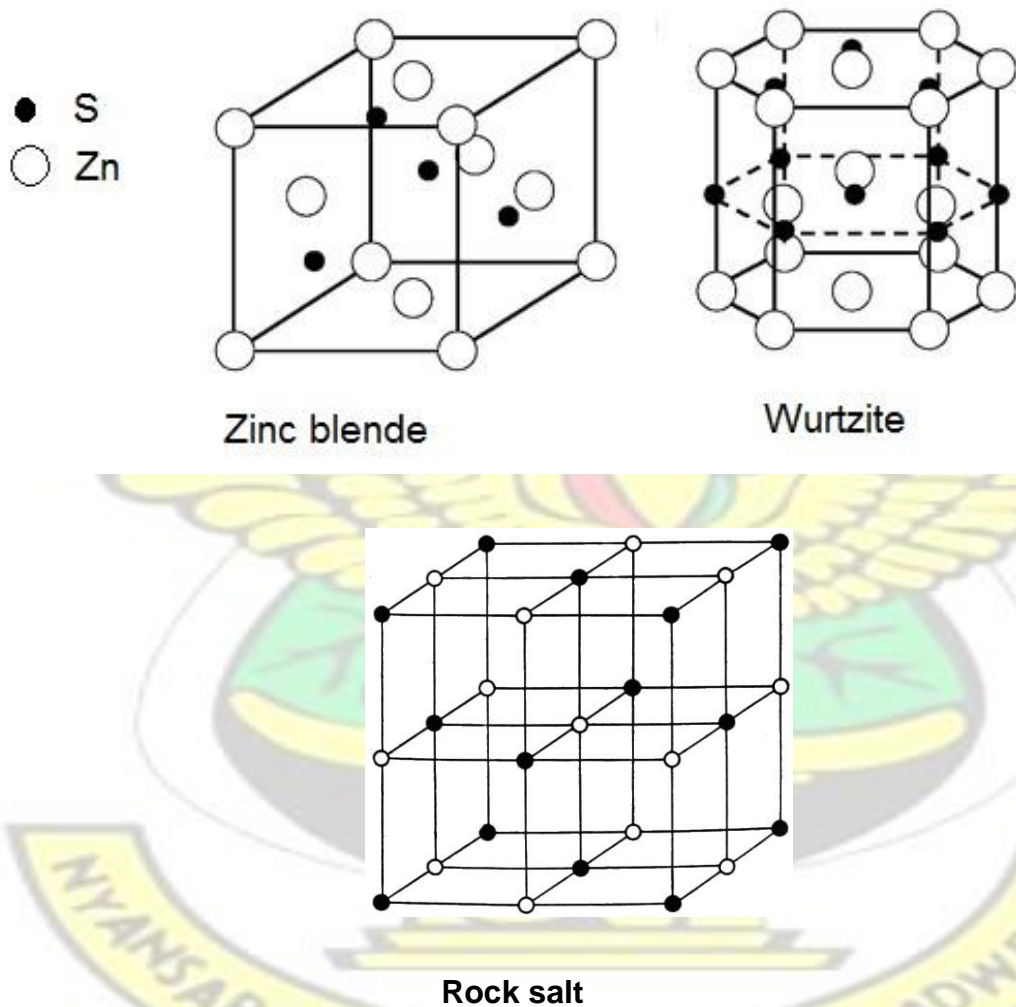


Figure 2.21: Zinc blende, wurtzite and rock salt crystal structures

Rarely, ZnS is also reported to show cubic rock salt phase (Porta et al., 2014). The zinc blende and wurtzite forms are covalently bonded solids and the co-ordination geometry at the Zn and S is tetrahedral (Fang et al., 2009; Kaur et al., 2016). The coordination number of each ion is 4 and the Zn:S ratio is a 1:1 stoichiometry. The difference between both structures is that (i) the zinc blende is based on a face centered cubic packing (fcc) of anions whilst the wurtzite is based on a hexagonal close packing (hcp) of anions, and (ii) the zinc blende has four asymmetric units in its unit cell whilst the wurtzite has two (Kaur et al., 2016). The zinc blende polymorph is the most stable form of ZnS at ambient temperature and pressure whilst the wurtzite is metastable. However, at temperatures above 1020 °C and also at small particle sizes (usually 2 – 3 nm), the wurtzite is stabilized thermodynamically (Han et al., 2006; Goodell et al., 2008; Dawood and Schaak, 2009; Khalkhali et al., 2016). The wurtzite exhibits more desirable optical properties compared to the sphalerite.

### 2.6.1.2 Polytypes

The free-energy difference between the sphalerite and wurtzite crystal structures is about 13 kJ mol<sup>-1</sup> (Gardner and Pang, 1988; Dawood and Schaak, 2009; Biswas and Kar, 2008). Thus, both common forms of ZnS usually co-exist as polytypes (Afzaal et al., 2007; Zhang and Banfield, 2009). Also, there are about 140 polytypes of ZnS all based on specific cubic close packing (ccp) and hexagonal close packing (hcp) arrangements that exist. Mixed phases of cubic and wurtzite structures have been reported in ZnS nanoparticles where each phase had equal stacking probability and are dependent on the synthesis history (Zhang and Banfield, 2009). High temperatures (> 1000 °C) favour the formation of bulk ZnS polytypes and are said to be

entropydriven (or thermodynamically favoured). Low temperatures favour the formation of ZnS nanoparticles with mixed stacking in solution and are found to be driven kinetically. However, understanding into growth of mixed layer stacking nanoparticles is still low. Low-angle X-ray diffraction, Debye function analysis (DFA) and Rietveld analysis are the techniques reported for the determination of the different proportions of polytypes stacking in bulk minerals, nanomaterials and synthesized nanoparticles (Zhang and Banfield, 2009).

### **2.6.1.3 Properties**

The properties of ZnS are shown in Table 2.2. The band gap energy of bulk ZnS material having a sphalerite structure is reported to be within 3.54 and 3.72 eV. For a wurtzite bulk ZnS, the band gap energy is within 3.77 and 3.91 eV (Fang et al., 2011; Kaur et al., 2016; Zhu et al., 2003). The wide band gap energy offers variety of advantages, (i) possibility of doping with other useful variety of metals in order to manipulate the band structure, (ii) serves as infrared window/buffer material in photovoltaics, and (iii) luminescence. Other important fundamental properties of ZnS are the polar surfaces, excellent electron transport properties, thermal stability and high electronic mobility (Huang et al., 2012; Liu et al., 2013; Balantseva et al., 2014). Thus, the ability to manipulate the band gap through synthetic procedures leads to fine-tuning of the electronic properties.

# KNUST

Table 2.2: Properties of ZnS

Property	Value		References
	Sphalerite	Wurtzite	
<b>Electronic Property</b>			
Bandgap (eV)	3.54	3.91	(Kaur et al., 2016)
	3.60		(Zhu et al., 2003)
	3.72	3.77	(Cheng et al., 2014)
Lattice constant (Å)	5.4093	a=3.817 c=6.249	(Kaur et al., 2016) (Zhang et al., 2004)
Dielectric constant	8.9	8.9	(Kaur et al., 2016)
Electron mobility (cm <sup>2</sup> /Vs)	180	180	(Kaur et al., 2016)
Hole mobility (cm <sup>2</sup> /Vs)	5	5	(Kaur et al., 2016)
<b>Thermal Property</b>			
Heat of formation (kJ/mol)	477	477	(Kaur et al., 2016)
Thermal coefficient of expansion (µm/m°C)	6.36	6.36	(Kaur et al., 2016)
Thermal conductivity (W/mK)	25.1	25.1	(Kaur et al., 2016)
Specific heat capacity (J/g°C)	0.472	0.472	(Kaur et al., 2016)
<b>Other properties</b>			
Refractive Index (at 632 nm)	2.36	2.36	(Cheng et al., 2014)
Melting point (°C)	1650	1650	(Porta et al., 2014)

#### 2.6.1.4 Synthesis of ZnS nanoparticles

The synthesis of ZnS nanoparticles has received considerable attention as nontoxic source of semiconductor nanomaterials. Some synthetic techniques and results reported for the synthesis of ZnS nanoparticles are shown in Table 2.3 (see page 76). ZnS is obtained by the reaction of a zinc salt and sulphur. The sulphur could be elemental sulphur or a sulphur-containing compound such as sodium sulphide, thiourea, cysteine and dodecanethiol (Goodell et al., 2008; He et al., 2016; Kole et al., 2014). There are also single molecules containing the two reactants already bonded together, usually termed as single source precursors (Afzaal et al., 2007; Shen et al., 2011). In order to control the nanoparticles growth or functionalize the nanoparticles with suitable organic molecules to ensure dispersibility in solvents, capping agents are employed in the synthesis (Joo et al., 2003; Shen et al., 2011). Capping agents attach to the surfaces of the nanoparticles and thereby, affect the reactivity of the nanoparticles (Chang and Waclawik, 2014).

The reported factors that control the phase of ZnS nanoparticles are the reaction temperature, nature of reactants, solvent media and heating procedure or source of heating. Synthesis usually performed at room temperature or lower temperature conditions yields sphalerite form of ZnS whilst those at high temperatures yield wurtzite ZnS. Goodell et al., (2008) and Gilbert et al., (2006) obtained sphalerite ZnS nanoparticles when they reacted zinc chloride and sodium sulphide in anhydrous methanol at room temperature. Similarly, Dawood and Schaak, (2009) reacted zinc chloride and thiourea at 160 °C in the presence of ethylene glycol and tetramethylammonium hydroxide as capping agent but obtained a wurtzite ZnS.

# KNUST



Table 2.3: Synthesis procedures reported for ZnS nanoparticles

Precursors or starting materials			Synthetic procedure	Brief result	References
<i>Metal precursor</i>	<i>Sulphur precursor</i>	<i>Capping agent</i>			
Zinc acetate	Sodium sulphide	Pyridinium di-nhexadecyldithiophosphate (PyDDP)	The sodium sulphide and PyDDP were dissolved in ethanol-water mixture at 55 °C and equimolar solution of zinc acetate was added drop wise to form the ZnS. The [S <sup>2-</sup> ]:[PyDDP] ratio was 1:2.	Average particle size: 4 nm.	(Chen and Liu, 1999)
Zinc chloride	Thiourea	Tetramethylammonium hydroxide (TMAH)	Zinc chloride and TMAH were dissolved in ethylene glycol (EG) and heated to 100 °C. EG solution of thiourea was added and the resultant mixture heated at 160 °C.	WZ-ZnS. Particle size: 4 – 7 nm.	(Dawood and Schaak, 2009)
Zinc chloride	Sodium sulphide	-	Methanolic solution of sodium sulphide was added drop wise to 2.5 mL of 1 M anhydrous methanol solution of Zinc chloride to form ZnS at room temperature.	ZB (Sphalerite)ZnS. Particle size: 3.2 – 3.6 nm	(Goodell et al., 2008; Gilbert et al., 2006)
Zinc nitrate hexahydrate	Sodium sulphide	Poly(vinyl alcohol) (PVA)		ZB (Sphalerite)ZnS. Particle size: 3 nm	(Han et al., 2006)

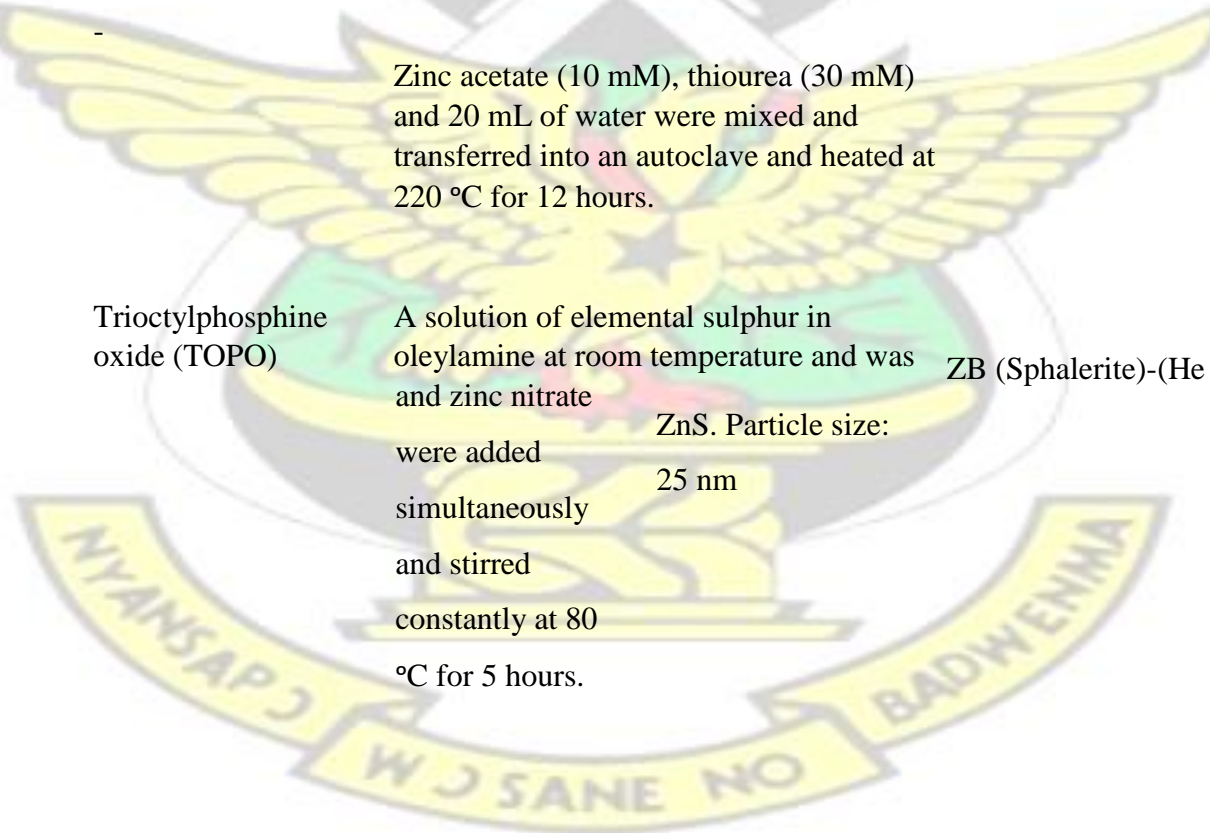
---

0.5 g PVA was discharged into a four-neck flask containing 100 mL deionized water and stirred to dissolve under nitrogen.

77



			Aqueous solutions of sodium sulphide	injected into a previously heated (170 °C) oleylamine solution of ZnCl <sub>2</sub> and TOPO. The resultant solution was heated to 320 °C and aged for 1 hour.
Zinc acetate	Cysteine	-	Equimolar amounts of Zinc acetate and cysteine together with 21 mL water were transferred into a 28 mL Teflon-lined stainless steel autoclave and heated at 160 °C for 12 hours to produce ZnS nanoparticles.	
Zinc acetate	Thiourea	-	Zinc acetate (10 mM), thiourea (30 mM) and 20 mL of water were mixed and transferred into an autoclave and heated at 220 °C for 12 hours.	
Zinc chloride	Elemental Sulphur	Trioctylphosphine oxide (TOPO)	A solution of elemental sulphur in oleylamine at room temperature and zinc nitrate were added simultaneously and stirred constantly at 80 °C for 5 hours.	ZB (Sphalerite)-(He et al., 2016)



WZ-ZnS nanobelts: (Kole et al., with length 400 nm and diameter 10 – 20 nm 2014)

ZB (Sphalerite)-ZnS. Particle size: 7 – 11 nm (Joo et al., 2003)

78

Zinc (Zn-DDTC) Oleic acid diethyldithiocarbamate (Zn-DDTC)

heated at 100 °C under vacuum for 20 min. The resultant solution was then heated at 200 °C at a rate of 15 °Cmin<sup>-1</sup> under nitrogen to obtain the ZnS nanoparticles

WZ-ZnS quantum dot. Particle size: 9.5 nm. (Shen et al., 2011) nm. With only ODE: WZ-ZnS nanowires with diameter 4.4 nm and length 300 nm

Zinc-oleate dodecanethiol - complex  
Slurry of Zn-DDTC, oleic acid, oleylamine and octadecene (ODE) was made and

Zinc-oleate was dissolved in 50 mL of oleylamine and 50 mL dodecanethiol at room temperature and the mixture was heated to 310 °C under argon for 30 mins.

ZB (Sphalerite)-ZnS. Particle size: 10nm (Choi et al., 2009)



# KNUST

79



It is interesting to note that the nature of reactants to some extent has a major influence on the phase of ZnS. He et al., (2016) and Kole et al., (2014) applied similar hydrothermal techniques but different sulphur compounds (cysteine and thiourea) and obtained sphalerite and wurtzite ZnS respectively. Also, Joo et al., (2003) and Choi et al., (2009) applied different synthesis techniques (i.e. hot-injection and heat-up synthesis) and precursors but obtained similar results (i.e. Sphalerite ZnS). Shen et al., (2011) decomposed thermally a single molecule which consisted of Zn and S already covalently bonded (Zinc diethyldithiocarbamate) in different solvent media at 200 °C and obtained only wurtzite ZnS nanoparticles but with different morphology.

This disparity in the control of the phase and morphology of ZnS nanoparticles opens avenue for further research to explore a wide range of precursors and synthesis techniques.

#### **2.6.1.5 Growth kinetics of ZnS nanocrystals**

The study of nanocrystal growth is fundamental to understanding the manipulation of materials properties so as to tailor for specific application. ZnS nanocrystals systems have received considerable amount of research because their high structural symmetry enhances the probability of oriented attachment growth mechanism (Huang et al., 2003). When the size of a nanocrystal is reduced, the electronic band structure is modified due to quantum confinement effect and results in an increment of the band gap energy of the nanocrystal. Practically, this increment in band gap energy is clearly observed as a blue shift in the absorption spectrum of the nanocrystal. This gives a clue as to how to probe the kinetics of the growth of the nanocrystal in solution. The time dependent evolution of UV-Vis absorption spectra has been extensively used to study the kinetics of ZnS nanocrystals (Tiemann et al., 2008; Tiemann et al., 2005; Huang et al., 2003).

The Brus equation (2.32) gives a relationship between the band gap energy and the radius of the nanocrystal based on reduced mass approximation:

$$\Delta E_g = E_{g(nc)} - E_{g(bulk)} = \frac{\hbar^2}{8r^2} \left( \frac{1}{m_e^*} + \frac{1}{m_h^*} \right) - \frac{1.8e^2}{4\pi\epsilon_0\epsilon r} \quad (2.32)$$

where  $\Delta E_g$  is the band gap energy difference between the band gap energy of the nanocrystal  $E_{g(nc)}$  and the bulk band gap energy  $E_{g(bulk)}$ . The effective masses for the electrons and holes are  $m_e^*$  and  $m_h^*$ . The  $\epsilon_0$  and  $\epsilon$  are permittivity of a vacuum and dielectric constant of the material in question respectively,  $\hbar$  is the Planck's constant and  $r$  is the radius of the spherical nanocrystal. The first term in equation 2.32 represents the kinetic energy of the exciton and dominates when  $r$  is small. The second term is the Coulombic interaction of the electron and hole (Whiffen et al., 2014). For ZnS,  $E_{g(bulk)}=3.6$  eV (some publications used 3.54 eV),  $m_e^* = 0.34m_e$ ,  $m_h^* = 0.23m_e$  and  $\epsilon = 8.76$  (Whiffen et al. 2014; Suyver et al. 2001). Suyver et al., (2001) calculated the radius  $r(E)$  of ZnS nanocrystals using the Brus equation in the solved form

$$\frac{\sqrt{\dots}}{\dots} \quad (2.33)$$

Tiemann et al., (2005) employed an in-situ stopped-flow UV absorption spectroscopy to investigate the growth of ZnS nanoparticles in a supersaturated aqueous medium. Aqueous solutions of ZnSO<sub>4</sub> and Na<sub>2</sub>S were injected simultaneously into an observation cell with pressure-driven syringes and the stopped-flow signal was triggered for data acquisition. This study concluded qualitatively that the growth of ZnS nanoparticles within 40 milliseconds (ms) is governed predominantly by Ostwald ripening, though other mechanisms such as coalescence may also occur. Huang et al., (2003), using similar technique, also investigated the role of oriented

attachment of ZnS crystal growth kinetics in both aqueous and mercaptoethanol-water solutions. Using XRD, HRTEM and kinetic modelling, they were able to conclude that in both systems, early crystal growth of ZnS nanocrystals occurs via crystallographically specific oriented attachment resulting in different stacking orders and faults, however, at longer reaction times, the surface irregularities are removed via diffusion controlled growth mechanism resulting in rounded particles with complex internal structures.

It is certain that in the coarsening of ZnS nanoparticles in solution, multiple kinetic mechanisms seem to occur. The hybrid kinetic equation combining the effects of Ostwald ripening (OR) and oriented attachment (OA) is given as

$$D = \frac{D_o(\sqrt[3]{2k_1t+1})}{(k_1t+1)} + k_2t^{1/n} \quad (2.34)$$

where  $D$  is the mean particle sizes at time  $t$ ,  $D_o$  is initial particle diameter at time  $t_o$ ,  $k$ , the temperature-dependent material constant,  $k_1$  and  $k_2$  are first and second rate constants and  $n$ , the exponent relevant to the coarsening process ( $n$  has value between 2 and 4, depending on how the ripening was controlled (by surface diffusion at the solid/liquid interface,  $n = 2$ , by volume diffusion in the liquid medium,  $n = 3$  and by dissolution kinetics,  $n = 4$ ) (Huang et al., 2003; Tiemann et al., 2008).

Equation 2.34 is obtained by substituting  $D_2$  in equation 2.28 (for OR) with  $D$  in equation 2.29 (for OA, and assuming  $t = 0$ ).

The growth component in the first term in equation 2.34 describes solely OA, which diminishes rapidly for the second term to dominate over longer time, thus, describing the two mechanisms

occurring simultaneously but do not affect each other. Also equation 2.34 clearly describes the crystal growth kinetics by the two different pathways (Huang et al., 2003). The activation energy for purely OA of ZnS in aqueous medium is reported to be  $E_a(k_1) = 125.0$  J/mol and the activation energy resulting from both OA and OR using equation 4.2.3 was  $E_a(k_2) = 42.4$  kJ/mol (Huang et al., 2003). However, Tiemann et al., (2008) obtained quite a low activation energy  $E_a$  of 25.7 kJ/mol. Equation 2.34 implies that with increasing time, hybrid crystal growth (resulting from OR and OA mechanisms) occurs. The effect of NaOH concentration on coarsening of ZnS nanoparticles in aqueous medium has also been studied. It was found that 2M concentration of NaOH was enough to ensure pure and multistep OA growth characteristics (Wang et al., 2007).

### 2.6.2 Manganese sulphide (MnS)

MnS is a *p*-type semiconductor compound with a wide band gap of about 3.7 eV (Zheng et al., 2006; Tian et al., 2009). MnS crystallizes in three different polymorphs: the octahedrally coordinated rock salt structure ( $\alpha$ -MnS, space group  $Fm\bar{3}m$ ), the tetrahedrally coordinated zinc blende structure ( $\beta$ -MnS, space group  $F\bar{4}3m$ ) and the tetrahedrally coordinated wurzite structure ( $\gamma$ -MnS, space group  $P6_3mc$ ) (Michel et al., 2006; Zheng et al., 2006). The  $\alpha$ -MnS phase (also known as alabandite) appears green and is the thermodynamically stable whilst the  $\beta$ -MnS and  $\gamma$ -MnS are pink and metastable (Lu et al., 2001).

The  $\beta$ -MnS and  $\gamma$ -MnS phases are antiferromagnetic with Néel temperature (magnetic ordering temperature) of 152 K (-121.15 °C) and 90 K (-183.15 °C) respectively (Lu et al., 2001). The metastable polymorphs form at low temperatures comparative to the stable polymorph which forms at relatively higher temperature (Michel et al., 2006). The metastable states transform to the

stable  $\alpha$ -MnS at 100 – 400 °C or at high pressures (Xiao et al., 2015). It has been reported that  $\gamma$ -MnS, though does not exist naturally (but exists under unusual laboratory conditions), exhibits superior chemical, electrical and magneto-optical properties than the most abundant  $\alpha$ MnS polymorph (Beltran-Huarac et al., 2014).

MnS has potential magnetic and optical applications. It is suggested by Zhang et al., (2004) that MnS may have acted as a catalyst for carbon fixation in the prebiotic world. MnS has been applied as a window/buffer material in solar cells and also for short wavelength opto-electronic devices (Puglisi et al., 2010; Tian et al., 2009). MnS is also an important dopant material in diluted magnetic semiconductors (DMS) which are immensely applied in spintronics (spin-based electronics) (Jun et al., 2002; Zheng et al., 2006).

MnS is also used as a battery electrode material due to its high capacity and excellent cyclability (Ha et al., 2015). It is attractive as a novel anode material in Li-ion batteries (Beltran-Huarac et al., 2014). The Gibbs free energy change ( $\Delta G$ ) and electromotive force (emf) of MnS are -202.50 kJ mol<sup>-1</sup> and 1.049 V respectively, and thus, it is expected to show a theoretical Li-storage capacity of about 616 mA h g<sup>-1</sup> (Liu et al., 2015).

MnS nanoparticles have recently attracted considerable attention as contrast agent in magnetic resonance imaging (MRI) which is widely applied for diagnosis and post-therapy evaluation (Meng et al., 2016). As a paramagnetic compound, MnS has a five unpaired electrons desirable to shorten the longitudinal relaxation time (rate of proton relaxation) which end up in enhancing the contrast in MRI images (Pan et al., 2011; Meng et al., 2016). In addition, MnS is less toxic comparative to the widely used Gadolinium (Gd)-based contrast agents (Meng et al., 2016; Taylor et al., 2008; Zhen and Xie, 2012).

### 2.6.3 Manganese-doped ZnS ( $Mn_xZn_{1-x}S$ )

Mn-doped ZnS nanoparticles are an interesting class of non-toxic doped semiconductor materials which have been extensively explored as phosphor, and in the fabrication of electroluminescence and sensing devices (Xu et al. 2014). The  $Mn^{2+}$  ions are known to create luminescent sites in ZnS host lattice (Sooklal et al., 1996). Upon photo-excitation, an electron is promoted from the valence band to the conduction band of the ZnS, leading to the generation of an electron-hole pair (exciton). This excited electron subsequently decays via a nonradiative recombination process to some surface or defect site or is captured by the  $Mn^{2+}$  ion in its  $^4T_1$  state after which it decays radiatively to the  $^6A_1$  state (Figure 2.22). In other words, the presence of Mn ions in ZnS lattice reduces the possibility of nonradiative recombination and causes the ZnS to phosphor at about 590 nm (Borse et al., 1999). However, the physical location and spatial organization of the Mn ions in the ZnS host lattice though essential for the devices efficiency, appears empirically challenging.

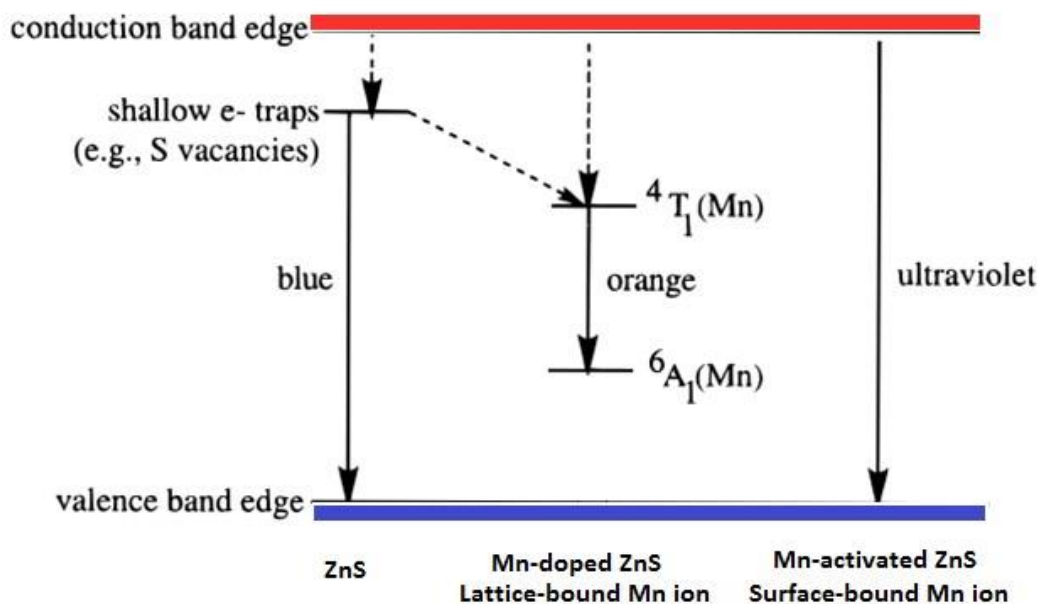


Figure 2.22: Transition states in Mn-doped ZnS nanoparticles

Thus, Sooklal et al. (1996) came up with the „inside“ and „outside“ concept describing the location of the Mn ion to be in the inside of the ZnS lattice (lattice bound) or outside (surface bound) (Figure 2.23). By using optical techniques, they associated a blue emission (at  $\lambda = 435$  nm) to freshly prepared ZnS nanoparticles, an orange emission (at  $\lambda = 585$  nm) to be emission due to the  ${}^4T_1 \leftarrow {}^6A_1$  transition for a Mn bound in ZnS lattice and an ultraviolet emission (at  $\lambda = 390$  nm) to a Mn activated ZnS or surface bound Mn on ZnS surface. Also, they noted that divalent metal ions on the surface of nanoclusters quenches red shifted emissions and efficiently promotes near band gap emissions. This concept has incited a number of research groups into investigating the local effect of Mn ions in ZnS host lattice.

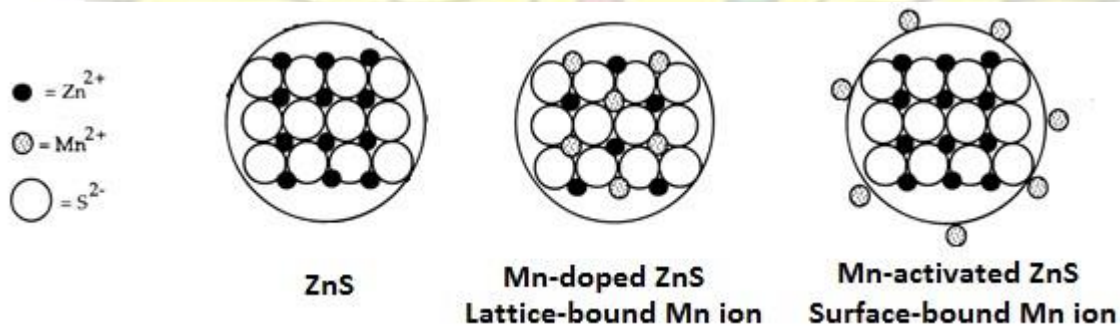


Figure 2.23: Sketch of model hypothesizing the physical location of Mn ions in lattice of ZnS (Sooklal et al., 1996)

To ascertain the local effect of Mn ion in ZnS lattice, Borse et al., (1999) using photoluminescence (PL) and electron-spin-resonance (ESR) techniques, came up with four different contributions of Mn ions; (i) Mn in tetrahedral cationic substitution site with  $T_d$  symmetry ( $S_T$ ), (ii) isolated Mn ions

at the surface or interstitial location ( $S_{II}$ ), (iii) Mn-Mn dipolar interactions ( $S_{III}$ ), and (iv) exchange-coupled Mn clusters ( $S_{IV}$ ). These models of Mn contributions were in different proportions and were substantiated with empirical results from ESR and PL. The various models of contribution are shown in Figure 2.24. Simply, the models mean that, at very low Mn concentration ( $S_I$ ), some ZnS nanoparticles are doped while some are not. As Mn concentration increases, more and more ZnS nanoparticles are doped which result in increase of the photoluminescence intensity. Further increment of the Mn concentration, that is from ( $S_{II}$ ) to ( $S_{IV}$ ), lead to quenching of the photoluminescence. The doping concentrations range considered in this work was 0.008 – 7.598 Mn wt % in ZnS. This implied that the luminescence increases to a limit and quenches depending on the concentration of the Mn in the ZnS host lattice.

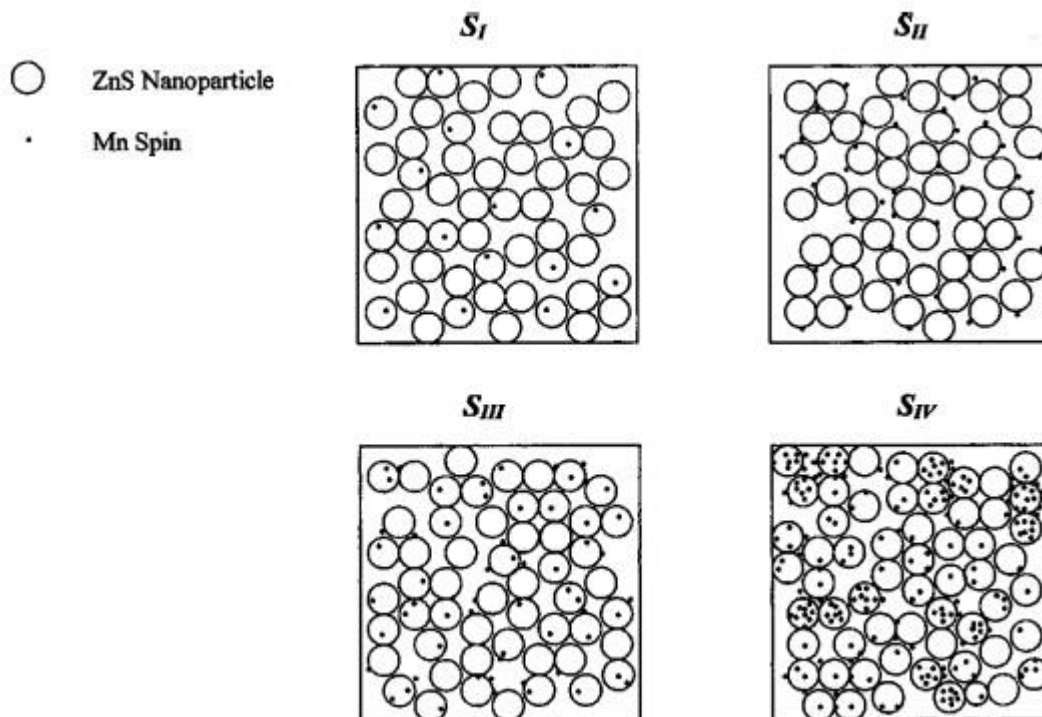


Figure 2.24: Different models describing the local effect of Mn ions in ZnS host lattice (Borse et al., 1999)

The decrease in  ${}^4T_1 \leftarrow {}^6A_1$  transition emission intensity with increasing Mn ions concentration in ZnS is widely reported. Most published papers on Mn-doped ZnS nanoparticles report the appearance of the emission peak at 580 – 600 nm corresponding to the  ${}^4T_1 \leftarrow {}^6A_1$  transition for a Mn bound in ZnS lattice (Table 2.4) (Cao et al., 2009; Ma et al., 2011; Srivastava et al., 2010). Jindal and Verma, (2008) observed an increase in emission intensity at 582 nm for ZnS doped with 5 % Mn ions and a drastic decrease for ZnS samples doped with 10 to 15 % Mn. Similarly, Beermann et al., (2006) observed the emission intensity curve at 590 nm go through a maximum as Mn content in ZnS was increased from 0.014 to 0.2 % (These numbers are found levels of Mn in Mn-doped ZnS samples obtained experimentally). They admitted that their synthesis technique could only allow Mn concentrations up to 0.3 %.

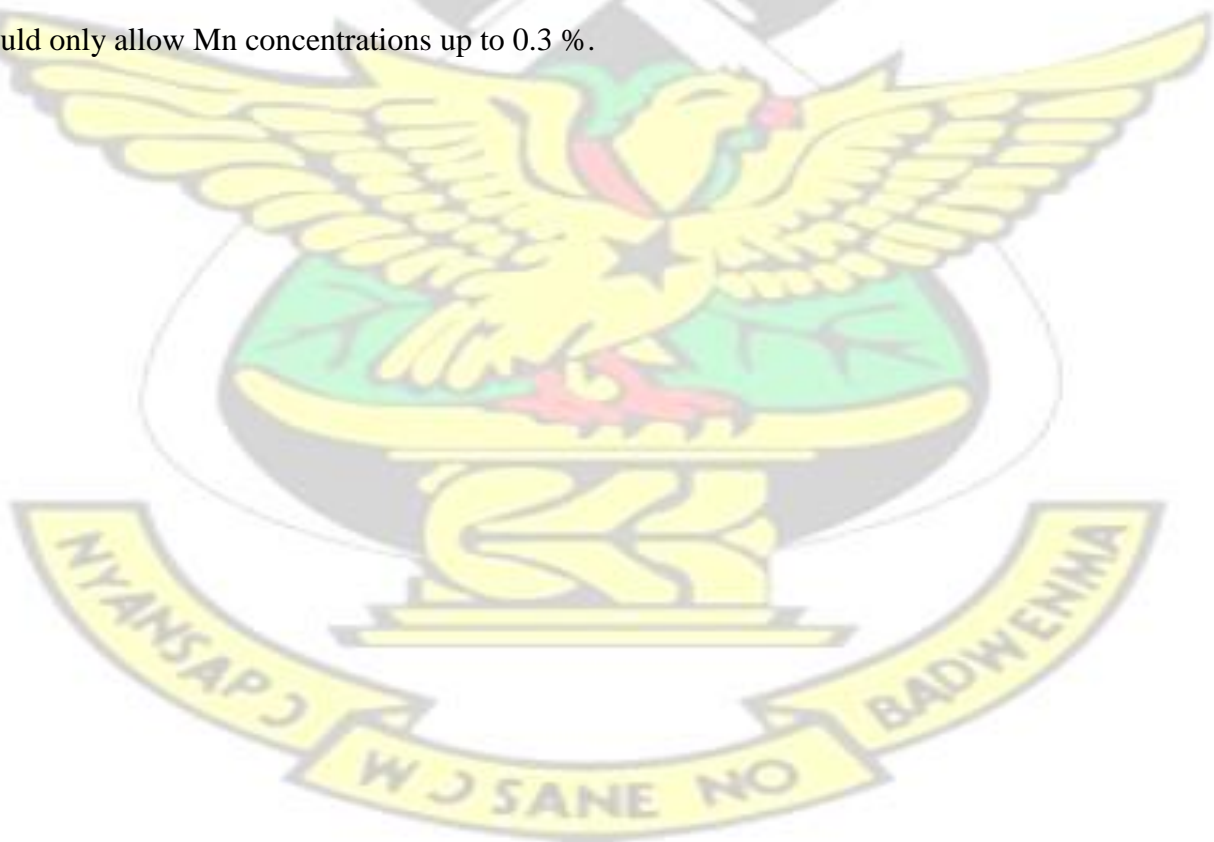
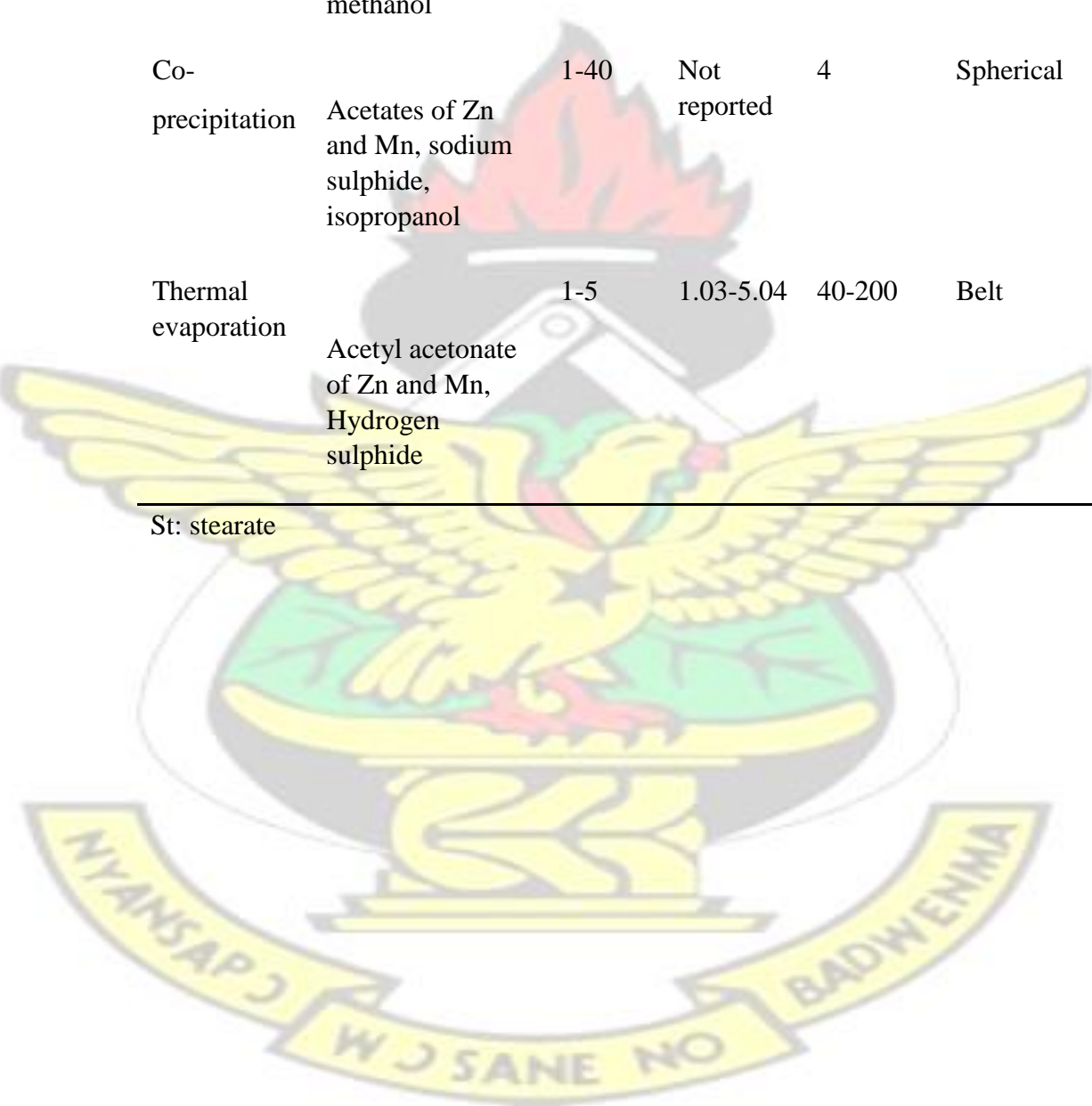


Table 2.4: Synthesis and properties of Mn-doped ZnS

Technique	Reagents	Mn % (Feed)	Mn % (Found)	Particle Size (nm)	Morpho- logy	Phase	EPR	Luminescence (nm)	Reference
Colloidal synthesis	Zn(NO <sub>3</sub> ) <sub>2</sub> , Mn(NO <sub>3</sub> ) <sub>2</sub> , Sulphur, Oleylamine	5-20	0.18-1.6	1.6-5.6	Rod	Wurtzite	Sextet	585	(Deng et al., 2011)
Colloidal synthesis	ZnSt <sub>2</sub> , MnSt <sub>2</sub> , Sulphur, octadecene, alkylamine	1	Less than feed	3.8	Spherical	Sphalerite	Sextet	585	(Srivastava et al., 2010)
Solvothermal	Acetates of Zn and Mn, ethanol, thiourea	3-11	1.9	10-16	Spherical	Sphalerite and traces of wurtzite	-	590	(Cao et al., 2009)
Reverse micelle	ZnCl <sub>2</sub> , MnCl <sub>2</sub> , Triton X-100, Cyclohexane, n-pentanol	1-5	0.04-0.18	3-5	Micro-scale compact chunk of nanoparticles	Sphalerite	Sextet	600	(Whiffen et al., 2014)
Co-	Acetates of Zn	5-15	0.38-1.03	3	Spherical	Sphalerite	-	600	(Peng et al.,

# KNUST

precipitation	and Mn, water, methanol								2005)
Co-precipitation	Acetates of Zn and Mn, sodium sulphide, isopropanol	1-40	Not reported	4	Spherical	Sphalerite	-	600, 640, 680	(Karar et al., 2004)
Thermal evaporation	Acetyl acetate of Zn and Mn, Hydrogen sulphide	1-5	1.03-5.04	40-200	Belt	Wurtzite	-	580	(Geng et al., 2004)
St: stearate									



# KNUST

90



The decrease in emission intensity at 590 nm was attributed to an exchanged-coupled  $d^{10}$  electron system arising from the dipole-dipole interaction between  $Mn^{2+}$  ions which induces fast decay of the  ${}^4T_1 \leftarrow {}^6A_1$  transition. Contrarily, Nazerdeylami et al., (2011) observed an increase in emission intensity when they varied Mn dopant concentration from 1 – 5 %. This observation by Nazerdeylami et al., (2011) is contradictory because only 3 Mn doping concentration was used and there was no elemental analysis to fully ascertain the actual levels on Mn in the ZnS nanoparticles.

EPR technique gives better understanding into the local effect of Mn ion bound in ZnS lattice. The appearance of a sextet in the EPR pattern gives an indication of the substitutionary replacement of  $Zn^{2+}$  with  $Mn^{2+}$  in the ZnS host lattice. This usually occurs at a lower percentage of Mn doping (Table 2.4). At higher amounts of  $Mn^{2+}$  in ZnS, some ZnS nanoparticles are doped with Mn whilst the remaining of Mn ions occupy the nanoparticles surfaces or interstitial positions resulting in Mn ion dipole-dipole interactions in the ZnS host lattice. Thus, a sextet in EPR is not usually expected in ZnS nanoparticles with higher concentrations of Mn ions but rather a broad peak arising from Mn ions interactions. From the pioneering work of Borse et al., (1999), one can qualitatively predict the location of Mn ions in the ZnS nanoparticles clusters.

The band gap energy of ZnS nanoparticles is reported to decrease with increasing Mn dopant concentration. Joicy et al. (2014) reported the decrease in band gap of ZnS nanoparticles from 4.18 to 3.94 eV as the Mn dopant concentration increased from 0 to 10 %. This decrease in band gap energy has also been observed by Jindal and Verma (2008). In contrast, other researchers have reported an increase in band gap energy with increasing Mn concentration in ZnS. Cao et al., (2009) found a decrease in band gap energy from 3.77 eV to 3.51 eV as they increased Mn concentration in ZnS from 0 to 0.11 %. Comparatively, Cao et al., (2009) used Mn concentrations far lower than those used by Joicy et al., (2014) and Jindal and Verma, (2008) which might have

resulted in the opposing trend reported. Also the synthesis techniques used were different and may give different results. However, this discrepancy may be due to the inability to accurately determine the exact positions of the Mn ions in the ZnS lattice. As Borse et al., (1999) noted that the exact location of the Mn ions can only be conceptualized as contributions emanating from the four different probabilities as shown in Figure 2.22.

It is worth noting that the amount of Mn ions that can diffuse into the ZnS host lattice is largely dependent on the synthesis technique but this is not quite clear in literature. Also it is obvious that proper elemental analysis to ascertain the actual Mn concentrations in ZnS nanoparticles is lacking in literature. As well, the effect of nanoparticles size and morphology on Mn doping of ZnS nanoparticles has not been well studied.



### 2.6.3.1 Applications of ZnS and $Mn_xZn_{1-x}S$

#### 2.6.3.1.1 Electronic devices

The well-known application of ZnS nanoparticles is in the electronic industry (Liu et al., 2013). The fundamental properties of ZnS such as the presence of polar surfaces, excellent electron transport properties, thermal stability and high electronic mobility makes it a suitable material for fabrication of photonics, nonlinear optical devices, light-emitting diodes, flat panel displays, infrared windows, field emitters, sensors, nanogenerators, solar cells and ultraviolet light (UV) lasers (Liu et al., 2013; Balantseva et al., 2014; Huang et al., 2012). The 39 meV exciton binding energy of ZnS (larger than 26 meV, thermal energy at room temperature) makes it an efficient exciton emitter at room temperature (Fang et al., 2009). Thus, lasers based on ZnS useful in scientific research, measurement, military, industrial processing, information technology, law enforcement, microelectronics, biomedicine, environmental monitoring, avionics, entertainment, telecommunications and non-thermal (cold) processing have been developed (Fang et al., 2009). Doping of ZnS with suitable activators renders it appropriate as phosphor material for cathode ray tubes (Fang et al., 2009; Dawood and Schaak, 2009).

#### 2.6.3.1.2 Solar cells

Solar cells are electrical devices used to convert incident light energy into electricity. The wellknown cells are the Si based solar cells. Theoretically, the conversion efficiency of a single junction solar cell with an optimal absorber band gap of 1.1 eV is 31 % according to the Shockley-Queisser model (Donne et al., 2013). This implies that about 69 % of the incident light energy is lost as heat. To improve the cells efficiency, Mn-doped ZnS is used as a *down-shifting* material to

exploit the high energy region of the solar spectrum. Down-shifting is a process whereby high energy photons convert to low energy photons which are emitted around the maximum quantum efficiency value of solar cells (Donne et al., 2013). ZnS has wide band gap of about 3.6 eV and absorbs higher energy photons. Upon excitation, electrons are promoted to the conduction band and decay through the triplet state created by the  $Mn^{2+}$  centers to emit an orange-red luminescence. This orange-red luminescence has enough energy to generate a low energy photon to excite electrons across the band gap of the photovoltaic cells. Using Mn-doped ZnS as down-shifter material, Donne et al., (2013) obtained an increment of short circuit current of around 1 % for crystalline-Si (c-Si) and 0.8 % for Cu(In, Ga)Se<sub>2</sub> (CIGS) based cells.

#### **2.6.3.1.3 Light-emitting diodes (LEDs)**

LEDs based on Mn-doped ZnS nanoparticles have been fabricated by Rath et al., (2010). The fabrication was done on indium tin oxide (ITO) coated glass substrate. Layers of PEDOT:PSS (poly(3,4-ethylenedioxythiophene) poly(styrenesulfonate)), TPD (N, N'' bis(3-methylphenyl)-N, N'' -diphenyl-benzidine, and Mn-ZnS nanoparticles were casted on the ITO glass substrate and finally was covered with a layer of aluminum as the electrode. The PEDOT:PSS is a conducting polymer whilst the TPD is a hole transport layer. The fabricated LED exhibited electroluminescence both from the Mn-doped ZnS nanoparticles and the TPD. The advantage of this LED is that an electron transport layer was not required (without compromising on the device efficiency) because of the wide band gap energy of the ZnS. The fabrication of the LED was motivated by the strong photoluminescence exhibited by the Mn-doped ZnS nanoparticles.

#### 2.6.3.1.4 Bio-medical probes or sensors

Targeted cancer imaging technique for cancer treatment is a promising area of cancer therapy (Geszke et al., 2011). ZnS nanoparticles are of interest as a versatile cyto-friendly luminescent nanomaterial. Nanoparticles are applied as phosphorescent bio-medical probes for imaging and sensing applications due to their unique luminescence and photo-physical properties compared to the conventional organic dyes and fluorescent proteins. ZnS is of interest because (i) it has no toxicity to normal cells and (ii) it provides the possibility of exciting luminescent centers in ZnS using bio-friendly visible light or deep tissue penetrating near-IR radiation. Zinc is an essential mineral component of the body. Unlike Zn, Cd based fluorescent probes are reported prone to oxidation releasing toxic Cd ions in *in vivo* studies. This issue of Cd toxicity has been addressed succinctly by coating the surface of the CdSe quantum dots with ZnS. The wide band gap energy of ZnS is found to create a high-energy barrier between CdSe core and oxidative bio-molecules and thus provide protection against Cd leaching and also prevent production of  $\cdot\text{OH}$  and  $\cdot\text{O}_2^-$  radical species (Lovric et al., 2005).

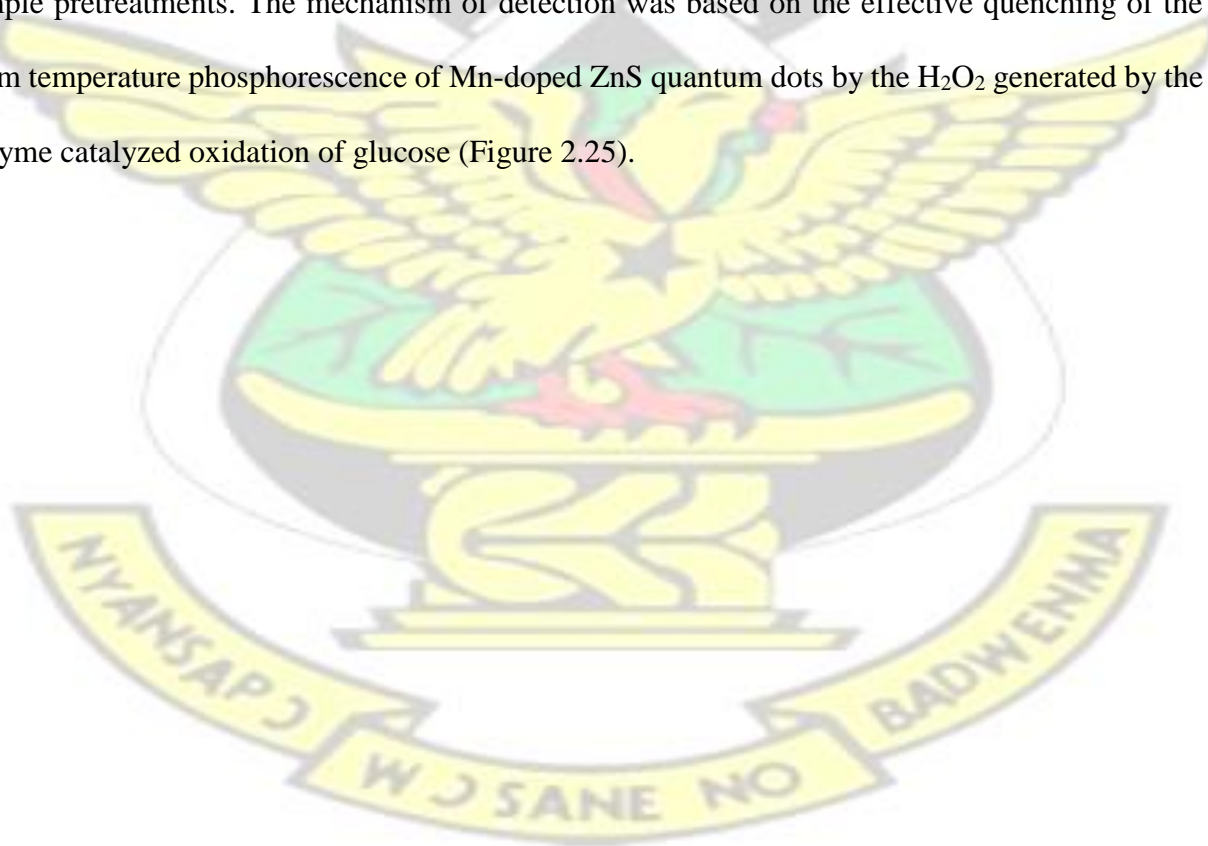
Manzoor et al., (2009) tested the cyto-toxicity of bare and folic acid (a cancer targeting drug) conjugated ZnS quantum dots in *in vitro* studies on normal lung fibroblast cell line, folatereceptor-positive (FR+) nasopharyngeal epidermoid carcinoma cell line and FR-negative (FR-) lung cancer cell line and found that the ZnS quantum dots showed no apparent toxicity even at high concentration of about 100  $\mu\text{M}$  and 48 hours of incubation. Also Geszke et al. (2011) demonstrated that a bare and folic acid conjugated Mn-ZnS quantum dots elicited only weak cyto-toxicity towards folate receptor-positive T47D cancer cells even at high concentrations after 72 hours incubation.

Cysteine-capped ZnS nanoparticle has also been reported as a fluorescence probe for rapid determination of DNA which demonstrates the biological application of ZnS (Li et al., 2004).

# KNUST

### 2.6.3.1.5 Chemical sensors

The large surface area exhibited by nanomaterials enables them to be integrated with enzymes which results in improved enzyme activity and stability. Wu et al., (2010), immobilized a glucose oxidase (GOD) onto a phosphorescent Mn-doped ZnS quantum dots and coupling with N-hydroxysuccinimide or 1-ethyl-3-(3-dimethylaminopropyl)carbodiimide (NHS/EDC), was able to detect glucose in real serum samples up to a detection limit of 3  $\mu\text{M}$  without any complicated sample pretreatments. The mechanism of detection was based on the effective quenching of the room temperature phosphorescence of Mn-doped ZnS quantum dots by the  $\text{H}_2\text{O}_2$  generated by the enzyme catalyzed oxidation of glucose (Figure 2.25).



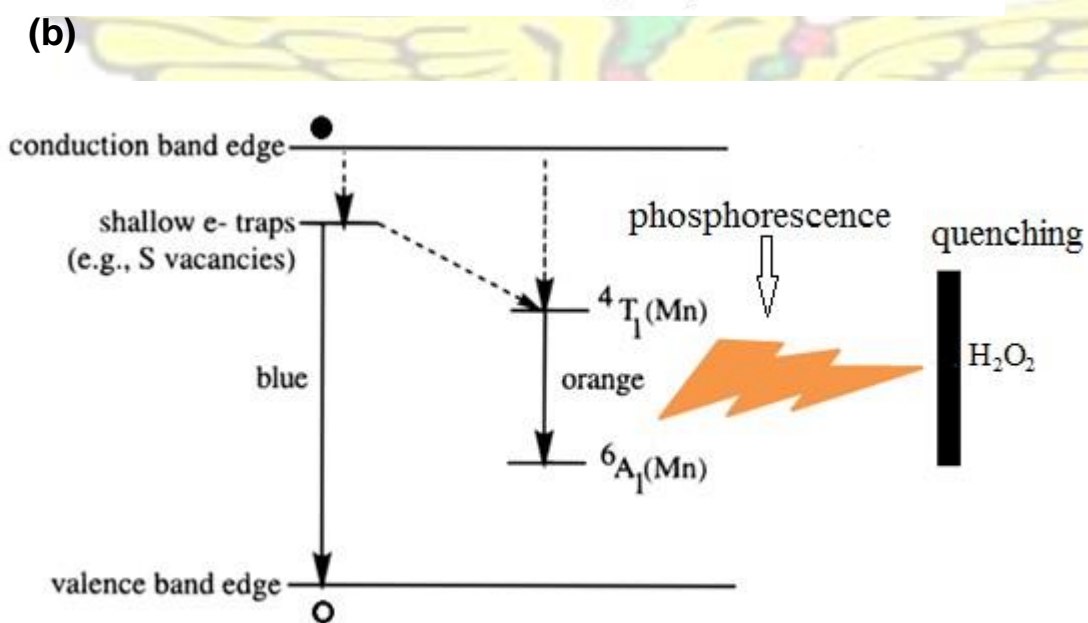
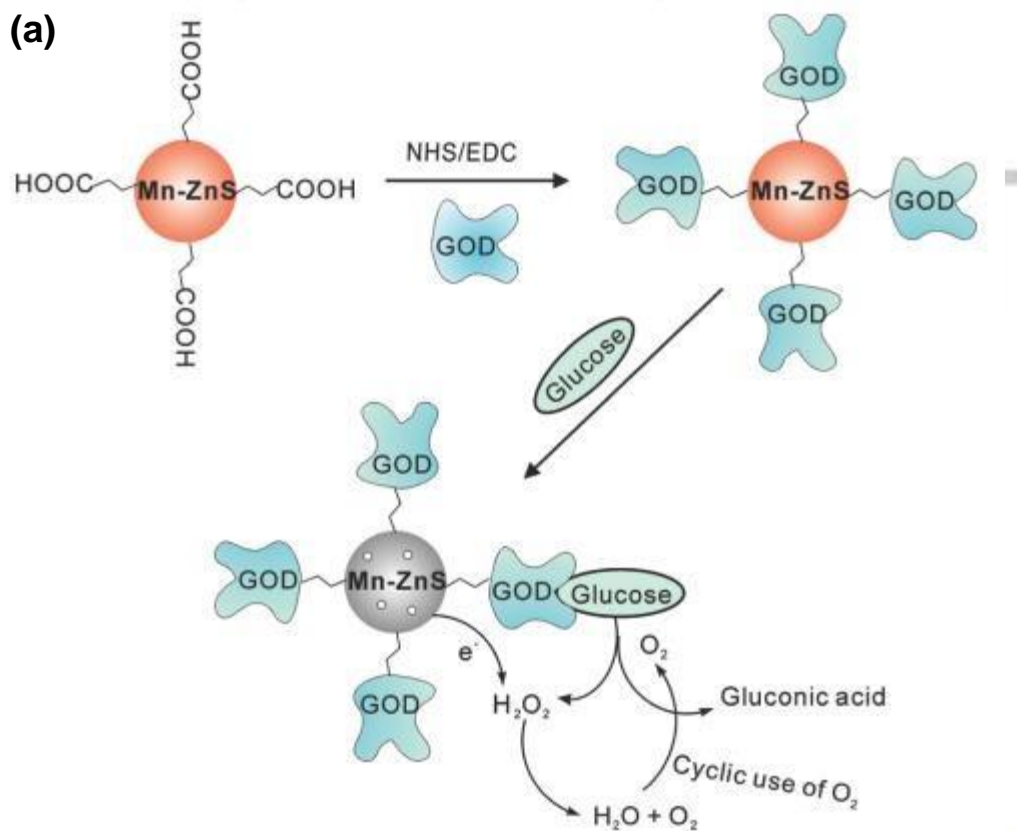


Figure 2.25: Mechanism of glucose phosphorescent sensor: (a) mechanism of quenching of phosphorescence by generation of  $H_2O_2$  by enzymatic oxidation of glucose (b) quenching of room temperature phosphorescence by  $H_2O_2$  (Wu et al., 2010; Sooklal et al., 1996).

The detection of traces of pentachlorophenol (up to 86 nM) in water has also been demonstrated by the use of a molecularly imprinted polymer anchored onto the surface of Mn-doped ZnS quantum dots. The detection is based on the room temperature phosphorescence of the Mn-doped ZnS quantum dots (Wang et al., 2009). Likewise enoxacin in biological fluids such as urine has been detected at detection limit of 58.6 nM without the need of deoxidants and other inducers using Mn-doped ZnS quantum dots based room temperature phosphorescence sensor. The quenching of the phosphorescence was said to be unaffected by  $\text{Na}^+$ ,  $\text{K}^+$ ,  $\text{Mg}^{2+}$ ,  $\text{Ca}^{2+}$  and amino acids (He et al., 2008). Similarly, Mn-doped ZnS based sensors have been developed to detect acetone and 4-nitrophenol in water (Liu et al., 2010; Sotelo-gonzalez et al., 2012).

#### **2.6.3.1.6 Photocatalysis**

ZnS has also been known to be an effective photo-active semiconductor suitable for antimicrobial and environmental remediation activities (He et al., 2016). ZnS nanoparticles have been proven to possess antifungal activities against drug resistant fungus *Candida albicans* (Suyana et al., 2014). The antifungal activity stems from the generation of reactive oxygen species such as hydrogen peroxide as ZnS nanoparticles come in contact with the microbe cell membrane, and thus, inducing oxidative stress to prevent cell growth. Intrinsic defects in ZnS nanoparticles generate electron-hole pairs which react with water to release  $\text{H}^+$  and  $\text{OH}^-$  ions. These ions react with dissolved oxygen molecules to form superoxide radicals which further react with hydrogen ions to produce hydrogen peroxide (Applerot et al., 2009; He et al., 2016; Suyana et al., 2014).

ZnS is a useful photo-catalyst for degradation of organic pollutants such as dyes, *p*-nitrophenol and halogenated benzene derivatives in waste water (Hu et al., 2005). The photo-catalytic activity of

ZnS enwrapped with amine functionalized fly ash has been investigated for the degradation of methylene blue dye under UV irradiation and antibacterial action against *Staphylococcus* and *Escherichia* (Kalpana and Selvaraj, 2015). Smaller size nanoparticles ( $> 100$  nm) show shorter cation exchange reaction time ( $\ll 1$  s) and thus, this feature enhances surface access and lower activation barriers to diffusing ions (Qu et al., 2014; Son et al., 2007). Owing to this feature, ZnS nanoparticles has been applied as an efficient sorbent for removal of about 99.9 % mercury in water within 1 min (Qu et al., 2014). Using Mn-doped ZnS nanoparticles as photocatalysts, Joicy et al., (2014) obtained photodegradation of methyl orange dye to the tune of 95.4 % at 4.28 % Mn doping. As already mentioned, the hydrogen peroxide generated as a result of exciton generation in the semiconductor nanoparticles was responsible for photodegradation of organic dyes.

#### **2.6.4 Cadmium sulphide (CdS) and lead sulphide (PbS)**

Cadmium(II) sulphide (CdS) (also called Greenockite) is one of the most studied II-VI luminescent metal chalcogenide semiconductor (Hullavarad et al., 2008). The interest in CdS is as a result of the fascinating size-dependent properties it exhibits at the nanometer scale. CdS has large direct band gap energy of 2.42 eV. It has a yellow to orange colour and in ancient days was used as pigment (Frenzel et al., 2007). It crystallizes into either hexagonal or cubic crystal structures and possesses n-type semiconductor characteristics (Hullavarad et al., 2008). Several morphologies including quantum dots, nanobelts, nanorods, nanosheets and nanowires of CdS have been reported (Zhang et al., 2012; Liu et al., 2008; Yang et al., 2000; Xiang et al., 2013; Barrelet et al., 2003; Frenzel et al., 2007). CdS nanoparticles have been applied in the photodecomposition of synthetic dyes, solar cell fabrication, lasers, light emitting diodes, hydrogen generation and drug delivery

systems (Upadhyay et al., 2012; Grynko et al., 2013; Hullavarad et al., 2008). CdS has been demonstrated as suitable n-type hetero-junction partner for PbS for fabrication of 3.3 % efficient quantum dot solar cell (Bhandari et al., 2013).

Lead(II) sulphide (PbS) is another important IV-VI metal chalcogenide semiconductor. It has a direct narrow band gap of 0.41 eV and large exciton Bohr radius of 18 nm (Liu et al., 2008). It crystallizes into a rocksalt structure (Kane et al., 1996). It has high static dielectric constant and possesses exceptional non-linear optical properties (Neo et al., 2009; Scheele et al., 2014). PbS has stable luminescence in the near-IR suggesting its potential application in communication, bioimaging and infrared photodetectors (Zhou et al., 2006). PbS quantum dots, nanocubes, nanostar-shaped dendrites, and nanorods have been reported (Zhou et al., 2006). PbS has the advantage to generate multiple excitons which makes it suitable for solar cell applications (Guchhait et al., 2010). PbS has been employed in transistors, DNA detections and solar cells applications (Scheele et al., 2014; Hansen et al., 2006; Guchhait et al., 2010).

Both CdS and PbS nanoparticles have been synthesized via different chemical routes including thermal decomposition of SSPs, co-precipitation, solvothermal, melt reactions, radiolytic, surfactant-assisted reflux and microwave assisted techniques (Hullavarad et al., 2008; SalavatiNiasari et al., 2010; Souici et al., 2009; Liu et al., 2008; Wang et al., 2006; Nyamen et al., 2014; Akhtar et al., 2010; Salavati-Niasari et al., 2012; McNaughten et al., 2016; Sun et al., 2009).

## **CHAPTER 3**

### **METHODOLOGY**

### 3.1 Materials

Cadmium(II) acetate dihydrate (98 %, Acros Organics), lead(II) acetate trihydrate (99.5 – 102.0 %, Sigma-Aldrich), potassium ethyl xanthogenate (96 %, Sigma-Aldrich), zinc acetate dihydrate (98 %, Sigma-Aldrich), manganese dichloride tetrahydrate ( $\geq 99$  %, Sigma-Aldrich), dodecanethiol ( $\leq 100$  %, Sigma-Aldrich), oleylamine ( $\leq 100$  %, Sigma-Aldrich), castor oil (Sigma-Aldrich), 1,2,3,4 -tetrahydroisoquinoline (95 %, Sigma-Aldrich), carbon disulphide ( $\geq 99$ %, Sigma-Aldrich), potassium hydroxide ( $\leq 100$  %, Sigma-Aldrich), sodium hydroxide ( $\geq 97$  %, Fisher Scientific), hydrochloric acid ( $\geq 30 - >50$  %, Sigma-Aldrich), ethylacetate ( $\leq 100$  %, Sigma-Aldrich), magnesium sulfate (Sigma-Aldrich), methanol (99.8 %, Sigma-Aldrich), ethanol ( $\geq 99.8$  %, Sigma-Aldrich) hexane ( $\geq 97$ , Honeywell/Riedel Haen) toluene (99.7 %, Sigma-Aldrich), chloroform ( $\leq 100$  %, Sigma-Aldrich) and acetone ( $\geq 99$  %, Honeywell/Riedel Haen) were all used without further purification.

### 3.2 Methods of Synthesis

#### 3.2.1 Synthesis of cadmium(II) ethyl xanthate (1)

Cadmium(II) ethyl xanthate,  $[\text{Cd}(\text{S}_2\text{COEt})_2]$ , was synthesized by reacting potassium ethyl xanthogenate (60 mmol, 9.62 g) and cadmium acetate dihydrate (30 mmol, 8.00 g) in water at

room temperature. The reaction scheme is shown in Figure 3.1. In the synthesis, 100 ml of aqueous solution of cadmium acetate dihydrate was added drop wise to 100 ml aqueous solution of potassium ethyl xanthogenate. The resultant mixture was stirred for an hour to form waterinsoluble precipitates of cadmium(II) ethylxanthate. The precipitates were vacuum filtered and then dried in the fumehood overnight. The precipitates were further recrystallized in acetone and characterized. [Cd(S<sub>2</sub>COEt)<sub>2</sub>]: m.pt: 165 °C, micro-elemental analysis calc. (found) (%): C 20.31 (20.38), H 2.84 (2.72), Cd 31.68 (31.16), S, 36.14 (36.02), significant IR (cm<sup>-1</sup>): 2969 ν(C-H stretch), 1430 – 1360 ν(CH<sub>2</sub> and CH<sub>3</sub> deformation), 1180 – 571 ν(C=S, C-O and CH<sub>2</sub> rocking).

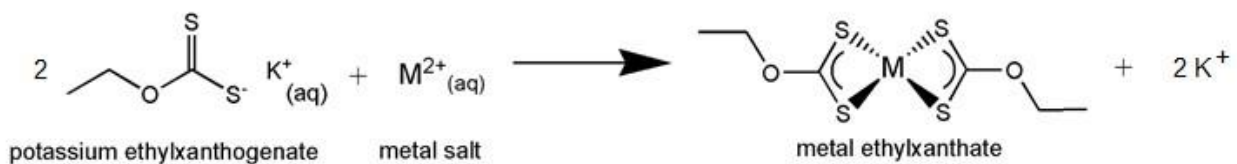


Figure 3.1: Reaction scheme for syntheses of ethyl xanthate complexes (M = Cd or Pb)

### 3.2.2 Synthesis of lead(II) ethyl xanthate (2)

In the same way, lead(II) ethyl xanthate, [Pb(S<sub>2</sub>COEt)<sub>2</sub>], was prepared by reacting lead acetate trihydrate (30 mmol, 11.38 g) and potassium ethyl xanthogenate (60 mmol, 9.62 g) in water at room temperature (Figure 3.1). The precipitates were filtered, dried, recrystallized in acetone and characterized. [Pb(S<sub>2</sub>COEt)<sub>2</sub>]: m.pt: 132 °C, micro-elemental analysis, Calc. (found) (%): C 16.03 (16.19), H 2.24 (1.96), S 28.53 (28.44), Pb 46.10 (45.90). Significant IR (cm<sup>-1</sup>): 2969 ν(CH stretch), 1430 – 1360 ν(CH<sub>2</sub> and CH<sub>3</sub> deformation), 1180 – 571 ν(C=S, C-O and CH<sub>2</sub>

rocking).

### 3.2.3 Syntheses of CdS and PbS nanoparticles

The CdS and PbS nanoparticles were synthesized by the heat-up method employed by Shen et al., (2012) with some modification. In a typical synthesis (synthesis set-up shown in Figure 3.2), 0.1 g of the precursor (0.282 mmol of  $[\text{Cd}(\text{S}_2\text{COEt})_2]$  or 0.222 mmol of  $[\text{Pb}(\text{S}_2\text{COEt})_2]$ ) and 5.0 ml castor oil were loaded into a three-necked flask at room temperature. The system was then purged by degassing and bubbling with nitrogen for an hour at 100 °C with constant stirring (using a standard Schlenkline apparatus). The temperature was then increased at a rate of 15 °C min<sup>-1</sup> and maintained at the target temperature for 15 minutes to allow decomposition and growth of nanoparticles. The reaction was quenched rapidly by cooling of the flask in a room temperature water bath followed by the addition of room temperature acetone when the reaction mixture reached 70 °C. The nanoparticles were purified by washing with methanol:toluene (7:1 v/v) solvent mixture three times, centrifuged and the final product dispersed in toluene for analyses.

The growth temperatures considered for CdS were 180, 200, 220, 240 and 280 °C and that of PbS were 140, 160, 180 and 200 °C. These temperatures were chosen based on the different decomposition patterns of the  $[\text{Cd}(\text{S}_2\text{COEt})_2]$  and  $[\text{Pb}(\text{S}_2\text{COEt})_2]$  precursors. The effect of time on nanoparticle growth was investigated by withdrawing aliquots of samples from the reaction mixture at 5, 10, 15, 30 and 60 minutes. The aliquots were analyzed using p-XRD, UV-Vis, PL and TEM.

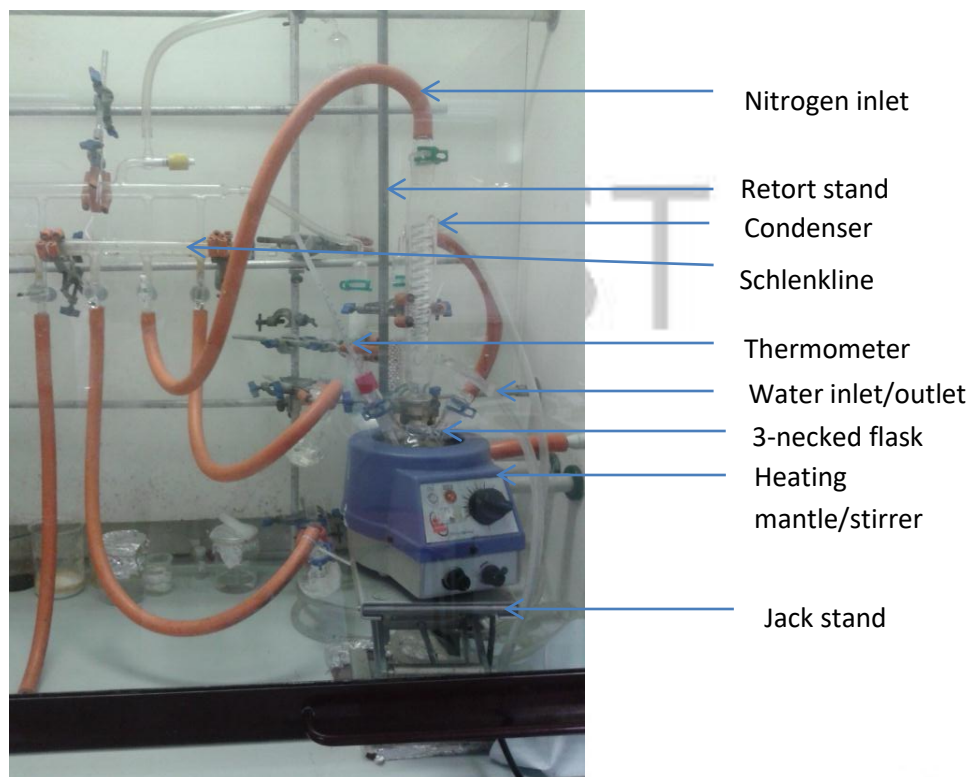


Figure 3.2: Experimental set-up for colloidal syntheses of nanocrystals

### 3.2.4 Extraction of ricinoleic acid from castor oil

The procedure for the isolation of ricinoleic acid from castor oil was adapted from Vaisman et al., (2008). About 50 g (54 mmol, 52 mL) of castor oil was hydrolyzed by refluxing with ethanolic potassium hydroxide solution (0.21 mol (12 g) dissolved in 200 ml of ethanol) for four hours. The reaction scheme is shown in Figure 3.3. The resulting mixture was added to 250 mL distilled water in 600 mL beaker and stirred to ensure complete mixing. The resulting mixture was acidified with HCl to a pH of 1 to release the ricinoleic acid which formed the upper layer. The ricinoleic acid was extracted with ethylacetate and dried over anhydrous magnesium sulfate. The ethylacetate was

evaporated and the extracted ricinoleic acid was clarified by adding 150 mL hexane and placed in the dark at 4 °C for 48 hours. Yield 80 – 85 %. Significant peaks IR

( $\nu_{max}/\text{cm}^{-1}$ ) for castor oil and ricinoleic acid: 3374.50  $\nu(\text{OH stretch, free hydroxyl})$ , 2853.90 – 2924.26  $\nu(\text{C-H stretch})$ , 1743.22  $\nu(\text{C=O stretch})$ , 1457.12  $\nu(\text{C-H bend})$ , 1162.53  $\nu(\text{C-O stretch})$  and 723.99  $\nu(\text{C-H rock})$ . The extracted ricinoleic acid was used for the syntheses of diricinoleate complexes of Zn (complex (3)) and Mn (complex (4)).

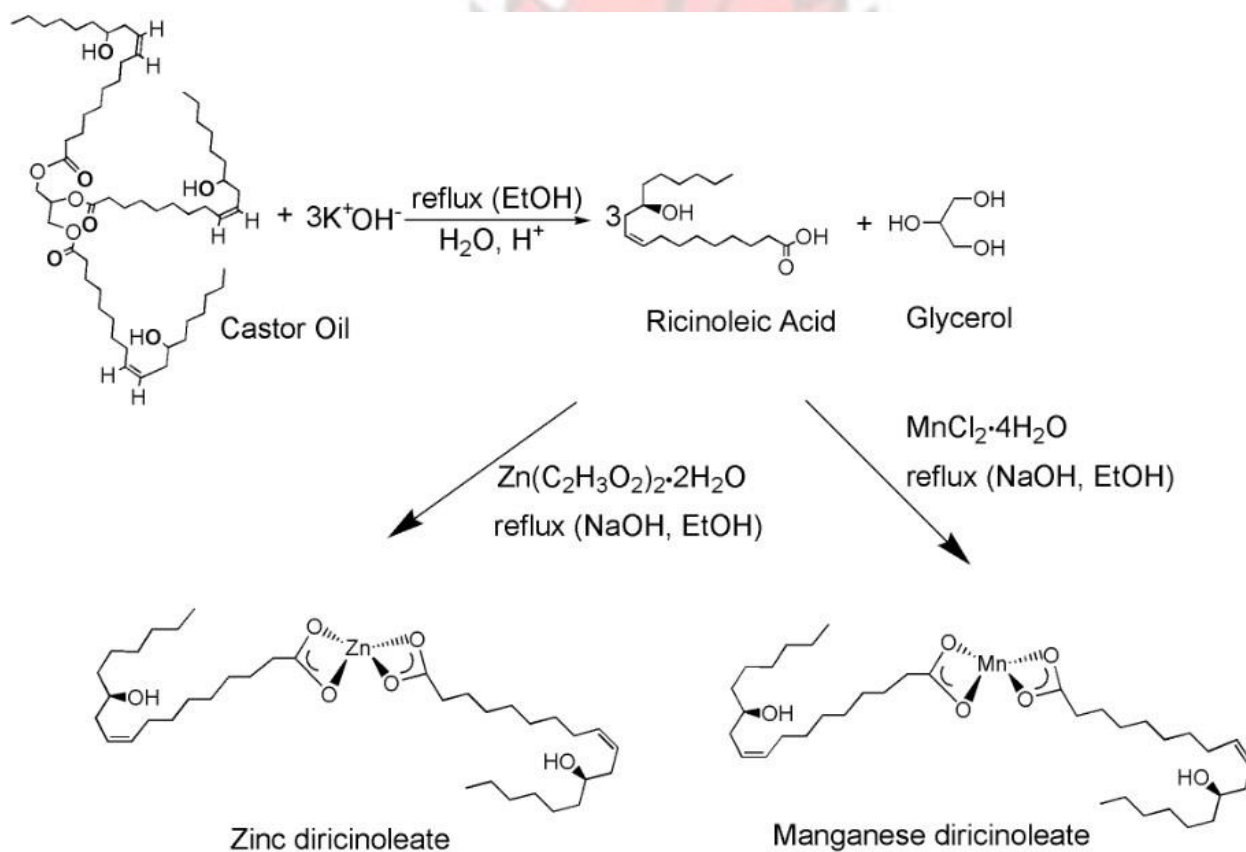


Figure 3.3: Extraction of ricinoleic acid from castor oil for syntheses of diricinoleate carboxylates of zinc (3) and manganese (4).

### 3.2.5 Synthesis of zinc(II) diricinoleate complex, [Zn(Ra)<sub>2</sub>] (3)

Zinc(II) diricinoleate complex (3) was synthesized following the method reported by Pereira et al., (2012) for synthesizing iron trioleate. In a typical synthesis, sodium ricinoleate was first of all synthesized by refluxing sodium hydroxide, 40 mmol (1.60 g) and ricinoleic acid, 40 mmol (12.63 mL) in ethanol (Figure 3.3). Aqueous solution of zinc acetate dihydrate, 20 mmol (4.39 g) and 84 mL hexane were added to the mixture which was stirred and refluxed for four hours. The molar ratio of the zinc acetate dihydrate and ricinoleic acid was 1: 2. The resultant mixture consisted of an upper organic and a lower aqueous layer. The upper layer contained complex (3) and hexane. The two layers were separated using a separating funnel. Hexane was allowed to evaporate at room temperature resulting in the precipitation of (3) as a white solid material. The solid was a waxy and sticky material. The stickiness was as a result of residual ricinoleic acid in the complex. Washing this product with acetone reduced the waxy nature and a drier material of (3) was obtained after drying in vacuum. Micro-elemental analysis gave the following results: calc. for (3) (found) (%): C 65.48 (65.16), H 10.07 (10.52). Significant FTIR ( $\nu_{max}/\text{cm}^{-1}$ ) peaks of [Zn(Ra)<sub>2</sub>]: 3319.29  $\nu$ (OH stretch, free hydroxyl), 2921.51 – 2850.19  $\nu$ (C-H stretch), 1712  $\nu$ (C=O stretch), 1547.33 – 1524.48  $\nu$ (C-H bend), 1071.90  $\nu$ (C-O stretch) and 743.35 – 722.16  $\nu$ (C-H bend). MS (ESI):  $m/z$  [ $M^+$ ] = 659.4 amu (molecular ion peak), 297.3 amu (base peak).

### 3.2.6 Synthesis of manganese(II) diricinoleate complex, [Mn(Ra)<sub>2</sub>] (4)

The synthesis of complex (4) was proceed as that of (3) by using manganese chloride tetrahydrate (15 mmol, 3.0 g) in place of zinc acetate dihydrate (Figure 3.3). The molar ratio of manganese chloride tetrahydrate and ricinoleic acid was 1: 2. A waxy brown precipitate, complex (4) formed

after evaporation of the hexane. In contrast to **(3)**, the washing of this product with acetone did not reduce its waxy nature. Micro-elemental analysis calc. for **(4)**

(found) (%): C 66.54 (65.76), H 10.24 (10.22). Significant FTIR ( $\nu_{max}/\text{cm}^{-1}$ ) peaks of [Mn(Ra)<sub>2</sub>]: 3319.29  $\nu$ (OH stretch, free hydroxyl), 2921.51 – 2850.19  $\nu$ (C-H stretch), 1712  $\nu$ (C=O stretch), 1547.33 – 1524.48  $\nu$ (C-H bend), 1071.90  $\nu$ (C-O stretch) and 743.35 – 722.16  $\nu$ (C-H bend). MS (ESI):  $m/z$  [ $M^+$ ] = 650.5 amu (molecular ion peak), 297.2 amu (base peak).

### 3.2.7 Syntheses and growth kinetic study of ZnS nanoparticles from complex **(3)**

ZnS nanoparticles were prepared following the simple and generalized method reported by Choi et al., (2009) with some modification. Typically, complex **(3)** (0.91 mmol, 0.6 g) was dissolved in a 1:1 solvent mixture of dodecanthiol (41.75 mmol, 10 ml) and oleylamine (30.39 mmol, 10 ml) in a three-necked flask under nitrogen gas atmosphere. The temperature of the mixture was raised to 300 °C and maintained for an hour. A clear and transparent solution was obtained. The resulting mixture was cooled to room temperature to obtain a white precipitate. This precipitate (ZnS nanoparticles) was washed with ethanol several times to remove the excess oleylamine and dodecanethiol. Finally, the ZnS nanoparticles were dispersed in toluene prior to analysis.

For growth kinetic studies of coarsening of ZnS in oleylamine/dodecanethiol, aliquots of ZnS samples were taken from the reaction vessel at 0, 10, 20, 30, 40, 50 and 60 minutes time intervals and analyzed with XRD and UV-Vis. Temperatures considered for the kinetic studies were 240, 250, 260, 270, 280, 290 and 300 °C.

### 3.2.8 Syntheses of MnS nanoparticles from complex (4)

MnS nanoparticles were synthesized in a similar manner as ZnS nanoparticles by replacing complex (3) with complex (4) (0.92 mmol, 0.6 g). A greenish solution appeared and upon cooling a greenish precipitate of MnS formed. The synthesized MnS was washed with ethanol and dispersed in toluene prior to analysis. This product was quite unstable at room temperature and was therefore kept at 4 °C prior to analysis.

### 3.2.9 Syntheses of Mn-doped ZnS nanoparticles from complexes (3) and (4)

The syntheses of Mn-doped ZnS nanoparticles ( $Mn_xZn_{1-x}S$ ) were carried out as with ZnS nanoparticles. In a typical synthesis, the required amounts of complex (3) and (4) were dissolved in a 1:1 solvent mixture of dodecanethiol (41.75 mmol, 10 mL) and oleylamine (30.39 mmol, 10 mL) and resulting mixture heated up to 300 °C for an hour. The doping concentrations of ratio of  $Mn^{2+}$  to  $Zn^{2+}$  were maintained in the range  $0 \leq x \leq 0.10$ . The doping concentrations were calculated based on the atomic ratios of Mn to Zn in complex (3) and (4) used. The resultant precipitates of Mn-doped ZnS were washed with excess ethanol and then dispersed in toluene prior to analyses.

### 3.2.10 Synthesis of ligand, sodium tetrahydroisoquinoline dithiocarbamate, $[Na(S_2CN(thiq))]$ (L)

An aqueous solution of NaOH (100 mmol, 4 g) was cooled in ice and 1,2,3,4-tetrahydroisoquinoline (100 mmol, 12.52 ml) was added to it. To this mixture,  $CS_2$  (100 mmol, 6 mL) was added drop wise, and the resultant stirred for an hour and then cool in ice overnight.

The product formed was washed with distilled water and vacuum dried. Colour: pale yellow. Yield: 42.3 %. M.pt. 151 C. IR  $^{\circ}$  ( $\nu_{max}/\text{cm}^{-1}$ ): 2408 – 2897 (C-H, S-H), 1420 – 1583 (C-C stretch, in ring), 1367 (C-N stretch, in ring), 1183 (-N-C=S) and, 739 (aromatic  $\text{Sp}^2$  C-H bend). The reaction schemes for the syntheses of ligand and complexes are shown in Figure 3.4.

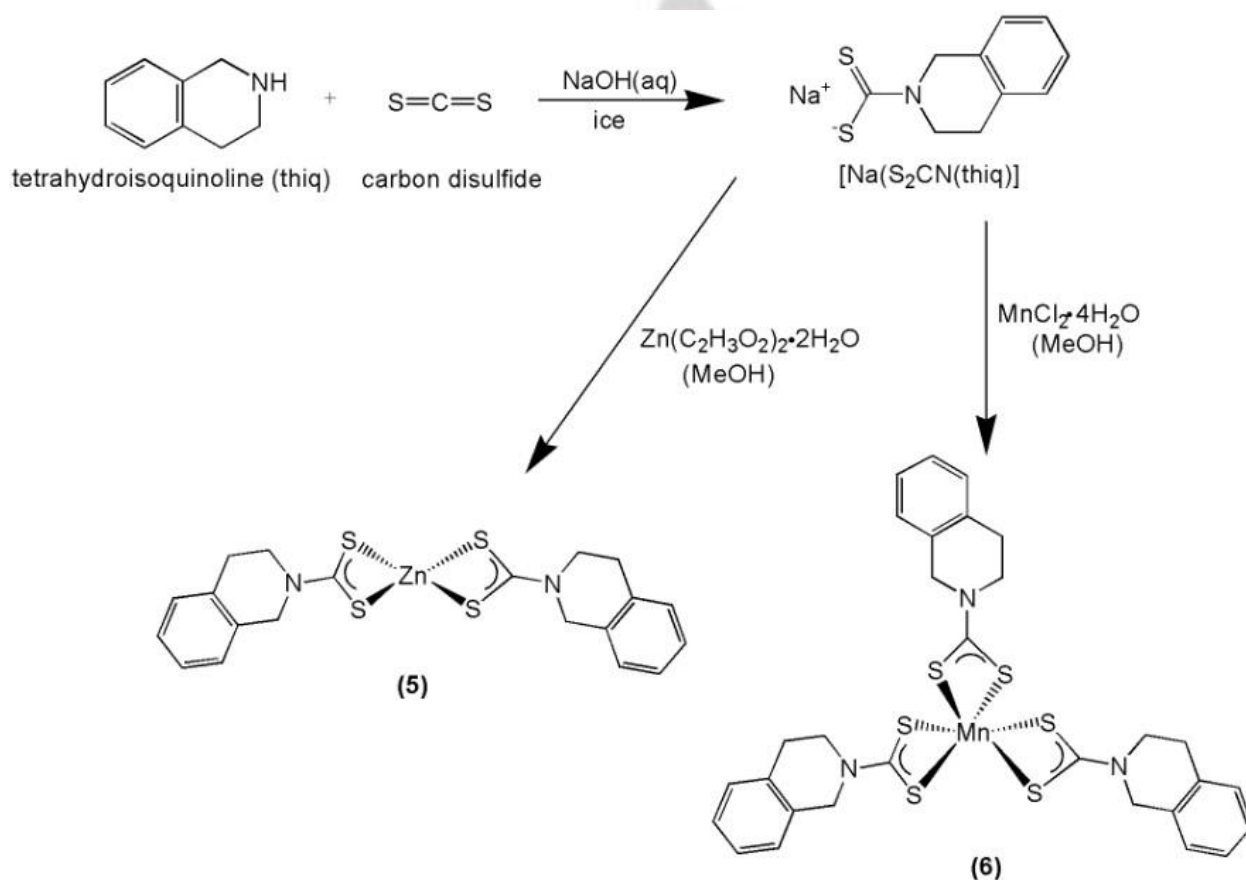


Figure 3.4: Reaction scheme for syntheses of ligand  $[\text{Na}(\text{S}_2\text{CN}(\text{thiq}))]$ , as well as  $[\text{Zn}(\text{S}_2\text{CN}(\text{thiq}))_2]$  (**5**) and  $[\text{Mn}(\text{S}_2\text{CN}(\text{thiq}))_3]$  (**6**) complexes

### 3.2.11 Synthesis of zinc(II) bis(tetrahydroisoquinolinyl dithiocarbamate),

### **[Zn(S<sub>2</sub>CN(thiq))<sub>2</sub>], (5)**

The ligand (L) (30 mmol, 6.96 g) was added to 200 mL methanol and the mixture stirred for an hour. Zinc acetate dihydrate (15 mmol, 3.3 g) was dissolved in 100 ml methanol and added to the ligand solution (Figure 3.4). The resulting mixture was stirred for 3 hours at room temperature and then left stationary overnight in the fume hood. White precipitates were formed which were filtered and washed with methanol and dried under vacuum. Yield: 66.40 %. M.pt.: 275 °C. Micro-elemental analysis calc. for [Zn(S<sub>2</sub>CN(thiq))<sub>2</sub>] (found) (%): C 49.83 (50.46), H 4.18 (4.26), N 5.81 (5.86), S 26.61 (26.02), Zn 13.57 (12.59). IR ( $\nu_{max}/\text{cm}^{-1}$ ): 2904.4 (C-H), 1474.01 (C-C stretch, in ring), 1427.83 (C-N stretch, in ring), 1213.79 – 925.58 (N-C=S) and, 746.17 (aromatic Sp<sup>2</sup> C-H bend). <sup>1</sup>H NMR (400 MHz, CDCl<sub>3</sub>)  $\delta$ : 3 ppm (*s*, 2H), 4.2 ppm (*s*, 2H), 5.2 ppm (*d*, H) (pipiridine ring), 7.2 ppm (*m*, 4H) (benzene ring). MS (APCI):  $m/z$  [M<sup>+</sup>] = 481.

### **3.2.12 Synthesis of manganese(III) tris(tetrahydroisoquinolinyl dithiocarbamate), [Mn(S<sub>2</sub>CN(thiq))<sub>3</sub>], (6)**

The procedure for the synthesis of complex (6) was similar to that of (5) with the difference of using manganese chloride tetrahydrate (15 mmol, 3.0 g) in place of zinc acetate dihydrate (Figure 3.4). The dark violet precipitates formed were filtered and washed with excess methanol.

The product formed, [Mn(S<sub>2</sub>CN(thiq))<sub>3</sub>] was found to be an oxidized product of [Mn(S<sub>2</sub>CN(thiq))<sub>2</sub>] (yellow but quickly changes to dark violet upon oxidation) which tend to form under aerial conditions (Preti et al. 1980). [Mn(S<sub>2</sub>CN(thiq))<sub>2</sub>] forms only under strict anaerobic conditions and is highly unstable and insoluble in most solvents (Hendrickson et al. 1974). Mn(II) is reported to form *tris*-chelated dithiocarbamate complexes (Hendrickson et al.

1974). Yield: 59.59 %. M.pt.: 147 °C. Micro-elemental analysis calc. for  $[\text{Mn}(\text{S}_2\text{CN}(\text{thiq}))_3]$  (found) (%): C 52.76 (53.13), H 4.87 (4.38), N 6.15 (6.16), S 28.17 (28.33), Mn 8.04 (7.88). IR ( $\nu_{\text{max}}/\text{cm}^{-1}$ ): 2904.4 (C-H), 1474.01 (C-C stretch, in ring), 1427.83 (C-N stretch, in ring), 1213.79 – 925.58 (N-C=S) and, 746.17 (aromatic  $\text{Sp}^2$  C-H bend).  $^1\text{H}$  NMR (400 MHz,  $\text{CDCl}_3$ )  $\delta$ : 3.1 ppm (s, 2H), 4.3 ppm (s, 2H), 5.3 ppm (d, H) (piperidine ring), 7.4 ppm (m, 4H) (benzene ring). MS (APCI):  $m/z$  [ $\text{M}^+$ ] = 472.1 amu.

### 3.2.13 Syntheses of ZnS nanocrystals from complex (5)

In a typical synthesis, 1.0 mmol (0.5 g) of complex (5) was dissolved in 15.2 mmol (5 ml) oleylamine with stirring by sonication. The complex completely dissolved in the oleylamine to yield a colourless mixture after 30 minutes of sonication at room temperature. This solution was swiftly injected into a prior heated (under nitrogen) oleylamine (60.8 mmol, 20 ml) at 280 °C and allowed to age for an hour. The hot reaction system was then cooled in water and the ZnS nanocrystals precipitates washed twice with methanol and once with methanol/toluene solvent mixture (20:1). The resultant precipitates were dispersed in toluene for further analyses.

### 3.2.14 Syntheses of MnS nanocrystals from complex (6)

The MnS nanocrystals were synthesized following the method for synthesizing the ZnS nanocrystals. However, in place of complex (5), complex (6) (0.59 mmol, 0.4 g) was used. A greenish solution of MnS was formed upon decomposition of complex (6) at 280 °C. The resultant greenish precipitate was washed, dispersed in toluene prior to analyses. The MnS nanocrystals

were quite unstable (changes from green to brown, suggesting possible oxidation) at room temperature condition and were therefore stored at 4 °C to minimize oxidation.

### **3.2.15 Syntheses of Mn-doped ZnS nanocrystals from complexes (5) and (6)**

Similarly, Mn-doped ZnS nanocrystals ( $Mn_xZn_{1-x}S$ ) were synthesized by dissolving complexes (5) and (6) at the appropriate molar ratios in 15.2 mmol (5 ml) oleylamine. The expected Mn doping concentration was kept in the range  $0 \leq x \leq 0.11$ . The mixture containing the dissolved complexes was swiftly injected into the hot oleylamine (60.8 mmol, 20 ml) at 280 °C to initiate the decomposition of the complexes and the growth of the nanoparticles. The reaction was aged for 1 hour and the resultant precipitate was washed and dispersed in toluene prior to analysis.

## **3.3 Characterization of Complexes and Nanoparticles**

### **3.3.1 Analyses of chemical structures of complexes**

The IR spectra ( $400 - 4000 \text{ cm}^{-1}$ ) were collected with a Bruker FT-IR tensor 27 spectrophotometer by directly placing a small portion of each sample on the diamond plate and then screwing to take measurement. The  $^1\text{H}$  NMR spectra were collected with an Ultrashield Advance Bruker 400 NMR spectrometer using  $\text{CDCl}_3$  and acetone- $d_6$  as solvent. The mass spectra were collected by the University of Manchester, School of Chemistry Mass Spectrometry Unit using electrospray ionization (ESI), and atmospheric pressure chemical ionization (APCI) techniques.

### 3.3.2 Elemental and thermal analyses

The micro-elemental analyses (CHNS) were performed by the University of Manchester Microanalytical Laboratory using a Thermo Scientific Flash 2000 Organic Elemental Analyser. The thermogravimetry (TGA) thermographs were obtained using a Perkin-Elmer Pyris 6TGA at heating rate of 10 °C min<sup>-1</sup> and temperature range of 30 – 600 °C. The metal analyses were done by the University of Manchester Microanalytical Laboratory using Thermo iCap 6300 Inductively Coupled Plasma Optical Emission Spectroscopy (ICP-OES).

### 3.3.3 p-XRD analyses

The X-ray diffraction patterns were obtained with a Bruker D8 diffractometer using a Cu-K $\alpha$  radiation ( $\lambda = 1.5418 \text{ \AA}$ , 30 kV, 40 mA,  $2\theta$  range (10 – 70°), with scan speed of 2.0 deg/min and step size of 0.05.

### 3.3.4 Optical analyses

The absorption spectra of the nanoparticles were collected with a UV-1800 Shimadzu UV spectrophotometer using a 1 cm path length quartz cuvette and toluene as a blank solvent. Photoluminescence (PL) measurements were similarly made using a Gilden photonics fluoroSENS spectrofluorimeter employing toluene and chloroform blank solvents. Electron paramagnetic resonance (EPR) spectra were collected by the University of Manchester EPR Unit. The powdered samples were placed in EPR capillary tubes prior to analyses.

### 3.3.5 Analyses of morphology and elemental composition of nanoparticle

Micrographs were obtained using a JEOL 1010 Transmission Electron Microscope (TEM) with accelerating voltage of 100 kV and equipped with Megaview III camera and Soft Imaging Systems iTEM software. Drops of dilute dispersions of nanoparticles were placed on carbon grids and dried off prior to the TEM analyses. FEI XL-30 FEG scanning electron microscope (SEM) equipped with RONTEC energy dispersive X-ray (EDX) spectrometer was used to obtain the morphology and elemental composition of the nanoparticles. Prior to SEM/EDXS analyses the nanoparticles were deposited on glass slides and carbon coated using Edwards E306A coating system.

### 3.4 Data Analyses

ChemDraw Ultra was used to draw the chemical structures. ACDLABS 12.0 was used in analyzing the NMR data. The graphs were drawn with OriginPro 8.5 data analysis software.

Details of the XRD patterns were extracted using X<sup>PERT</sup> HighScore Plus, X-ray Diffraction Data Analysis and Match!3 software packages. The nanoparticle sizes and size distribution were analyzed with imageJ/Fiji software package.

## CHAPTER 4

## RESULTS AND DISCUSSIONS

### 4.1 Syntheses of CdS nanoclusters and PbS nanobelts via facile thermolysis of ethyl xanthate complexes in castor oil

#### 4.1.1 Introduction

Complexes of xanthates, thiobiurets, carbamates, thiosemicarbazides, dithiobiureas, thioureas, dithiophosphinates and N,N'-bis(thiocarbamoyl)hydrazines have been used as single source precursors (SSPs) for the syntheses of metal chalcogenide nanoparticles (Abdelhady et al., 2013; Mlowe et al., 2014; Mlondo et al., 2009; Nair et al., 2003; Moloto et al., 2007; Byrom et al., 2000; Nair et al., 2001). The advantages of SSPs over multiple source precursors are their low level of toxicity, ease of control of reaction stoichiometry and simplicity of handling because of their air-stability (Fan et al., 2007). This work investigates the application of the heat-up method as a facile technique for the syntheses of high quality CdS and PbS nanoparticles using ethylxanthate complexes and castor oil as green solvent. Castor oil is used as an alternative to toxic the phosphine based solvents.

## 4.1.2 Results and discussions

### 4.1.2.1 Analysis of castor oil

Castor oil consists of triglycerides molecules. Each of the triglyceride molecules is made up of three long-chain fatty acids connected to a glycerol backbone (Figure 4.1.1). The uniqueness of castor oil stems from the fact that about 85 – 95 % of the fatty acids is ricinoleic acid. Ricinoleic acid is a hydroxylated fatty acid. The mass spectrum (GC-MS, ESI) of the castor oil showed a molecular ion peak of 933.9 m/z which closely relates to the molecular mass of castor oil triglyceride (933.45 g/mol), where the three fatty acids are all ricinoleic acid. Da Silva et al., (2011) evaluated the molecular weight of castor oil by vapour pressure osmometry and GC and found it to be 927.88 g/mol and 928.31 g/mol respectively. The mass spectrum also showed a base peak of 160.7 m/z and this indicated a possible cleavage at the alkene functional group to give the most abundant fragment to be  $C_9H_{15}O_2$  with molecular mass of 155.21 g/mol.

From the  $^1H$  NMR spectrum below, the labels *a*, *b*, *c*, *d*, *e* and *f* correspond to the various hydrogen environments that describe the triglyceride nature of castor oil (Figure 4.1.1). The labels *a* ( $\delta$ , 5.55 ppm) and *d* ( $\delta$ , 4.30 ppm) are multiplets that show the hydrogen atoms connected to the glycerol backbone. Labels *b* ( $\delta$ , 5.43 ppm) and *c* ( $\delta$ , 5.27 ppm) are multiplets relating to the alkene and hydroxyl functional groups hydrogen environment respectively. It was expected that *c* gives a singlet instead of a multiplet because it has one hydrogen atom attached to oxygen to form the hydroxyl functional group. However, the multiplet resulted because the hydrogen was surrounded by neighbouring hydrogens per the spatial arrangement of the triglyceride molecule. The unlabelled peaks relate to the alkane part of the structure. These hydrogen environments indicated

that the castor oil molecular structure consisted of ricinoleic acid molecules attached to glycerol backbone.

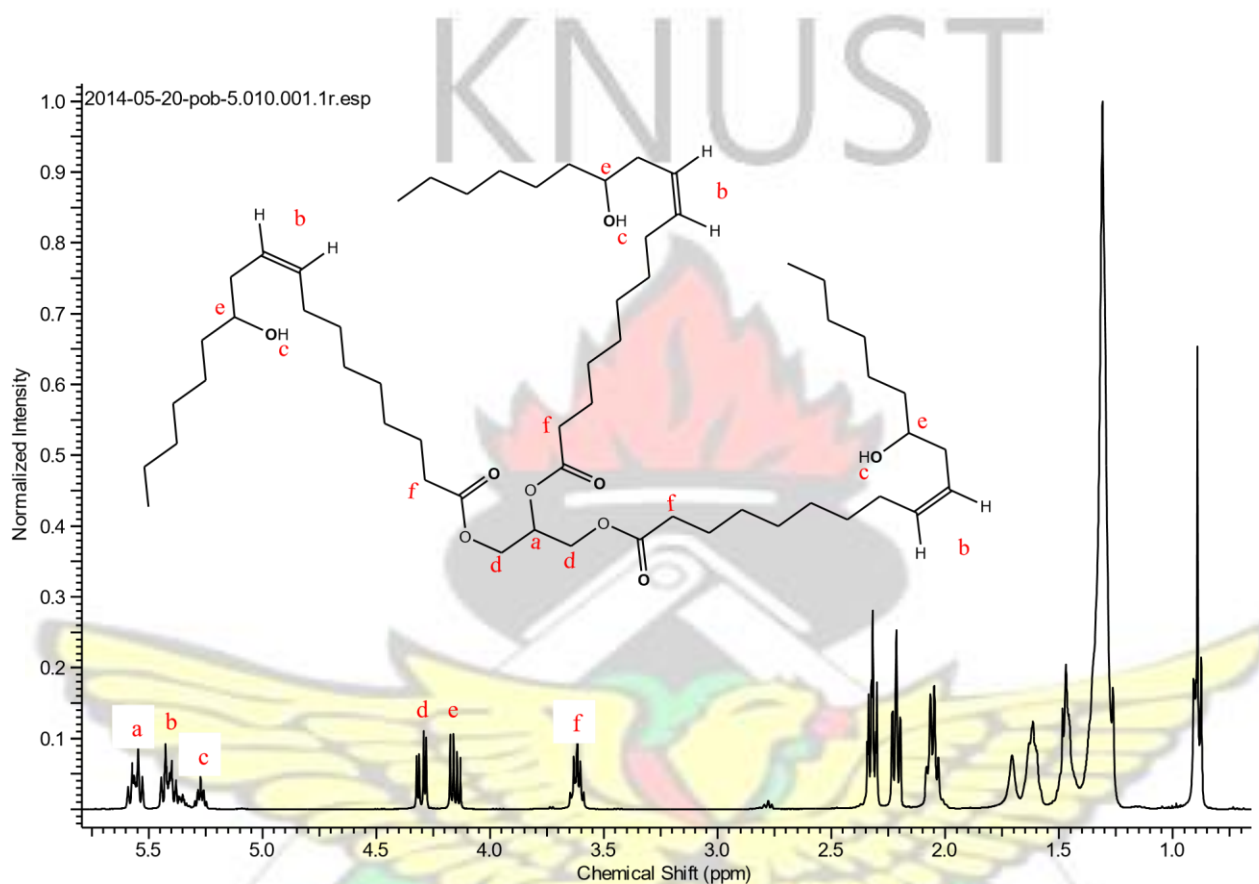


Figure 4.1.1: <sup>1</sup>H NMR of castor oil

#### 4.1.2.2 Thermal analyses of ethyl xanthate of Cd and Pb complexes

The TGA thermgrams for the decomposition of the ethyl xanthate complexes of cadmium (**1**) and lead (**2**) from 30 to 600 °C at a heating rate of 10 °C min<sup>-1</sup> under nitrogen gas are shown in Figure 4.1.2. The thermal analysis indicated a single step decomposition with the loss of

$C_3H_5OS^*$  and  $S^*$  moieties in both precursors. The expected residues after the decomposition process were CdS and PbS. The found percentage residues at 317 °C and 170 °C were 40.70 % (expected 40.59 %) and 53.22 % (expected 52.98 %) of the respective precursors and confirmed the formation of the desired products (CdS and PbS). Nair et al., (2002) obtained similar TGA curve for cadmium ethyl xanthate.

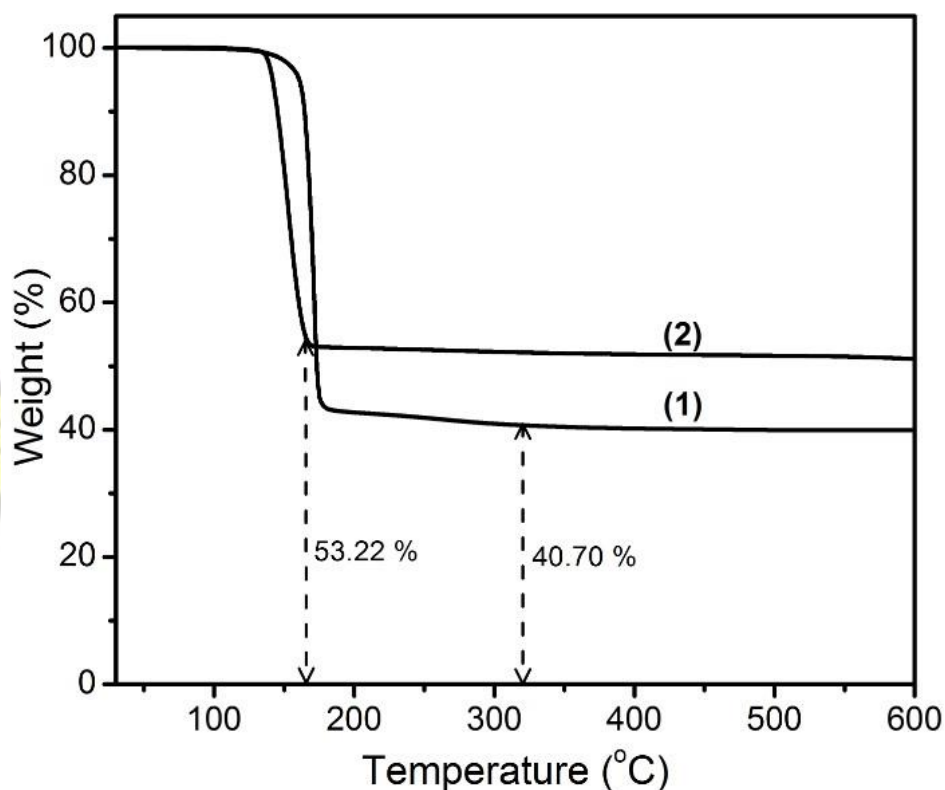


Figure 4.1.2: TGA thermograms of cadmium(II) ethyl xanthate (1) and lead(II) ethyl xanthate (2) (at 30 – 600 °C under nitrogen, at heating rate of 10 °C min<sup>-1</sup>)

The inflection point indicating the temperature at which there was intense decomposition of precursor was 171.45 °C for complex (1) whereas the onset and endset temperatures were 165.33 °C and 174.33 °C respectively. Similarly, the inflection point, onset and endset temperatures were 152.50 °C, 144.41 °C and 163.03 °C for complex (2) respectively. From the TGA it implied that

more energy was required to increase the temperature of a unit mass of complex (1) to 1 °C than for (2). Lead(II) ethyl xanthate easily get heated, enhancing a quick decomposition compared to the cadmium(II) ethyl xanthate.

KNUST

#### 4.1.2.3 CdS nanoclusters

##### 4.1.2.3.1 p-XRD analysis of CdS

The p-XRD patterns for CdS nanoparticles synthesized at 200 and 280 °C using castor oil as both solvent and capping agent are shown in Figure 4.1.3.

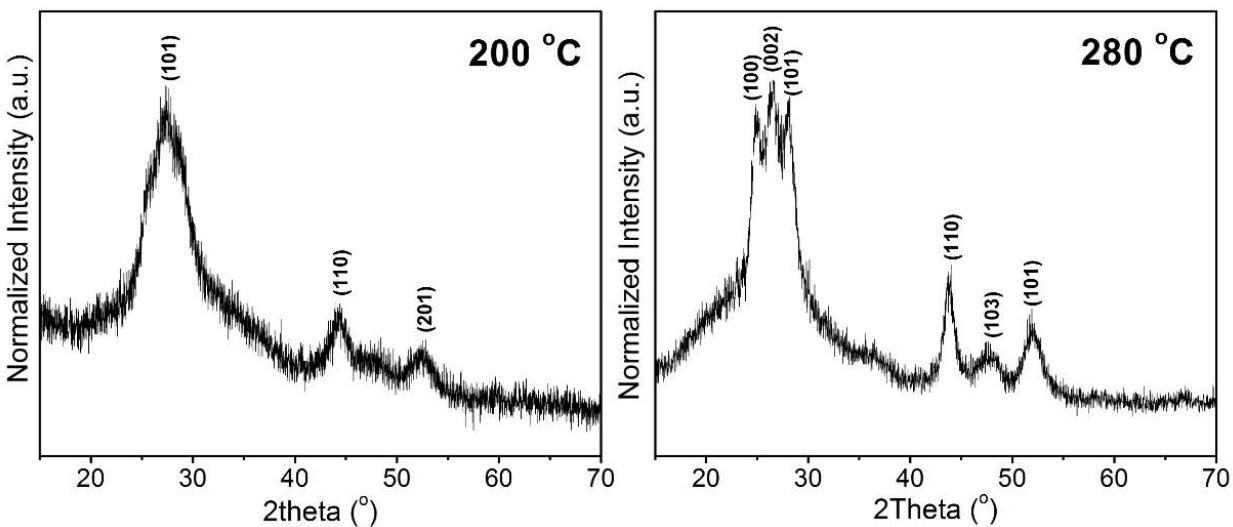


Figure 4.1.3: p-XRD patterns of CdS nanocrystals synthesized by heating up cadmium ethyl xanthate in castor oil at 200 °C and 280 °C for 15 minutes.

The diffraction pattern of the CdS synthesized at 200 °C showed three major distinct peaks at  $2\theta$  values of  $27.81^\circ$ ,  $44.67^\circ$  and  $52.79^\circ$  corresponding to (101), (110) and (201) planes of cubic crystal system (zinc blende structure) as previously observed by Shombe et al., (2015) and Ouyang et al., (2009). The p-XRD pattern also suggests a zinc blende/wurtzite polytypism of CdS nanoparticles. On the other hand, the pattern for CdS synthesized at 280 °C has six distinct peaks at  $2\theta$  values of  $25.51^\circ$ ,  $26.57^\circ$ ,  $28.13^\circ$ ,  $43.89^\circ$ ,  $47.64^\circ$  and  $51.85^\circ$  corresponding to the (100), (002), (101), (110), (103) and (112) planes of the hexagonal or wurzite phase. The broad peaks also suggest that the crystallite sizes were small demonstrating the effectiveness of the capping activity of the castor oil. The Scherer calculated crystallite sizes (along the 101 plane) were 4.08 nm and 4.41 nm for CdS at the two different temperatures respectively. It is worthy to note that, Nair et al., (2002) reported Scherer calculated crystallite size of CdS synthesized by thermolysis of cadmium ethyl xanthate in TOPO to be 3.9 nm.

#### 4.1.2.3.2 Optical properties of CdS

The optical properties of the CdS nanocrystals synthesized in castor oil are shown in Figure 4.1.4. As the temperature increased from 180 to 280 °C, the absorption maximum (excitonic peak) shifted from 447.87 nm to 464.71 nm indicative of a redshift (Figure 4.1.4(a)). From the absorption maxima, the bandgap energy and nanocrystal size were determined using the Brus equation (4.1.1):

$$E_g^{nano} - E_g^{bulk} = \Delta E = \frac{h^2}{8r^2} \left[ \frac{1}{m_e^*} + \frac{1}{m_h^*} \right] - \frac{1.8e^2}{4\pi\epsilon\epsilon_0 r} - 0.248E_{RY}^* \quad (4.1.1)$$

where  $E_g^{nano}$  is bandgap of the nanoparticle,  $E_g^{bulk}$  is band gap of bulk material,  $\Delta E$  is the

difference between the bandgap of the bulk and nanomaterial,  $h$  is Planck's constant,  $r$  is radius of nanoparticle,  $m_e^*$  and  $m_h^*$  are effective masses of excited electron and hole,  $\epsilon$  is relative permittivity,  $\epsilon_0$  is permittivity of vacuum and  $E_{RY}^*$  is the Rydberg Energy (Prabhu and Khadar, 2005).

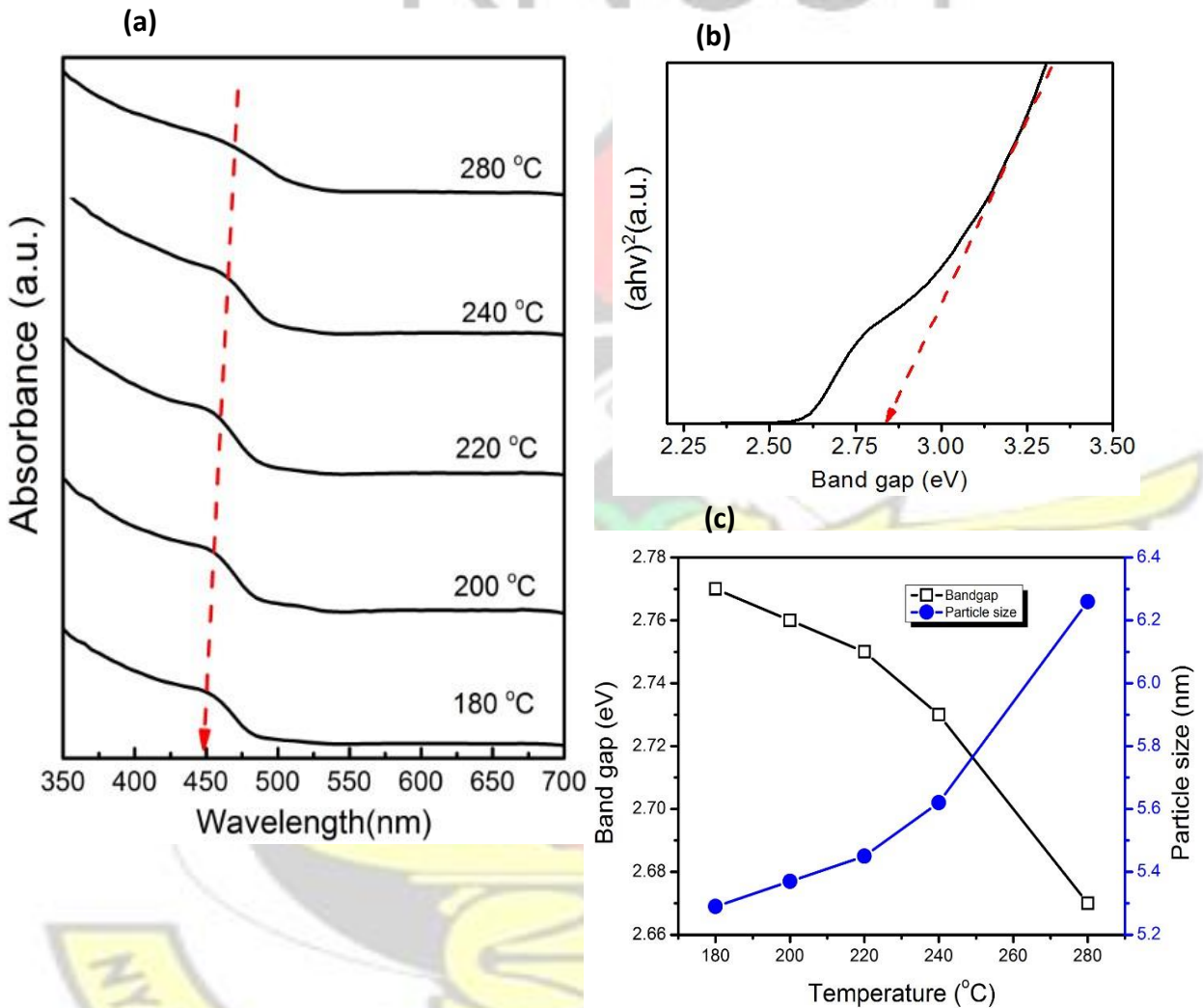


Figure 4.1.4: (a) UV-Vis spectra of CdS nanocrystals synthesized at 180, 200, 220, 240 and 280 °C by heating up cadmium ethyl xanthate in castor oil for 15 minutes, (b) Tauc plot showing estimation of band gap energy, and (c) Plot of band gap energy and particle size against reaction temperature

Figure 4.1.4(c) shows the calculated band gaps and nanocrystal sizes of the CdS samples against reaction temperature. The calculated bandgap energy for CdS synthesized at 180 °C to be 2.84 eV

which is higher than the bulk CdS of 2.42 eV showing some level of quantum confinement. From Figure 4.1.4(a), the absorption shifted from lower wavelength to higher wavelength as the temperature was increased. This observation confirmed the fact that increasing temperature usually leads to increasing particle sizes and decreasing band gap energies. The Scherrer calculated nanocrystallite sizes obtained from the XRD patterns were about 24 % lower than those obtained from the Brus equation which suggests that the particle sizes could be made up of a number of crystallites. Increasing the time of reaction from 5 to 60 minutes and concentration of precursor from 0.02 to 0.08 g/mL (at 200 °C) did not show significant effect on the absorption maxima which demonstrates the effective capping activity of castor oil (Figure 4.1.5).

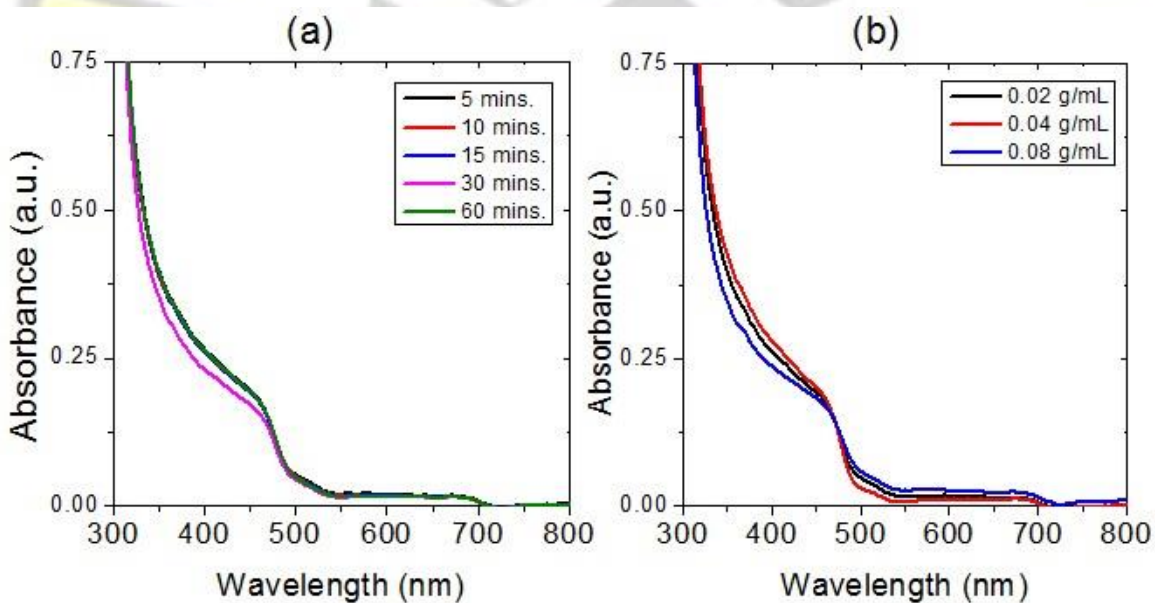


Figure 4.1.5: UV-Vis spectra of CdS nanocrystals synthesized at 200 °C via heating up cadmium ethyl xanthate in castor oil at different (a) reaction time and (b) concentration of precursor.

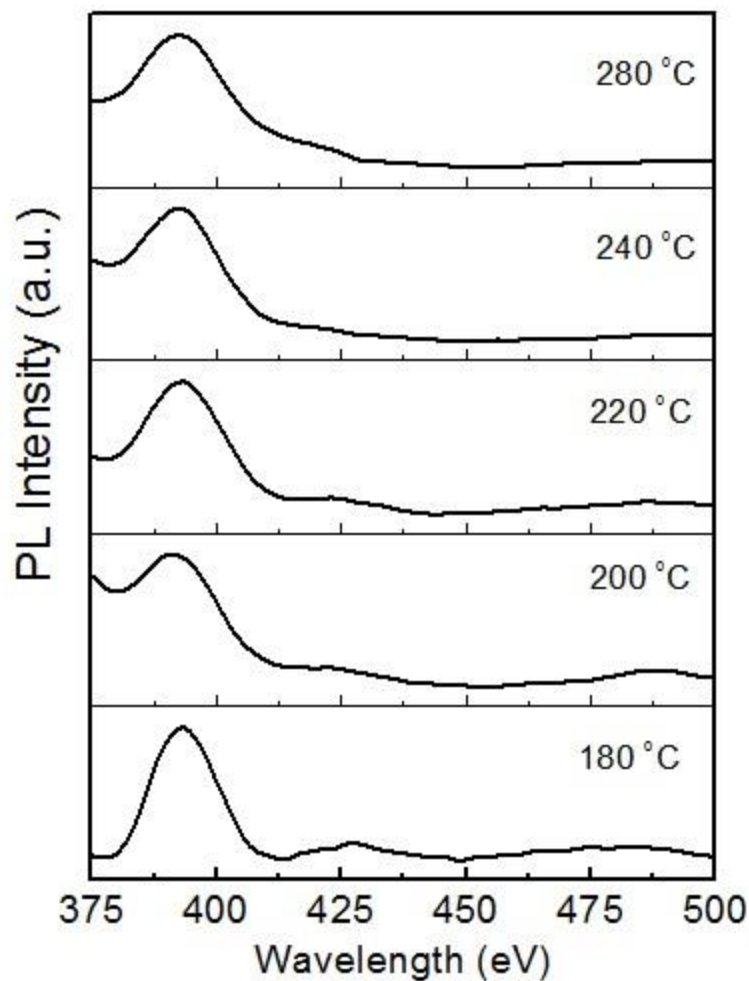


Figure 4.1.6: PL spectra of CdS nanocrystals synthesized at different temperatures via heating up cadmium ethyl xanthate in castor oil for 15 minutes

In Figure 4.1.6, the photoluminescence properties of the CdS nanocrystals synthesized in castor oil are shown. All the spectra at the different temperatures showed intense emissions at 391 – 393 nm. There was also no significant shift in the emission maxima implying that the effect of increasing temperature from 200 °C to 280 °C was minimal. However, there were some prominent emission peaks at 425 nm in the spectrum at 220 °C and also at 487.5 nm in the spectrum of 200 °C. These peaks indicate the emission from larger particles which grew too quickly to affect the monodispersity of the nanoparticles at those temperatures. The relatively high intensity of the peak

at 391 – 393 nm overshadowed the peaks at 425 and 487.5 nm. In other words, the emission was strong in the near-UV and weak in the visible region of the electromagnetic spectrum which implied that majority of the CdS particles synthesized were in the strong quantum confinement regime and suggest formation of very small CdS particles. This observation pertaining to CdS was also made by Chan et al., (2002), when they stated that CdS and ZnSe quantum dots emit blue to near-UV light.



### 4.1.2.3.3 Morphology of CdS

The TEM micrographs of CdS nanoparticles synthesized at 200 °C showed interesting morphology (Figure 4.1.7 (a) and (b)).

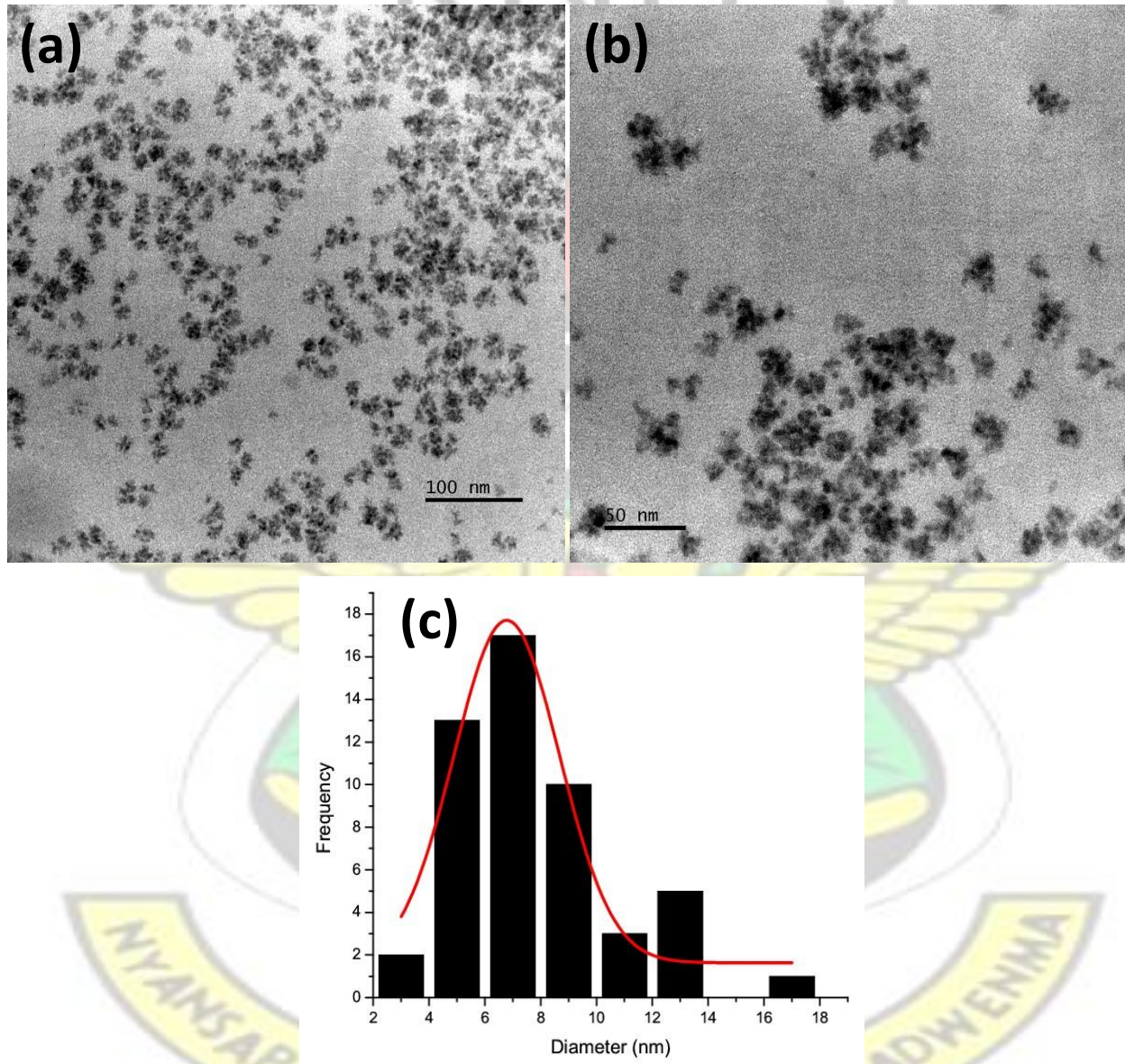


Figure 4.1.7: TEM images of CdS nanocrystals synthesized at 200 °C via heating up cadmium ethyl xanthate in castor oil for 15 minutes, (a) micrograph at 100 nm magnifications, (b) micrograph at 50 nm magnifications, and (c) nanoparticles size distribution.

The average particle size was found to be  $6.78 \pm 1.89$  nm which is about 22 % higher than the 5.37 nm found using the Brus equation (4.1.1). The particles are spherical in shape in the form of nanoclusters. The polydispersity was calculated to be 27.88 % which indicated that the particles sizes were uniform with the majority being within 6 – 8 nm (Figure 4.1.7(c)). Shombe et al., (2015) thermolyzed piperidine and tetrahydroquinoline dithiocarbamate complexes of Cd in castor oil and ricinoleic acid at 190 – 300 °C for 30 – 120 minutes and obtained spherical to oval shaped CdS nanoparticles with sizes within 10 – 22 nm. However, it must be noted that the band gap energies for CdS obtained by Shombe et al., (2015) were lower than that of bulk CdS which suggest interference from decomposed products (at such high temperatures) from castor oil and ricinoleic acid. Elemental analysis by SEM-EDX showed that the CdS nanoparticles synthesized at 200 °C were made up of 49.51 % of Cd and 50.49 % of S.

#### **4.1.2.4 PbS nanobelts**

##### **4.1.2.4.1 p-XRD analysis of PbS**

The p-XRD patterns of PbS synthesized at 140, 160 and 180 °C in castor oil are shown in Figure 4.1.8. The p-XRD patterns were clean without any peak relating to any other impurities implying that there was complete decomposition of the lead(II) ethyl xanthate precursor to pure crystalline PbS nanoparticles. The diffraction pattern at each temperature showed nine distinct peaks at  $2\theta$  values of 25.63°, 29.73°, 42.84°, 50.8°, 53.26°, 62.4°, 68.72°, 70.82° and 78.79° assigned to the (111), (200), (220), (311), (222), (400), (331), (420) and (422) planes for cubic PbS. The average

Scherrer calculated crystallite sizes using the full width at half maximum (FWHM) values of peaks at (111), (200) and (220) planes were within 19.74 – 26.19 nm. The d-spacing was found to be 3.00 Å at all the temperatures along the (200) plane.

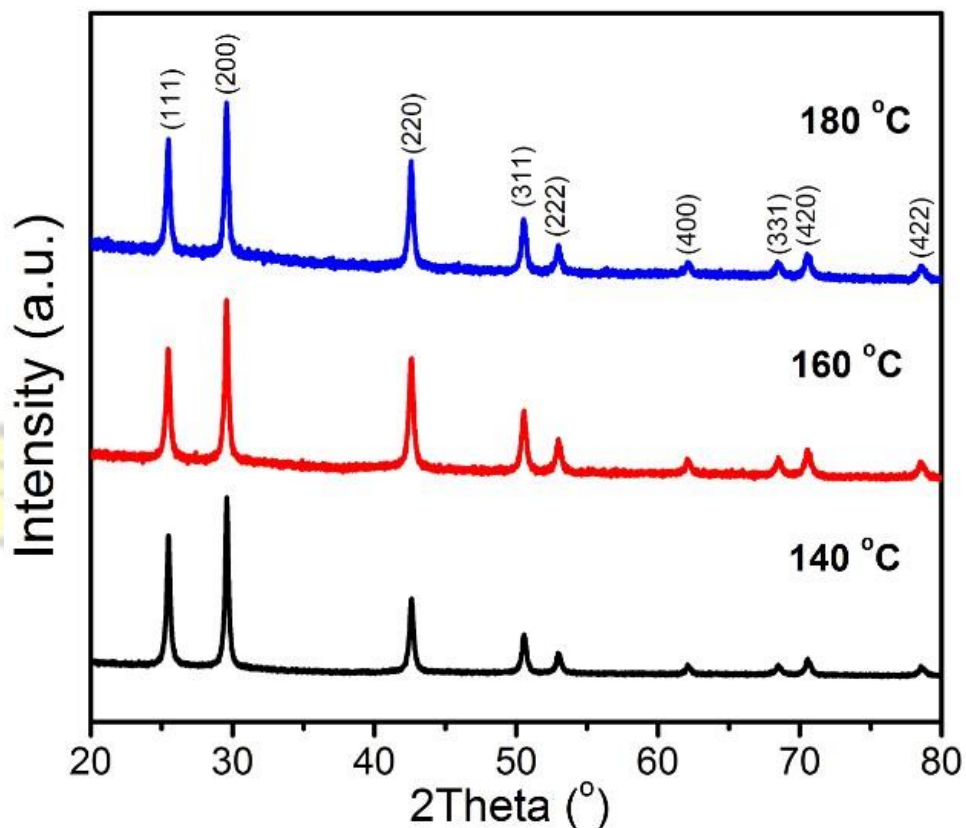


Figure 4.1.8: XRD patterns of PbS nanoparticles synthesized by heating up lead(II) ethyl xanthate in castor oil at 140, 160 and 180 °C for 15 minutes.

#### 4.1.2.4.2 Morphology of PbS

Interesting morphology of castor oil capped PbS synthesized at 140 °C and 200 °C are shown in Figure 4.1.9. The morphology is a mixture of cubic, rod, belt and star shaped PbS nanoparticles.

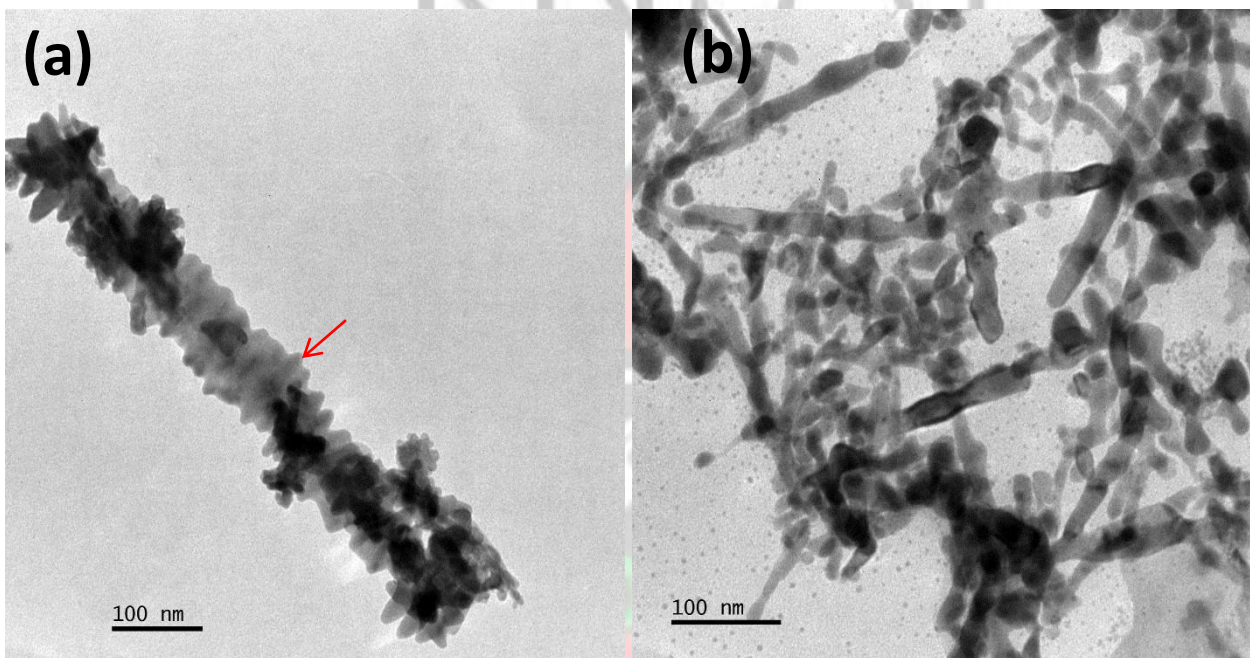


Figure 4.1.9: TEM images of PbS synthesized at (a) 140 °C (showing nanoplates and rod) and (b) 200 °C (showing nanobelts) obtained by heating up lead(II) ethyl xanthate in castor oil for 15 minutes

The cubic morphology is common to PbS nanoparticles, however, rods made of plates, belts and stars are not usually observed. At 140 °C cubes were observed alongside packing of the square plates to form a rod (Figure 4.1.9(a)). The nano-plates have average dimensions of  $44.30 \pm 4.18 \times 48.83 \pm 2.33$  nm and the formed rod had length of 715.09 nm. At 200 °C, nanobelts and some cubes of PbS were obtained, however, the belts were dominating (Figure 4.1.9(b)). The average width of the belts was  $22.19 \pm 2.33$  nm and the average length was  $225.94 \pm 23.32$  nm. Different

morphologies have been observed by other researchers. Star shaped morphology of PbS has been observed by Wang et al., (2006), when they refluxed lead acetate trihydrate and thiourea in ethylene glycol at 197 °C for 3 hours. They observed a cross shaped PbS consisting of six pods. Similarly, Phuruangrat and coworkers, (2012) also observed cubic and star-shaped dendritic PbS structures by solvothermal reaction (using an autoclave) between lead nitrate and thiosemicarbazide in propylene glycol at 120 °C for 10 hours.

Sun et al., (2009) also used a microwave-assisted method and obtained a flower-like PbS crystals by thermolysing lead diethyldithiocarbamate in ethylenediamine. Jin et al., (2010) prepared PbS of different morphologies including flowerlike, microsphere, multipod, six-armed star and truncated octahedron via citric acid assisted hydrothermal synthesis. It is worth mentioning that these different morphologies of PbS are common to growing PbS nanocrystals using heat-up, refluxing and hydrothermal processes (Salavati-Niasari et al., 2012). SEM-EDX elemental analysis showed that the PbS synthesized at 200 °C had a composition of 49.42 % Pb and 50.58 % S which indicates very good stoichiometric proportions of the two elements.

#### **4.1.2.4.3 Optical properties of PbS**

Figure 4.1.10(a) shows the NIR spectra of PbS nanocrystals synthesized at 140, 180 and 200 °C. The narrow absorption peaks of PbS synthesized at 180 and 200 °C imply that the particle sizes may be uniformly distributed. The absorption maximum appeared at 1414 nm and by plotting the Tauc's plot (Figure 4.1.10(b)). The band gaps were found to be 0.84, 0.85 and 0.86 eV at 140, 180 and 200 °C respectively. There was not much variation in the bandgaps at the different temperatures which suggested that the lead(II) ethyl xanthate decomposed far too quickly before

reaching the target temperatures. The average bandgap (i.e. 0.85 eV) obtained for the PbS nanoparticles was about 107 % higher than that of bulk PbS (i.e. 0.41 eV) implying that the castor oil was effective in tuning of the bandgap.

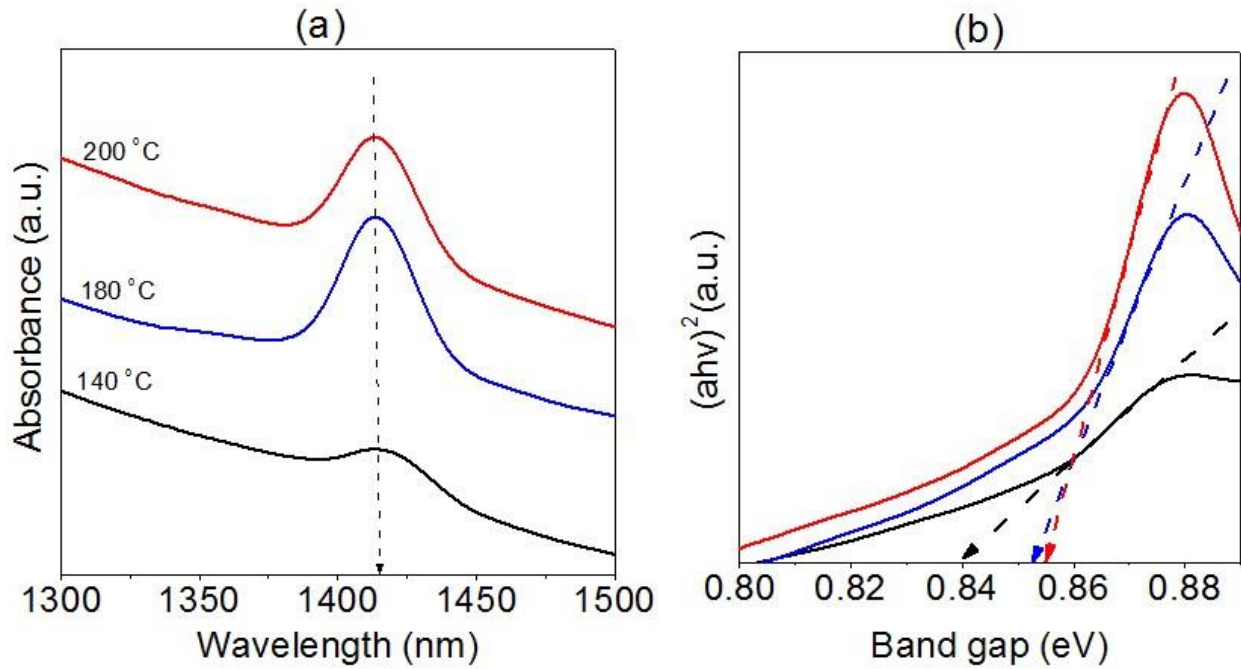
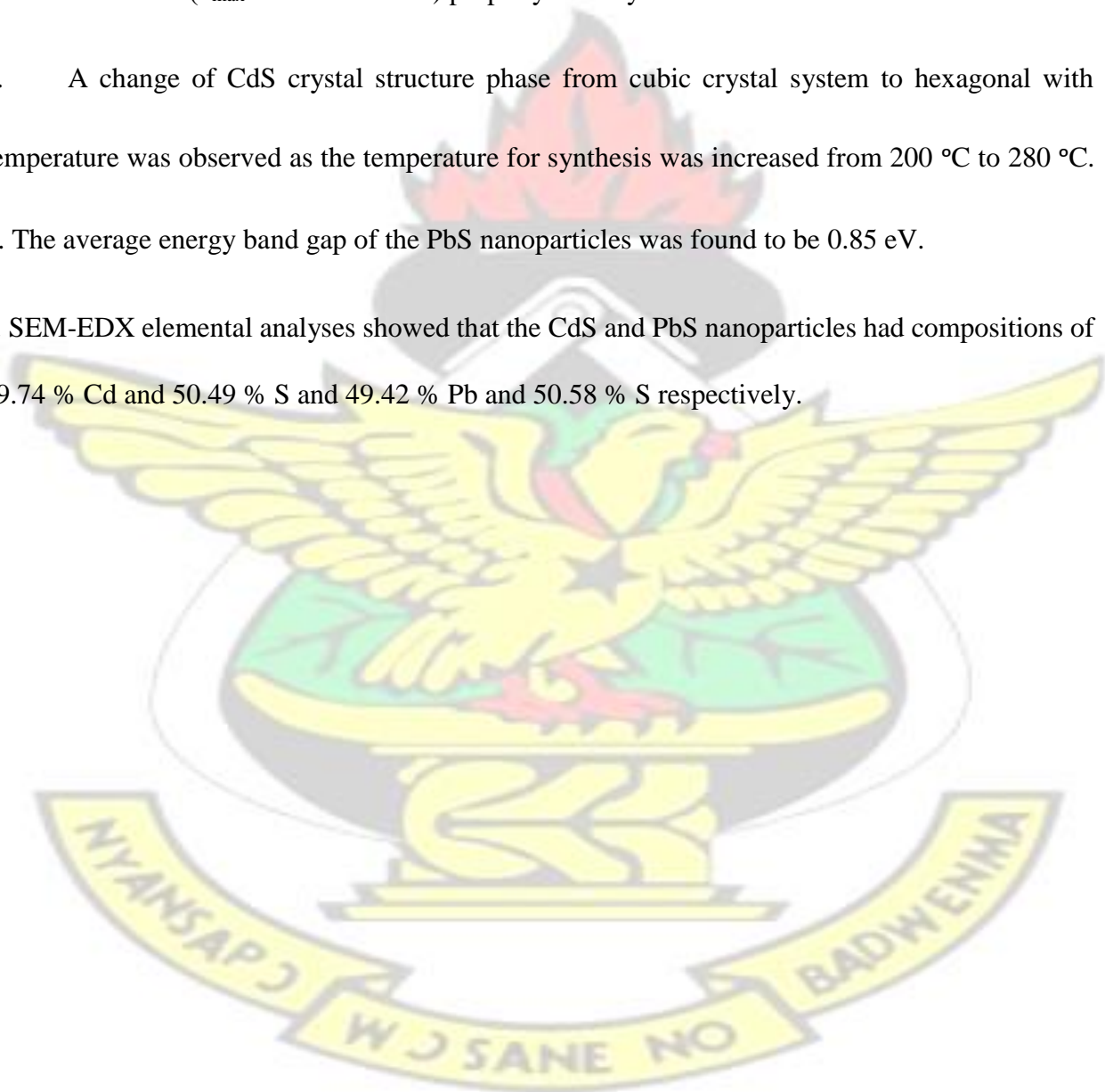


Figure 4.1.10: NIR spectra (a) and Tauc's plot (b) of PbS nanocrystals synthesized at 140, 180 and 200 °C via heating up lead(II) ethyl xanthate in castor oil for 15 minutes.

### 4.1.3 Summary of main findings

1. Castor oil has been demonstrated as a suitable solvent for synthesis of CdS nanoclusters and PbS with unusual and interesting morphologies (such as nanobelts, nanorods, nanoplates).
2. About  $6.78 \pm 1.89$  nm size CdS nanoclusters with band gap energy 2.63 – 2.73 eV and nearUV emission ( $\lambda_{\text{max}} = 391 - 393$  nm) property were synthesized.
3. A change of CdS crystal structure phase from cubic crystal system to hexagonal with temperature was observed as the temperature for synthesis was increased from 200 °C to 280 °C.
4. The average energy band gap of the PbS nanoparticles was found to be 0.85 eV.
5. SEM-EDX elemental analyses showed that the CdS and PbS nanoparticles had compositions of 49.74 % Cd and 50.49 % S and 49.42 % Pb and 50.58 % S respectively.



## 4.2 Growth Kinetics of ZnS Nanoparticles Synthesized by the Thermal Decomposition of Zinc Diricinoleate Carboxylate in Oleylamine/ Dodecanethiol

### 4.2.1 Introduction

The growth kinetics or coarsening of ZnS nanoparticles in aqueous media have been reported. However, coarsening of ZnS in colloidal systems consisting of organic solvents and amphiphilic capping agents (such as ricinoleic acid derived castor oil) have not been reported. The thermal decomposition of metal fatty acid salts in the presence of alkylthiol/ alkylamine solvent system is reported to be an excellent route for synthesis of high quality monodispersed nanocrystals. This route is reproducible and more suitable for large scale synthesis compared to the aqueous systems (Choi et al., 2009).

### 4.2.2 Results and discussions

#### 4.2.2.1 Analysis of isolated ricinoleic acid from castor oil

Ricinoleic acid, (*R,Z*)-12-hydroxyoctadec-9-enoic acid, is an unsaturated omega-9 fatty acid. It is distinct from oleic acid in that it contains hydroxyl functional group at the 12<sup>th</sup> carbon of its chemical structure. The <sup>1</sup>H NMR spectra of ricinoleic acid isolated from castor oil and standard ricinoleic acid purchased from Sigma-Aldrich are shown in Figure 4.2.1 (a and b). Ricinoleic acid contains carboxylic acid, alkene and hydroxyl functional groups. From the spectra, the broad singlet peak ( $\delta$ , 6.78 ppm in (a) and 5.90 ppm in (b)) show the hydrogen environment at the carboxylic functional group. The alkene and hydroxyl functional groups hydrogen environments

appeared at chemical shifts of 5.57 ppm and 5.43 ppm respectively. The two  $^1\text{H}$  NMR spectra are identical, except that there is a multiplet in spectrum (a) at 4.05 ppm indicating the presence of other fatty acids or chromophores in the isolated ricinoleic acid.

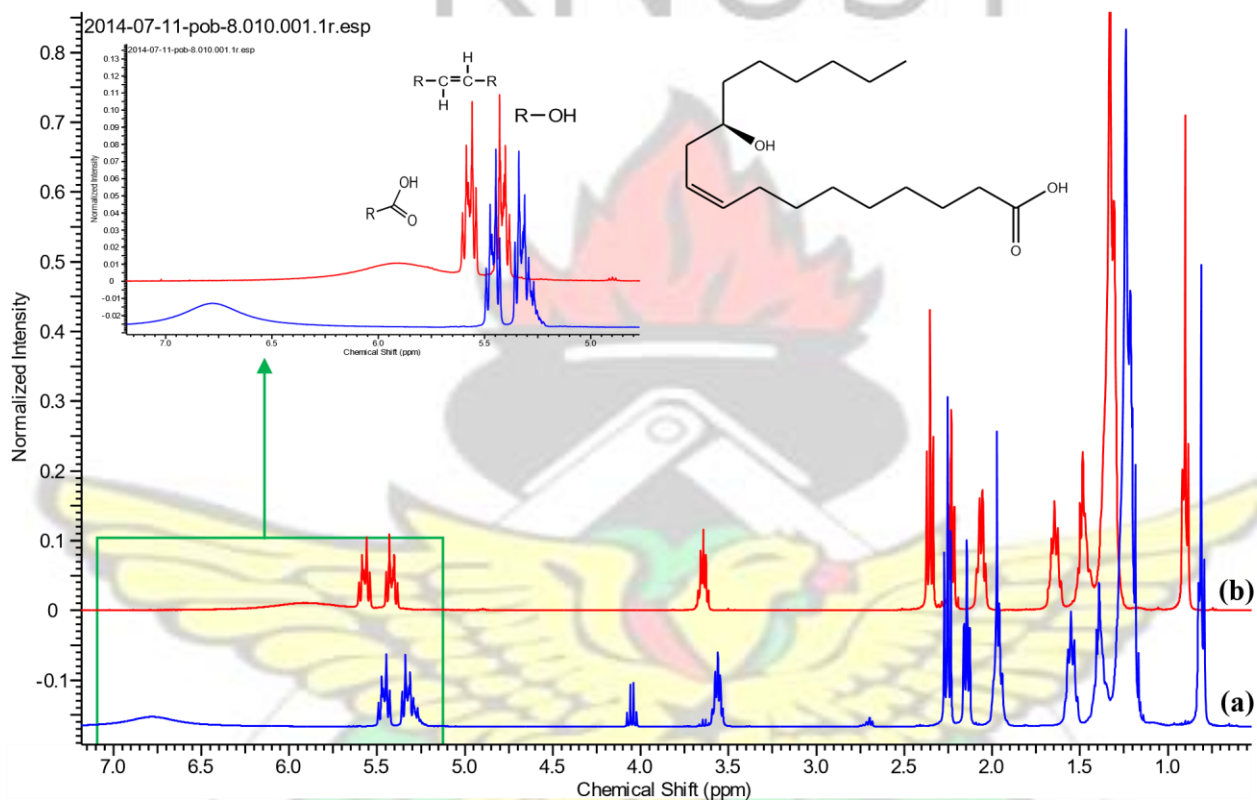


Figure 4.2.1:  $^1\text{H}$  NMR of (a) ricinoleic acid isolated from castor oil and (b) standard ricinoleic acid bought from Sigma-Aldrich

#### 4.2.2.2 Formation and thermal analysis of zinc diricinoleate carboxylate precursor

The zinc diricinoleate complex,  $[\text{Zn}(\text{Ra})_2]$  was formed by refluxing zinc acetate and the isolated ricinoleic acid in ethanolic solution of sodium hydroxide. The TGA of the  $[\text{Zn}(\text{Ra})_2]$  was obtained from 30 – 600  $^\circ\text{C}$  at 10  $^\circ\text{C min}^{-1}$  under nitrogen gas atmosphere (shown in Figure 4.2.2).

The thermal decomposition of  $[\text{Zn}(\text{Ra})_2]$  occurred with the loss of the ricinoleic acid groups leaving  $\text{ZnO}$  (which forms 12.32 % of the complex) at 471.32 °C. The complex further decomposed to  $\text{Zn}$  metal representing about 9.90 % of the complex which remained as residue. Intense decomposition of the complex occurred at 452.38 °C with the onset and endset temperatures at 384.29 and 468.82 °C respectively.

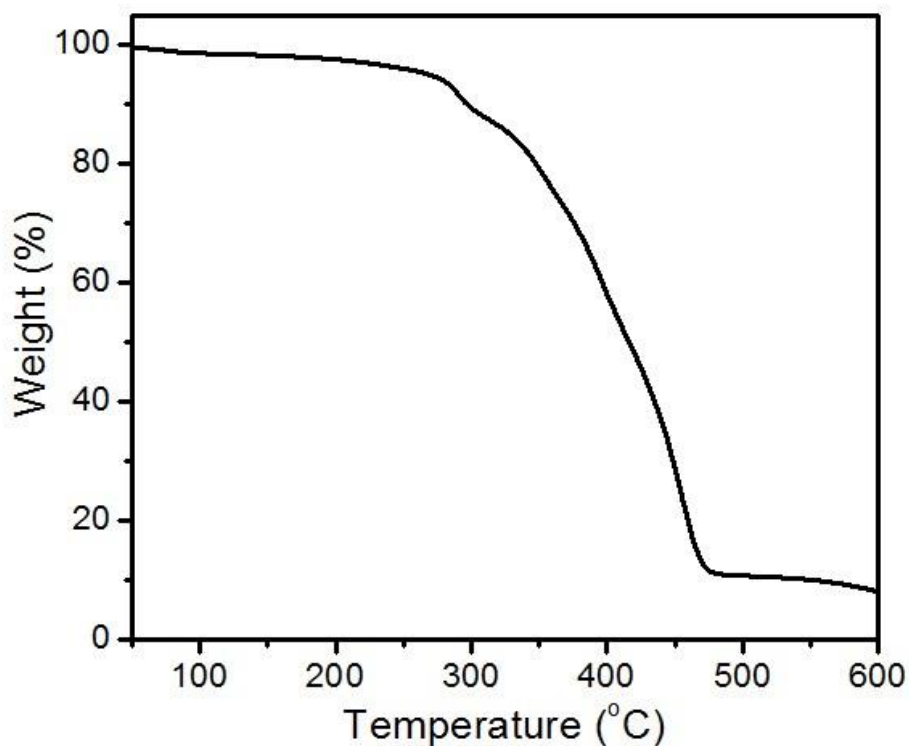


Figure 4.2.2: TGA pattern of decomposition of  $[\text{Zn}(\text{Ra})_2]$  carboxylate precursor (at 30 – 600 °C under nitrogen, at heating rate of 10 °C  $\text{min}^{-1}$ )

#### 4.2.2.3 Formation and growth of $\text{ZnS}$ nanoparticles

The  $\text{ZnS}$  nanoparticles were formed by decomposing the zinc diricinoleate carboxylate complex in dodecanethiol/oleylamine at reaction temperatures above 240 °C. The thermal decomposition of transition metal carboxylates has been reported to occur via the cleavage of the  $\text{M-OC}$  and  $\text{MO-}$

C bonds in the metal carboxylates to release radical species (as shown in equations 4.2.1 and 4.2.2) (Cha et al., 2007).



In the presence of dodecanethiol, the generated radical species react to form the ZnS nanoparticles (equation 4.2.3).

The oleylamine used as solvent is said to enhance the reactivity of metal carboxylates precursors via aminolysis reaction and thereby lowering the reaction temperature for the metal sulphide formation (Liu et al., 2008). Oleylamine is a primary amine which can act as electron donor at high temperatures. Oleylamine controls nanoparticles morphology and crystallinity by exhibiting affinity to the metals through its  $\text{NH}_2$  functional group (Mourdikoudis and Liz-Marza, 2013). It was observed that at reaction temperatures below  $240\text{ }^\circ\text{C}$ , there was no formation of ZnS nanoparticles. Instead, white powder precipitates were obtained at the lower temperatures and showed no X-ray diffraction suggesting that the material was amorphous.

#### 4.2.2.4 p-XRD measurement on ZnS nanoparticles

The p-XRD pattern of the ZnS nanoparticles synthesized at  $300\text{ }^\circ\text{C}$  is shown in Figure 4.2.3. Pure phase of ZnS was obtained. The diffraction pattern strongly corresponds to a face-centered cubic  $\beta$ -ZnS with a sphalerite (Zinc blende) crystal structure (ICDD number 00-005-0566). The pXRD

pattern showed three distinct peaks at  $2\theta$  values of  $28.55^\circ$ ,  $47.54^\circ$  and  $56.44^\circ$  matching the X-ray diffraction at  $hkl$  (111), (220) and (311) planes in ZnS. The ZnS nanoparticles were 100 % sphalerite. The lattice parameter calculated was approximately  $5.4064 \text{ \AA}$  which compares with  $5.4060 \text{ \AA}$  for standard ZnS. The XRD also detected no formation of zinc oxide in any of the synthesized samples.

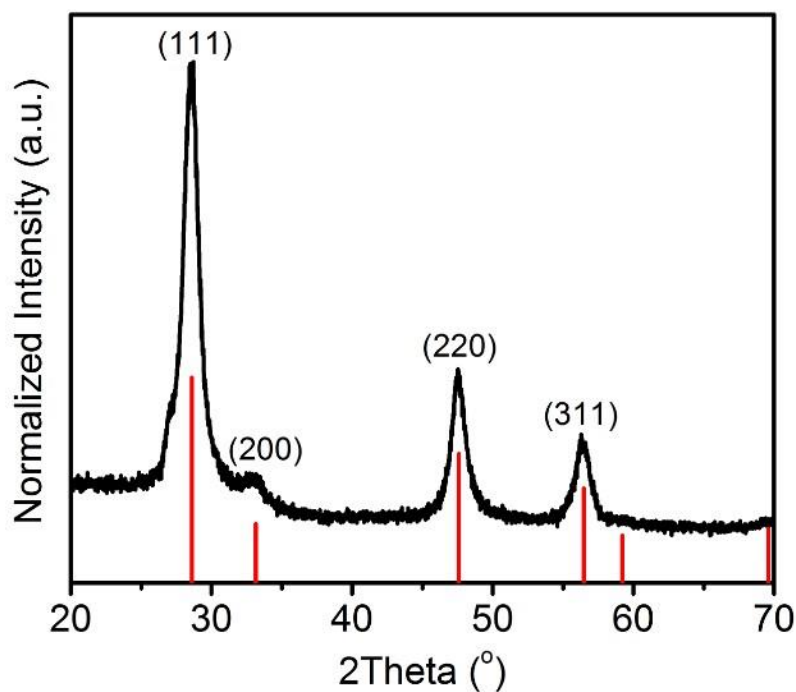


Figure 4.2.3: p-XRD pattern of ZnS nanoparticles obtained by decomposing zinc diricinoleate carboxylate complex in oleylamine/dodecanethiol solvent system at  $300^\circ\text{C}$  for 1 hour. The red lines are standard pattern sphalerite ZnS

#### 4.2.2.5 Particle size determination of ZnS nanoparticles

The particle sizes of the ZnS nanoparticles were determined with XRD, UV-Vis and TEM methods. The XRD is a suitable method for determining the average particle size of crystallites in nanoparticles (Holzwarth and Gibson, 2011). From the p-XRD patterns, the crystallite sizes of the synthesized ZnS nanoparticles were calculated using the Scherer equation (equation 4.2.4).

$$d_{hkl} = \frac{K\lambda}{B_{hkl}\cos\theta} \quad (4.2.4)$$

where the  $d_{hkl}$  is the crystallite size,  $hkl$  are the Miller indices of the crystallite planes being analyzed,  $K$  is the crystallite-shape factor,  $\lambda$  is wavelength of the X-ray,  $B_{hkl}$  is the full-width at half maximum (FWHM) of the diffraction peak in radians and  $\theta$  is the Bragg angle (Holzwarth and Gibson, 2011). The crystallite sizes were obtained based on the  $hkl$  (111) diffraction plane which was the most preferred orientation of the ZnS crystallites. The average crystallite size of the ZnS nanoparticles synthesized at 300 °C was calculated to be 5.28 nm.

To confirm the particle sizes obtained for the ZnS samples, the particle sizes were also obtained from the UV-Vis absorption spectra of the ZnS nanoparticles. The Brus equation (see equation 2.32) gives an approximation of nanoparticle sizes from their band gap energies. The optical band gap energies of the ZnS nanoparticles samples were estimated by using the Tauc's relation shown in equation (4.2.5).

$$(\epsilon hv) = C(hv - E_g)^n \quad (4.2.5)$$

where the  $\epsilon$  is the molar extinction coefficient,  $h$  is the Planck's constant,  $\nu$  is the frequency, ( $h\nu =$  photon energy),  $C$  is a constant and  $E_g$  is the average band gap energy of the absorbing material.  $n = \frac{1}{2}$  when the  $E_g$  is a direct allowed band gap energy (such as those for ZnS). The band gap energy

was calculated by plotting  $(\epsilon h\nu)^2$  against  $h\nu$  and extrapolating the tangent of the absorbance curve to the x-axis (Jacob et al., 2012). The absorption spectrum of the synthesized ZnS nanoparticles and estimation of the optical band gap energy are shown in Figure 4.2.4(a). The band gap energy of the ZnS nanoparticles was estimated to be 3.72 eV which is about 3.33 % higher than that of the bulk ZnS suggesting some level of quantum confinement.

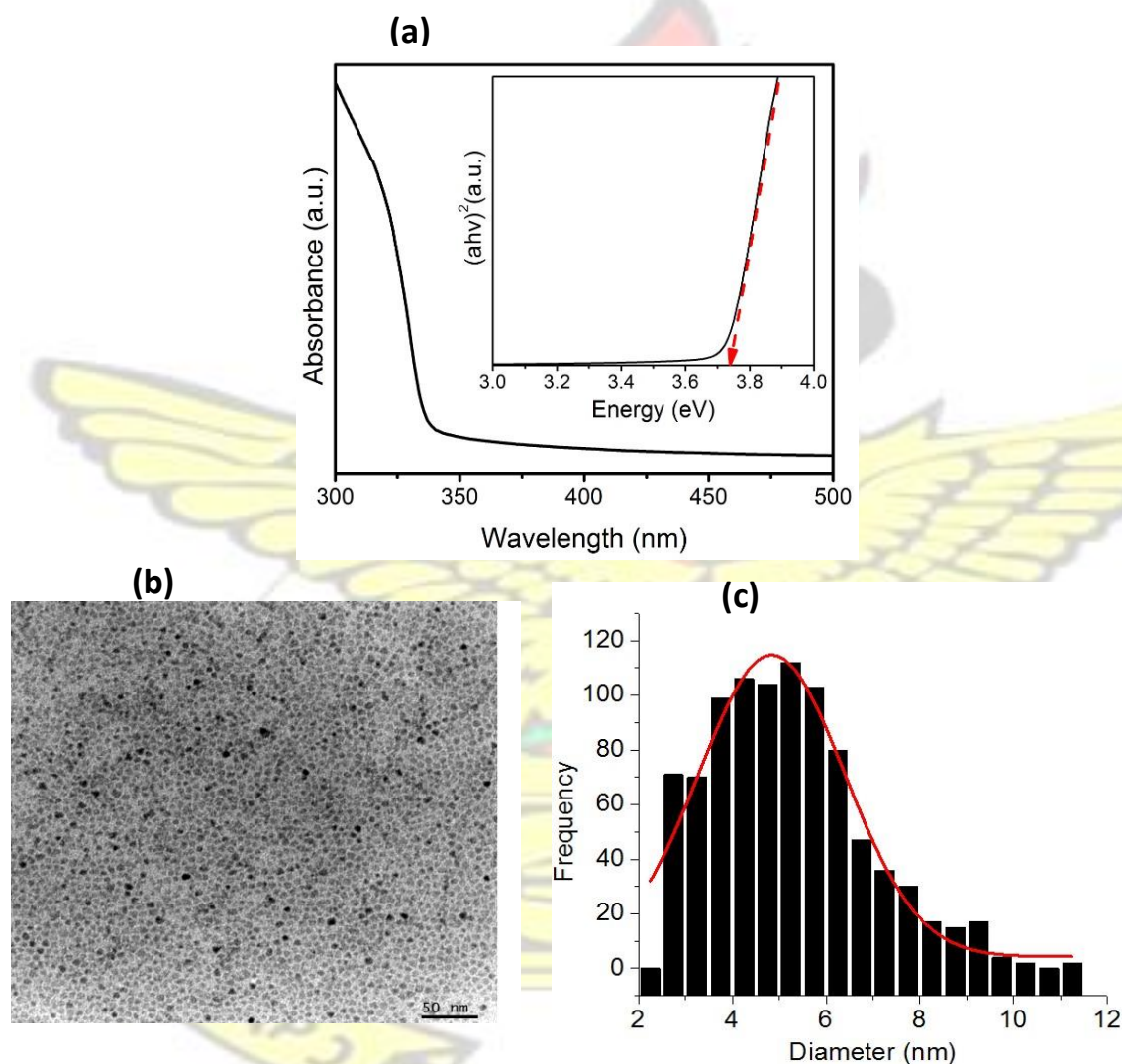


Figure 4.2.4: Graphs showing (a) Absorption spectrum (The insert graph is the Tauc's plot showing the optical band gap energy), (b) TEM image and (c) particles size distribution histogram of the ZnS nanoparticles obtained by decomposing zinc diricinoleate carboxylate complex in oleylamine/dodecanethiol at 300 °C for 1 hour.

The solved form of the Brus equation by Suyver et al. (2001) for ZnS is given in the form shown in equation (4.2.6).

$$\frac{\sqrt{\dots}}{\dots} \quad (4.2.6)$$

where  $E_{g(bulk)} = 3.6 \text{ eV}$ ,  $m_e^* = 0.34m_e$ ,  $m_h^* = 0.23m_e$  and  $\varepsilon = 8.76$  (Suyver et al. 2001; Whiffen et al., 2014). The application of the Brus equation resulted in particle size of 4.85 nm for the ZnS nanoparticles synthesized at 300 °C. This value compares closely to the 5.28 nm obtained from the XRD, only about 8.9 % lower. A more precise technique for nanoparticle size and size distribution is the TEM. The TEM image showing the morphology of the ZnS nanoparticles synthesized at 300 °C is shown in Figure 4.2.4(b) and the particle size distribution histogram in Figure 4.2.4(c). From the TEM image, the average particle size of the ZnS nanoparticles was calculated to be  $4.84 \pm 1.56$  nm which matches closely to the particle sizes obtained by the UVVis and XRD.

The good correlation that exists between values of particle sizes determined by XRD, UV-Vis and TEM, renders these techniques to be used extensively for the determination of particle size of semiconductor nanoparticles (Tiemann et al., 2005; Zhang and Banfield, 2009; Porta et al., 2014; Logar et al., 2009). The particle sizes determined by XRD and UV-Vis for the same ZnS nanoparticles samples are plotted in Figure 4.2.5. The values of the particle sizes obtained by XRD correlates closely ( $R^2 = 0.81$ ) to those obtained by the UV-Vis method. However, the UVVis method appears quite simpler and has been widely applied to study the growth kinetics or coarsening kinetics of ZnS nanoparticles (Li et al., 2008; Tiemann et al., 2008; Tiemann et al., 2005).

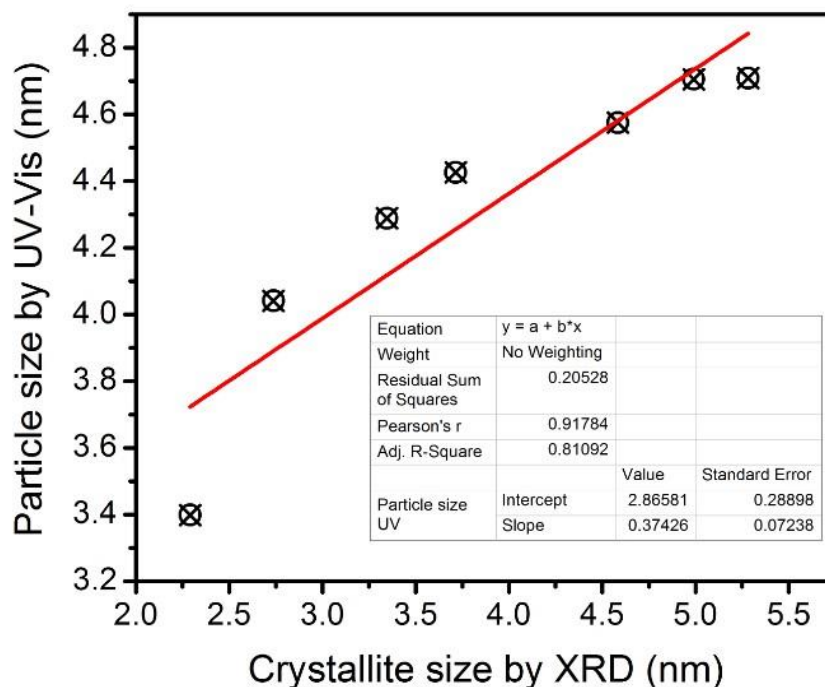


Figure 4.2.5: Correlation between particle sizes of ZnS nanoparticles determined by XRD and UV-Vis methods.

#### 4.2.2.6 Effect of temperature on particle size

The p-XRD patterns of the ZnS nanoparticles synthesized at different temperatures (240 – 300 °C) are shown in Figure 4.2.6. There was no ZnS crystal phase change observed with increasing reaction temperature (within the temperature range chosen). The diffraction pattern of the ZnS nanoparticles synthesized at 240 °C appeared broadened compared to those synthesized at 300 °C. This broadening of the diffraction peaks was observed to be decreasing as the reaction temperature was increasing. The broadening of XRD diffraction peaks is reported by Scherer to be inversely proportional to the size of the crystallites (Holzwarth and Gibson, 2011). The fullwidth half-maximum (FWHM) of the diffraction peaks of the ZnS nanoparticles reduced by 57 % as the

reaction temperature was increased from 240 °C to 300 °C. This observation asserts the fact that the ZnS crystallite sizes decreased with increasing reaction temperature.

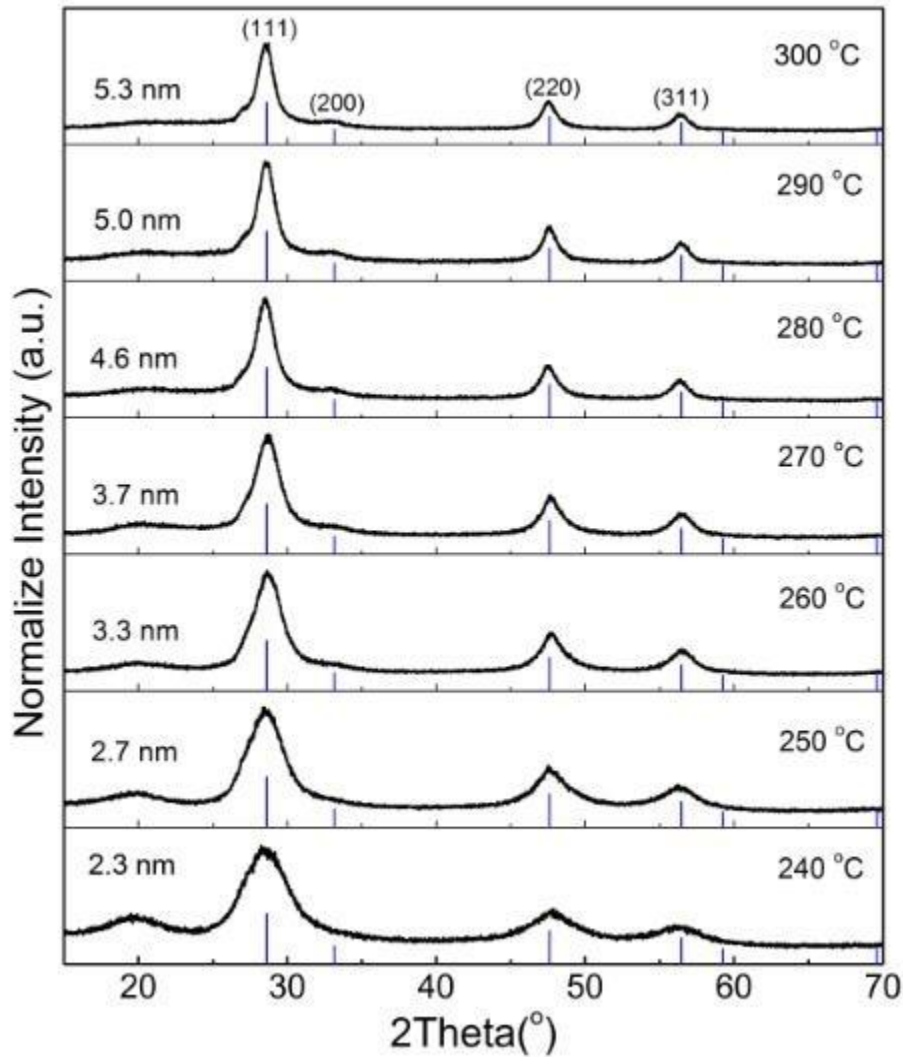


Figure 4.2.6: p-XRD patterns of ZnS nanoparticles obtained by decomposing diricinoleate carboxylate precursors in oleylamine/dodecanethiol at different temperatures for 1 hour. The blue lines are standard patterns for sphalerite ZnS.

The crystallite sizes of the ZnS nanoparticles increased from 2.3 nm to 5.3 nm as the reaction temperature was increased from 240 °C to 300 °C. The percentage increment in the particle size

was calculated to be 130 % which corresponds to 57 % reduction in the FWHM of the diffraction peak (reflection at (111) plane) as the temperature was increased to 300 °C. Comparatively, Huang et al., (2003) obtained 2.0 nm and 2.4 nm particle size of ZnS nanoparticles synthesized via hydrothermal method using water and mercaptoethanol-water as solvents respectively. The nanoparticles obtained in this work were crystalline quantum dots of ZnS relative to those obtained by the aqueous route.

#### **4.2.2.7 Effect of reaction time on particle size**

The p-XRD patterns of the ZnS nanoparticles synthesized at different time intervals at 270 °C are shown in Figure 4.2.7(a). The crystallinity of the ZnS nanoparticles improved as the reaction progressed for longer period of time (60 minutes). The material obtained at 10 minutes of reaction at 270 °C showed no X-ray diffraction indicating that the material was less crystalline. Increasing the reaction time to 60 minutes resulted in comparatively more crystalline material. The evolution of the optical spectra of the ZnS nanoparticles synthesized at different time intervals at 250 °C is shown in Figure 4.2.7(b). The corresponding Tauc plot estimation of the optical band gap energies is also shown in Figure 4.2.7(c). The ZnS nanoparticles showed interesting time dependent evolution of absorption spectra (Figure 4.2.7(b)). Good quality ZnS nanoparticles were obtained after the first 20 minutes of reaction at 250 °C. The time dependent absorption of ZnS nanoparticle has been employed by Tiemann et al., (2005) and Li et al., (2008) for the study of the coarsening kinetics of ZnS in aqueous systems.

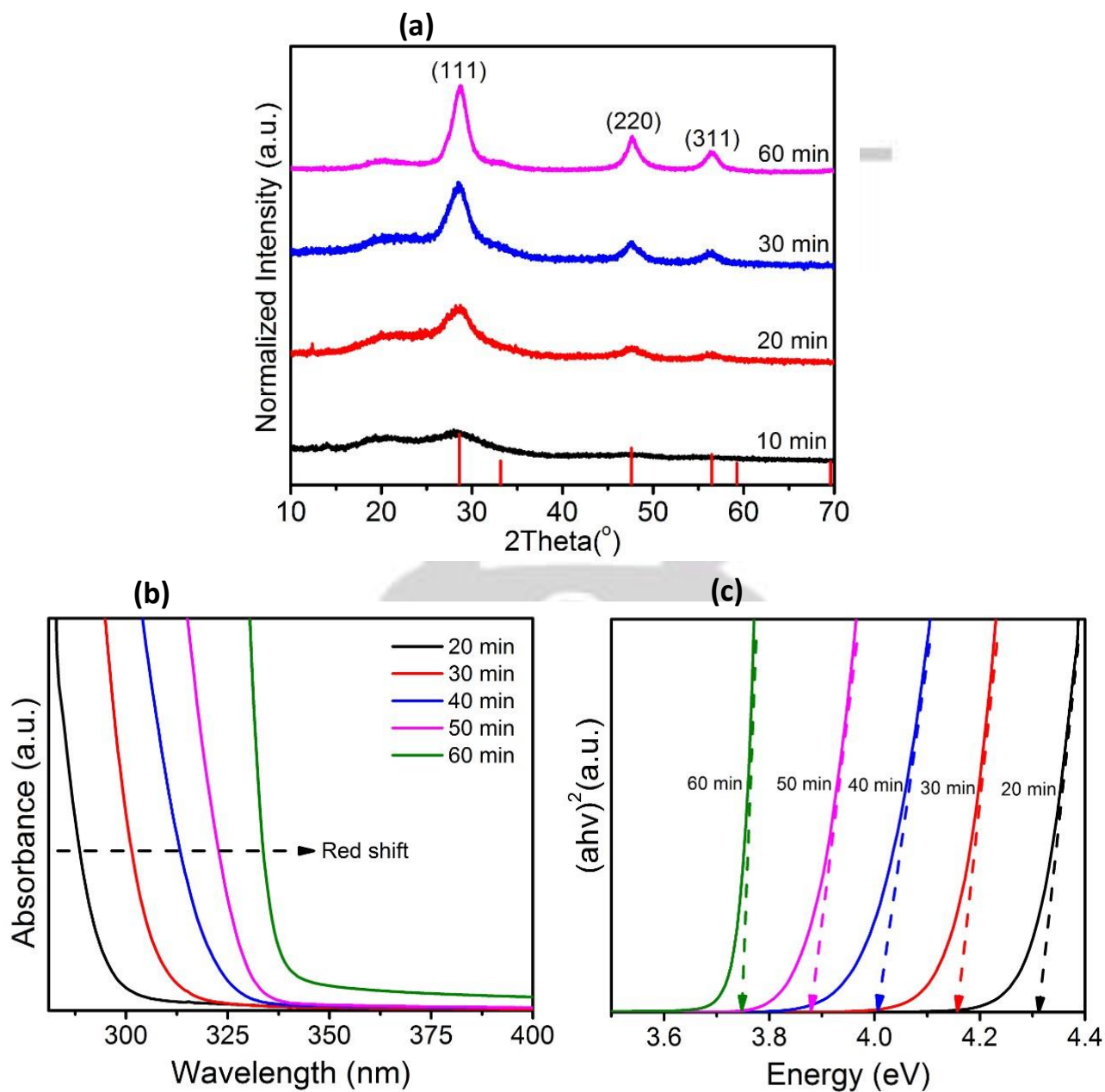


Figure 4.2.7: The effect of reaction time on (a) p-XRD pattern, (b) absorption spectra and (c) optical band gap energy of ZnS nanoparticles synthesized by colloidal thermolysis of zinc diricinoleate precursor in oleylamine/ dodecanethiol.

The band gap energy obtained for the ZnS nanoparticles synthesized at 250 °C after the first 20 minutes of reaction was 4.27 eV and 3.73 eV after 60 min. This red shift of the optical spectra of

the ZnS nanoparticles to higher wavelength (or to lower energy) is due to the increase in the particle size with reaction time (Figure 4.2.7(c)). This observation has been widely reported on ZnS nanoparticles and also on very important metal chalcogenide nanoparticles such as CdS and CdSe (Su et al., 2010; Sun et al., 2009; Zhang et al., 2010; Yordanov et al., 2006; Jia et al., 2013; Sapra et al., 2006; Li et al., 2008).

#### 4.2.2.8 Determination of activation energy of ZnS nanoparticles growth

The coarsening kinetics of the ZnS nanoparticles in solution taking into consideration the Ostwald ripening and oriented attachment kinetic models is given by equation 4.2.7 (Tiemann et al., 2008; Zhang and Banfield, 2009; Thanh et al., 2013; Huang et al., 2003).

$$D = \frac{D_o(\sqrt[3]{2k_1t+1})}{(k_1t+1)} + k_2t^{1/n} \quad (4.2.7)$$

where  $D$  is the particle diameter at time  $t$ ,  $D_o$  is the initial particle diameter, the  $k_1$  and  $k_2$  are reaction rate constants for the two step reaction in the crystal growth reaction. However, the growth component in the second term of equation (4.2.7) dominates the coarsening activity over a longer period of reaction compared to the first term which diminishes rapidly in the course of the reaction. Thus,  $k_2$  dominates over  $k_1$  and it is often reported in literature as the rate constant for ZnS nanoparticles crystal growth. The temporal evolution of ZnS nanoparticles sizes at different temperatures are shown in Figure 4.2.8.

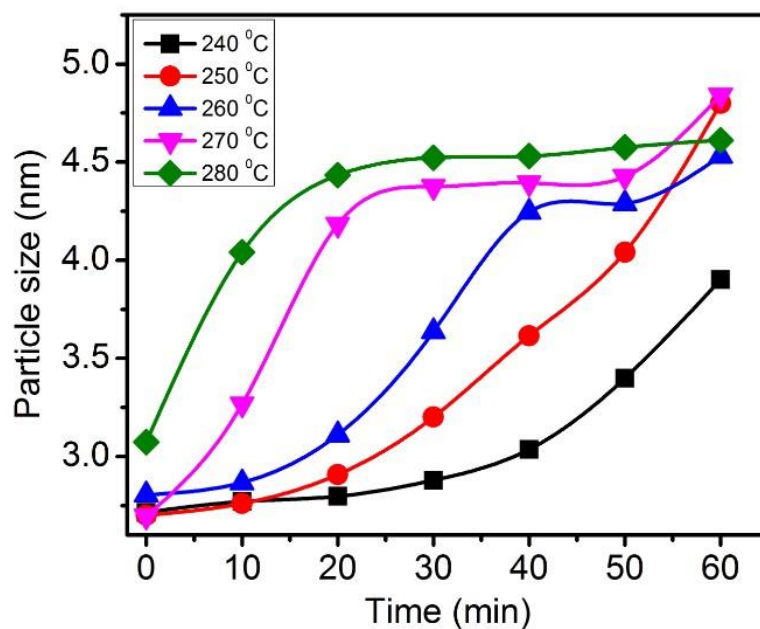


Figure 4.2.8: Temporal evolution of the average particle size of ZnS nanoparticles at different temperatures.

The general observation from Figure 4.2.8 (especially at 280 °C) is that the particle size increases rapidly during the first 30 to 40 minutes and stabilizes or slows down afterwards. This suggests the possible size focusing mechanism occurring after the first 40 minutes of the reaction. During size focusing, according to the diffusion controlled model, the larger particles grow slowly whereas the smaller particles grow rapidly due to the large supply or diffusion of monomers/solutes to their surface. Thus, well uniform size distribution of nanoparticles of ZnS with monodispersity of 67.8 % was obtained.

However, Ostwald ripening and oriented attachment mechanisms seem also to coexist for reactions at 240 to 270 °C. In Ostwald ripening mechanism, the larger particles grow in the expense of the smaller particles. This is explained by assuming that the concentration of the solutes at the surfaces

of the bigger particles is low compared to that of the smaller particles and thus solutes diffuse from the surfaces of the smaller particles to the bigger particles resulting in the growth of the bigger particles. Oriented attachment mechanism assumes coalescence of adjacent particles that share common crystallographic orientation. Equation 4.2.7 combines the effects of these two mechanisms. Thus, the diameter of the ZnS nanoparticles ( $D$ ) was plotted against time (in the form  $t^{1/n}$ , assuming a volume diffusion of the liquid medium,  $n = 3$ ) to obtain rate constant ( $k$ ) for each temperature (Tiemann et al., 2008). The activation energy ( $E_A$ ) of the coarsening reaction was calculated by employing the Arrhenius equation in the form

$$\ln(k) = -\frac{E_A}{RT} + \ln(X) \quad (4.2.8)$$

where  $R$  is the ideal gas constant,  $T$  is the temperature in Kelvin, and  $X$  is the pre-exponential factor. Plot of  $\ln(k)$  against the reciprocal of the temperature is shown in Figure 4.2.9. The slope of the linear fit gives the activation energy. The  $E_A$  value obtained for growth of ZnS nanoparticles in a mixture of oleylamine and dodecanethiol was 54.31 kJ/mol. This value agrees with the 42.4 kJ/mol reported by Huang et al., (2003) for coarsening of ZnS nanoparticles in aqueous/mercaptoethanol medium. However, Tiemann et al., (2008) also obtained  $E_A$  of 25.7 kJ/mol for coarsening of ZnS nanoparticles in aqueous medium. The  $E_A$  value obtained in this work takes into account all the possible crystal growth mechanisms which are accounted for in equation (4.2.7).

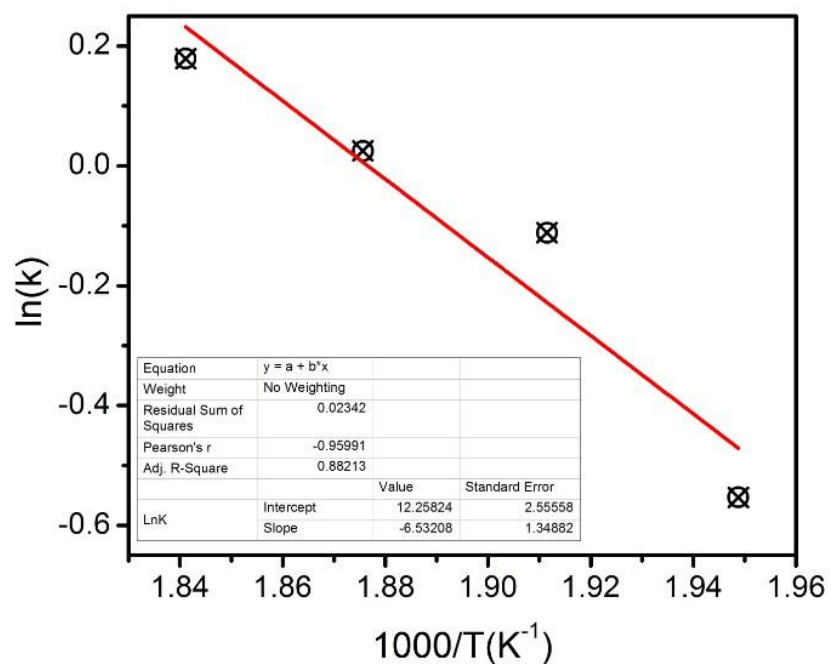
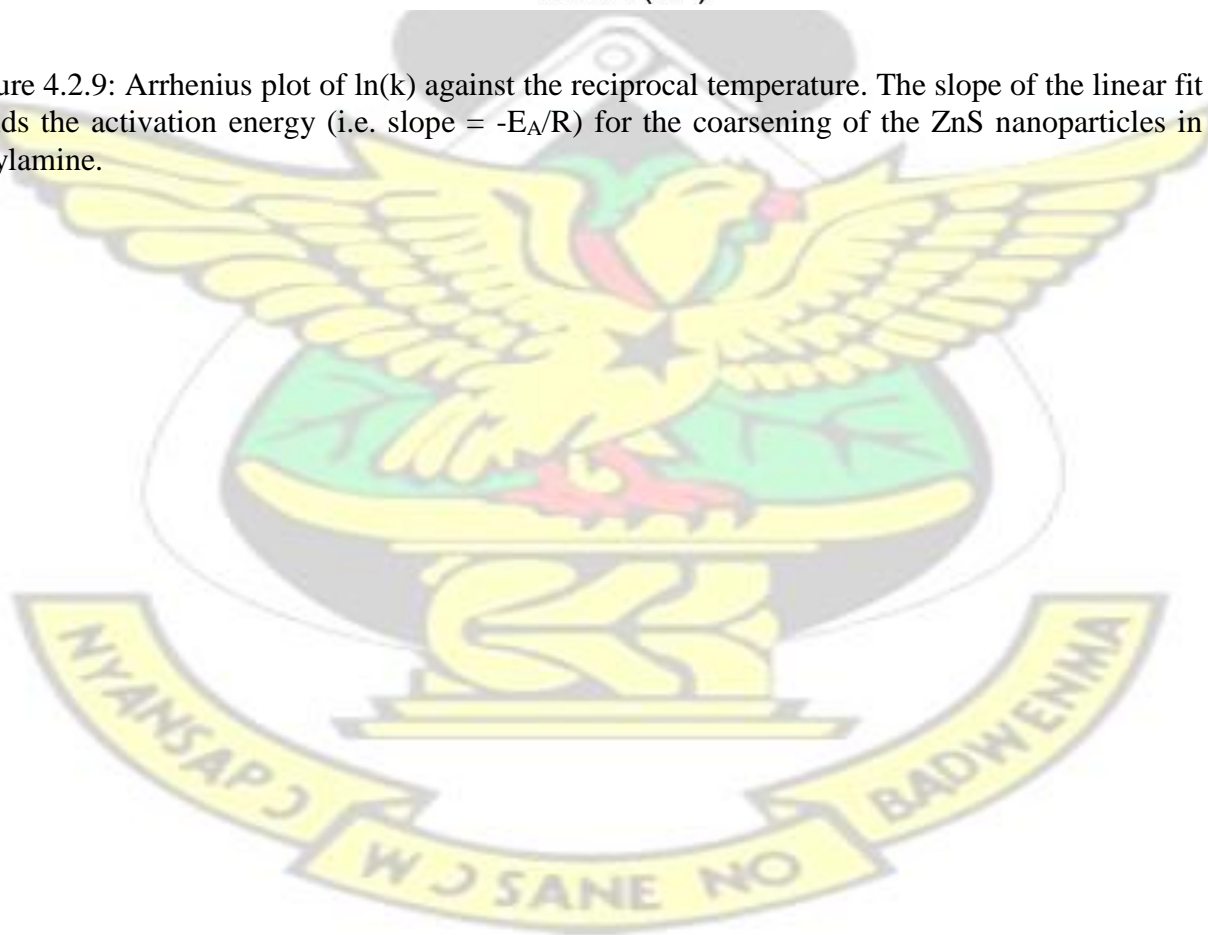


Figure 4.2.9: Arrhenius plot of  $\ln(k)$  against the reciprocal temperature. The slope of the linear fit yields the activation energy (i.e. slope =  $-E_A/R$ ) for the coarsening of the ZnS nanoparticles in oleylamine.



### 4.2.3 Summary of main findings

1. The reactivity of zinc diricinoleate carboxylate complex was found to occur at temperatures higher than 240 °C in oleylamine/dodecanethiol.
2. Pure crystalline sphalerite monodispersed ZnS nanoparticles with quantum dot sizes 2.3 – 5.3 nm were obtained by the thermal decomposition of zinc diricinoleate carboxylate complex in oleylamine/dodecanethiol at  $\geq 240$  °C for  $\geq 20$  minutes.
3. The particles size and optical band gap energies of the ZnS nanoparticles were found to be dependent on temperature and time of reaction
4. The activation energy for coarsening kinetics of ZnS nanoparticles synthesized by the thermal decomposition of zinc diricinoleate carboxylate complex in oleylamine/dodecanethiol was determined to be 54.31 kJ/mol

### 4.3 The Syntheses of Manganese doped Zinc Sulphide ( $Mn_xZn_{1-x}S$ ) Nanocrystals by the

## Thermal Decomposition of Ricinoleate Carboxylates in Oleylamine/ Dodecanethiol

### 4.3.1 Introduction

To date, cadmium sulphide (CdS) based doped nanocrystals have been applied as luminescent probes. There are however, concerns related to the toxicity of cadmium which limit their potential application. In contrast, the closely related  $Mn_xZn_{1-x}S$  are considerably more benign and also possess longer dopant emission and good photostability (Ban et al., 2013; Srivastava et al., 2010; Yang et al., 2005). Despite the interest in  $Mn_xZn_{1-x}S$  nanocrystals application, the physical location and distribution of the Mn(II) ions in the host lattice of ZnS could result in improved photoluminescent and electrochromic device efficiency (Sooklal et al., 1996).

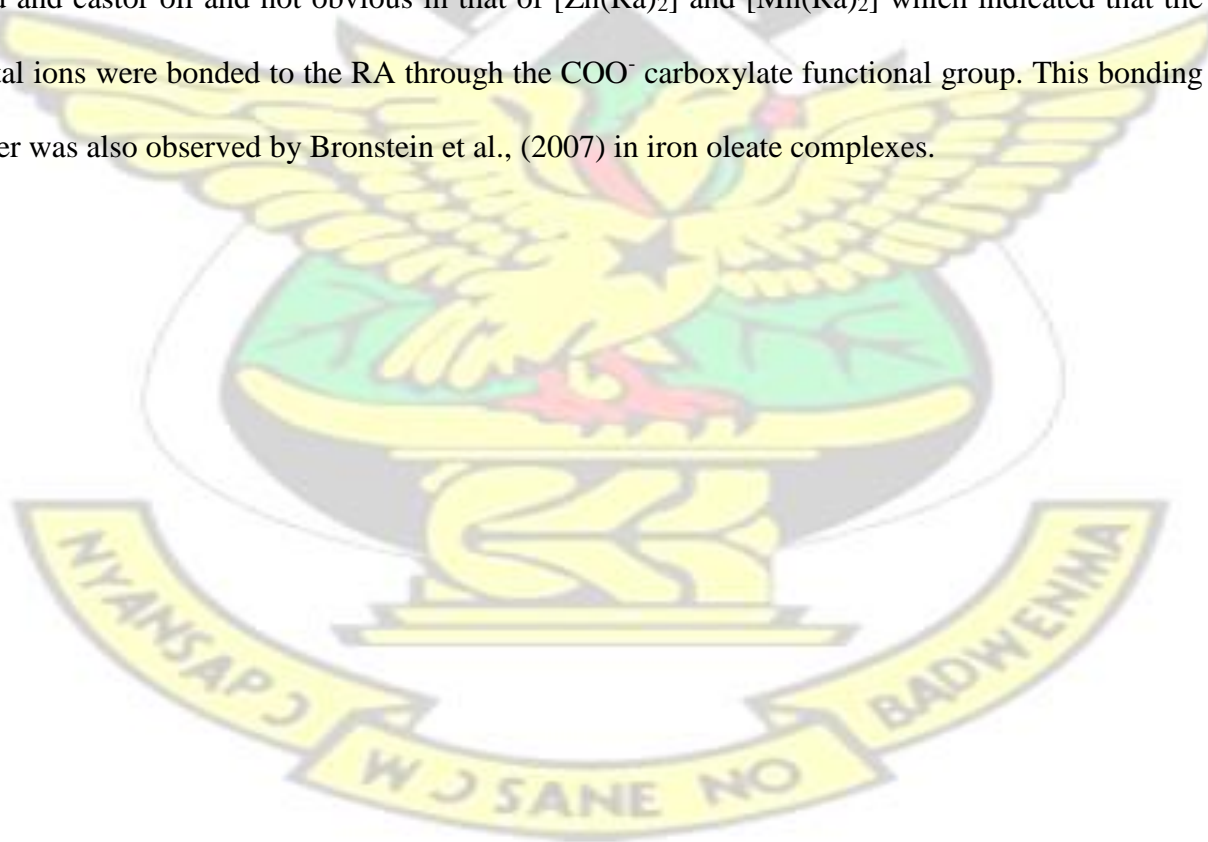
However, the syntheses techniques for incorporation of Mn(II) ions into substitutionary positions of  $Zn^{2+}$  ions in host ZnS lattice is experimentally quite challenging (Zhang et al., 2011). There is currently no single method for syntheses of doped nanocrystals. In this work, the syntheses of ZnS, MnS and  $Mn_xZn_{1-x}S$  nanocrystals by the thermolyses of ricinoleic acid metal carboxylates in oleylamine/ dodecanethiol solvent system is reported. This route has been reported to be more reproducible, yield good quality crystalline monodispersed nanocrystals and highly scalable (Patel et al., 2012; Srivastava et al., 2010; Kwon and Hyeon, 2008; Kwon and Hyeon, 2011). Our approach applies the growth-doping techniques, whereby a minimum amount of the dopant precursor is added to the host precursor and reacted together to generate the nuclei (of both the dopant and host) and the subsequent growth of nanocrystals (Srivastava et al., 2010).

## 4.3.2 Results and discussions

### 4.3.2.1 Diricinoleate carboxylate complexes of Zn and Mn

Ricinoleic acid represents a new source of fatty acid with potential application in nanoparticles synthesis. The alkali hydrolysis of castor oil yielded ricinoleic acid. The diricinoleate carboxylate complexes  $[\text{Zn}(\text{Ra})_2]$  and  $[\text{Mn}(\text{Ra})_2]$  as synthesized per literature were white and dark brown in colour respectively. Their structures were studied with FTIR and GC-MS.

The FTIR spectra for the castor oil, ricinoleic acid and the complexes contain strong bands  $3319.29\text{ cm}^{-1}$  and  $2921.51 - 2850.19\text{ cm}^{-1}$  which can be assigned to free OH and C-H stretching vibrations (Figure 4.3.1). The band at  $1710\text{ cm}^{-1}$  relating to C=O stretch was seen in both spectra for ricinoleic acid and castor oil and not obvious in that of  $[\text{Zn}(\text{Ra})_2]$  and  $[\text{Mn}(\text{Ra})_2]$  which indicated that the metal ions were bonded to the RA through the  $\text{COO}^-$  carboxylate functional group. This bonding order was also observed by Bronstein et al., (2007) in iron oleate complexes.



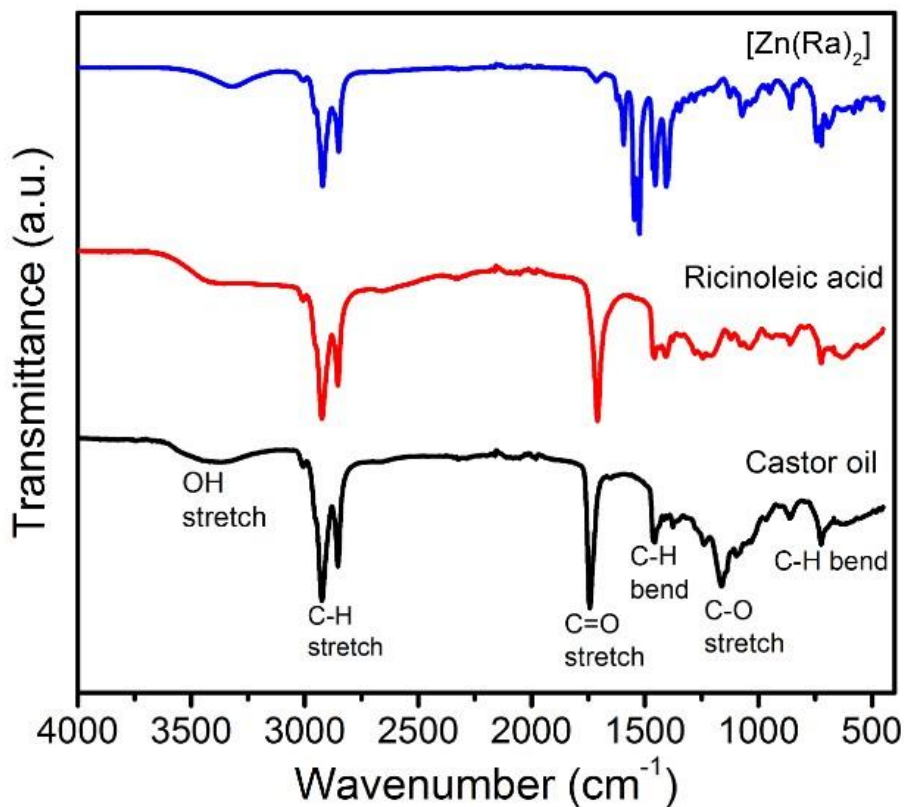


Figure 4.3.1: FT-IR spectra of castor oil, ricinoleic acid and zinc diricinoleate complex,  $[\text{Zn}(\text{Ra})_2]$

The characteristic IR bands for asymmetric and symmetric vibrations in metal carboxylates ( $\nu(\text{COO}^-)$ ) are in the range of  $1650 - 1510 \text{ cm}^{-1}$  and  $1400 - 1280 \text{ cm}^{-1}$  respectively. Thus, the bands in the region  $1300 - 1700 \text{ cm}^{-1}$  can be used to indicate the metal coordination mode (Figure 4.3.2). When the position and separation ( $\Delta$ ) of  $\nu(\text{COO}^-)$  bands is  $\Delta > 200 \text{ cm}^{-1}$ , a unidentate ligand is expected and when  $\Delta < 100 \text{ cm}^{-1}$ , then a bidentate ligand is expected (Bronstein et al., 2007).

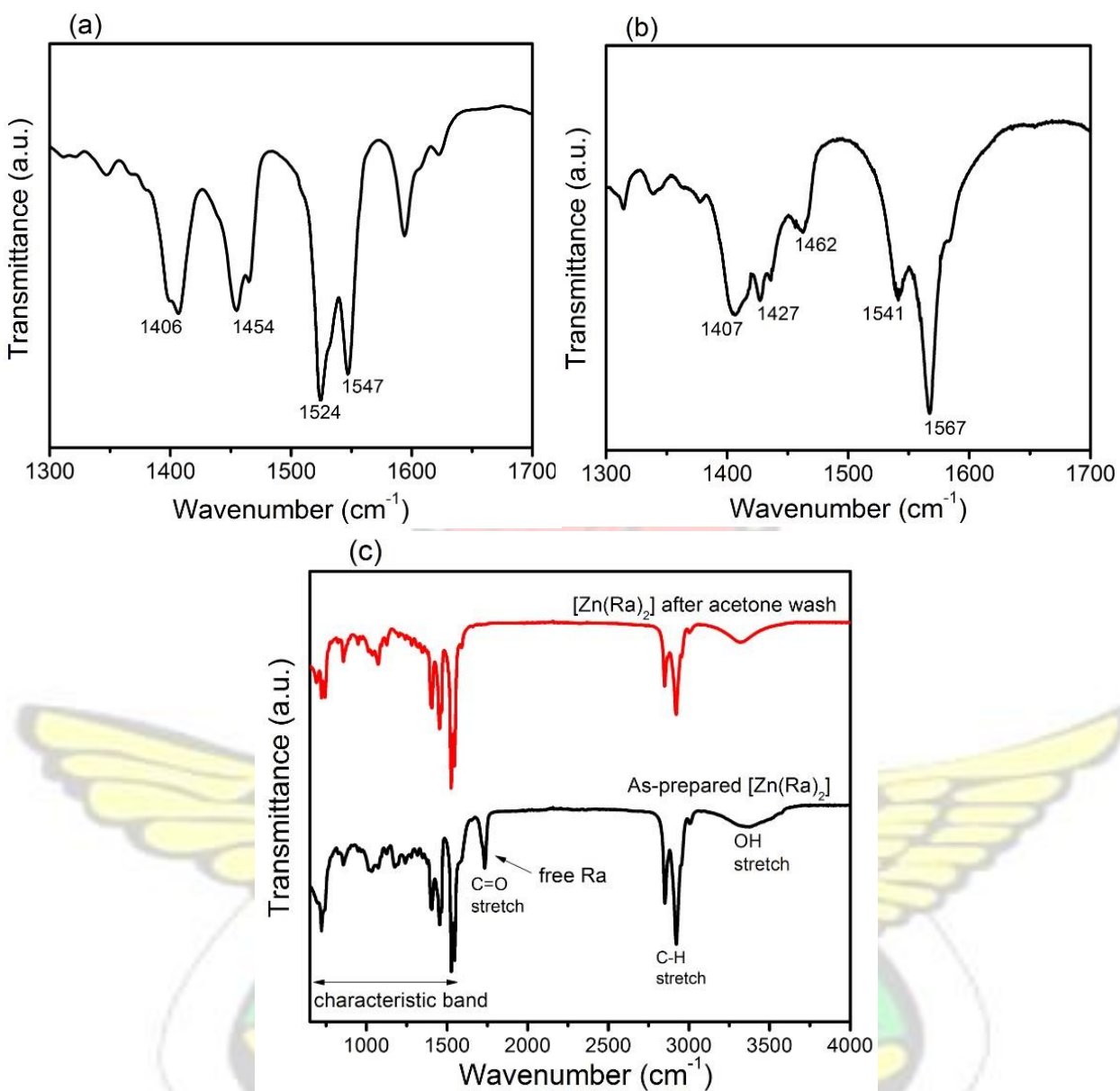


Figure 4.3.2: Characteristic FT-IR spectra ( $\nu(\text{COO}^-) = 1300 - 1700 \text{ cm}^{-1}$ ) of (a)  $[\text{Zn}(\text{Ra})_2]$  and (b)  $[\text{Mn}(\text{Ra})_2]$  indicating a bidentate coordination mode in the carboxylate complexes, and (c) FT-IR of  $[\text{Zn}(\text{Ra})_2]$  showing the effect of washing the complexes with acetone

From Figure 4.3.2, the difference between the characteristic bands at  $1524 \text{ cm}^{-1}$  and  $1454 \text{ cm}^{-1}$  for  $[\text{Zn}(\text{Ra})_2]$  is  $70 \text{ cm}^{-1}$  indicating a bidentate coordination mode (Figure 4.3.2(a)). Similarly, the difference between the characteristic bands at  $1541 \text{ cm}^{-1}$  and  $1462 \text{ cm}^{-1}$  for  $[\text{Mn}(\text{Ra})_2]$  is  $79 \text{ cm}^{-1}$

indicating a bidentate coordination mode (Figure 4.3.2(b)). Thus, the ricinoleic acid binds to the Zn and Mn metal ions in a bidentate coordination mode fashion. This means that each metal ion is bonded to two molecules of ricinoleic acid.

The  $[\text{Zn}(\text{Ra})_2]$  was waxy after preparation but when washed with acetone and vacuum dried, the stickiness reduced drastically which was indicated by the FTIR spectra in Figure 4.3.2(c). The waxy nature was due to excess ricinoleic acid present in the precursor and after washing with acetone the excess acids were removed. However, when the excess ricinoleic acid in  $[\text{Mn}(\text{Ra})_2]$  was extracted with acetone, its waxy nature remained indicating perhaps strong attachment of the free acid to the Mn ion. In nanocrystals synthesis, these free acids can act as extra capping agents.

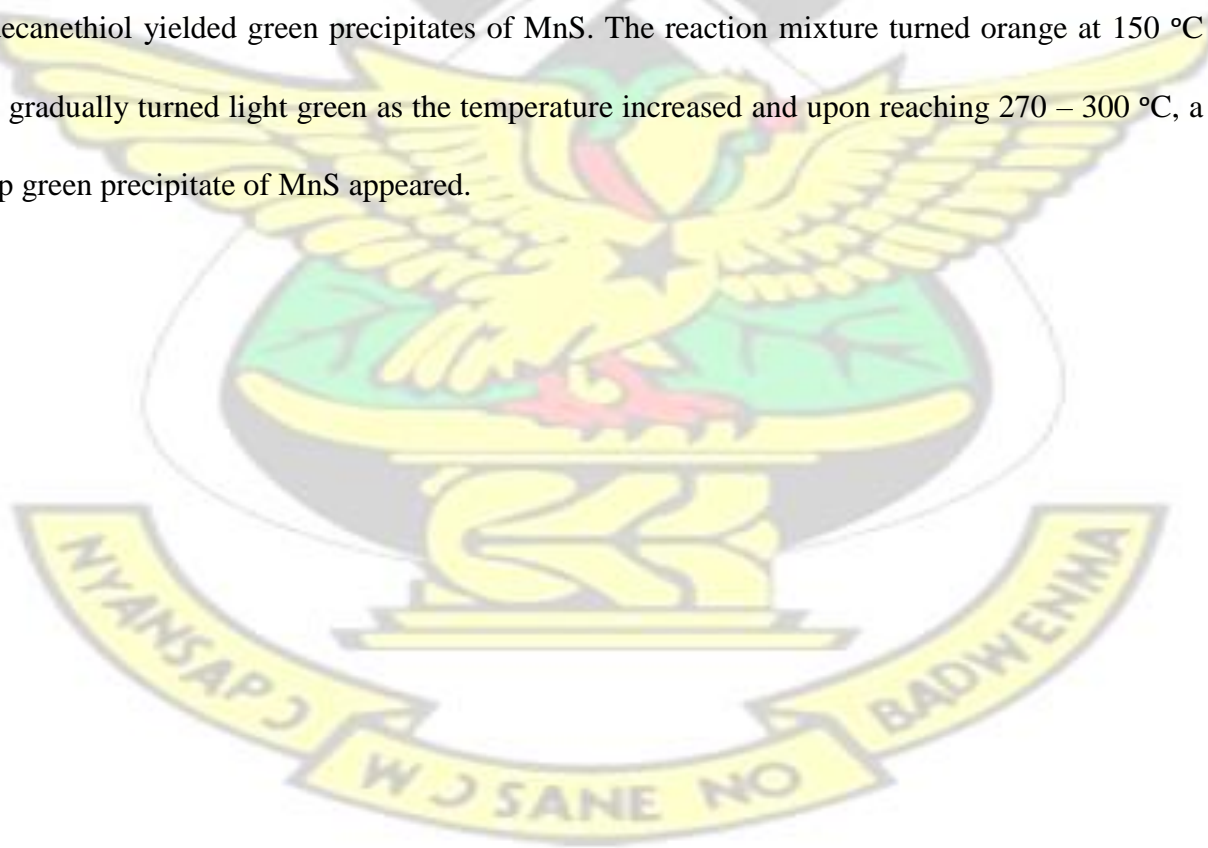
The mass spectra of  $[\text{Zn}(\text{Ra})_2]$  showed molecular ion peak at  $m/z [\text{M}^+] = 659.4$  amu and base peak at 297.3 amu. The molecular ion and base peaks found for  $[\text{Mn}(\text{Ra})_2]$  were  $m/z [\text{M}^+] = 650.5$  amu and 297.2 amu respectively. Ricinoleic acid has a molecular mass of 298.5 g/mol and reduces to 297.5 g as it binds with the metal ion through the  $\text{COO}^-$ . The 297.3 amu and 297.2 amu base peaks found in the mass spectra for  $[\text{Zn}(\text{Ra})_2]$  and  $[\text{Mn}(\text{Ra})_2]$  respectively confirmed the coordination mode of ricinoleic acid to the metal ions in the complexes.

#### 4.3.2.2 Syntheses and composition of Mn-doped ZnS nanocrystals

The  $\text{Mn}_x\text{Zn}_{1-x}\text{S}$  nanocrystals were synthesized by loading the respective amounts of  $[\text{Zn}(\text{Ra})_2]$  and  $[\text{Mn}(\text{Ra})_2]$  into the reaction solvent system (oleylamine/ dodecanethiol (1:1)) and decomposing thermally at 300 °C. The resultant precipitates were white and upon drying turned to crystalline yellowish brown materials. The expected dopant concentration was calculated based on the ratios of Mn to Zn in the complexes (3) and (4). The expected and found (by EDX and ICP-OES) dopant

concentrations in the  $Mn_xZn_{1-x}S$  nanocrystals are shown in Figure 4.3.3(a). The combination of ICP-OES and EDX techniques gave very convincing results. The dopant concentrations determined by EDX correlate closely to the concentrations determined by ICPOES ( $R^2 = 0.999$ ) (Figure 4.3.3(b)). The average doping efficiency was calculated to be 52 %. This implies that per the synthesis technique employed, only about half of the Mn in the feed gets incorporated into the ZnS nanocrystals. However, to confirm the effect of  $Mn^{2+}$  on the crystal lattice structure of the ZnS host, p-XRD patterns of the undoped and doped nanocrystals were collected.

For comparison, undoped ZnS and MnS nanocrystals were synthesized. Unlike the  $[Zn(Ra)_2]$ , the  $[Mn(Ra)_2]$  gave a transient green colour upon interaction with the dodecanethiol in the reaction mixture at room temperature. The thermal decomposition of  $[Mn(Ra)_2]$  in oleylamine containing dodecanethiol yielded green precipitates of MnS. The reaction mixture turned orange at 150 °C and gradually turned light green as the temperature increased and upon reaching 270 – 300 °C, a deep green precipitate of MnS appeared.



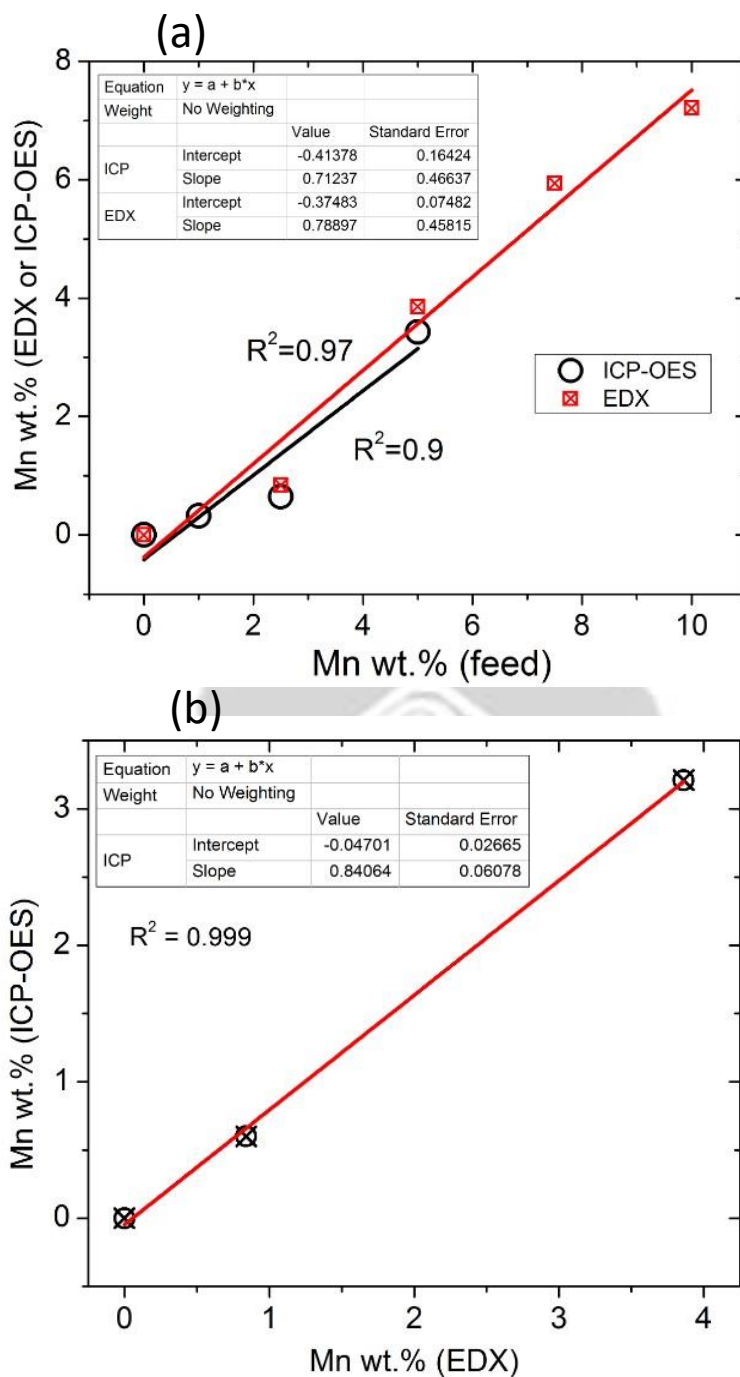


Figure 4.3.3: Plot of Mn wt.% found in elemental analyses of  $Mn_xZn_{1-x}S$  ( $0 \leq x \leq 0.1$ ) nanocrystals produced by colloidal thermolysis at 300 °C by (a) EDX and ICP-OES spectroscopies as a function of varying Mn wt.% in the colloidal thermolysis feed, (b) plot showing correlation of Mn wt.% determine by EDX and ICP-OES

### 4.3.2.3 XRD measurements on ZnS, MnS and $Mn_xZn_{1-x}S$

The p-XRD patterns for the ZnS, MnS and  $Mn_xZn_{1-x}S$  nanocrystals are shown in Figure 4.3.4. The diffraction pattern for the synthesized ZnS is in good agreement with a face-centered cubic  $\beta$ -ZnS sphalerite (zinc blende).

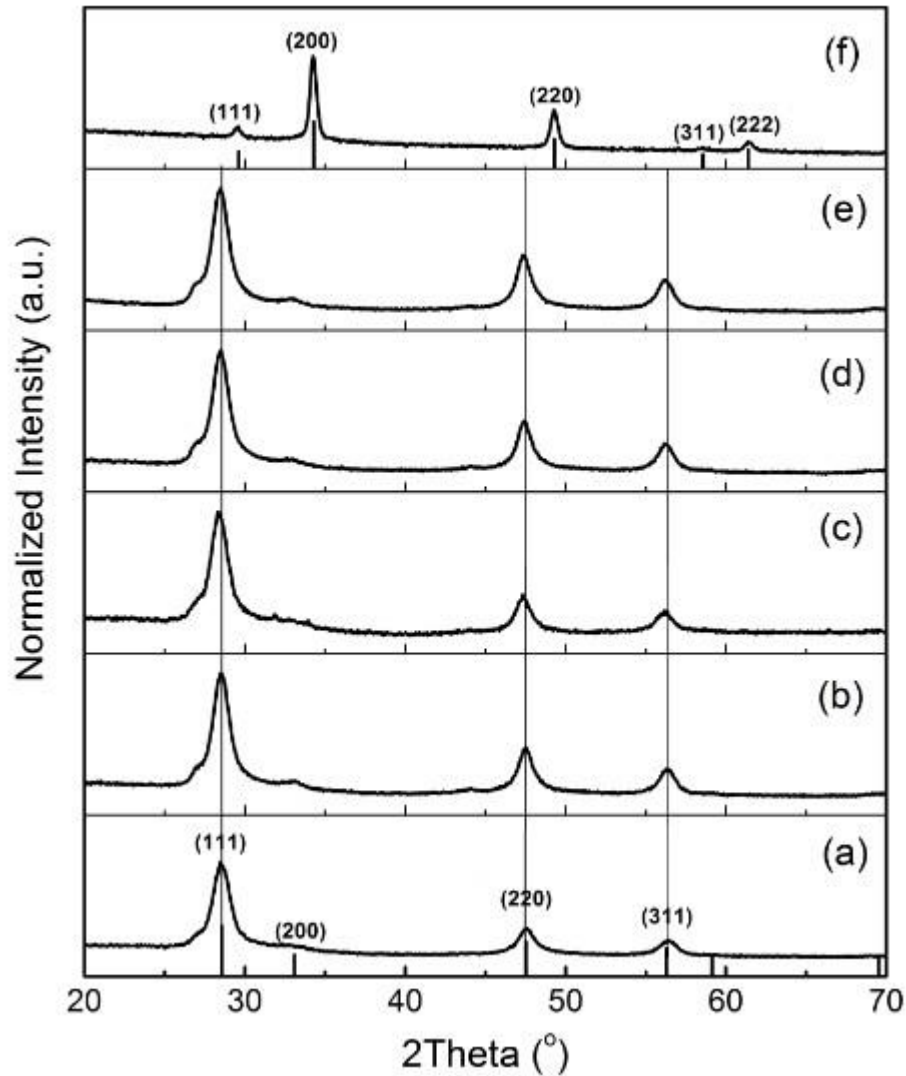


Figure 4.3.4: p-XRD patterns of (a) ZnS, (b-e)  $Mn_xZn_{1-x}S$  where  $x$  is equal to (b) 0.0085, (c) 0.0386, (d) 0.0594, (e) 0.0721 and (f) MnS nanocrystals obtained by decomposing diricinolate carboxylate precursors in oleylamine/dodecanethiol at 300 °C for 1 hour.

A molecular structure of a unit cell of a face-centered cubic ZnS sphalerite is shown in Figure 4.3.5((a) and (b)). Each zinc atom is bonded to four sulphur atoms and vice versa.

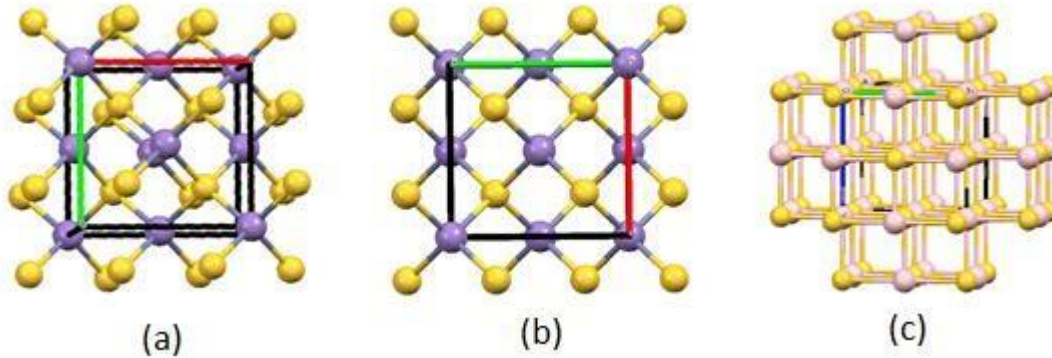


Figure 2.3.5: Molecular structures of face-centered cubic ZnS (sphalerite) unit cell (a) in 3dimensional and (b) in 2-dimensional crystal structures, and (c) rocksalt structure of MnS (alabandite). The violet, yellow and pink balls are zinc, sulphur and manganese atoms respectively.

The p-XRD pattern showed three distinct peaks at  $2\theta$  values of  $28.46^\circ$ ,  $47.62^\circ$  and  $56.51^\circ$  for  $hkl$  (111), (220) and (311) planes of ZnS. The lattice parameter ( $a$ ) was calculated using equation (4.3.1).

$$a = \sqrt{d^2(h^2 + k^2 + l^2)} \quad (4.3.1)$$

where the  $d$  is the d-spacing. The lattice parameter values were obtained as average for  $hkl$  (111), (220) and (311) planes. The lattice parameter calculated for the as synthesized ZnS was  $5.409 \pm 0.015 \text{ \AA}$  which agrees with  $5.4093 \text{ \AA}$  for synthetic sphalerite ZnS reported by Skinner, (1961) in the American Mineralogist Crystal Structure Database (AMCSD 0000110). The pattern for the as synthesized MnS is in good agreement with alabandite mineral with a rocksalt structure (AMCSD 0007512) (Figure 4.3.5(c)). The p-XRD pattern showed four distinct peaks at  $2\theta$  values of  $29.56^\circ$ ,  $34.24^\circ$ ,  $49.28^\circ$  and  $61.41^\circ$  for  $hkl$  (111), (200), (220) and (222) planes of MnS.

The lattice parameter for the MnS was  $5.227 \pm 0.005 \text{ \AA}$  which is close to  $5.2245 \text{ \AA}$  for a standard alabandite (AMCSD 0007512). The unit cell volumes of the sphalerite ZnS and alabandite MnS are  $158.25 \text{ \AA}^3$  and  $142.81 \text{ \AA}^3$  respectively. The broadened diffraction peaks suggest that the sizes of the particles obtained were in nano-sizes.

The Scherer crystallite sizes and the strain in the nanocrystals were calculated using equation 4.3.2 (Kripal et al., 2010):

$$B \cos \theta = \frac{k\lambda}{L} + \eta \sin \theta \quad (4.3.2)$$

where  $B$  is the full-width-half-maximum (FWHM) in radian,  $\theta$  is the diffraction/ Bragg angle (in degrees),  $k$  is a constant or the shape factor,  $\lambda$  is the wavelength of the X-rays,  $L$  is the average crystallite size and  $\eta$  is the strain in the material. A plot of  $B \cos \theta$  against  $\sin \theta$  yield a linear plot of which the intercept is equal to  $k\lambda/L$  and the slope is equal to  $\eta$ . The crystallite sizes obtained for ZnS and MnS nanocrystals were 5.78 nm and 21.5 nm respectively. Choi and coworkers (2009) obtained particles sizes of 10 nm and 11 nm for an oleic acid capped ZnS and MnS nanocrystals from the thermolysis of metal-oleate complexes at  $310 \text{ }^\circ\text{C}$  and  $280 \text{ }^\circ\text{C}$  respectively in oleylamine/dodecanethiol (1:1). Patel et al., (2012) obtained particle size of 7 nm for an oleic acid capped ZnS by reacting zinc acetate dihydrate with oleic acid and thioacetamide in hexane at  $140 \text{ }^\circ\text{C}$ .

The estimated crystallite size, strain, lattice parameter and agglomeration number (number of primary particles per dot) of  $\text{Mn}_x\text{Zn}_{1-x}\text{S}$  are shown in Table 4.3.1.

Table 4.3.1: Structural properties of as synthesized ZnS and  $\text{Mn}_x\text{Zn}_{1-x}\text{S}$

Sample	Crystallite size (nm)	Strain	Lattice Parameter (Å)	Agglomeration number (n)	
				Zn	Mn
ZnS	5.78	-0.1114	5.4092	2555	0
Mn <sub>0.0032</sub> Zn <sub>0.9968</sub> S	5.65	-0.2256	5.4131	2368	8
Mn <sub>0.0084</sub> Zn <sub>0.9916</sub> S	5.94	-0.1328	5.4139	2740	23
Mn <sub>0.0386</sub> Zn <sub>0.9614</sub> S	5.58	-0.192	5.4208	2193	88
Mn <sub>0.0594</sub> Zn <sub>0.9406</sub> S	5.76	-0.1769	5.4229	2358	149
Mn <sub>0.0721</sub> Zn <sub>0.9279</sub> S	5.93	-0.149	5.4241	2540	197

The negative strain indicates a compressive strain in the Mn<sub>x</sub>Zn<sub>1-x</sub>S nanocrystals (Kripal et al., 2010). Each nanoparticle was formed by agglomeration of basic units or molecules of ZnS. For a perfect spherical particle with a face centered cubic arrangement, the agglomeration number ( $n$ ) is calculated using equation (4.3.3) (Mehta et al., 2009)

$$n = \frac{16\pi r^3}{3a^3} \quad (4.3.3)$$

where  $r$  and  $a$  are the radius and lattice parameter respectively. The estimated number of particles (agglomeration number) per ZnS dot ranges between 2281 - 2740. The number of Mn particles per ZnS dot ranges between 8 – 197 for Mn(II) dopant concentration of 0.32 % to 7.21 %. However, the observed p-XRD patterns for the Mn(II) doped ZnS did not change compared to the parent host pattern. No extra diffraction peak for MnS up to 7.21 % Mn(II) dopant. An appreciable shift in the lattice parameter of the doped materials was seen as the dopant concentration increased (Figure

4.3.6). There was a slight change in the crystallite size of the  $Mn_xZn_{1-x}S$  with doping (Table 4.3.1).

The mean crystallite size was calculated to be 5.77 nm.

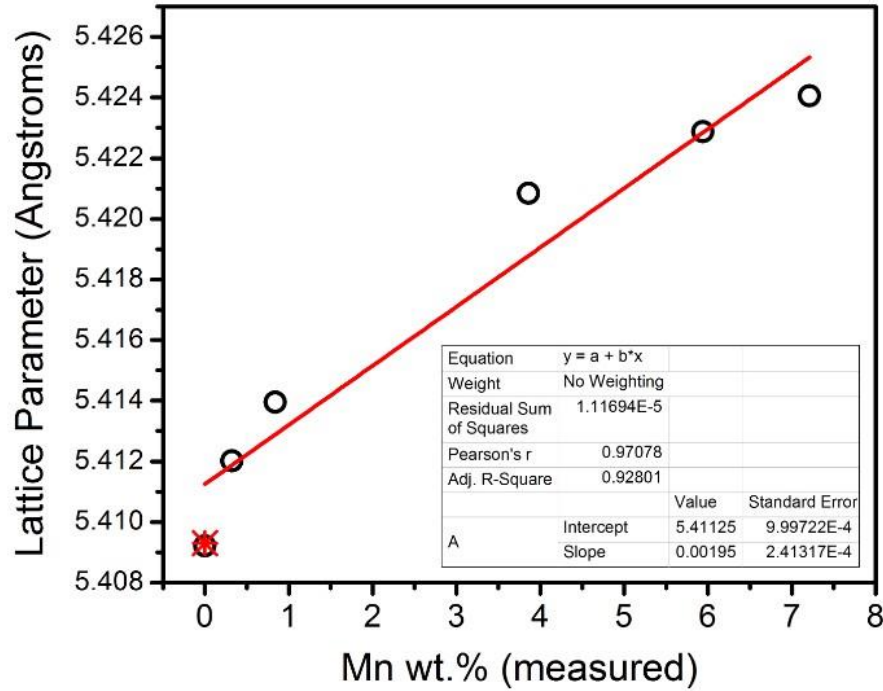


Figure 4.3.6: Lattice parameter measured by p-XRD against increasing Mn wt.% (measured) in ZnS. Bullet in red is the standard lattice parameter for sphalerite ZnS (AMCSD 0000110).

#### 4.3.2.4 Morphology of undoped ZnS and Mn-doped ZnS

The TEM images of the undoped ZnS and  $\text{Mn}_{0.0386}\text{Zn}_{0.9614}\text{S}$  nanocrystals and their particles size distribution histograms are shown in Figure 4.3.7(a, b, c and d).

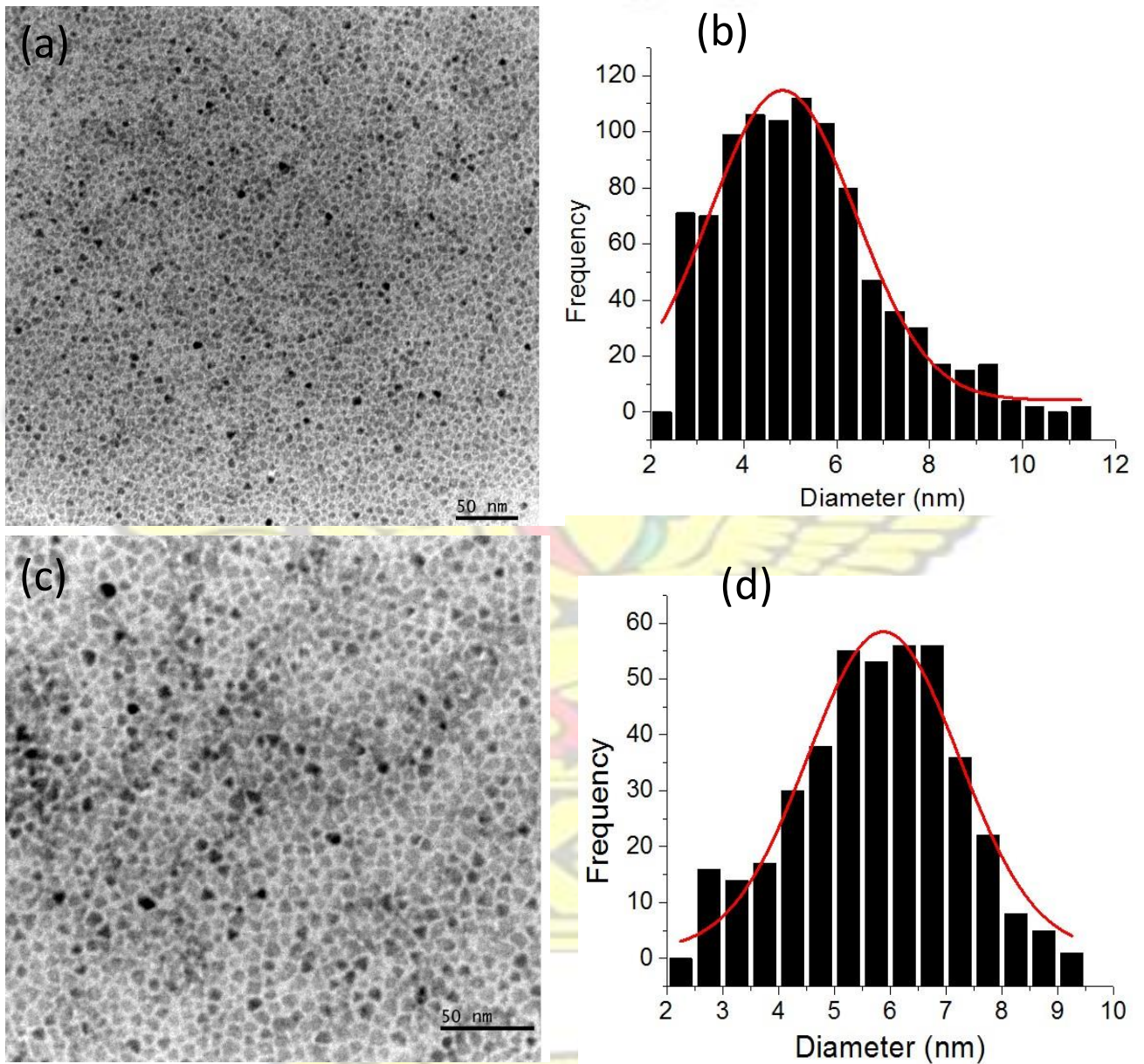


Figure 4.3.7: TEM images of (a) undoped ZnS nanocrystals and its (b) particles size distribution histogram, (c)  $\text{Mn}_{0.0386}\text{Zn}_{0.9614}\text{S}$  nanocrystals and its (d) particles size distribution histogram

The image analyses of the particles size and size distributions were obtained using imageJ software package. The TEM images show that the particles have near-spherical shapes. The shape of particles obtained for undoped ZnS nanocrystals are similar to those obtained for the doped ZnS nanocrystals. From the TEM images, it could be ascertained that the nanocrystals sizes for both samples were uniformly distributed. The average particle size of the undoped ZnS nanocrystals was calculated to be  $4.84 \pm 1.56$  nm and the polydispersity was 32.18 %. This implied that about 67.8 % of the nanocrystals had sizes close to the mean particle size. The average particle size for the doped ZnS nanocrystals was  $5.88 \pm 1.35$  nm and the polydispersity was 23.06 %, implying that the particles were 76.94 % monodispersed. The average particles size calculated confirmed the Scherer calculated crystallite size of 5.58 nm obtained from the XRD pattern for  $Mn_{0.0386}Zn_{0.9614}S$ . The average nanoparticle sizes obtained agree with the 5.1 nm reported by both Sooklal et al., (1996) and Suyver et al., (2001) for  $Mn_xZn_{1-x}S$  synthesized via co-precipitation of  $Zn^{2+}$ ,  $Mn(II)$  and  $S^{2-}$  ions from aqueous solutions of nitrate and acetate metal salts and sodium sulphide at room temperature.

#### **4.3.2.5 Optical properties of undoped ZnS and Mn-doped ZnS**

The absorption spectra of the as-synthesized undoped ZnS and  $Mn_xZn_{1-x}S$  nanocrystals are shown in Figure 4.3.8(a). The inserts are Tauc's plot showing extrapolation to determine the band gap energy of the absorbing material. The band gap energy of bulk sphalerite ZnS is reported to be 3.6 eV (Zhu et al., 2003). The band gap energy of the synthesized undoped ZnS nanocrystals in this study was found to be 3.67 eV which is about 2 % higher than that of the bulk, and suggest some

level of quantum confinement. Mehta et al., (2009), similarly obtained a band gap energy of 3.88 eV for cetyltrimethylammonium bromide (CTAB) capped ZnS

synthesized by reacting zinc acetate and sodium sulphide in double distilled water at 25 °C.

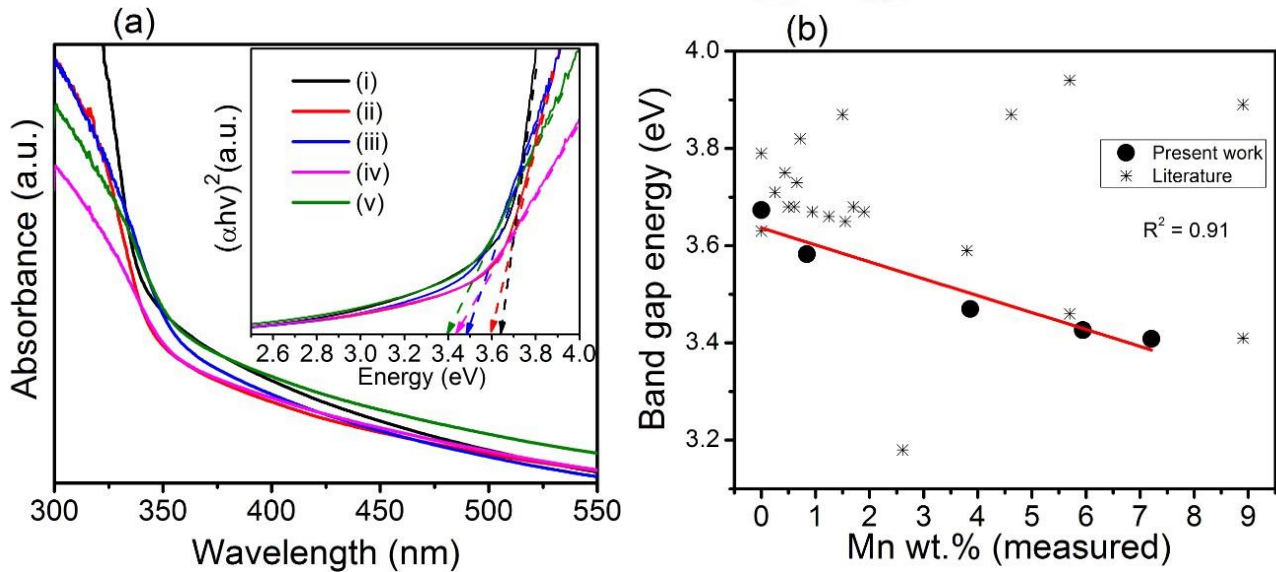


Figure 4.3.8: (a) Absorption spectra of (i) ZnS, (ii)  $\text{Mn}_{0.0084}\text{Zn}_{0.9916}\text{S}$ , (iii)  $\text{Mn}_{0.0386}\text{Zn}_{0.9614}\text{S}$ , (iv)  $\text{Mn}_{0.0594}\text{Zn}_{0.9406}\text{S}$  and (v)  $\text{Mn}_{0.0721}\text{Zn}_{0.9279}\text{S}$ . (Insert is Tauc's plot used in estimating the band gap energy). (b) Plot showing changes in band gap energy with increasing Mn dopant concentration: band gap energies obtained in the present work (●) and literature (\*).

The local effect of the Mn(II) ions has been explained by Sooklal et al., (1996) to be caused by the introduction of a triplet state into the energy band gap of the ZnS. The triplet state is formed as a result of the parallel spins of the Mn(II) impurity introduced into the ZnS host (Figure 4.3.9 for electronic configuration of Mn(II)). Generally, triplet states lie lower in energy than singlet states.

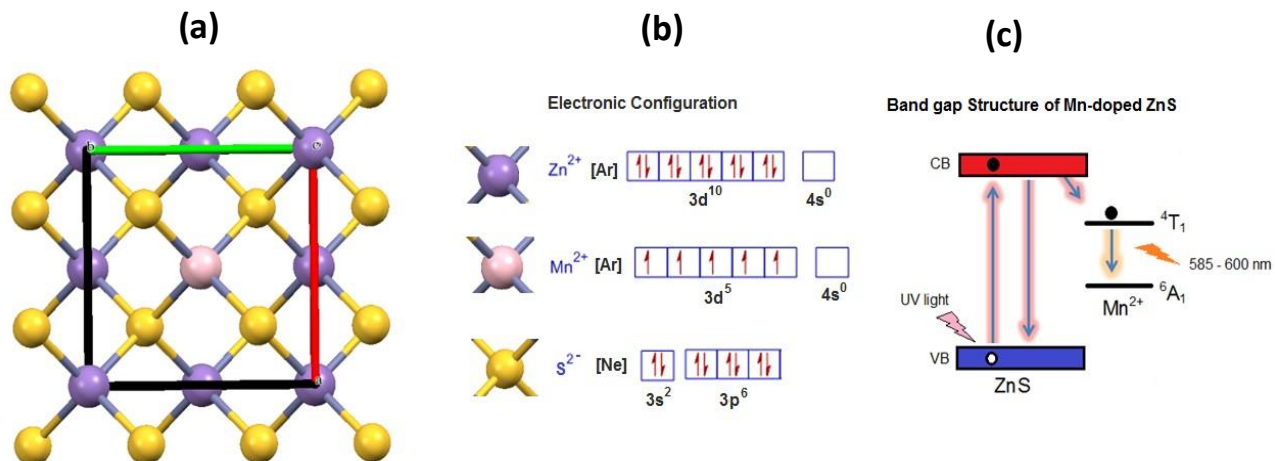


Figure 4.3.9: (a) Molecular representation of unit cell crystal structure of sphalerite ZnS with one Zn<sup>2+</sup> replaced with Mn<sup>2+</sup>, (b) electronic configuration of Zn<sup>2+</sup>, Mn<sup>2+</sup> and S<sup>2-</sup> (c) band structure of Mn<sub>x</sub>Zn<sub>1-x</sub>S

In this work, the band gap energy of the ZnS was found to decrease with increasing Mn dopant concentration (Figure 4.3.8(b)). The percentage reduction in the band gap energy with 7.21 % Mn dopant was calculated to be 7.8 % from the undoped ZnS nanoparticles. Joicy et al., (2014) similarly observed a reduction of the band gap energy of ZnS up to the tune of about 6.7 % with increasing Mn dopant concentration (up to 10 %). Various other studies have reported band gap changes on the doping of ZnS with Mn(II), these are compared to the band gap changes obtained in this work (Figure 4.3.8(b)). The reduction in band gap energy can be attributed to the Mn<sup>2+</sup> infusion into the crystal lattice of the ZnS host nanocrystals.

To study the Mn(II) in the host lattice of ZnS, photoluminescence (PL) and electron paramagnetic resonance (EPR) spectra were recorded. These two techniques have been used to probe the location of the Mn(II) in ZnS host lattice, either in lattice/substitutionary site or on the surface of the nanocrystals. The Mn(II) ion in a Zn<sup>2+</sup> lattice site in the host lattice leads to the <sup>4</sup>T<sub>1</sub> ← <sup>6</sup>A<sub>1</sub> of the

isolated Mn(II) ion. On photo-excitation, an electron is promoted from the valence band to the conduction band of the ZnS. This excited electron subsequently decays via a nonradiative recombination process to some surface or defect site or is captured by the Mn(II) ion in its  $^4T_1$  state after which it decays radiatively to the  $^6A_1$  state. The emission from the  $^4T_1 \leftarrow ^6A_1$  transition appears at 585 – 600 nm in the PL spectra of  $Mn_xZn_{1-x}S$  nanocrystals (Cao et al., 2009; Deng et al., 2011; Geng et al., 2004; Srivastava et al., 2010; Whiffen et al., 2014). The emission has also been reported at 510 nm (Malik et al., 2001). The PL spectra of the as synthesized  $Mn_xZn_{1-x}S$  nanoparticles are shown in Figure 4.3.10.

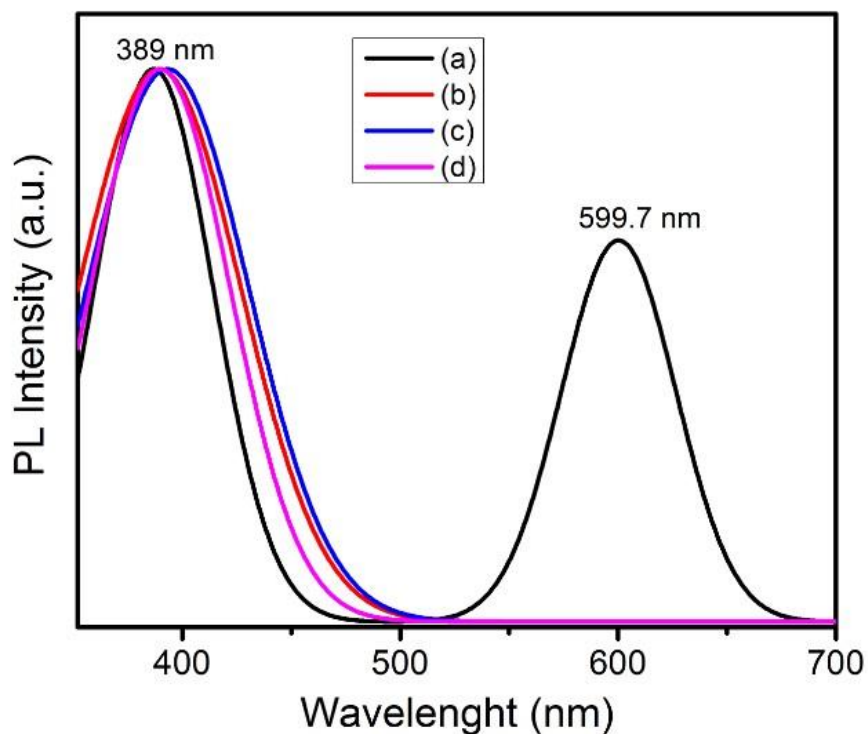


Figure 4.3.10: PL spectra showing the luminescence of the  $Mn_xZn_{1-x}S$  nanoparticles where x is equal to (a) 0.0084, (b) 0.0386, (c) 0.0594, (d) 0.0721

In toluene, emissions at 389 nm and 599.7 nm are seen as in the  $Mn_{0.0084}Zn_{0.9916}S$  nanocrystals.

The 389 nm emission is associated with the ZnS (Chen et al., 2000). The 599.7 nm emission can

be attributed to the expected  ${}^4T_1 \leftarrow {}^6A_1$  transition of Mn(II) in the ZnS host lattice. Joicy et al., (2014) and O'Brien and coworkers, (2001) observed similar emission at 582 nm and 510 nm respectively. However, this emission was not observed in the  $Mn_xZn_{1-x}S$  samples with higher dopant concentrations ( $\geq 0.01$ ). Photoluminescence in the highly doped samples were quenched. This can be attributed to an exchanged-coupled  $d^{10}$ -electron system arising from the dipole-dipole interaction between Mn(II) ions which induces fast decay of the  ${}^4T_1 \leftarrow {}^6A_1$  transition (Beermann et al., 2006; Jindal and Verma, 2008). Borse et al., (1999) also attributed photoluminescence quenching to (i) isolated Mn ions at the surface or occupying interstitial location with octahedral symmetry, (ii) Mn-Mn dipolar interactions, and (iii) exchange-coupled Mn clusters. Thus, incorporation or diffusion of Mn(II) into ZnS host lattice seems to be efficient at lower dopant concentrations.

To further study whether the Mn(II) ions occupied lattice sites or the surface or interstitial positions in the ZnS nanocrystals, the EPR spectra of the undoped ZnS, 0.1 % (feed), 0.32 %, 0.84 % and 7.21 % Mn-doped ZnS were obtained (Figure 4.3.11). The Mn(II) ions occupying an isolated substitutionary site in a cubic ZnS lattice, a characteristic six hyperfine line (sextet) is expected. Mn(II) has a half-filled d-shell ( $3d^5$ ) with spin quantum number (S) of 5/2 and angular momentum (L) of zero (0) (Figure 4.3.9). However, the EPR spectra obtained for the undoped ZnS nanocrystals showed six EPR lines which may be ascribed to defect centers due to vacancies or dangling bonds which are intrinsically present in ZnS and are detectable by EPR (Kaftelen et al., 2013). The EPR of the 0.1 % Mn-doped ZnS nanocrystals also showed a sextet similar to the undoped ZnS. The ICP-OES showed no Mn present in the 0.1 % Mn-doped ZnS sample. On increasing the concentration of Mn to 0.32 % in ZnS, a well separated six hyperfine lines of EPR spectra was observed which provides a clear evidence of Mn(II) incorporation into  $Zn^{2+}$

substitutionary sites in ZnS lattice. As the Mn concentration was increased to 0.84 %, broadening of the EPR line evolved and further increment to 7.21 % the six hyperfine lines spectrum converged to a single broad peak. The broadening of the EPR spectrum has been observed on samples containing high concentrations of Mn dopant (Borse et al., 1999). This single broad peak has been attributed to Mn(II) ions occupying surface/interstitial locations or as a result of persistent strong Mn-Mn dipole-dipole interactions (Borse et al., 1999; Kaftelen et al., 2013).

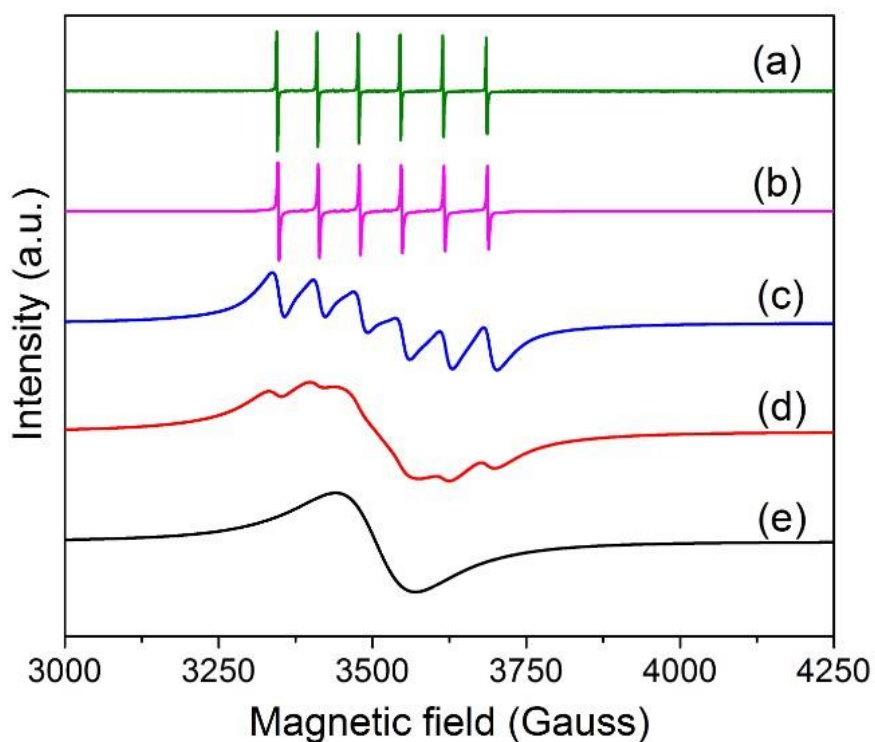
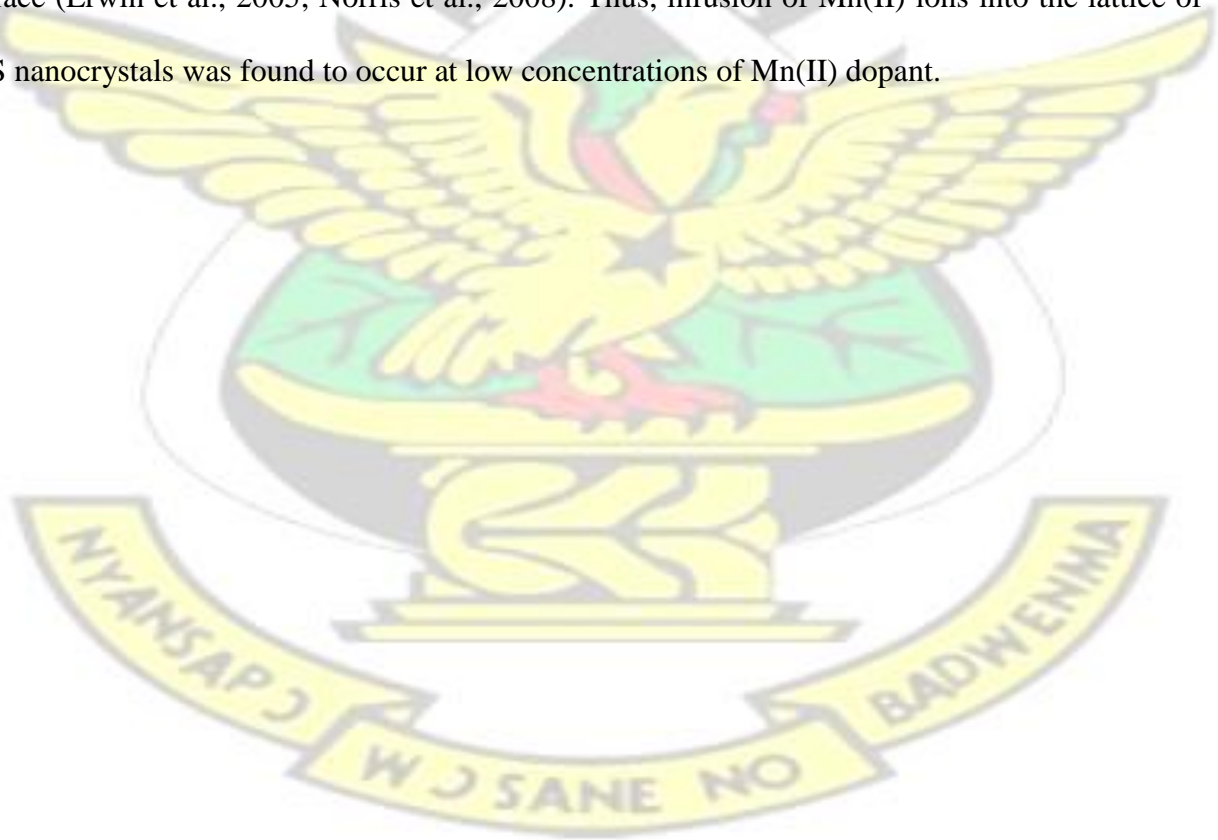


Figure 4.3.11: EPR spectra of (a) undoped ZnS, (b) 0.1 % (feed), (c) 0.32 %, (d) 0.84 % and (e) 7.21 % Mn-doped ZnS nanocrystals produced by thermolysis of diricinoleate carboxylates in oleylamine/dodecanethiol at 300 °C for 1 hour.

EPR spectra show that at higher Mn dopant concentrations, some ZnS nanocrystals maybe doped with more than a single Mn(II) ion whereas some have their surfaces/interstitial positions occupied with high concentrations of Mn(II) such that Mn-Mn dipole-dipole interactions dominates the EPR

signal. The estimated average number of primary particles (agglomeration number) per ZnS dot was 2537. The Mn(II) particles found in the 0.32 % Mn-doped ZnS was 8 which increased to 23 with 0.83 % Mn(II) doping. At higher Mn(II) doping ( $\geq 3.9$  %), the number of Mn(II) particles increased to  $\geq 88$  per dot (Table 4.3.1). The broadening of the EPR peak occurred when the agglomeration number of Mn(II) particles reached 23 per ZnS dot (Table 4.3.1 and Figure 4.3.11). This observation can be explained by a „self-purification“ model where the mode of Mn(II) diffusion is thermodynamically controlled (Norris et al., 2008). The „self-purification“ model asserts that for thermodynamic reasons, the dopants are expelled to the surface of the nanocrystals due to their low solubility in the host lattice. The diffusion of Mn(II) ions into lattice sites in II-VI semiconductors has been reported to be negligible but faster at the surface (Erwin et al., 2005; Norris et al., 2008). Thus, infusion of Mn(II) ions into the lattice of ZnS nanocrystals was found to occur at low concentrations of Mn(II) dopant.



### 4.3.3 Summary of main findings

1. Good quality luminescent  $\text{Mn}_x\text{Zn}_{1-x}\text{S}$  nanocrystals were successfully synthesized by the thermal decomposition of diricinoleate carboxylate complexes in oleylamine/ dodecanethiol (1:1) at 300 °C.
2. The p-XRD patterns showed that the synthesized  $\text{Mn}_x\text{Zn}_{1-x}\text{S}$  nanocrystals were sphalerites and the shift in the lattice parameter observed indicated the successful incorporation of the Mn(II) into the ZnS host lattice structure for  $0 \leq x \leq 0.072$ .
3. The band gap energy was found to decrease with increasing Mn(II) dopant which indicated the possible introduction of trap states into the energy band structure of the host ZnS.
4. The  ${}^4\text{T}_1 \leftarrow {}^6\text{A}_1$  emission characteristic of Mn(II) ion incorporation into the ZnS host lattice was observed at 599.7 nm for  $\leq 0.8$  % Mn dopant.
5. EPR studies confirmed the presence of Mn(II) ions in substitutionary sites. At high concentrations of Mn dopant ( $\geq 1$  %), the Mn(II) ions were found to occupy surface/interstitial sites in ZnS.

### 4.4 The Syntheses of Manganese doped Zinc Sulphide ( $\text{Mn}_x\text{Zn}_{1-x}\text{S}$ ) Nanocrystals by the

## Thermal Decomposition of Heterocyclic Dithiocarbamate Single Source Precursors in Oleylamine

# KNUST

### 4.4.1 Introduction

The decomposition of single source precursors (SSPs) in high boiling point organic solvents has become an attractive and innovative route to facile syntheses of good quality crystalline nanomaterials (Afzaal et al., 2007; Nair et al., 2002; Abdelhady et al., 2013; Mlowe et al., 2014; Nyamen et al., 2014). However, the synthesis of Mn-doped ZnS nanocrystals using SSPs is not yet reported. Research efforts had led to obtaining high quality ZnS, PbS and CdS semiconductor nanocrystals by thermal decomposition of heterocyclic dithiocarbamate complexes in coordinating solvents (Nyamen et al., 2014; Mthethwa et al., 2009). The syntheses and thermolyses of bis(tetrahydroisoquinolinyldithiocarbamato)zinc(II) ( $[\text{Zn}(\text{S}_2\text{CN}(\text{thiq}))_2]$ ) and tris(tetrahydroisoquinolinyldithiocarbamato) manganese(III) ( $[\text{Mn}(\text{S}_2\text{CN}(\text{thiq}))_3]$ ) in oleylamine is reported in this thesis. This approach to the syntheses of Mn-doped ZnS yielded comparable good quality and monodispersed nanocrystals.

## 4.4.2 Results and discussions

### 4.4.2.1 Heterocyclic dithiocarbamate complexes of Zn and Mn

The chemistry of heterocyclic dithiocarbamate complexes of Zn(II) and their thermal decomposition to ZnS nanoparticles is well studied (Marcotrigiano et al., 1974; Nyamen et al., 2014; Srinivasan et al., 2009; Srinivasan and Thirumaran, 2014). However, the synthesis of heterocyclic dithiocarbamate complexes of Mn(II) are neglected (Hendrickson et al., 1974). The reason is attributed to the unstable nature of divalent dithiocarbamate complexes of Mn(II) and their readiness to undergo aerial oxidation (Preti et al., 1980). The existence and isolation of yellow divalent dithiocarbamate complexes  $[\text{Mn}(\text{R}_2\text{dte})_2]$  and their ready oxidation to dark-violet trivalent complexes  $[\text{Mn}(\text{R}_2\text{dte})_3]$  have been earlier reported (Hendrickson et al., 1974; Preti et al., 1980). Dithiocarbamate ligands tend to form *tris*-chelated complexes with Mn(II), Mn(III) and Mn(IV) (Hendrickson et al., 1974). In the present work, the heterocyclic dithiocarbamate complexes of  $[\text{Zn}(\text{S}_2\text{CN}(\text{thiq}))_2]$  and  $[\text{Mn}(\text{S}_2\text{CN}(\text{thiq}))_3]$  were prepared in methanol by reacting the synthesized ligand, sodium tetrahydroisoquinoline dithiocarbamate with the respective hydrated divalent metal salts at room temperature conditions. In the solid state, Mn remained as stable Mn(III) dithiocarbamate chelated complex.

The FT-IR spectra of the ligand and the complexes are shown in Figure 4.4.1. The ligand and complexes gave similar FT-IR spectra. All the spectra showed bands at  $1427 - 1367 \text{ cm}^{-1}$  emanating from the C-N bond formed by the reaction of the amine, tetrahydroisoquinoline and carbon disulphide. The ligand showed a broad band at  $2408 - 2897 \text{ cm}^{-1}$  relating to C-H and S-H stretch. The C-H and S-H bands were found at lower intensity in the complexes suggesting a cleavage of the S-H bond to form the metal-sulphur (M-S) bond. The metal cations coordinate with

the ligand through the C=S (C-S) bond connected to the nitrogen atom of the amine. The most significant vibration band relating to N-C=S functional group appeared at 1213 – 925  $\text{cm}^{-1}$  confirming the formation of a dithiocarbamate complex (Sharma et al., 1996, Hall, 1969).

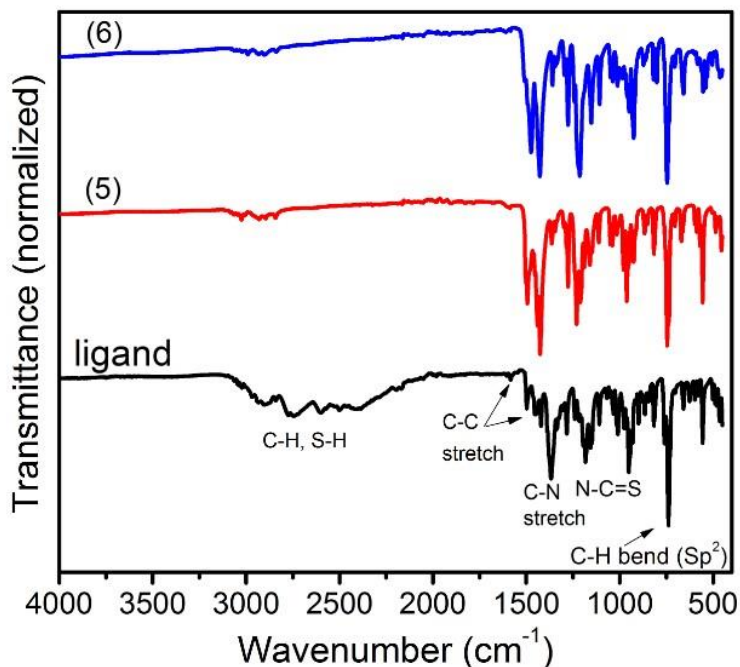


Figure 4.4.1: Comparison of FT-IR spectra of the ligand  $[\text{Na}(\text{S}_2\text{CN}(\text{thiq}))]$  and the complexes  $[\text{Zn}(\text{S}_2\text{CN}(\text{thiq}))_2]$  (5) and  $[\text{Mn}(\text{S}_2\text{CN}(\text{thiq}))_3]$  (6)

The thermal characteristics of the ligand and complexes (5) and (6) in nitrogen atmosphere are shown in the TGA thermographs in Figure 4.4.2. The ligand thermally decomposed in a single step at onset and endset temperatures of 156.14  $^\circ\text{C}$  and 201.30  $^\circ\text{C}$  respectively. The decomposition temperature of the ligand was found to be 188.71  $^\circ\text{C}$ . The ligand completely disappeared at 300  $^\circ\text{C}$  (Figure 4.4.2). However, the decomposition patterns for the two heterocyclic dithiocarbamate complexes appeared entirely different for the different metals (Figure 4.4.2).

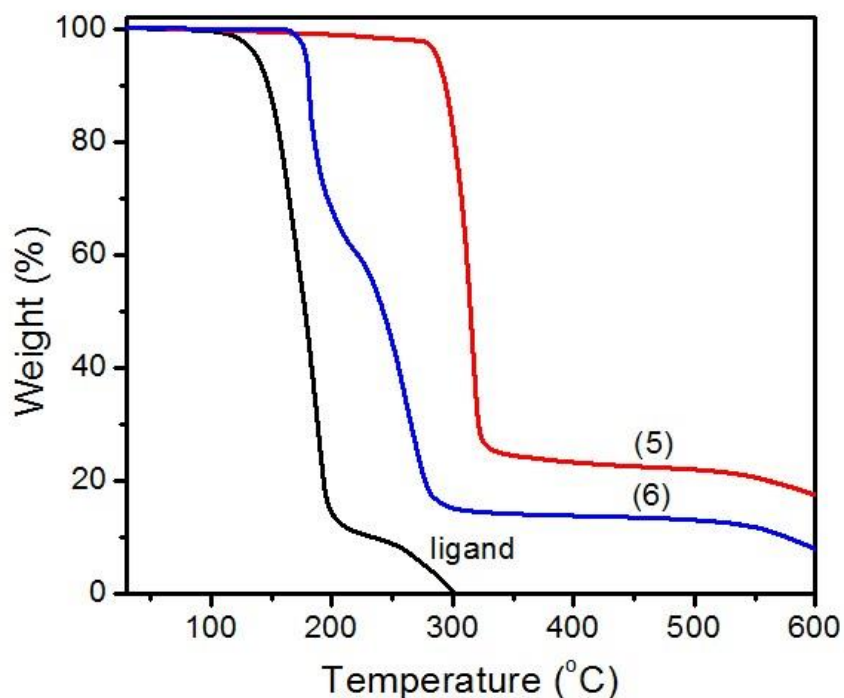


Figure 4.4.2: TGA of the ligand  $[\text{Na}(\text{S}_2\text{CN}(\text{thiq}))]$ , complexes  $[\text{Zn}(\text{S}_2\text{CN}(\text{thiq}))_2]$  (**5**) and  $[\text{Mn}(\text{S}_2\text{CN}(\text{thiq}))_3]$  (**6**) recorded from 30 °C to 600 °C under nitrogen gas, at heating rate of 10 °C  $\text{min}^{-1}$

Complex (5) thermally decomposed in a single step with the loss of the two molecules of the ligands attached to the Zn atom to produce a fairly stable residue. The residue formed was about 25 % (at 338 °C) and 20.65 % (at 550 °C) of the complex. The residue corresponds to ZnS which forms about 20.22 % of complex (5). Complex (5) was fairly stable up to the onset temperature of 300.79 °C. The decomposition and endset temperatures were 316.79 °C and 321.59 °C respectively.

In contrast, complex (6) decomposed in two steps to form a fairly stable residue of MnS. The first and second decomposition temperatures were 180.61 °C (onset 179 °C and endset 198 °C) and

260.41 °C (onset 198 °C and endset 300 °C) respectively. The thermal decomposition of complex (6) occurred with the loss of 30.5 % of it in the first step and 54.95 % in the second step leaving a residue consisting of 12.94 % at 514 °C (Figure 4.4.3). The 12.94 % MnS residue suggests the formation of a tris-dithiocarbamate complex, ( $[\text{Mn}(\text{S}_2\text{CN}(\text{thiq})_3)]$ ). The microelemental analysis obtained for complex (6) was consistent with the observed  $[\text{Mn}(\text{S}_2\text{CN}(\text{thiq})_3)]$  complex.

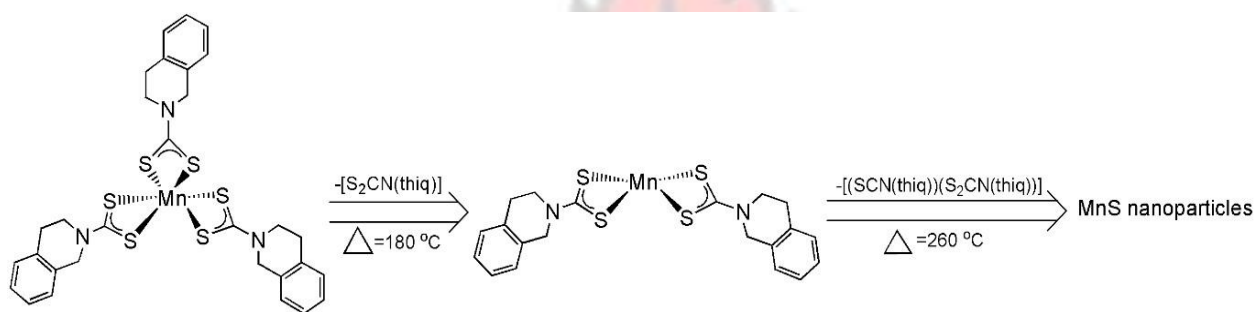


Figure 4.4.3: Thermal decomposition of manganese (III) tris(tetrahydroisoquinolinyl dithiocarbamate), ( $[\text{Mn}(\text{S}_2\text{CN}(\text{thiq})_3)]$ )

#### 4.4.2.2 Syntheses and composition of Mn-doped ZnS nanocrystals

The syntheses of the undoped and doped nanoparticles were carried out using the hot-injection method. Briefly, the complexes were dissolved in oleylamine and swiftly injected into a preheated oleylamine solvent (at 280 °C) to initiate the decomposition to release nuclei for growth of the nanoparticles. Complex (5) decomposed in the oleylamine to form a transparent colourless mixture of ZnS whereas complex (6) decomposed to form a green mixture of MnS. Oleylamine is reported in literature to lower the decomposition temperature of dithiocarbamate complexes (Jung et al., 2010; Hollingsworth et al., 2014). This occurs when oleylamine coordinates to the dithiocarbamate

complex to induce a trans-amidation reaction to replace the secondary amine of the dithiocarbamate complex with oleylamine. The oleylamine then initiates a nucleophilic attack on the most electron-deficient thiocarbonyl carbon of the dithiocarbamate which leads to the decomposition to generate the desired metal sulphide nanoparticles and some decomposition products such as thiourea and hydrogen sulphide (Jung et al., 2010).

Likewise, the Mn-doped ZnS nanoparticles were synthesized by dissolving the respective amounts of complex (5) and (6) into a minimum amount of oleylamine and swiftly injected into a hot oleylamine at 280 °C. The resultant precipitate was white and upon drying turned to crystalline yellowish brown material. The expected dopant concentration was calculated based on the ratios of Mn to Zn in complexes (5) and (6). The expected and found (by EDX and ICPOES) Mn dopant concentrations in the Mn-doped ZnS nanoparticles are shown in Figure

4.4.4(a).

The dopant concentrations determined by EDX correlate closely to the concentrations determined by ICP-OES ( $R^2 = 0.998$ ) (Figure 4.4.4(b)). The average doping efficiency was calculated to be 54 % which showed that about half of the Mn in the feed gets integrated into the ZnS nanoparticles. However, the p-XRD patterns of the undoped and doped nanoparticles were collected to confirm the effect of Mn(II) on the crystal lattice structure of the ZnS host.

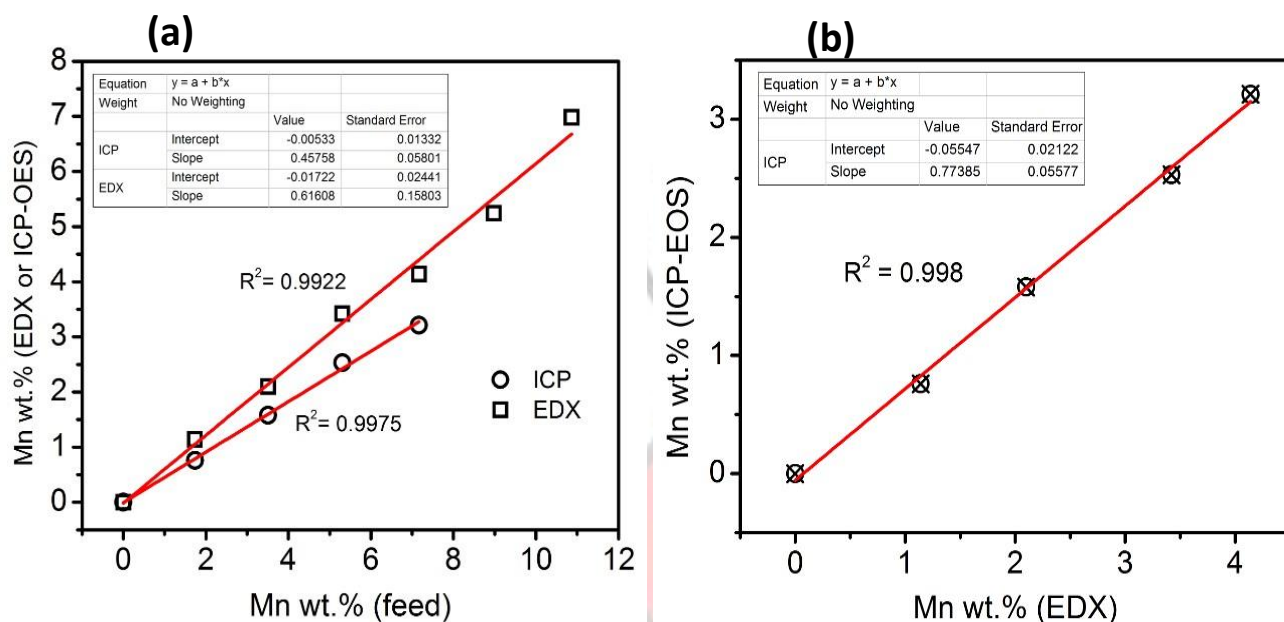


Figure 4.4.4: Plot of wt.% Mn found in elemental analysis of  $Mn_{1-x}Zn_xS$  ( $0 \leq x \leq 0.1$ ) nanoparticles produced by colloidal thermolysis of complexes (5) and (6) at 280 °C by (a) EDX or ICP-OES spectroscopies as a function of varying wt.% of Mn in the colloidal thermolysis feed, (b) plot showing comparison of wt.% of Mn determined by EDX and ICP-OES

#### 4.4.2.3 XRD measurements on ZnS, MnS and $Mn_{1-x}Zn_xS$ nanocrystals

The p-XRD patterns for the ZnS and MnS nanoparticles are shown in Figure 4.4.5. The diffraction pattern for the synthesized ZnS is in good agreement with a face-centered cubic  $\beta$ ZnS with a sphalerite (zinc blende) crystal structure (AMCSD 0000110). The p-XRD pattern showed three distinct peaks at 2 theta values of 28.53°, 47.56° and 56.36° signifying the  $hkl$  (111), (220) and (311) planes in ZnS. The lattice parameter calculated for the ZnS was  $5.408 \pm 0.007$  Å which is close to 5.4093 Å for a standard sphalerite ZnS (AMCSD 0000110).

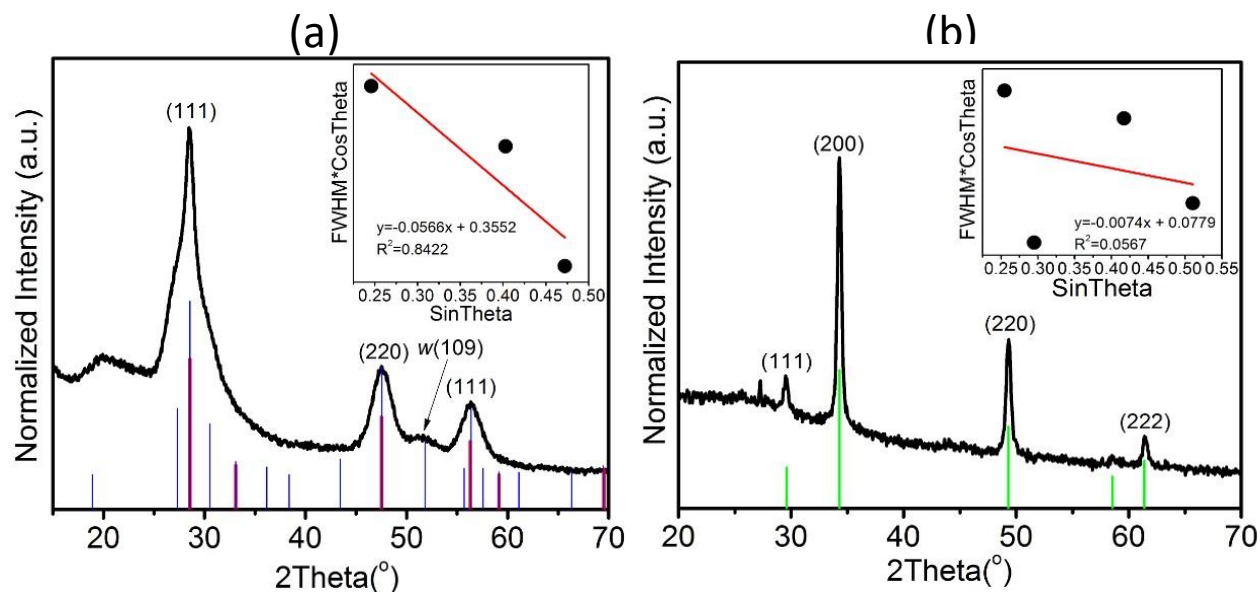


Figure 4.4.5: p-XRD patterns of (a) ZnS and (b) MnS nanoparticles synthesized by thermal decomposition of heterocyclic dithiocarbamate complexes in oleylamine at 280 °C for 1 hour (the insert graph is a plot for estimation of the crystallite size). The red, blue and green lines are standard sphalerite ZnS, wurtzite ZnS and alabardite MnS respectively. *w* represent wurtzite

However, the as synthesized ZnS p-XRD spectrum also bears characteristics of polytypism (that is consisting of different crystal structure phases). The diffraction peak at 2 theta value of 51.7° is characteristic of a wurtzitic ZnS. The broadened diffraction peaks confirms the polytypic nature and also the nanosizes of the synthesized ZnS. The Sherrer crystallite size of the ZnS nanoparticles was estimated to be 3.91 nm which implied that the particles were quantum confined. The exciton Bohr radius for bulk ZnS is reported to be 2.5 nm (Bhargava and Gallagher, 1994; Goudarzi et al., 2009; Whiffen et al., 2014). Nyamen et. al., (2014), decomposed bis(ditetrahydroisoquinoline dithiocarbamate) zinc(II) in hot hexadecylamine at 180 °C and obtained particle size of ZnS to be 5.94 nm. The EDX elemental analyses showed that the ZnS nanoparticles stoichiometrically consisted of 50.40 *at. %* Zn and 49.60 *at. %* S.

The diffraction pattern for the synthesized MnS is similar to alabandite mineral with a rocksalt crystal structure (AMCSD 0007512). The diffraction pattern shows four distinct peaks at 2 theta values of 29.51°, 34.34°, 49.33° and 61.46° signifying the *hkl* (111), (200), (220) and (222) planes in MnS. The Sherrer crystallite size for the MnS was estimated to be 17.81 nm. The lattice parameter calculated for the MnS was  $5.226 \pm 0.009 \text{ \AA}$  which is comparable to 5.224 Å for a standard alabandite mineral (AMCSD 0007512). The EDX elemental analyses of the MnS nanoparticles showed they stoichiometrically consisted of 53.63 *at. %* Mn and 46.37 *at. %* S.

The p-XRD patterns for the as synthesized Mn-doped ZnS are shown in Figure 4.4.6. The diffraction patterns for the Mn-doped ZnS are similar to the parent host ZnS pattern.



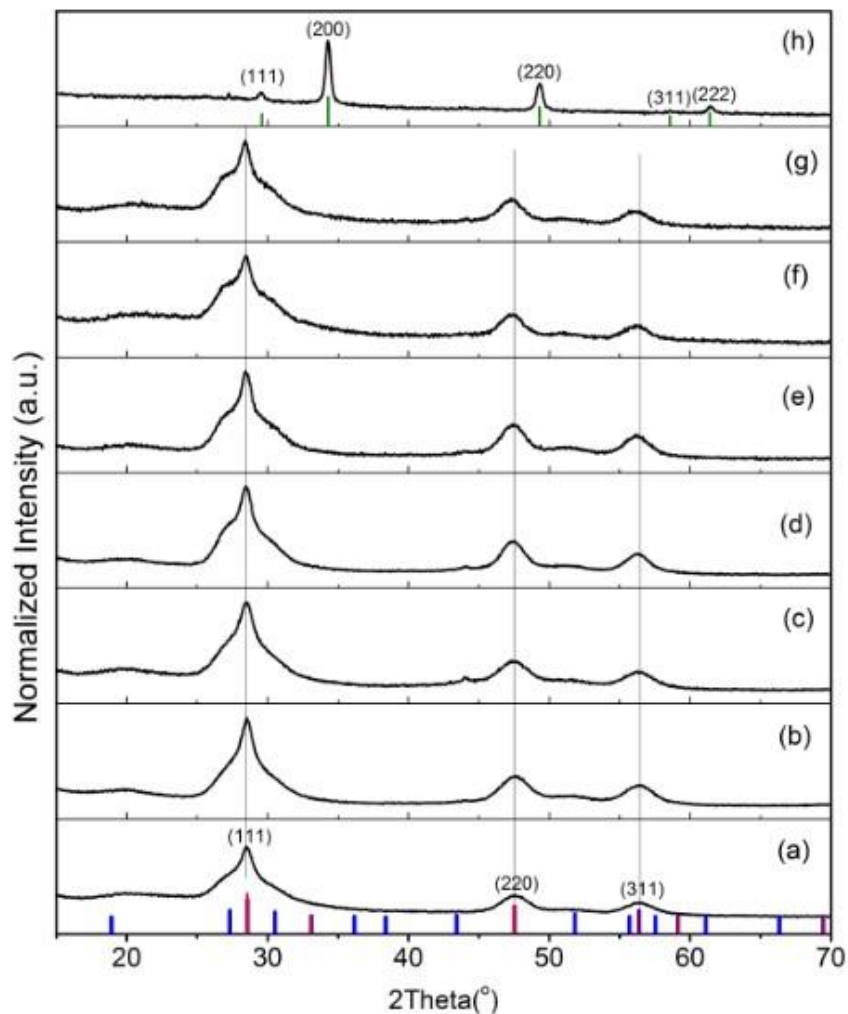


Figure 4.4.6: p-XRD patterns for (a) ZnS, (b-g)  $Mn_xZn_{1-x}S$  where  $x$  is equal to (b) 0.0076, (c) 0.0158, (d) 0.0253, (e) 0.0321, (f) 0.0524, (g) 0.0698 and (h) MnS nanoparticles obtained by decomposing tetrahydroisoquinoline dithiocarbamate complexes in oleylamine at 280 °C for 1 hour. The red, blue and green lines are standard sphalerite ZnS, wurtzite ZnS and albadite MnS respectively.

There are no extra diffraction peaks related to MnS impurity in the p-XRD patterns for the doped nanoparticles even at 7 % of Mn doping, indicating that pure Mn-doped ZnS nanoparticles were obtained from the syntheses. The crystallite sizes did not increase linearly with doping. The average crystallite size for the doped nanoparticles was calculated to be  $3.84 \pm 1.25$  nm.

However, there was appreciable shift in the lattice parameter as the Mn dopant concentration was increased (Figure 4.4.7). The lattice parameter for the undoped ZnS was  $5.408 \pm 0.007 \text{ \AA}$  and it shifted to  $5.410 \pm 0.009 \text{ \AA}$  with 2.53 % Mn doping, indicating a percentage shift of 0.03 %. The average shift in the lattice parameter with Mn doping was found to be 0.21 %. The shift suggested the possible incorporation of the Mn(II) ions into the host ZnS lattice (Bryan and Gamelin, 2005).

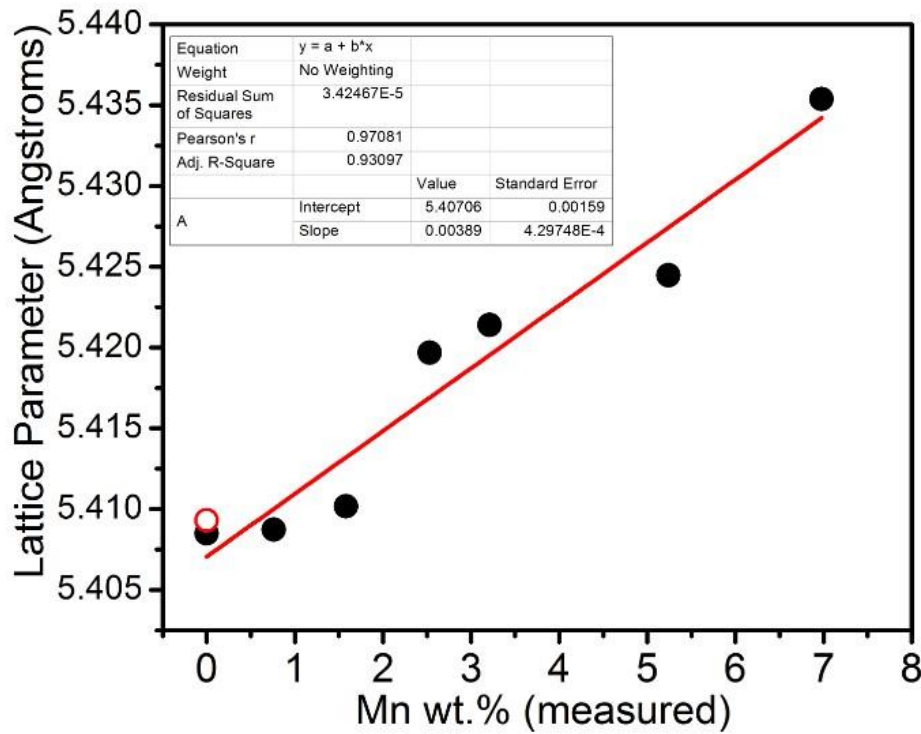


Figure 4.4.7: Lattice parameter measured by p-XRD as against increasing Mn wt. % concentration (measured) in  $Mn_xZn_{1-x}S$ . Bullet in red is the standard lattice parameter for ZnS.

#### 4.4.2.4 Morphology of Mn-doped ZnS nanocrystals

The TEM images of 0.76 % Mn-doped ZnS nanoparticles at different magnifications are shown in Figure 4.4.8 (a, b and c) with the nanoparticles size distribution histogram in Figure 4.4.8 (d).

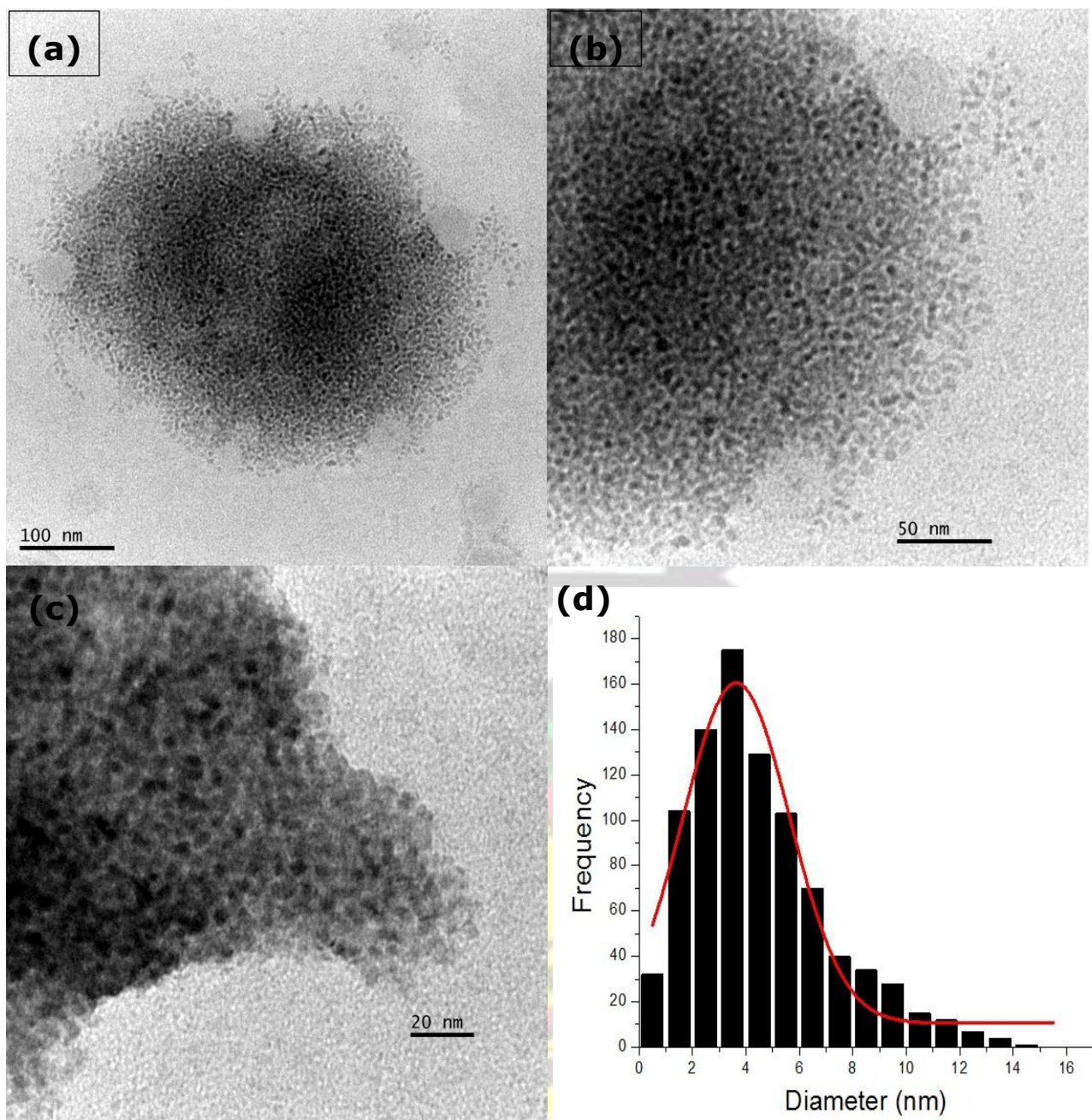


Figure 4.4.8: TEM images of 0.76 % Mn-doped ZnS nanoparticles at different magnifications (a) 100 nm, (b) 50 nm and (c) 20 nm and (d) the particles size distribution histogram

The average size of the Mn-doped ZnS nanoparticles obtained was  $3.64 \pm 1.99$  nm and is comparable to the average calculated crystallite size of  $3.84 \pm 1.25$  nm obtained from the XRD patterns. Similarly, decomposing  $[\text{Zn}(\text{S}_2\text{CN}(\text{thq}))_2]$  precursor in TOPO at 240 °C, Nyamen et al., (2014) obtained average ZnS nanoparticle size of  $5.9 \pm 0.25$  nm. The nanoparticles were both

spherical and oval in shape. The polydispersity of the size distribution was found to be about 54.7 % with majority of the particles having sizes between 3 and 4 nm. However, from the histogram, the growth of the nanoparticles can be thought of (i) the generation of particles with sizes within 1 and 2 nm and (ii) gradual growth of the sizes into larger size particles even up to about 15 nm. It is interesting to note that, colloidal thermolysis of heterocyclic dithiocarbamate was efficient in producing quantum sizes of Mn-doped ZnS nanoparticles compared to the exciton Bohr diameter of 5 nm as reported by Goudarzi et al., (2009) for ZnS.

#### 4.4.2.5 Optical properties of undoped ZnS and Mn-doped ZnS nanocrystals

The optical properties of the synthesized undoped ZnS and Mn-doped ZnS nanoparticles are shown in Figure 4.4.9 (a) and (b). The insert graph is Tauc's plot showing estimation of the band gap energy (in eV) of the absorbing material. The band gap energy of bulk sphalerite ZnS is reported to be 3.6 eV (Zhu et al., 2003). The band gap energy of the undoped ZnS nanoparticles was found to be 3.765 eV which is about 4.58 % higher than that of the bulk, suggesting some level of quantum confinement. Ramasamy et al., (2012) obtained a close value of 3.88 eV for ZnS synthesized via coprecipitation in aqueous media at room temperature.

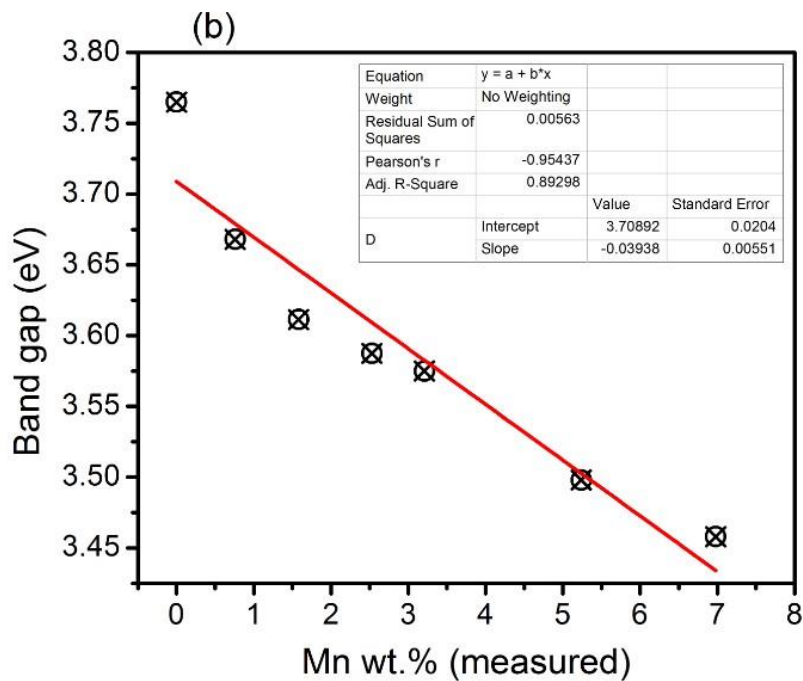
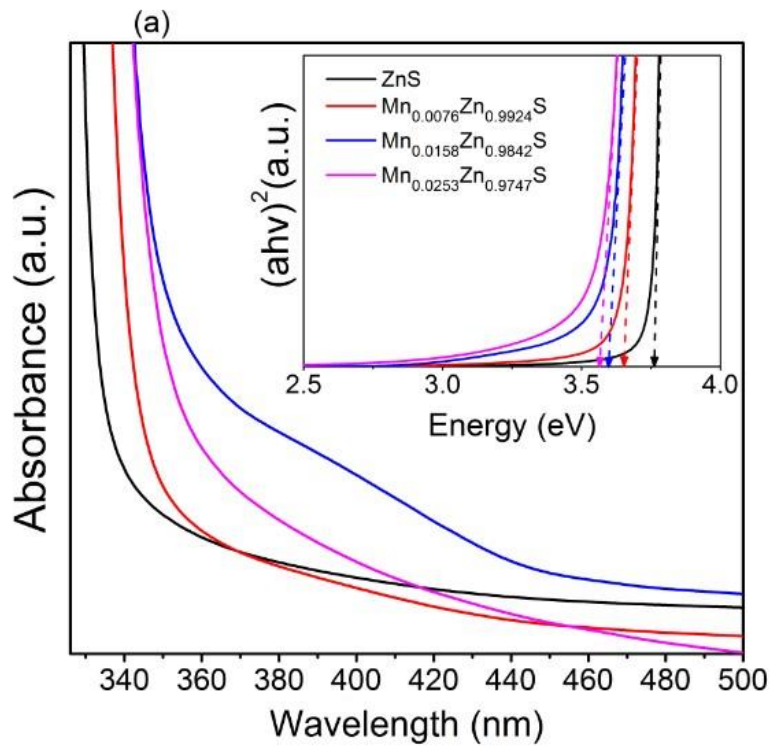


Figure 4.4.9: Graphs showing (a) absorption spectra and band gap energies of Mn-doped ZnS nanoparticles (Insert graph is Tauc's plot), and (b) plot of the band gap energy against Mn wt.% concentration measured in the doped samples.

The band gap energy for the ZnS was found decreasing with increasing Mn(II) dopant concentration (Figure 4.4.9(b)). The decrease in band gap indicated the introduction of triplet state into the forbidden zone of the ZnS energy band structure (Sooklal et al., 1996). The band gap energy of the 2.53 % Mn-doped ZnS nanoparticles was measured to be 3.59 eV which is similar to that of the bulk ZnS. The band gap energy further decreased to 3.46 eV with 6.98 % Mn(II) dopant concentration. The average percentage reduction in the band gap energy with Mn(II) doping was calculated to be 5.3 %. Joicy et al., (2014), Kripal et al., (2016) and Kanmani et al., (2011) made similar observation about the reduction in band gap energy with increasing Mn(II) dopant concentration. The reduction in band gap energy can be partly attributed to the infusion of Mn(II) into the crystal lattice of the ZnS host nanoparticles and partly due to the changes in the crystallite sizes.

In Figure 4.4.10(a), the 0.76 % Mn-doped ZnS nanoparticles showed emissions both at 450 nm and 587 nm, with the latter less intense than the former. The emission peak at 450 nm may be associated to defect-related emissions of ZnS (Geng et al., 2004). The 587 nm emission can be attributed to the expected emission from the  ${}^4T_1 \leftarrow {}^6A_1$  transition state which suggests that some Mn(II) ions occupy some substitutionary  $Zn^{2+}$  sites in the ZnS host lattice. The agglomeration number calculated for the 0.76 % Mn-doped ZnS is 2787 basic entities per nanoparticle dot; out of which 21 are Mn(II) basic units. Nazerdeylami et al., (2011) observed a similar emission at 594 nm. However, the emission was not observed in the Mn-doped ZnS samples with higher dopant concentrations ( $\geq 1$  %). Borse et al., (1999) attributed luminescence quenching to (i) isolated Mn ions at the surface or occupying interstitial location with octahedral symmetry, (ii) Mn-Mn dipolar interactions, and (iii) exchange-coupled Mn clusters. Thus, efficient doping was achieved at lower Mn dopant concentration.

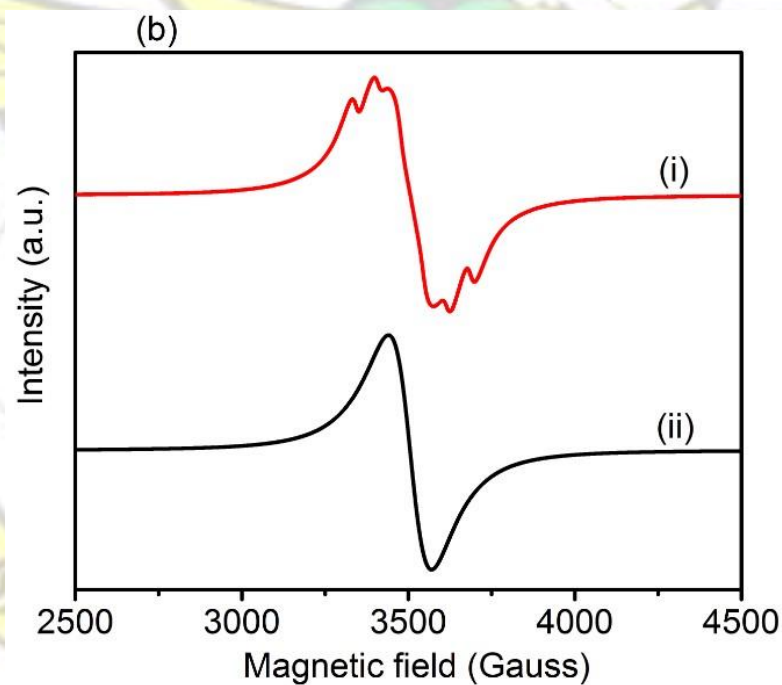
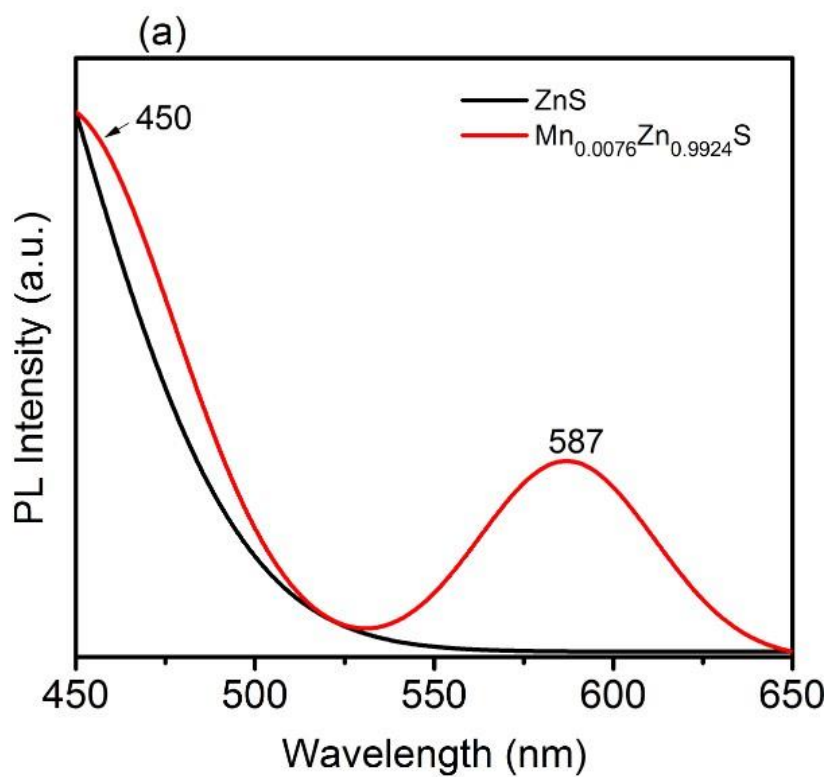


Figure 4.4.10: Graphs showing (a) PL spectra of undoped ZnS and 0.76 % Mn-doped ZnS and (b) EPR spectra of (i) 0.76 % and (ii) 6.98 % Mn-doped ZnS nanoparticles

EPR spectra of the 0.76 % and 6.98 % Mn-doped ZnS were obtained (Figure 4.4.10(b)). The

EPR spectra obtained for 6.98 % Mn-doped ZnS was a single broad peak which is associated to Mn-Mn dipole interactions suggesting that the Mn(II) ions occupied the surface/interstitial location in the ZnS host lattice (Borse et al., 1999). On reducing the Mn dopant concentration to 0.76 %, a broad peak with six smaller peaks were observed which are characteristic of Mn(II) ions both in substitutionary and surface/interstitial sites in the ZnS host lattice. Similar, EPR spectra have been reported by Nazerdeylami et al., (2011).



#### 4.4.3 Summary of main findings

1. Tetrahydroisoquinoline dithiocarbamate ligand (in methanol, under aerial conditions) was found to form a *tris*-chelated complex with manganese in the +2 oxidation state. However, the decomposition of the oxidized product  $[\text{Mn}(\text{S}_2\text{CN}(\text{thiq}))_3]$  in oleylamine yields MnS nanoparticles with stoichiometric proportions of 53.63 *at.*% Mn and 46.37 *at.*% S which suggested reduction to Mn(II).
2. Mn-doped ZnS nanoparticles were successfully synthesized by colloidal thermolyses of tetrahydroisoquinoline dithiocarbamate complexes of zinc and manganese in oleylamine at 280 °C.
3. The p-XRD patterns showed that the Mn-doped ZnS nanoparticles were polytypic (i.e. consisted of both sphalerite and wurtzite crystal structures) and the shift in the lattice parameter indicated a successful incorporation of the Mn(II) into the ZnS host lattice structure.
4. The band gap energy was found to be decreasing with increasing Mn(II) dopant concentration which indicated the possible introduction of triplet state into the band structure of the host ZnS.
5. The PL spectra of the 0.76 % Mn-doped ZnS nanoparticles showed the characteristic Mn  ${}^4\text{T}_1 \leftarrow {}^6\text{A}_1$  luminescence at 587 nm which suggested the incorporation of Mn(II) in ZnS lattice.
6. EPR studies on the 0.76 % Mn-doped ZnS nanoparticles showed that the Mn(II) ions occupied both substitutionary and surface/interstitial sites in the ZnS host lattice.

## 4.5 General Discussions

The properties of the as-synthesized CdS, PbS, ZnS, MnS and  $Mn_xZn_{1-x}S$  nanoparticles are discussed in relation to the different approaches employed and compared to literature.

### 4.5.1 CdS and PbS Nanocrystals

The syntheses of CdS nanoclusters and PbS nanobelts via the thermolysis of ethyl xanthate complexes in castor oil have been shown in this study. This approach used less toxic xanthate complexes and castor oil as precursors and coordinating solvent respectively, relative to the traditional toxic dimethylcadmium and phosphine based solvents employed by Murray et al., (1993). The properties of the as synthesized CdS nanomaterials obtained are unique compared to those reported by Kyobe et al., (2016), and Shombe et al., (2016) who also applied castor oil as solvent in their work but employed different synthetic techniques and precursors. The transition of cubic (zinc blende) crystal system to hexagonal (wurtzite) which was observed for CdS nanoparticles as the reaction temperature was increased from 200 to 280 °C is new and not yet reported for metal chalcogenide syntheses involving vegetable oils as solvent. Also the CdS nanoparticles displayed near-UV emissions ( $\lambda_{max}$  391 – 393 nm) which make them suitable for potential applications in UV/Vis sensors. The PbS nanoparticles showed nanobelts, nanorods, and nanoplates morphologies which are not usually reported.

## 4.5.2 ZnS and MnS Nanocrystals

The syntheses of the ZnS, and MnS nanocrystals were made via colloidal thermolyses of (i) tetrahydroisoquinoline dithiocarbamates and (ii) diricinoleate carboxylates precursors in oleylamine. The p-XRD patterns of the ZnS and MnS nanocrystals are compared in Figure 4.5.1.

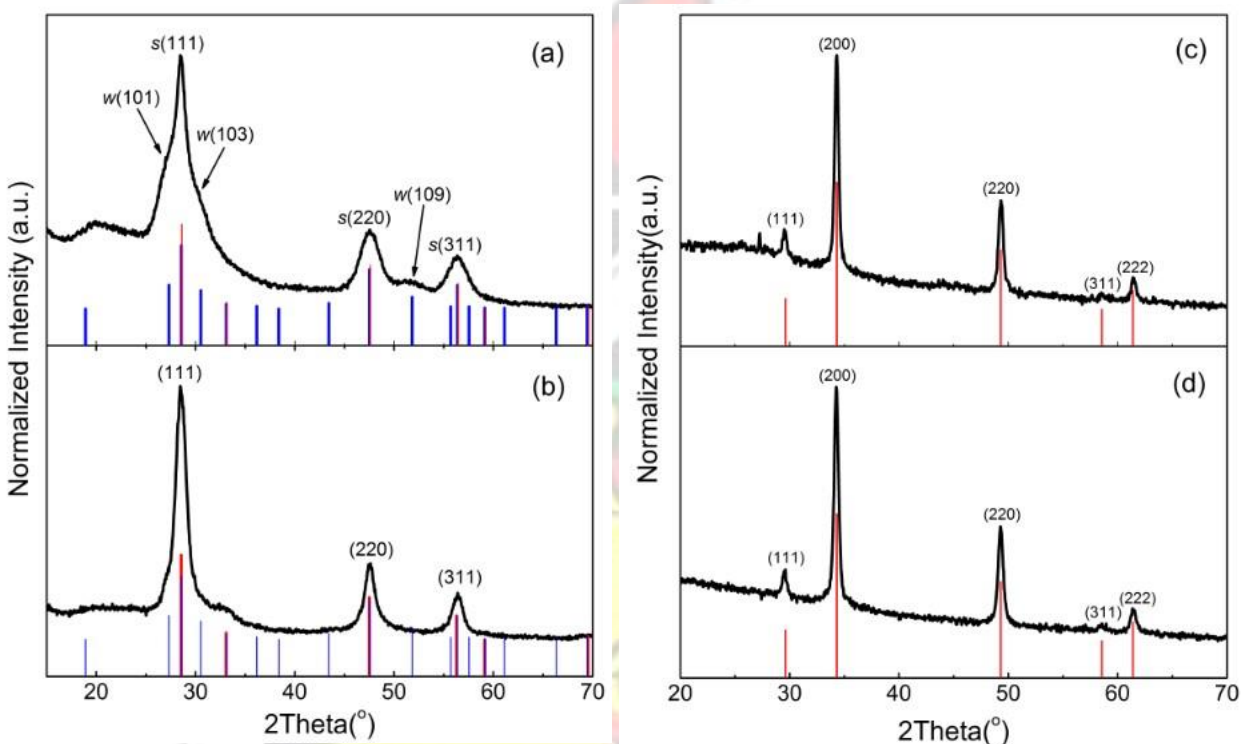


Figure 4.5.1: Comparison of p-XRD patterns of ZnS and MnS obtained by thermal decomposition of (a) bis(tetrahydroisoquinolinyl dithiocarbamate) zinc, (b) zinc diricinoleate carboxylate, (c) bis(tetrahydroisoquinolinyl dithiocarbamate) manganese and (d) manganese diricinoleate carboxylate in oleylamine. The red and blue lines in (a) and (b) are standard sphalerite (*s*) and wurtzite (*w*) phases of ZnS. The red lines in (c) and (d) are standard alabandite MnS.

The dithiocarbamate route yielded a polytypic ZnS, showing characteristics of sphalerite and wurtzite crystal structures (Figure 4.5.1(a)) whereas the carboxylate route yielded a pure sphalerite

ZnS (Figure 4.5.1(b)). Using Match!3 software package, the estimated percentages of sphalerite and wurtzite structures in ZnS (synthesized by the dithiocarbamate route) were 46.2 % and 53.8 % respectively. In Figure 4.5.1(a), the p-XRD pattern shows a diffraction peak at 2 theta value of  $51.81^\circ$  representing the diffraction plane with Miller indices  $hkl$  (109) characteristic of a wurtzite ZnS. Also, the  $hkl$  (111) diffraction peak appears merged with the wurtzitic planes  $hkl$  (101) and (103) resulting in peak broadening (Figure 4.5.1(a)). It is interesting to note that the wurtzite ZnS was obtained by thermally decomposing heterocyclic dithiocarbamate complexes at a lower temperature (280 °C) which is of advantage to other techniques requiring high temperatures of about 1200 °C reported in literature (Fang et al., 2011). However, similar lattice parameters of 5.409 Å and 5.408 Å were calculated for the two different ZnS nanoparticles. The crystallite size calculated for the ZnS obtained via the dithiocarbamate and carboxylate routes were 3.91 nm and 5.78 nm respectively. The difference in the crystallite sizes may be due to the different temperatures used in the syntheses (280 °C and 300 °C for the dithiocarbamate and carboxylate routes respectively).

The p-XRD patterns of MnS nanoparticles synthesized using the two different precursors are shown in Figure 4.5.1(c and d). The MnS precipitates in both cases were green. Both routes yielded MnS nanocrystals with similar p-XRD pattern. The crystal structures agree with alabandite mineral with rocksalt crystal structure. The lattice parameters calculated for the MnS nanocrystals synthesized via the carboxylate and dithiocarbamate routes were 5.226 Å and 5.227 Å respectively. The MnS crystallite sizes obtained using the carboxylate route was 21.5 nm bigger than the 17.81 nm obtained via the dithiocarbamate route.

### 4.5.3 Mn-doped ZnS nanocrystals

The syntheses of the Mn-doped ZnS nanocrystals were accomplished via colloidal thermolyses of (i) tetrahydroisoquinoline dithiocarbamates and (ii) diricinoleate carboxylates precursors in oleylamine. A shift in the lattice parameter was observed with both synthesis pathways (Figure 4.5.2(a)). The shift varied linearly with the dopant concentration. The correlation ( $R^2$ ) value obtained for both routes was 0.93. Similarly, the concentration of Mn dopant found in the  $Mn_xZn_{1-x}S$  nanocrystals samples varied linearly with the Mn dopant concentration in the feed for the two syntheses pathways (Figure 4.5.2(b)). Also, similar doping efficiency of about 50 % was achieved for both routes.

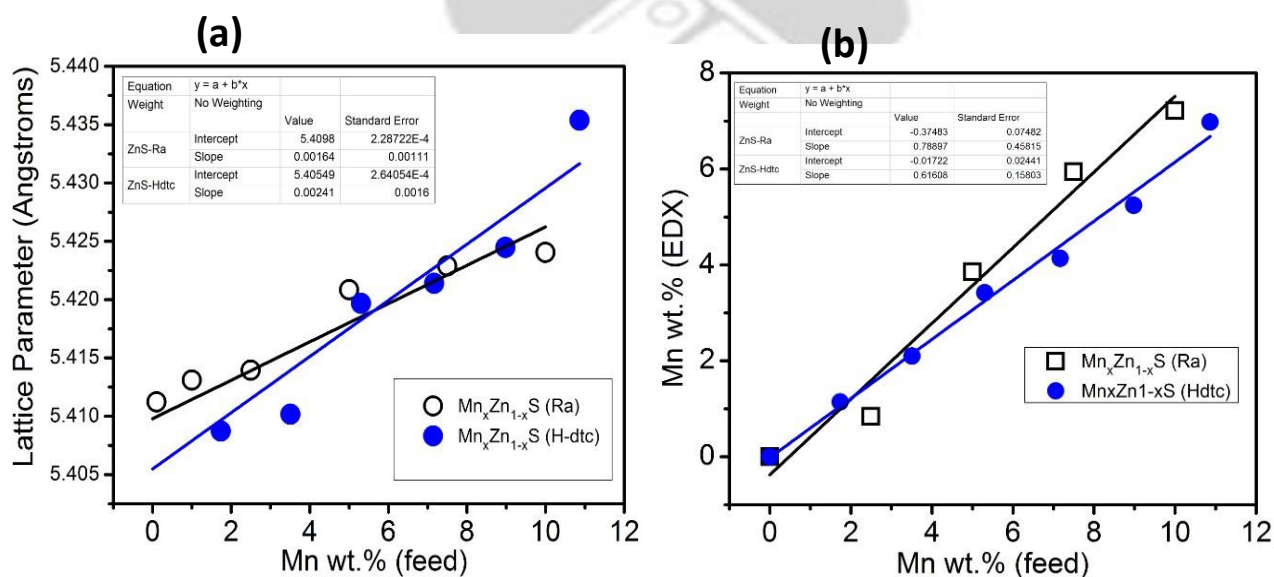


Figure 4.5.2: Plot of (a) lattice parameter obtained from p-XRD patterns of  $Mn_xZn_{1-x}S$  nanocrystals, (b) Mn wt.% measured (by EDX) in  $Mn_xZn_{1-x}S$  nanocrystals, against Mn wt.% in feed.

The optical band gap energy obtained for the undoped ZnS nanocrystals synthesized using carboxylates precursors was 3.67 eV as against 3.77 eV for ZnS synthesized using the heterocyclic

dithiocarbamate. The difference in the band gap energies has to do with the particle size and structural composition of the nanoparticles obtained via the different routes. However, the decrease in the optical band gap energy of the  $Mn_xZn_{1-x}S$  nanocrystals with increasing Mn dopant concentration was observed in the two different syntheses approaches (Figure 4.5.3). The characteristic  ${}^4T_1 \leftarrow {}^6A_1$  Mn emission appeared at 587 nm and 599.7 nm for  $Mn_xZn_{1-x}S$  nanocrystals synthesized with heterocyclic dithiocarbamate and carboxylate complexes respectively. The PL and EPR studies of the  $Mn_xZn_{1-x}S$  nanocrystals synthesized using both routes suggested that the Mn(II) occupied substitutionary  $Zn^{2+}$  site in ZnS at  $x \leq 0.1$ .

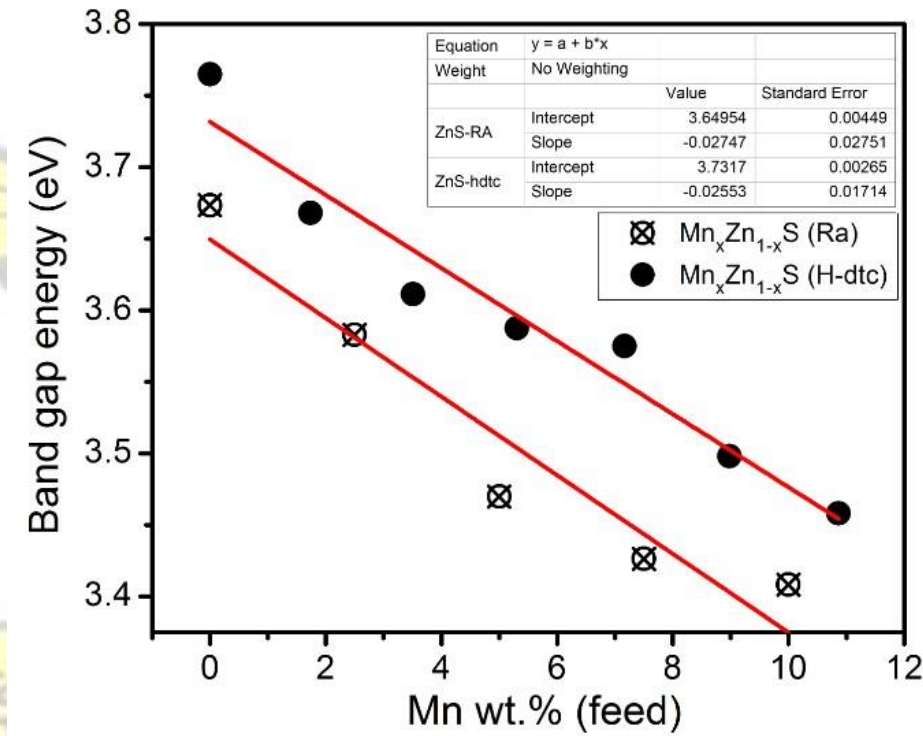


Figure 4.5.3: Plot of optical band gap energies of  $Mn_xZn_{1-x}S$  nanocrystals against Mn wt.% (feed).

## CHAPTER 5

## CONCLUSIONS AND RECOMMENDATIONS

### 5.1 Conclusions

Castor oil, diricinoleate carboxylate and heterocyclic dithiocarbamate complexes have been shown in this work to be suitable green materials for the syntheses of good quality metal chalcogenide semiconductor nanomaterials. The following were the main findings made:

1. Castor oil has been demonstrated as a suitable solvent for synthesis of CdS nanoclusters and PbS with unusual and interesting morphologies (such as nanobelts, nanorods, nanoplates).
2. About  $6.78 \pm 1.89$  nm size CdS nanoclusters with band gap energy 2.63 – 2.73 eV and near-UV emission ( $\lambda_{\text{max}} = 391 - 393$  nm) property were synthesized.
3. A change of CdS crystal structure phase from cubic crystal system to hexagonal with temperature was observed as the temperature for synthesis was increased from 200 °C to 280 °C.
4. The average energy band gap of the PbS nanobelts/rods/plates was found to be 0.85 eV.
5. The reactivity of zinc diricinoleate carboxylate complex was found to occur at temperatures higher than 240 °C in oleylamine/dodecanethiol.
6. Pure crystalline sphalerite monodispersed ZnS nanoparticles with quantum dot sizes 2.3 – 5.3 nm were obtained by the thermal decomposition of zinc diricinoleate carboxylate complex in oleylamine/dodecanethiol at  $\geq 240$  °C for  $\geq 20$  minutes.

7. The particles size and optical band gap energies of the ZnS nanoparticles were found dependent on temperature and time of reaction
8. The activation energy for coarsening kinetics of ZnS nanoparticles synthesized by the thermal decomposition of zinc diricinoleate carboxylate complex in oleylamine/dodecanethiol was determined to be 54.31 kJ/mol
9. Tetrahydroisoquinoline dithiocarbamate ligand (in methanol, under aerial condtions) was found to form a *tris*-chelated complex with manganese in (II) oxidation state. However, the decomposition of the oxidized product  $[\text{Mn}(\text{S}_2\text{CN}(\text{thiq}))_3]$  in oleylamine yielded MnS nanoparticles with stoichiometric proportions of 53.63 at.% Mn and 46.37 at.% S which suggested reduction to Mn(II).
10. Crystalline monodispersed luminescent  $\text{Mn}_x\text{Zn}_{1-x}\text{S}$  nanocrystals were successfully synthesized by the thermal decomposition of diricinoleate carboxylate and heterocyclic dithiocarbamate complexes of zinc and manganese in oleylamine.
11. The p-XRD measurement showed that the  $\text{Mn}_x\text{Zn}_{1-x}\text{S}$  nanocrystals were sphalerites and the shift in the lattice parameter observed indicated the successful incorporation of the Mn(II) into the ZnS host lattice structure for  $0 \leq x \leq 0.072$ . However, the Mndoped ZnS nanoparticles synthesized using the dithiocarbamate complexes were polytypic (i.e. consisted of both sphalerite and wurtzite crystal structures)
12. The band gap energy was found to decrease with increasing Mn(II) dopant which indicated the possible introduction of trap states into the energy band structure of the host ZnS. This reduction in band gap was observed with both synthesis pathways.
13. The  ${}^4\text{T}_1 \leftarrow {}^6\text{A}_1$  emission characteristic of Mn(II) ion incorporation into the ZnS host lattice was observed at 587 – 599.7 nm for  $\leq 0.76 - 0.8$  % Mn dopant.

14. EPR studies confirmed the presence of Mn(II) ions in substitutionary sites. At high concentrations of Mn dopant ( $\geq 1\%$ ), the Mn(II) ions were found to occupy surface/interstitial sites in ZnS.

## 5.2 Recommendations

1. The syntheses of Mn-doped ZnS nanoparticles should be extended using other green sources of materials/precursors (e.g. single source precursors such as xanthates).
2. The coordination of different heterocyclic dithiocarbamates with Mn in different oxidation states should be considered.
3. From this work, it appears pure wurtzite ZnS nanoparticles could be obtained from the thermal decomposition of heterocyclic dithiocarbamates which maybe relatively cheaper route to the high temperature routes ( $>1000\text{ }^{\circ}\text{C}$ ) reported in literature (Zhang and Banfield, 2009).

## REFERENCES

- Abdelhady, A.L., Malik, M.A. and O'Brien, P., (2013). Colloidal synthesis of ZnS, CdS and  $\text{Zn}_x\text{Cd}_{1-x}\text{S}$  nanoparticles from zinc and cadmium thiobiuret complexes. *J. Inorg. Organomet. Polym.*, pp.1-15
- Afzaal, M., Malik, M.A. and O'Brien, P., (2007). Preparation of zinc containing materials. *New J. Chem.*, 31, pp.2029–2040.

- Akhtar, J, Malik, M.A., O'Brien, P., Wijayantha, K.G.U., Dharmadasa, R., Hardman, S.J.O., Graham, D.M., Spencer, B.F., Stubbs, S.K., Flavell, W.R., Binks, D.J., Sirotti, F., Kazzi, M.E., Silly, M., (2010). A greener route to photoelectrochemically active PbS nanoparticles. *J. Mater. Chem.*, (60 C), pp.2336–2344.
- Alam, M.N., Roy, N., Mandal, D., Begum, N.A., (2013). Green chemistry for nanochemistry: exploring medicinal plants for the biogenic synthesis of metal NPs. *RSC Adv.*, pp.1–22.
- Alivisatos, A.P., (1996). Perspectives on the physical chemistry of semiconductor nanocrystals. *J. Phys. Chem.*, 100(31), pp.13226–13239.
- Anand, K.V., (2015). Optical and photoluminescence properties of HMTA capped transition metals (Cu, Co and Mn) doped ZnS nanoparticles. *J. Chem. Pharm. Res.*, 7(3), pp.286–290.
- Anand, K.V., Mohan, R. and Jayavel, R., (2016). Facile one-pot hydrothermal synthesis and structural characterization of transition metals (Cu, Co and Mn) doped ZnS nanoparticles in HMTA matrix. *J. Mater. Environ. Sci.*, 7(2), pp.679–684.
- Applerot, G., Lipovsky, A., Dror, R., Perkas, N., Nitzan, Y., Lubart, R., Gedanken, A., (2009). Enhanced antibacterial activity of nanocrystalline ZnO due to increased ROS-mediated cell injury. *Adv. Funct. Mater.*, 19, pp.842–852.
- Balantseva, E., Berlier, G., Camino, B., Lessio, M., Ferrari, A.M., (2014). Surface properties of ZnS nanoparticles: A combined DFT and experimental study. *J. Phys. Chem. C*, pp.A-J.
- Ban, R., Li, J., Cao, J., Zhang, P., Zhang, J., Zhu, J., (2013). Highly luminescent glutathionecapped ZnS:Mn/ZnS core/shell doped quantum dots for targeted mannosyl groups expression on the cell surface. *Anal. Methods*, 5, pp.5929–5937.

- Barrelet, C.J., Wu, Y., Bell, D.C., Lieber, C.M., (2003). Synthesis of CdS and ZnS nanowires using single-source molecular precursors. *J. A. Chem. Soc.*, 125, pp.11498–11499.
- Bastami, T.R. and Entezari, M.H., (2010). Sono-synthesis of Mn<sub>3</sub>O<sub>4</sub> nanoparticles in different media without additives. *Chemical Engineering Journal*, 164(1), pp.261–266.
- Baugher, B.W.H., Churchill, H.O.H., Yang, Y., Jarillo-herrero, P., (2014). Optoelectronic devices based on electrically tunable p – n diodes in a monolayer dichalcogenide. *Nature Nanotechnology*, pp.1–6.
- Baxter, J., Bian, Z., Chen, G., Danielson, D., Dresselhaus, M.S., Fedorov, A.G., Fisher, T.S. Jones, C.W., Maginn, E., Kortshagen, U., Manthiram, A., Nozik, A., Rolison, D.R., Sands, T., Shi, L., Sholl, D., Wu, Y., (2009). Nanoscale design to enable the revolution in renewable energy. *Energy Environ. Sci.*, 2, pp.559–588.
- Beaulac, R., Archer, P.I. and Gamelin, D.R., (2008). Luminescence in colloidal Mn<sup>2+</sup>-doped semiconductor nanocrystals. *Journal of Solid State Chemistry*, 181, pp.1582–1589.
- Beermann, P.A.G., Mcgarvey, B.R., Skadtchenko, B.O., Muralidharan, S., Sung, R.C.W., (2006). Cationic substitution sites in Mn<sup>2+</sup>-doped ZnS nanoparticles. *Journal of Nanoparticle Research*, 8, pp.235–241.
- Beltran-Huarac, J., Palomino, J., Resto, O., Wang, J., Jadwisienczak, W.M., Weiner, B.R., Morell, G., (2014). Highly-crystalline gamma-MnS nanosaws. *RSC Adv.*, 4, pp.38103– 38110.
- Bhandari, K.P., Roland, P.J., Mahabaduge, H., Haugen, N.O., Grice, C.R., Jeong, S., Dykstra, T., Gao, J., Ellingson, R.J., (2013). Thin film solar cells based on the heterojunction of colloidal PbS quantum dots with CdS. *Solar Energy Materials and Solar Cells*, 117, pp.476–482.

- Bhargava, R.N. and Gallagher, D., (1994). Optical properties of manganese-doped ZnS. *Physical Review Letters*, 72(3), pp.1–4.
- Biswas, S. and Kar, S., (2008). Fabrication of ZnS nanoparticles and nanorods with cubic and hexagonal crystal structures: a simple solvothermal. *Nanotechnology*, 45710, pp.1–11.
- Biswas, S., Kar, S. and Chaudhuri, S., (2005). Optical and magnetic properties of manganese-incorporated zinc sulphide nanorods synthesized by a solvothermal process. *J. Phys. Chem. B*, 109, pp.17526–17530.
- Bol, A.A., Beek, R.V. and Meijerink, A., (2002). On the incorporation of trivalent rare earth ions in II - VI semiconductor nanocrystals. *Chem. Mater.*, (13), pp.1121–1126.
- Bol, A.A. and Meijerink, A., (2000). Doped semiconductor nanoparticles - a new class of luminescent materials? *Journal of Luminescence*, 89, pp.315–318.
- Borse, P.H., Srinivas, D., Shinde, R.F., Date, S.K., Vogel, W., Kulkarni, S.K., (1999). Effect of  $Mn^{2+}$  concentration in ZnS nanoparticles on photoluminescence and electron-spin-resonance spectra. *Physical Review B*, 60(12), pp.8659–8664.
- Bronstein, L.M., Huang, X., Retrum, J., Schmucker, A., Pink, M., Stein, B.D., Dragnea, B., (2007). Influence of iron oleate complex structure on iron oxide nanoparticle formation. *Chem. Mater.*, (15), pp.3624–3632.
- Bryan, J.D. and Gamelin, D.R., (2005). Doped semiconductor nanocrystals: Synthesis, characterization, physical properties, and applications. *Progress in Inorganic Chemistry*, 54, pp.47–126.
- Bwatanglang, I.B., Mohammad, F., Yusof, N.A., Abdullah, J., Hussein, M.Z., Alitheen, N.B.

- Abu, N., (2016). Folic acid targeted Mn : ZnS quantum dots for theranostic applications of cancer cell imaging and therapy. *International Journal of Nanomedicine*, 11, pp.413–428.
- Byrom, C., Malik, M.A., O'Brien, P., White, A.J.P., Williams, D.J., (2000). Synthesis and X-ray single crystal structures of bis(diisobutyldithiophosphinato)cadmium(II) or zinc(II) : Potential single-source precursors for II / VI materials. *Polyhedron*, 19, pp.211–215.
- Cao, J., Yang, J., Zhang, Y., Yang, L., Wang, Y., Wei, M., Liu, Y., Gao, M., Liu, X., Xie, Z., (2009). Optimized doping concentration of manganese in zinc sulphide nanoparticles for yellow-orange light emission. *Journal of Alloys and Compounds*, 486, pp.890–894.
- Cha, H.G., Lee, D.K., Kim, Y.H., Kim, C.W., Lee, C.S., Kang, Y.S., (2007). Solventless nanoparticles synthesis under low pressure. *Inorganic Chemistry*, 47(1), p.121.
- Chakrabarti, M.H. and Ahmad, R., (2008). Transesterification studies on castor oil as a first step towards its use in biodiesel production. *Pak. J. Bot.*, 40(3), pp.1153–1157.
- Chan, W.C.W., Maxwell, D.J., Gao, X., Bailey, R.E., Han, M., Nie, S., (2002). Luminescent quantum dots for multiplexed biological detection and imaging. *Current Opinion in Biotechnology*, 13, pp.40–46.
- Chang, J. and Waclawik, E.R., (2014). Colloidal semiconductor nanocrystals: controlled synthesis and surface chemistry in organic media. *RSC Adv.*, 4, pp.23505–23527.
- Chantada-vázquez, M.P., Sánchez-Gonzalez, J., Peña-Vázquez, E., Tabernero, J.M., Bermejo, A.M., Bermejo-Barrera, P., Moreda-Piñeiro, A., (2015). Synthesis and characterization of novel molecularly imprinted polymer-coated Mn-doped ZnS quantum dots for specific fluorescent recognition of cocaine. *Biosensors and Bioelectronic*, pp.1–25.

- Chen, C.J., Lai, H.Y., Lin, C.C., Wang, J.S., Chiang, R.K., (2009). Preparation of monodisperse iron oxide nanoparticles via the synthesis and decomposition of iron fatty acid complexes. *Nanoscale Research Letters*, 4(11), pp.1343–1350.
- Chen, S. and Liu, W., (1999). Preparation and characterization of surface-coated ZnS nanoparticles. *Langmuir*, 15(14), pp.8100–8104.
- Chen, W., Li, G., Malm, J., Huang, Y., Wallenberg, R., Han, H., Wang, Z., Bovin, J., (2000). Pressure dependence of  $Mn^{2+}$  fluorescence in ZnS:  $Mn^{2+}$  nanoparticles. *Journal of Luminescence*, 91, pp.139–145.
- Chen, Z., Tian, Q., Song, Y., Yang, J., Hu, J., (2010). One-pot synthesis of  $Zn_xCd_{1-x}S$  nanocrystals with tunable optical properties from molecular precursors. *Journal of Alloys and Compounds*, 506(2), pp.804–810.
- Cheng, Y., Lin, Z., Lu, H., Zhang, L., Yang, B., (2014). ZnS nanoparticles well dispersed in ethylene glycol: coordination control synthesis and application as nanocomposite optical coatings. *Nanotechnology*, 25(115601), pp.1–10.
- Choi, S., Na, H.B., Park, Y.I., An, K., Kwon, S.G., Jang, Y., Park, M., Moon, J., Son, J.S., Song, I.C., (2008). Simple and generalized synthesis of oxide - metal heterostructured nanoparticles and their applications in multimodal biomedical probes. *J. Am. Chem. Soc.*, 130, pp.15573–15580.
- Choi, S.-H., An, K., Kim, E.-G., Yu, J.H., Kim, J.H., Hyeon, T., (2009). Simple and generalized synthesis of semiconducting metal sulphide nanocrystals. *Adv. Funct. Mater.*, 19(10), pp.1645–1649.

- Concei, M.M., Fernandes, V.J., Bezerra, A.F., Silva, M.C.D., Santos, I.M.G., Silva, F.C., Souza, A.G., (2007). Dynamic kinetic calculation of castor oil biodiesel. *J. Therm. Anal. Cal.*, 87, pp.865–869.
- Da Silva, E.C., Da Silva, M.G.A., Meneghetti, S.M.P., Machado, G., Alencar, M.A.R.C., Hickmann, J.M., Meneghetti, M.R., (2008). Synthesis of colloids based on gold nanoparticles dispersed in castor oil. *J Nanopart Res*, 10, pp.201–208.
- Da Silva, N.D.L., Batistella, C., Filho, R.M., Maciel, M.R.W., (2011). Determination of castor oil molecular weight by vapour pressure osmometry technique. *Chemical Engineering Transactions*, 24, pp.601–606.
- Dawood, F. and Schaak, R.E., (2009). ZnO-templated synthesis of wurtzite-type ZnS and ZnSe nanoparticles. *J. Am. Chem. Soc.*, 131, pp.424–425.
- Deng, Z., Tong, L., Flores, M., Lin, S., Cheng, J.X., Yan, H., Liu, Y., (2011). High quality manganese-doped zinc sulphide quantum rods with tunable dual-color and multi-photon emissions. *J. Am. Chem. Soc.*, 133(14), pp.5389–5396.
- Devi, B.S.R., Raveendran, R. and Vaidyan, A. V, (2007). Synthesis and characterization of Mn<sup>2+</sup>-doped ZnS nanoparticles. *Pramana-Journal of Physics*, 68(4), pp.679–687.
- Dickerson, B.D., Irving, D.M., Herz, E., Claus, R.O., Spillman Jr., W.B., Meissner, K.E., Dickerson, B.D., Irving, D.M., Herz, E., Claus, R.O., Spillman, W.B., (2005). Synthesis kinetics of CdSe quantum dots in trioctylphosphine oxide and in stearic acid. *Appl. Phys. Lett.*, 86(171915), pp.86–89.

- Dinda, S., Kakran, M., Zeng, J., Sudhaharan, T., Ahmed, S., Das, D., Selvan, S.T., (2016). Grafting of ZnS: Mn-doped nanocrystals and an anticancer drug onto graphene oxide for delivery and cell labeling. *ChemPlusChem*, pp.100–107.
- Donne, A. L., Jana, S.K., Banerjee, S., Basu, S., Binetti, S., (2013). Optimized luminescence properties of Mn doped ZnS nanoparticles for photovoltaic applications. *J. Appl. Phys.*, 113(14903), pp.1–5.
- Duran, N. and Marcato, P.D., (2013). Nanobiotechnology perspectives. Role of nanotechnology in the food industry : a review. *International Journal of Food Science and Technology*, 48, pp.1127–1134.
- Dushkin, C.D.U., Saita, S., Yoshie, K., Yamaguchi, Y., (2000). The kinetics of growth of semiconductor nanocrystals in a hot amphiphile matrix. *Advances in Colloid and Interface Science*, 88, pp.37–78.
- Erwin, S.C., Zu, L., Haftel, M., Efros, A.L., Kennedy, T.A., Norris, D.J., (2005). Doping semiconductor nanocrystals. *Nature*, 436, pp.91–94.
- Fabretti, A.C., Ferrari, M., Franchini, G.C., Giusti, A., Preti, C., Tosi, G., (1983). Magnetic and thermogravimetric studies on copper (II) heterocyclicdithiocarbamates. *Transition Met. Chem.*, 8, pp.8–10.
- Fan, D., Afzaal, M., Mallik, M.A., Nguyen, C.Q., O'Brien, P., Thomas, P.J., (2007). Using coordination chemistry to develop new routes to semiconductor and other materials. *Coordination Chemistry Reviews*, 251, pp.1878–1888.
- Fang, X., Bando, Y., Gautam, U.K., Zhai, T., Zeng, H., Xu, X., Liao, M., Golberg, D., (2009).

ZnO and ZnS nanostructures: Ultraviolet-light emitters, lasers, and sensors. *Critical Reviews in Solid State and Materials Science*, 34, pp.37–41.

Fang, X., Zhai, T., Gautam, U.K., Li, L., Wu, L., Bando, Y., Golberg, D., (2011). ZnS nanostructures : From synthesis to applications. *Progress in Materials Science*, 56(2), pp.175–287.

Foglia, T.A., Jones, K.C. and Sonnet, P.E., (2000). Selectivity of lipases: isolation of fatty acids from castor, coriander, and meadowfoam oils. *European Journal of Lipid Science and Technology*, 102(10), pp.612–617.

Forghieri, F., Preti, C., Tassi, L., Tosi, G., (1988). Preparation, properties and reactivity of gold complexes with some heterocyclic dithiocarbamates as ligands. *Polyhedron*, 7(14), pp.1231–1237.

Frenzel, J., Joswig, J. and Seifert, G., (2007). Optical excitations in cadmium sulphide nanoparticles. *J. Phys. Chem. C*, pp.A-I.

Furlan, M., Kluge, J., Mazzotti, M., Lattuada, M., (2010). Preparation of biocompatible magnetite–PLGA composite nanoparticles using supercritical fluid extraction of emulsions. *The Journal of Supercritical Fluids*, 54(3), pp.348–356.

Garcia-Fontan, S. and Rodriguez-Seoane, P., (1993). Spectroscopic study of cadmium(II) dithiocarbamate ligands complexes with heterocyclic. *Inorganica Chimica Acta*, 211, pp.211–215.

- Gardner, P.J. and Pang, P., (1988). Thermodynamics of the zinc sulphide transformation, sphalerite-wurtzite, by modified entrainment. *J. Chem. Soc., Faraday Trans. 1*, 84(6), pp.1879–1887.
- Garg, B.S., Garg, R.K. and Reddy, M.J., (1994). Synthesis and spectroscopic studies of dithiocarbamate complexes of some 3d-metals ions. *J. Coord. Chem.*, 33, pp.109–116.
- Geng, B.Y., Zhang, L.D., Wang, G.Z., Xie, T., Zhang, Y.G., Meng, G.W., (2004). Synthesis and photoluminescence properties of ZnMnS nanobelts. *Appl. Phys. Lett.*, 84(12), pp.2157–2159.
- Gergely, A., Bowman, D. and Chaudhry, Q., (2010). Small Ingredients in a big picture: Regulatory perspectives on nanotechnologies in foods and food contact materials. *RSC Nanoscience and Nanotechnology*, 14, pp.150–181.
- German, S. V., Navolokin, N.A., Kuznetsova, N.R., Zuev, V.V., Inozemtseva, O.A., Aniskov, A.A., Volkova, E.K., Bucharskaya, A.B., Maslyakova, G.N., Fakhrullin, R.F., Terentyuk, G.S., Vodovozova, E.L., Gorin, D A., (2015). Liposomes loaded with hydrophilic magnetite nanoparticles: Preparation and application as contrast agents for magnetic resonance imaging. *Colloids and Surfaces B: Biointerfaces*, pp.1–28.
- Geszke-Moritz, M., Piotrowska, H., Murias, M., Balan, L., Moritz, M., Lulek, J., Schneider, R., (2013). Thioglycerol-capped Mn-doped ZnS quantum dot bioconjugates as efficient twophoton fluorescent nano-probes for bioimaging. *J. Mater. Chem. B*, 1, pp.698–706.
- Geszke, M., Murias, M., Balan, L., Medjahdi, G., Korczynski, J., Moritz, M., Lulek, J., Schneider, R., (2011). Folic acid-conjugated core/shell ZnS: Mn/ZnS quantum dots as targeted probes for two photon fluorescence imaging of cancer cells. *Acta Biomaterialia*, 7(3), pp.1327–1338.

- Gilbert, B., Huang, F., Lin, Z., Goodell, C., Zhang, H., Banfield, J.F., (2006). Surface chemistry controls crystallinity of ZnS nanoparticles. *Nano Letters*, 6(4), pp.605–610.
- Goodell, C.M., Gilbert, B., Weigand, S.J., Banfield, J.F., (2008). Kinetics of water adsorption-driven structural transformation of ZnS nanoparticles. *J. Phys. Chem. C*, 112, pp.4791–4796.
- Goudarzi, A., Aval, G.M., Park, S.S., Choi, M., (2009). Low-temperature growth of nanocrystalline Mn-doped ZnS thin films prepared by chemical bath deposition and optical properties. *Chem. Mater.*, 21(1), pp.2375–2385.
- Green, M., (2010). The nature of quantum dot capping ligands. *J. Mater. Chem.*, 20(28), pp.5797–5809.
- Grynko, D.O., Fedoryak, O.M., Smertenko, P.S., Ogurtsov, N.A., Pud, A.A., Noskov, Y.V., Dimitriev, O.P., (2013). Application of a CdS nanostructured layer in inverted solar cells. *J. Phys. D: Appl. Phys.*, 46(495114), pp.1–8.
- Guchhait, A., Rath, A.K. and Pal, A.J., (2010). Near-IR activity of hybrid solar cells: Enhancement of efficiency by dissociating excitons generated in PbS nanoparticles. *Appl. Phys. Lett.*, 96(73505), pp.1–3.
- Gyergyek, S., Makovec, D. and Drogenik, M., (2011). Colloidal stability of oleic- and ricinoleic acid-coated magnetic nanoparticles in organic solvents. *Journal of Colloid and Interface Science*, 354, pp.498–505.

- Ha, D., Ly, T., Caron, J.M., Zhang, H., Fritz, K.E., Robinson, R.D., (2015). A general method for high-performance Li-ion battery electrodes from colloidal nanoparticles without the introduction of binders or conductive-carbon additives: The Cases of MnS, Cu<sub>2-x</sub>S, and Ge. *ACS Appl. Mater. Interfaces*, 7, pp.25053–25060.
- Hablot, E., Zheng, D., Bouquey, M., Ave, L., (2008). Polyurethanes based on castor oil: Kinetics, chemical, mechanical and thermal properties. *Macromol. Mater. Eng.*, 293, pp.922–929.
- Halls, D.J., (1969). The Properties of dithiocarbamates. *Mikrochim. Acta*, pp.62–77.
- Han, J., Zhang, W., Chen, W., Thamizhmani, L., Azad, A.K., Zhu, Z., (2006). Far-infrared characteristics of ZnS nanoparticles measured by terahertz time-domain spectroscopy. *J. Phys. Chem. B*, 110, pp.1989–1993.
- Hannah, W. and Thompson, P.B., (2008). Nanotechnology, risk and the environment: a review. *J. Environ. Monit.*, 10, pp.291–300.
- Hansen, J.A., Mukhopadhyay, R., Hansen, J., Gothelf, K.V., (2006). Femtomolar electrochemical detection of DNA targets using metal sulphide nanoparticles. *J. Am. Chem. Soc.*, 128, pp.3860–3861.
- Hassan, E.A. and Zayed, S.E., (2014). Dithiocarbamates as precursors in organic chemistry; Synthesis and uses. *Phosphorus, Sulphur, and Silicon*, 189, pp.300–323.
- He, B., Zhou, L. and Huang, J., (2014). One-step synthesis of water-dispersible hydroxylfunctionalized NaYF<sub>4</sub>:Yb/Er upconversion nanoparticles. *Materials Letters*, 117, pp.142–145.

- He, W., Jia, H., Cai, J., Han, X., Zheng, Z., Wamer, W.G., Yin, J., (2016). Production of reactive oxygen species and electrons from photoexcited ZnO and ZnS nanoparticles: A comparative study for unraveling their distinct photocatalytic activities. *The Journal of Physical Chemistry C*, pp.1–33.
- He, Y., Wang, H. and Yan, X., (2008). Exploring Mn-doped ZnS quantum dots for the roomtemperature phosphorescence detection of enoxacin in biological fluids. *Anal. Chem.*, 80(10), pp.3832–3837.
- Hendrickson, A.R., Martin, R.L. and Rohde, N.M., (1974). Tris(dithiocarbamate) complexes of manganese(II), manganese(III), and manganese(IV). An electrochemical study. *Inorganic Chemistry*, 13(8), pp.1933–1939.
- Hobson, D.W., (2009). Commercialization of nanotechnology. *Advanced Review*, 1, pp.189–202.
- Hollingsworth, N., Ro, A., Islam, H., Mercy, M., Roldan, A., Bras, W., Wolthers, M., Catlow, C.R.A., Sankar, G., Hogarth, G., Leeuw, N.H.D., (2014). Active nature of primary amines during thermal decomposition of nickel dithiocarbamates to nickel sulphide nanoparticles. *Chem. Mater.*, 26, pp.6281–6292.
- Holzwarth, U. and Gibson, N., (2011). The Scherrer equation versus the “Debye – Scherrer equation.” *Nature Nanotechnology*, 6, p.534.
- Hosamani, K.M., Ganjihal, S.S. and Chavadi, D. V., (2004). Alternanthera triandra seed oil: A moderate source of ricinoleic acid and its possible industrial utilisation. *Industrial Crops and Products*, 19(2), pp.133–136.

- Hu, J.-S., Ren, L.-L., Guo, Y.-G., Liang, H.-P., Cao, A.-M., Wan, L.-J., Bai, C.-L., (2005). Mass production and high photocatalytic activity of ZnS nanoporous nanoparticles. *Angew. Chem.*, 117, pp.1295–1299.
- Huang, F., Zhang, H. and Banfield, J.F., (2003). Two-stage crystal-growth kinetics observed during hydrothermal coarsening of nanocrystalline ZnS. *Nano Letters*, 3(3), pp.373–378.
- Huang, X., Wang, M., Willinger, M., Shao, L., Su, D.S., Meng, X., (2012). Assembly of threedimensional nanorod and single crystalline hollow ZnS nanotube arrays. *ACS Nano*, (8), pp.7333–7339.
- Hullavarad, N. V, Hullavarad, S.S. and Karulkar, P.C., (2008). Cadmium sulphide (CdS) nanotechnology: Synthesis and applications. *J. Nanosci. Nanotechnol.*, 8(7), pp.3272–3299.
- Humeres, E., Debacher, N.A. and Sierra, M.M.D.S., (1999). Mechanisms of acid decomposition of Dithiocarbamates. 2. Efficiency of the intramolecular general acid catalysis. *J. Org. Chem.*, (11), pp.1807–1813.
- Isbell, T.A., (2011). Chemistry and physical properties of estolides. *GRASAS Y ACEITES*, 62(1), pp.8–20.
- Islam, H.-U., Roffey, A., Hollingsworth, N., Catlow, R., Wolthers, M., Leeuw, N.D., Bras, W., Sankar, G., Hogarth, G., (2013). In situ XAS of the solvothermal decomposition of dithiocarbamate complexes. *Journal of Physics: Conference Series*, 430, pp.1–5.
- Iv, M., Telischak, N., Holdsworth, S.J., Yeom, K.W., Daldrup-Link, H., (2015). Clinical applications of iron oxide nanoparticles for magnetic resonance imaging of brain tumors. *Nanomedicine*, 10, pp.993–1018.

- Jacintho, G.V.M., Kosaka, P.M., Petri, D.F.S., Suarez, P.A.Z., Rubim, J.C., (2009). Synthesis and characterization of magnetic composites based on cis-polyisoprene and  $\text{CoFe}_2\text{O}_4$  nanoparticles. *Journal of Nanoscience and Nanotechnology*, 9(6), pp.3617–3621.
- Jacob, S.S.K., Kumar, S.S. and Saravanan, R., (2012). Synthesis and characterization of the nano semiconducting material cadmium sulphide. *Materials Science Forum*, 699, pp.79–88.
- Jafari, M., Kadivar, M. and Goli, S.A.H., (2013). Response surface-optimized synthesis of cis -9, trans-11-octadecadienoic acid through dehydration of castor oil. *International Food Research Journal*, 20(4), pp.1997–2003.
- Jahanbin, T., Gaceur, M., Gros-Dagnac, H., Benderbous, S., Merah, S.A., (2015). High potential of Mn-doped ZnS nanoparticles with different dopant concentrations as novel MRI contrast agents: synthesis and in vitro relaxivity studies. *J. Nanopart Res*, 17(258), pp.1–12.
- Jana, S., Srivastava, B.B. and Pradhan, N., (2011). Correlation of dopant states and host bandgap in dual-doped semiconductor nanocrystals. *J. Phys. Chem. Lett.*, 2, pp.1747–1752.
- Jassby, D., Wiesner, M. and Carolina, N., (2011). Characterization of ZnS nanoparticle aggregation using photoluminescence. *Langmuir*, 27(3), pp.902–908.
- Jia, J., Tian, J., Mi, W., Tian, W., Liu, X., Dai, J., Wang, X., (2013). Growth kinetics of CdSe nanocrystals synthesized in liquid paraffin via one-pot method. *J Nanopart Res*, pp.1–12.
- Jiang, P., Zhu, D.-L., Zhu, C.-N., Zhang, G.-J., Pang, D.-W., (2014). Highly reactive chalcogenide precursor for the synthesis of metal chalcogenide quantum dots. *Nanoscale*, 2(2), p.303.
- Jin, R., Chen, G., Wang, Q., Pei, J., Wang, G., Wang, L., (2010). Flowerlike PbS microcrystals :

citric acid assisted synthesis, shape evolution, and electrical conductivities. *Eur. J. Inorg. Chem.*, pp.5700–5708.

Jindal, Z. and Verma, N.K., (2008). Photoluminescent properties of ZnS: Mn nanoparticles with in-built surfactant. *J Mater Sci*, 43, pp.6539–6545.

Joicy, S., Saravanan, R., Prabhu, D., Ponpandian, N., Thangadurai, P., (2014). Mn<sup>2+</sup> ion influenced optical and photocatalytic behaviour of Mn-ZnS quantum dots prepared by microwave assisted technique. *RSC Adv.*, 4, pp.44592–44599.

Joo, J., Na, Hyon B., Yu, T., Yu, J.H., Kim, Y.W., Wu, F., Zhang, J.Z., Hyeon, T., (2003). Generalized and facile synthesis of semiconducting metal sulphide nanocrystals. *J. Am. Chem. Soc.*, 125, pp.11100–11105.

Joris, J., Aspila, K.I. and Chakrabarti, C.L., (1969). On the mechanism of decomposition of dithiocarbamates. *The Journal of Physical Chemistry*, pp.860–865.

Jun, Y., Jung, Y. and Cheon, J., (2002). Architectural control of magnetic semiconductor nanocrystals. *J. Am. Chem. Soc.*, 124(4), pp.615–619.

Jung, Y.K., Kim, J. I. and Lee, J., (2010). Thermal decomposition mechanism of single-molecule precursors forming metal sulphide Nanoparticles. *J. Am. Chem. Soc.*, (21), pp.178–184.

Kaftelen, H., Tuncer, M., Tu, S., Repp, S., Gocmez, H., Thomann, R., Weber, S., Erdem, E., (2013). Mn-substituted spinel Li<sub>4</sub>Ti<sub>5</sub>O<sub>12</sub> materials studied by multifrequency EPR spectroscopy. *J. Mater. Chem. A*, 1, pp.9973–9982.

Kalpana, K. and Selvaraj, V., (2015). Photodegradation and antibacterial studies of ZnS enwrapped fly ash nanocomposite for multipurpose industrial applications. *RSC Adv.*, pp.1–

30.

- Kane, R.S., Cohen, R.E. and Silbey, R., (1996). Theoretical study of the electronic structure of PbS nanoclusters. *J. Phys. Chem.*, 100, pp.7928–7932.
- Kanmani, S.S., Rajkumar, N. and Ramachandran, K., (2011). Structural, optical and magnetic properties of  $Zn_{1-x}M_xS$  ( $x=0.00, 0.01$  and  $0.03$ ) nanoparticles. *J. Nano- Electron. Phys.*, 3, pp.1064–1070.
- Kar, S. and Chaudhuri, S., (2005). Controlled synthesis and photoluminescence properties of ZnS nanowires and nanoribbons. *J. Phys. Chem. B*, 109, pp.3298–3302.
- Karar, N., Raj, S. and Singh, F., (2004). Properties of nanocrystalline ZnS:Mn. *Journal of Crystal Growth*, 268, pp.585–589.
- Karpakavalli, M., Arthi, I. and Seena, K.X., (2012). Microwave assisted isolation of hesperidin, ricinoleic acid and piperic acid. *Journal of Scientific Research in Pharmacy*, 1(3), pp.76–79.
- Kaur, N., Kaur, S., Singh, J., Rawat, M., (2016). A review on zinc sulphide nanoparticles: From synthesis, properties to applications. *J Bioelectron Nanotechnol*, 1(1), pp.0–5.
- Khalkhali, M., Zeng, H., Liu, Q., Zhang, H., (2016). Structural evolutions of ZnS nanoparticles in hydrated and bare states. *The Journal of Physical Chemistry C*, pp.1–41.
- Khosravi, A.A., Kundu, M., Kuruvilla, B.A., Shekhawat, G.S., Gupta, R.P., Sharma, A.K., Vyas, P.D., Kulkarni, S.K., (1995). Manganese doped zinc sulphide nanoparticles by aqueous method. *Appl. Phys. Lett.*, 67(17), pp.10–13.
- Kim, B.H., Lee, N., Kim, H., An, K., Park, Y., Choi, Y., Shin, K., Lee, Y., Kwon, S.G., Na,

- H.B., Park, J.-G., Ahn, T.-Y., Kim, Y.-W., Moon, W.K., Choi, S.H., Hyeon, T., (2011). Large-scale synthesis of uniform and extremely small-sized iron oxide nanoparticles for high-resolution T<sub>1</sub> magnetic resonance imaging contrast agents. *J. Am. Chem. Soc.*, 133, pp.12624–12631.
- Kim, J., Park, K., Vazquez-Zuniga, L.A., Kim, H., Han, M., (2015). Optical characteristics of Mn<sup>2+</sup> doped ZnS nanoparticles for laser based bio-sensing. *Advanced Photonics*, 1(1), pp.3–5.
- Kole, A.K., Tiwary, C.S. and Kumbhakar, P., (2014). Morphology controlled synthesis of wurtzite ZnS nanostructures through simple hydrothermal method and observation of white light emission from ZnO obtained by annealing the synthesized ZnS nanostructures. *J. Mater. Chem. C*, pp.1–9.
- Kripal, R., Gupta, A.K., Mishra, S.K., Srivastava, R.K., Pandey, A.C., Prakash, S.G., (2010). Photoluminescence and photoconductivity of ZnS: Mn<sup>2+</sup> nanoparticles synthesized via coprecipitation method. *Spectrochimica Acta Part A: Molecular and Biomolecular Spectroscopy*, 76(5), pp.523–530.
- Kulkarni, M.G. and Sawant, S.B., (2003). Kinetics of the catalytic esterification of castor oil with lauric acid using n-butyl benzene as a water entrainer. *JAOCS*, 80(10), pp.1033–1038.
- Kumari, M.M. and Philip, D., (2013). Facile one-pot synthesis of gold and silver nanocatalysts using edible coconut oil. *Spectrochimica Acta - Part A: Molecular and Biomolecular Spectroscopy*, 111, pp.154–160..

- Kwon, S.G. and Hyeon, T., (2008). Colloidal chemical synthesis and formation kinetics of uniformly sized nanocrystals of metals, oxides and chalcogenides. *Accounts of Chemical Research*, 41(12), pp.1696–1709.
- Kwon, S.G. and Hyeon, T., (2011). Formation mechanisms of uniform nanocrystals via hotinjection and heat-up methods. *Small*, (19), pp.2685–2702.
- Kwon, S.G. and Hyeon, T., (2009). Nanoscale materials in chemistry, K. J. Klabunde and R. M. Richards, eds. *John Wiley and Sons, Inc.*, pp.142–150.
- Kyobe, J.W., Mubofu, E.B., Makame, Y.M.M., Mlowe, S., Revaprasadu, N., (2016). Cadmium sulphide quantum dots stabilized by castor oil and ricinoleic acid. *Physica E: LowDimensional Systems and Nanostructures*, 76, pp.95–102.
- Kyobe, J.W.M., Mubofu, E.B. and Makame, Y.M.M., (2016). The use of castor oil and ricinoleic acid in lead chalcogenide nanocrystal synthesis. *International Nano Letters*. pp.1-8
- Lai, C.-H., Lu, M. and Chen, L., (2012). Metal sulphide nanostructures: synthesis, properties and applications in energy conversion and storage. *J Mater Sci*, 22(19), pp.19–30.
- Lattuada, M. and Hatton, T.A., (2007). Functionalization of monodisperse magnetic nanoparticles. *Langmuir*, 29(24), pp.2158–2168.
- Lesnyak, V., Gaponik, N. and Eychmuller, A., (2012). Colloidal semiconductor nanocrystals: the aqueous approach. *Chem Soc Rev*, pp.1–24.
- Lewis, E., Haigh, S. and O'Brien, P., (2014). The synthesis of metallic and semiconducting nanoparticles from reactive melts of precursors. *J. Mater. Chem. A*, 2, pp.570–580.

- Li, Y., Qian, F., Xiang, J., Lieber, C.M., (2006). Nanowire electronic and optoelectronic devices. *Materialstoday*, 9(10), pp.18–27.
- Li, Y., Chen, J., Zhu, C., Wang, L., Zhao, D., Zhuo, S., Wu, Y., (2004). Preparation and application of cysteine-capped ZnS nanoparticles as fluorescence probe in the determination of nucleic acids. *Spectrochimica Acta Part A*, 60, pp.1719–1724.
- Li, Z., Wang, J., Xu, X., Ye, X., (2008). The evolution of optical properties during hydrothermal coarsening of ZnS nanoparticles. *Materials Letters*, 62, pp.3862–3864.
- Lin, J., (2009). Ratios of regioisomers of triacylglycerols containing dihydroxy fatty acids in castor oil by mass spectrometry. *J. Am. Oil Chem Soc*, pp.1031–1035.
- Lin, J.-T. and Chen, G.Q., (2012). Ratios of regioisomers of minor acylglycerols less polar than triricinolein in castor oil estimated by mass spectrometry. *J. Am. Oil Chem Soc*, 89, pp.1785–1792.
- Liu, H., Hu, L., Watanabe, K., Hu, X., Dierre, B., Kim, B., Sekiguchi, T., Fang, X., (2013). Cathodoluminescence modulation of ZnS nanostructures by morphology, doping, and temperature. *Adv. Funct. Mater.*, 23, pp.3701–3709.
- Liu, J., Chen, H., Lin, Z., Lin, J., (2010). Preparation of surface imprinting polymer capped Mn-doped ZnS quantum dots and their application for chemiluminescence detection of 4-nitrophenol in tap water. *Anal. Chem.*, 82(17), pp.7380–7386.
- Liu, J., Yu, H., Wu, Z., Wang, W., (2008). Size-tunable near-infrared PbS nanoparticles synthesized from lead carboxylate and sulphur with oleylamine as stabilizer. *Nanotechnology*, 19, pp.1–9.

- Liu, X., Jiang, Y., Lan, X., Li, S., Wu, D., Han, T., Zhong, H., Zhang, Z., (2011). Synthesis of high quality and stability CdS quantum dots with overlapped nucleation-growth process in large scale. *Journal of Colloid and Interface Science*, 354, pp.15–22.
- Liu, X., Du, J., Li, C., Han, X., Hu, X., Cheng, F., Chen, J., (2015). The anion effect on the oxygen reduction of MnX (X = O, S, and Se) catalysts. *J. Mater. Chem. A*, pp.1–7.
- Logar, M., Jancar, B., Recnik, A., Suvorov, D., (2009). Controlled synthesis of pure and doped ZnS nanoparticles in weak polyion assemblies: growth characteristics and fluorescence properties. *Nanotechnology*, 20, pp.1–11.
- Lopez-sanchez, O., Lembke, D., Kayci, M., Radenovic, A., Kis, A., (2013). Ultrasensitive photodetectors based on monolayer MoS<sub>2</sub>. *Nature Nanotechnology*, pp.1–5.
- Lovric, J., Bazzi, H.S., Cuie, Y., Fortin, G.R.A., Winnik, F.M., Maysinger, D., (2005). Differences in subcellular distribution and toxicity of green and red emitting CdTe quantum dots. *J Mol Med*, 83, pp.377–385.
- Lu, J., Qi, P., Peng, Y., Meng, Z., Yang, Z., (2001). Metastable MnS crystallites through solvothermal synthesis. *Chem. Mater.*, 13, pp.2169–2172.
- Ma, X., Song, J. and Yu, Z., (2011). The light emission properties of ZnS:Mn nanoparticles. *Thin Solid Films*, 519(15), pp.5043–5045.
- Malik, M.A., Afzaal, M. and O'Brien, P., (2010). Precursor chemistry for main group elements in semiconducting materials. *Chem. Rev.*, 110, pp.4417–4446.
- Malik, M.A., O'Brien, P. and Revaprasadu, N., (2001). Synthesis of TOPO-capped Mn-doped ZnS and CdS quantum dots. *J. Mater. Chem.*, 11, pp.2382–2386.

- Manzoor, K., Johny, S., Thomas, D., Setua, S., (2009). Bio-conjugated luminescent quantum dots of doped ZnS: a cyto-friendly system for targeted cancer imaging. *Nanotechnology*, 20, pp.1–13.
- Marbaniang, E. and Donboklang, (2014). Nanotechnology - A new era in medicine and diagnostics. *Int J Cur Res Rev*, 6(24), pp.7–10.
- Marcotrigiano, G., Pellacani, G.C. and Preti, C., (1974). Piperidine-, thiomorpholine-4- and n-methylpiperazine-4-carbodithioate transition metal complexes. *J. Inorg. Nucl. Chem.*, 36, pp.3709–3712.
- Massoud, T.F. and Gambhir, S.S., (2003). Molecular imaging in living subjects: seeing fundamental biological processes in a new light. *Genes Dev.*, 17, pp.545–580.
- Mathew, M.E., Mohan, J.C., Manzoor, K., Nair, S.V., Tamura, H., Jayakumar, R., (2010). Folate conjugated carboxymethyl chitosan – manganese doped zinc sulphide nanoparticles for targeted drug delivery and imaging of cancer cells. *Carbohydrate Polymers*, 80(2), pp.442–448.
- McNaughter, P.D., Saah, S.A., Akhtar, M., Abdulwahab, K., Malik, M.A., Raftery, J., Awudza, A.M., O'Brien, P., (2016). The effect of alkyl chain length on the structure of lead(II) xanthates and their decomposition to PbS in melt reactions. *Dalton Trans.*, 45, pp.16345–16353.
- Mehta, S.K., Kumar, S., Chaudhary, S., Bhasin, K.K., Gradzielski, M., (2009). Evolution of ZnS nanoparticles via facile CTAB aqueous micellar solution route: A study on controlling parameters. *Nanoscale Res Lett*, 4, pp.17–28.

- Meneghetti, S.M.P., Meneghetti, M.R., Wolf, C.R., Silva, E.C., Lima, G.E.S., Silva, L.D.L., Serra, T.M., Cauduro, F., (2006). Biodiesel from castor oil: A comparison of ethanolysis versus methanolysis., *Energy & Fuels*, 20(5), pp.2262–2265.
- Meng, J., Zhao, Y., Li, Z., Wang, L., Tian, Y., (2016). Phase-transfer preparation of ultrasmall MnS nanocrystals with high performance of MRI contrast agent. *RSC Adv.*, pp.1–26.
- Michel, F.M., Schoonen, M.A.A., Zhang, X.V., Martin, S.T., Parise, J.B., (2006). Hydrothermal synthesis of pure  $\alpha$ -phase manganese(II) sulphide without the use of organic reagents. *Chem. Mater.*, 18, pp.1726–1736.
- Miller, M.A., Gadde, S., Pfirschke, C., Engblom, C., Sprachman, M.M., Kohler, R.H., Yang, K.S., Laughney, A.M., Wojtkiewicz, G., Kamaly, N., Bhonagiri, S., Pittet, M.J., Farokhzad, O.C., Weissleder, R., (2015). Predicting therapeutic nanomedicine efficacy using a companion magnetic resonance imaging nanoparticle. *Bioengineering*, 7(314), pp.1–13.
- Mlondo, S.N., Revaprasadu, N., Christian, P., Helliwell, M., O'Brien, P., (2009). Cadmium thiosemicarbazide complexes as precursors for the synthesis of nanodimensional crystals of CdS. *Polyhedron*, 28(11), pp.2097–2102.
- Mlowe, S., Lewis, D.J., Malik, M.A., Raftery, J., Mubofu, E.B., O'Brien, P., Revaprasadu, N., (2014). Bis(piperidinedithiocarbamate)pyridinecadmium(II) as a single-source precursor for the synthesis of CdS nanoparticles and aerosol-assisted chemical vapour deposition (AACVD) of CdS thin films. *New Journal of Chemistry*, 38, pp.6073–6080.
- Moloto, N., Revaprasadu, N., Moloto, M.J., O'Brien, P., Helliwell, M., (2007). N, N'-Diisopropyl- and N, N'-dicyclohexylthiourea cadmium (II) complexes as precursors for the synthesis of CdS nanoparticles. *Polyhedron*, 26, pp.3947–3955.

- Mondal, S.P., Bera, S., Narender, G., Ray, S.K., (2012). CdSe quantum dots-poly (3hexylthiophene) nanocomposite sensors for selective chloroform vapor detection at room temperature. *Appl. Phys. Lett.*, 101(173108), pp.1–4.
- Mourdikoudis, S. and Liz-Marza, L.M., (2013). Oleylamine in nanoparticle synthesis. *Chem. Mater.*, pp.A-L.
- Mthethwa, T., Pullabhotla, V.S.R.R., Mdluli, P.S., Wesley-smith, J., Revaprasadu, N., (2009). Synthesis of hexadecylamine capped CdS nanoparticles using heterocyclic cadmium dithiocarbamates as single source precursors. *Polyhedron*, 28(14), pp.2977–2982.
- Mubofu, E.B., (2016). Castor oil as a potential renewable resource for the production of functional materials. *Sustain. Chem. Process*, 4(1), pp.1–12.
- Murray, C.B., Norris, D.J. and Bawendi, M.G., (1993). Synthesis and characterization of nearly monodisperse CdE(E=S, Se, Te) semiconductor nanocrystallites. *J. Am. Chem. Soc.*, 115(19), pp.8706–8715.
- Murugadoss, G., (2012). Luminescence properties of co-doped ZnS:Ni, Mn and ZnS:Cu, Cd nanoparticles. *Journal of Luminescence*, 132, pp.2043–2048.
- Mutlu, H. and Meier, M.A.R., (2010). Castor oil as a renewable resource for the chemical industry. *Eur. J. Lipid Sci. Technol.*, 112, pp.10–30.
- Nair, P.S., Radhakrishnan, T., Revaprasadu, N., Kolawole, G., O'Brien, P., (2002). Cadmium ethylxanthate: A novel single-source precursor for the preparation of CdS nanoparticles. *J. Mater. Chem.*, 12, pp.2722–2725.

- Nair, P.S., Radhakrishnan, T., Revaprasadu, N., Kolawole, G.A., O'Brien, P., (2003). Cd(NH<sub>2</sub>CSNHNHCSNH<sub>2</sub>)Cl<sub>2</sub>: a new single-source precursor for the preparation of CdS nanoparticles. *Polyhedron*, 22, pp.3129–3135.
- Nair, P.S., Revaprasadu, N., Radhakrishnan, T., Kolawole, G.A., (2001). Preparation of CdS nanoparticles using the cadmium(II) complex of N,N'-bis(thiocarbamoyl)hydrazine as a simple single-source precursor. *J. Mater. Chem.*, 1(112), pp.1555–1556.
- Nazerdeylami, S., Saievar-iranizad, E., Dehghani, Z., Molaei, M., (2011). Synthesis and photoluminescent and nonlinear optical properties of manganese doped ZnS nanoparticles. *Physica B: Physics of Condensed Matter*, 406(1), pp.108–111.
- Neo, M.S., Venkatram, N., Li, G.S., Chin, W.S., Wei, J., (2009). Size-dependent optical nonlinearities and scattering properties of PbS nanoparticles. *J. Phys. Chem. C*, 113, pp.19055–19060.
- Neves, J. D., Amiji, M.M., Bahia, F.M., Sarmiento, B., (2010). Nanotechnology-based systems for the treatment and prevention of HIV/AIDS. *Advanced Drug Delivery Reviews*, 62(4–5), pp.458–477.
- Ng, S.M., Koneswaran, M. and Narayanaswamy, R., (2016). A review on fluorescent inorganic nanoparticles for optical sensing applications, *RSC Adv.*, 6, pp.21624-21661
- Norris, D.J., Efros, A.L. and Erwin, S.C., (2008). Doped nanocrystals. *Science*, 319, pp.1776–1779.
- Nyamen, L.D., Pullabhotla, V.S.R.R., Nejo, A.A., Ndifon, P.T., Revaprasadu, N., (2011). Heterocyclic dithiocarbamates: precursors for shape controlled growth of CdS nanoparticles. *New J. Chem.*, 35, pp.1133–1139.

- Nyamen, L.D., Nejo, A.A., Pullabhotla, V.S.R., Ndifon, P.T., Malik, M.A., Akhtar, J., O'Brien, P., Revaprasadu, N., (2014). The syntheses and structures of Zn(II) heterocyclic piperidine and tetrahydroquinoline dithiocarbamates and their use as single source precursors for ZnS nanoparticles. *Polyhedron*, 67, pp.129–135.
- Nyamen, L.D., Revaprasadu, N. and Ndifon, P.T., (2014). Low temperature synthesis of PbS and CdS nanoparticles in olive oil. *Materials Science in Semiconductor Processing*, 27(1), pp.191–196.
- Ogunniyi, D.S., (2006). Castor oil: A vital industrial raw material. *Bioresource Technology*, 97(9), pp.1086–1091.
- Onwudiwe, D.C. and Ajibade, P.A., (2010). Synthesis and characterization of metal complexes of N -alkyl- N -phenyl dithiocarbamates. *Polyhedron*, 29(5), pp.1431–1436.
- Ouyang, J., Vincent, M., Kingston, D., Descours, P., Boivineau, T., Zaman, B., Wu, X., Yu, K., (2009). Noninjection, one-pot synthesis of photoluminescent colloidal homogeneously alloyed CdSeS quantum dots. *J. Phys. Chem.*, 113, pp.5193–5200.
- Ozcan, H M, and Sagiroglu, A., (2009). Production of ricinoleic acid from castor oil by immobilised lipases., *Preparative Biochemistry and Biotechnology*, 39(2), pp.170–182.
- Pacheco-torgal, F. and Jalali, S., (2010). Nanotechnology: Advantages and drawbacks in the field of construction and building materials. *Construction and Building Materials*, pp.1–9.
- Pan, D., Schmieder, A.H., Wickline, S.A., Lanza, G.M., (2011). Manganese-based MRI contrast agents: past, present, and future. *Tetrahedron*, 67(44), pp.8431–8444.

- Park, J., Joo, J., Kwon, S.G., Jang, Y., Hyeon, T., (2007). Synthesis of monodisperse spherical nanocrystals. *Angew. Chem. Int. Ed.*, 46, pp.4630–4660.
- Parthasarathi, V. and Thilagavathi, G., (2011). Synthesis and characterization of zinc oxide nanoparticles and its application on fabrics for microbe resistant defence clothing. *Int J Pharm Pharm Sci*, 3(4), pp.392–398.
- Patel, J.D., Mighri, F. and Ajji, A., (2012). Generalized chemical route to develop fatty acid capped highly dispersed semiconducting metal sulphide nanocrystals. *Materials Research Bulletin*, 47(8), pp.2016–2021.
- Peng, W.Q., Qu, S.C., Cong, G.W., Zhang, X.Q., Wang, Z.G., (2005). Optical and magnetic properties of ZnS nanoparticles doped with  $Mn^{2+}$ . *Journal of Crystal Growth*, 282, pp.179–185.
- Peng, Z.A. and Peng, X., (2001). Formation of high-quality CdTe, CdSe, and CdS nanocrystals using CdO as precursor. *J. Am. Chem. Soc.*, 123(1), pp.183–184.
- Penn, R.L. and Banfield, J.F., (1999). Morphology development and crystal growth in nanocrystalline aggregates under hydrothermal conditions: Insights from titania. *Geochimica et Cosmochimica Acta*, 63(10), pp.1549–1557.
- Pereira, A.S., Silva, N.J.O., Trindade, T., Pereira, S., (2012). A single-source route for the synthesis of metal oxide nanoparticles using vegetable oil solvents. *Journal of Nanoscience and Nanotechnology*, 12(12), pp.8963–8968.
- Pérez-de-Luque, A. and Rubiales, D., (2009). Nanotechnology for parasitic plant control. *Pest Manag Sci*, 65, pp.540–545.

- Phuruangrat, A., Thongtem, T., Kuntalue, B., Thongtem, S., (2012). Characterization of cubic and star-shaped dendritic PbS structures synthesized by a solvothermal method. *Materials Letters*, 81, pp.55–58.
- Piazza, G.J. and Farrell, H.M., (1991). Generation of ricinoleic acid from castor oil using the lipase from ground oat (*Avena Sativa* L.) seeds as a catalyst. *Biotechnology Letters*, 13(3), pp.179–184.
- Poole, C.P. and Owens, F.J., (2003). Introduction to nanotechnology. *John Wiley and Sons, Inc.*, ISBN 0-471, pp.1–400.
- Porta, F.A. L., Andre, J., Li, M.S., Sambrano, J.R., Varela, J.A., Longo, E., (2014). Zinc blende versus wurtzite ZnS nanoparticles: control of the phase and optical properties by tetrabutylammonium hydroxide. *Phys. Chem. Chem. Phys.*, 16, pp.20127–20137.
- Prabhu, R.R. and Khadar, M.A., (2005). Characterization of chemically synthesized CdS nanoparticles. *Pramana - J. Phys.*, 65(5), pp.801–807.
- Pradhan, N., Katz, B. and Efrima, S., (2003). Synthesis of high-quality metal sulphide nanoparticles from alkyl xanthate single precursors in alkylamine solvents. *J. Phys. Chem. B*, 107, pp.13843–13854.
- Pradhan, N. and Sarma, D.D., (2011). Advances in light-emitting doped semiconductor nanocrystals. *J. Phys. Chem. Lett.*, 2, pp.2818–2826.
- Preti, C., Tosi, G. and Zannini, P., (1980). Investigations of chromium(III), manganese(III), tin(II) and lead(II) dithiocarbamate complexes. *Journal of Molecular Structure*, 65, pp.283–292.

- Puglisi, A., Mondini, S., Cenedese, S., Ferretti, A.M., Santo, N., Ponti, A., (2010). Monodisperse octahedral alpha-MnS and MnO nanoparticles by the decomposition of manganese oleate in the presence of sulphur. *Chem. Mater.*, 22, pp.2804–2813.
- Purbia, R. and Paria, S., (2015). Yolk/shell nanoparticles: Classifications, synthesis, properties and applications. *Nanoscale*, pp.1–230.
- Qu, L., Peng, Z.A. and Peng, X., (2001). Alternative routes toward high quality CdSe nanocrystals. *Nano Letters*, 1(6), pp.333–337.
- Qu, Z., Yan, L., Li, L., Xu, J., Liu, M., Li, Z., Yan, N., (2014). Ultra effective ZnS nanocrystals sorbent for mercury(II) removal based on size-dependent cation exchange. *ACS Appl. Mater. Interfaces*, p.A-G.
- Ramasamy, V., Praba, K. and Murugadoss, G., (2012). Synthesis and study of optical properties of transition metals doped ZnS nanoparticles. *Spectrochimica Acta Part A: Molecular and Biomolecular Spectroscopy*, 96, pp.963–971.
- Ramsden, J.J., (2005). What is nanotechnology? *Nanotechnology Perceptions*, 1, pp.3–17.
- Rana, A.K., Rana, S.B., Kumari, A., Kiran, V., (2009). Significance of nanotechnology in construction engineering. *International Journal of Recent Trends in Engineering*, 1(4), pp.6–8.
- Rao, S.S., Durga, I.K., Tulasi-varma, C.V., Punnoose, D., Kim, S., Kim, H., (2015). Enhance the performance of quantum dot- sensitized solar cell by manganese-doped ZnS films as a passivation layer. *Organic Electronics*, 26, pp.200–207.

- Rath, A.K., Bhaumik, S. and Pal, A.J., (2010). Mn-doped nanocrystals in light-emitting diodes: Energy-transfer to obtain electroluminescence from quantum dots. *Appl. Phys. Lett.*, 97(113502), pp.1–4.
- Reddy, D.A., Sambasivam, S., Murali, G., Poornaprakash, B., Vijayalakshmi, R.P., Aparna, Y., Reddy, B.K., Rao, J.L., (2012). Effect of Mn co-doping on the structural, optical and magnetic properties of ZnS: Cr nanoparticles. *Journal of Alloys and Compounds*, 537, pp.208–215.
- Rempel, J.Y., Bawendi, M.G. and Jensen, K.F., (2009). Insights into the kinetics of semiconductor nanocrystal nucleation and growth. *J. Am. Chem. Soc.*, 131, pp.4479–4489.
- Resch-Genger, U., Grabolle, M., Cavaliere-Jaricot, S., Nitschke, R., Nann, T., (2008). Quantum dots versus organic dyes as fluorescent labels. *Nature methods*, 5(9), pp.763–775.
- Ribeiro, C., Lee, E.J.H., Longo, E., Leite, E.R., (2005). A kinetic model to describe nanocrystal growth by the oriented attachment mechanism. *ChemPhysChem*, 6, pp.690–696.
- Rofouei, M.K., Tajarrod, N., Masteri-Farahani, M., Zadmand, R., (2015). A new fluorescence sensor for cerium (III) ion using glycine dithiocarbamate capped manganese doped ZnS quantum dots. *J Fluoresc*, pp.1–12.
- Rowland, C.E., Susumu, K., Stewart, M.H., Oh, E., Mäkinen, A.J., Shaughnessy, T.J.O., Kushto, G., Wolak, M.A., Erickson, J.S., Alexander, L., Huston, A.L., Delehanty, J.B., (2015). Imaging cellular membrane potential through ionization of quantum dots. *Proc. of SPIE*, 9722, pp.1–8.
- Salavati-Niasari, M., Ghanbari, D. and Loghman-estarki, M.R., (2012). Star-shaped PbS nanocrystals prepared by hydrothermal process in the presence of thioglycolic acid. *Polyhedron*, 35(1), pp.149–153.

- Salavati-niasari, M., Sobhani, A. and Davar, F., (2010). Synthesis of star-shaped PbS nanocrystals using single-source precursor. *Journal of Alloys and Compounds*, 507(1), pp.77–83.
- Salimon, J., Noor, D.A.M., Nazrizawati, A.T., Firdaus, M.Y.M., Noraishah, A., (2010). Fatty acid composition and physicochemical properties of Malaysian castor bean *ricinus communis* L. seed oil. *Sains Malaysiana*, 39(5), pp.761–764.
- Sanna, V., Pala, N. and Sechi, M., (2014). Targeted therapy using nanotechnology: focus on cancer. *International Journal of Nanomedicine*, 9, pp.467–483.
- Santra, P.K. and Kamat, P. V, (2012). Mn-doped quantum dot sensitized solar cells: A strategy to boost efficiency over 5%. *J. Am. Chem. Soc.*, 134, pp.23–26.
- Sapra, S., Rogach, A.L. and Feldmann, J., (2006). Phosphine-free synthesis of monodisperse CdSe nanocrystals in olive oil. *J. Mater. Chem.*, 16, pp.3391–3395.
- Sarkar, R., Tiwary, C.S., Kumbhakar, P.Ã., Basu, S., Mitra, A.K., (2008). Yellow-orange light emission from Mn<sup>2+</sup>-doped ZnS nanoparticles. *Physica E*, 40, pp.3115–3120.
- Sawhney, A.P.S., Singh, K.V., Pang, S.S., Li, G., Hui, D., (2008). Modern applications of nanotechnology in textiles. *Textile Research Journal*, 78(8), pp.731–739.
- Scheele, M., Hanifi, D., Zhrebetsky, D., Chourou, S.T., Axnanda, S., Rancatore, B.J., Thorkelsson, K., Xu, T., Liu, Z., Wang, L., Liu, Y., Alivisatos, A.P., (2014). PbS nanoparticles capped with tetrathiafulvalenetetracarboxylate: Utilizing energy level alignment for efficient carrier transport. *ACS nano*, 8(3), pp.2532–2540.
- Schneider, R.C.D.S., Baldissarelli, V.Z., Trombetta, F., Martinelli, M., Caramao, B.E., (2004). Optimization of gas chromatographic – mass spectrometric analysis for fatty acids in

- hydrogenated castor oil obtained by catalytic transfer hydrogenation. *Analytica Chimica Acta*, 505, pp.223–226.
- Sekhon, B.S., (2010). Food nanotechnology – an overview. *Nanotechnology, Science and Applications*, 3, pp.1–15.
- Serrano, E., Rus, G. and Garc, J., (2009). Nanotechnology for sustainable energy. *Renewable and Sustainable Energy Reviews*, 13, pp.2373–2384.
- Shamsipur, M. and Reza, H., (2014). Study of photocatalytic activity of ZnS quantum dots as efficient nanoparticles for removal of methyl violet: Effect of ferric ion doping. *Spectrochimica Acta Part A: Molecular and Biomolecular Spectroscopy*, 122, pp.260–267.
- Sharma, A.K., (1986). Thermal behaviour of metal-dithiocarbamates. *Thermochimica Acta*, 104, pp.339–372.
- Sharma, J., Singh, Y., Bohra, R., Rai, A.K., (1996). Synthesis and spectral studies of diorganotin heterocyclic dithiocarbamate complexes: The crystal structure of  $(\text{CH}_3)_2\text{Sn}[\text{S}_2\text{CNCH}_2\text{CH}_2\text{CH}_2\text{CH}_2\text{CH}_2]_2$ . *Polyhedron*, 15(7), pp.1097–1102.
- Shen, H., Yuan, H., Wu, F., Bai, X., Zhou, C., Wang, H., Lu, T., Qin, Z., Ma, L., Li, L.S., (2012). Facile synthesis of high-quality  $\text{CuInZn}_x\text{S}_{2+x}$  core/shell nanocrystals and their. *J. Mater. Chem.*, 22, pp.18623–18630.
- Shen, S., Zhang, Y., Peng, L., Xu, B., Du, Y., Deng, M., Xu, H., Wang, Q., (2011). Generalized synthesis of metal sulphide nanocrystals from single-source precursors: size, shape and chemical composition control and their properties. *CrystEngComm*, 13, pp.4572–4579.

- Shen, S. and Wang, Q., (2012). Rational tuning the optical properties of metal sulphide nanocrystals and their applications. *Chemistry of Materials*, pp.1–14.
- Shombe, B.G., Mubofu, B.E., Mlowe, S., Revaprasadu, N., (2015). Synthesis and characterization of castor oil and ricinoleic acid capped CdS nanoparticles using single source precursors. *Materials Science in Semiconductor Processing*, pp.1–8.
- Singh, D.P., Daoudi, A., Gupta, S.K., Pandey, S., Vimal, T., Manohar, R., Kole, A.K., Kumbhakar, P., Kumar, A., (2016). Mn<sup>2+</sup> doped ZnS quantum dots in ferroelectric liquid crystal matrix: Analysis of new relaxation phenomenon, faster optical response, and concentration dependent quenching in photoluminescence. *J. Appl. Phys.*, 119(94101), pp.1–9.
- Singh, P.K., Sharma, P.K., Kumar, M., Dutta, R., Sundaram, S., Pandey, A.C., (2014). Red luminescent manganese-doped zinc sulphide nanocrystals and their antibacterial study. *J. Mater. Chem. B*, 2, pp.522–528.
- Singhal, S., Garg, A.N. and Chandra, K., (2004). Thermal decomposition of transition metal dithiocarbamates. *Journal of Thermal Analysis and Calorimetry*, 78, pp.941–952.
- Sitbon, G., Bouccara, S., Tasso, M., Francois, A., Bezdetnaya, L., Marchal, F., Beaumont, M., Pons, T., 2014. Multimodal Mn-doped I–III–VI quantum dots for imaging: from synthesis to in vivo application. *Nanoscale*, 6, pp.9264–9272.
- Skinner, B.J., (1961). Unit-cell edges of natural and synthetic sphalerites. *The American Mineralogist*, 46, pp.1399–1411.
- Smith, A.M. and Nie, S., (2010). Semiconductor nanocrystals: Structure, properties, and band gap engineering. *Accounts of Chemical Research*, 43(2), pp.190–200.

- Smith, B.A., Zhang, J.Z., Joly, A., Liu, J., (2000). Luminescence decay kinetics of Mn<sup>2+</sup>-doped ZnS nanoclusters grown in reverse micelles. *Physical Review B*, 62(3), pp.2021–2028.
- Sooklal, K., Cullum, B.S., Angel, S.M., Murphy, C.J., (1996). Photophysical properties of ZnS nanoclusters with spatially localized Mn<sup>2+</sup>. *J. Phys. Chem.*, 100, pp.4551–4555.
- Sotelo-gonzalez, E., Fernandez-argüelles, M.T., Costa-fernandez, J.M., Sanz-medel, A., (2012). Mn-doped ZnS quantum dots for the determination of acetone by phosphorescence attenuation. *Analytica Chimica Acta*, 712, pp.120–126.
- Souici, A.H., Keghouche, N., Delaire, J.A., Remita, H., Etcheberry, A., Mostafavi, M., (2009). Structural and optical properties of PbS nanoparticles synthesized by the radiolytic method. *J. Phys. Chem. C*, pp.A-H.
- Srinivasan, N. and Thirumaran, S., (2014). Synthesis of ZnS nanoparticles from pyridine adducts of zinc(II) dithiocarbamates. *C. R. Chimie*, 17(9), pp.964–970.
- Srinivasan, N., Thirumaran, S. and Ciattini, S., (2009). Effect of phenyl and benzyl group in heterocyclic dithiocarbamates on the ZnS<sub>4</sub>N chromophore: Synthesis, spectral, valencebond parameters and single crystal X-ray structural studies on (pyridine)bis(1, 2, 3, 4-tetrahydroquinolinedithiocarbamato)zinc(II) and (pyridine) bis (1, 2, 3, 4-tetrahydroisoquinolinedithiocarbamato)zinc(II). *Journal of Molecular Structure*, 921(1–3), pp.63–67.
- Srinivasan, N., Thirumaran, S. and Ciattini, S., (2012). Synthesis and crystal structures of diimine adducts of Cd(II) tetrahydroquinolinedithiocarbamate and use of cadmium(II) for the preparation of CdS nanorods. *Journal of Molecular Structure*, 1026, pp.102–107.
- Srivastava, B.B., Jana, S., Karan, N.S., Paria, S., Jana, N.R., Sarma, D.D., Pradhan, N., (2010).

- Highly luminescent Mn-doped ZnS nanocrystals: Gram-scale synthesis. *J. Phys. Chem. Lett.*, 1, pp.1454–1458.
- Stegh, A.H., (2012). Toward personalized cancer nanomedicine – past, present, and future. *Integr. Biol.*, pp.1–17.
- Su, H., Dixon, D.J., Wang, A.Y., Low, J., Xu, J., Wang, J., (2010). Study on growth kinetics of CdSe nanocrystals with a new model. *Nanoscale Res Lett*, 5, pp.823–828.
- Sun, J.Q., Shen, X.P., Guo, L.J., Chen, K.M., Liu, Q., (2009). Microwave-assisted synthesis of flower-like PbS crystals. *Physica E: Low-Dimensional Systems and Nanostructures*, 41(8), pp.1527–1532.
- Sun, M., Yu, H., Yang, W., Qi, L., Yang, F., Yang, X., (2009). Shape evolution of CdSe nanocrystals in vegetable oils: A synergistic effect of selenium precursor. *Colloids and Surfaces A: Physicochem. Eng. Aspects*, 350, pp.91–100.
- Suyana, P., Kumar, S.N., Kumar, B.S.D., Nair, B.N., Pillai, S.C., Mohamed, A.P., Warriar, K.G.K., Hareesh, U.S., (2014). Antifungal properties of nanosized ZnS particles synthesised by sonochemical precipitation. *RSC Adv.*, 4, pp.8439–8445.
- Suyver, J.F., Wuister, S.F., Kelly, J.J., Meijerink, A., (2001). Synthesis and photoluminescence of nanocrystalline ZnS:Mn<sup>2+</sup>. *Nano Letters*, 1(8), pp. 429-433.
- Taylor, K.M.L., Rieter, W.J. and Lin, W., (2008). Manganese-based nanoscale metal - organic frameworks for magnetic resonance imaging. *J. Am. Chem. Soc.*, pp.14358–14359.
- Thanh, N.T.K. and Green, L.A.W., (2010). Functionalisation of nanoparticles for biomedical applications. *Nano Today*, 5(3), pp.213–230.

- Thanh, N.T.K., Maclean, N. and Mahiddine, S., (2013). Mechanisms of nucleation and growth of nanoparticles in solution. *Chem. Rev*, 3(1), pp.A-U.
- Thilagavathi, G., Raja, A.S.M. and Kannaian, T., (2008). Nanotechnology and protective clothing for defence personnel. *Defence Science Journal*, 58(4), pp.451–459.
- Tian, L., Yep, L.Y., Ong, T.T., Yi, J., Ding, J., Vittal, J.J., (2009). Synthesis of NiS and MnS nanocrystals from the molecular precursors (TMEDA)M(SC{O}C<sub>6</sub>H<sub>5</sub>)<sub>2</sub> (M=Ni, Mn). *Crystal Growth & Design*, 9(1), pp.352–357.
- Tiemann, M., Weiß, Ö., Hartikainen, J., Marlow, F., Linden, M., (2005). Early stages of ZnS nanoparticle growth studied by in-situ stopped-flow UV absorption spectroscopy. *ChemPhysChem*, 6, pp.2113–2119.
- Tiemann, M., Marlow, F., Hartikainen, J., Weiss, O., Linden, M., (2008). Ripening effects in ZnS nanoparticle growth. *J. Phys. Chem. C*, 112, pp.1463–1467.
- Tunaru, S., Althoff, T.F., Nüsing, R.M., Diener, M., Offermanns, S., (2012). Castor oil induces laxation and uterus contraction via ricinoleic acid activating prostaglandin EP3 receptors. *PNAS*, 2, pp.9179–9184.
- Upadhyay, R.K., Sharma, M., Singh, D.K., Amritphale, S.S., Chandra, N., (2012). Photo degradation of synthetic dyes using cadmium sulphide nanoparticles synthesized in the presence of different capping agents. *Separation and Purification Technology*, 88, pp.39–45.
- Vaisman, B., Shikanov, A. and Domb, A.J., (2008). The isolation of ricinoleic acid from castor oil by salt-solubility-based fractionation for the biopharmaceutical applications. *J Am Oil Chem Soc*, 85(2), pp.169–184.

- Venkataramana, S., Ramanaiah, K. and Sarcar, M.M.M., (2016). Studies on photo- and thermal stability of PVA-encapsulated Mn-doped ZnS nanoparticles. *Appl. Phys. A*, 122(4), pp.1–6.
- Wang, H., He, Y., Ji, T., Yan, X., (2009). Surface molecular imprinting on Mn-doped ZnS quantum dots for room-temperature phosphorescence optosensing of pentachlorophenol in water. *Anal. Chem.*, 81(4), pp.1615–1621.
- Wang, S.F., Gu, F., Lu, M.K., Wang, D.Z., Yang, Z.S., Zhang, H.P., Zhou, Y.Y., Zhang, A.Y., (2006). Synthesis of cross-shaped PbS nanostructures by a surfactant-assisted reflux process. *Materials Letters*, 60, pp.2759–2763.
- Wang, Y., Zhang, J., Yang, Y., Huang, F., Zheng, J., Chen, D., Yan, F., Lin, Z., Wang, C., (2007). NaOH concentration effect on the oriented attachment growth kinetics of ZnS. *J. Phys. Chem. B*, 111, pp.5290–5294.
- Wender, H., de Oliveira, L.F., Feil, A.F., Lissner, E., Migowski, P., Meneghetti, M.R., Teixeira, S.R., Dupont, J., (2010). Synthesis of gold nanoparticles in a biocompatible fluid from sputtering deposition onto castor oil. *Chem. Commun.*, 46(37), pp.7019–21.
- Whiffen, K.R.M., Jovanovi, D.J., Antic, Ž., Bártová, B., Milivojevi, D., Dramicanin, M.D., Brik, M.G., (2014). Structural, optical and crystal field analyses of undoped and Mn<sup>2+</sup>-doped ZnS nanoparticles synthesized via reverse micelle route. *Journal of Luminescence*, 146, pp.133–140.
- Whitesides, G.M., (2005). Nanoscience, Nanotechnology, and Chemistry. *Small*, 1(2), pp.172–179.

- Wu, P., He, Y., Wang, H., Yan, X., (2010). Conjugation of glucose oxidase onto Mn-Doped ZnS quantum dots for phosphorescent sensing of glucose in biological fluids. *Anal. Chem.*, 82(4), pp.1427–1433.
- Wu, P. and Yan, X.-P., (2013). Doped quantum dots for chemo/biosensing and bioimaging. *Chem Soc Rev*, pp.1–33.
- Xia, Y. and Larock, R.C., (2010). Vegetable oil-based polymeric materials: synthesis, properties, and applications. *Green Chemistry*, 12(11), pp.1893–1909.
- Xiang, Q., Cheng, B. and Yu, J., (2013). Hierarchical porous CdS nanosheet-assembled flowers with enhanced visible-light photocatalytic H<sub>2</sub>-production performance. *Applied Catalysis B, Environmental*, 138–139, pp.299–303.
- Xiao, G., Yang, X., Zhang, X., Wang, K., Huang, X., Ding, Z., Ma, Y., Zou, G., (2015). A protocol to fabricate nanostructured new phase: B31-type MnS synthesized under high pressure. *J. Am. Chem. Soc.*, pp.1–9.
- Xiao, N., Dai, Q., Wang, Y., Ning, J., Liu, B., Zou, G., Zou, B., (2012). ZnS nanocrystals and nanoflowers synthesized by a green chemistry approach: Rare excitonic photoluminescence achieved by the tunable molar ratio of precursors. *Journal of Hazardous Materials*, 211–212, pp.62–67.
- Xu, C., Zhou, R., He, W., Wu, L., Wu, P., Hou, X., (2014). Fast imaging of eccrine latent fingerprints with nontoxic Mn-doped ZnS QDs. *Anal. Chem.*, 86, pp.3279–3283.
- Yang, H., Santra, S. and Holloway, P.H., (2005). Syntheses and applications of Mn-doped II-VI semiconductor nanocrystals. *J. Nanosci. Nanotech*, 5(9), pp.1364–1375.

- Yang, J., Zeng, J., Yu, S., Yang, L., Zhou, G., Qian, Y., (2000). Formation process of CdS nanorods via solvothermal route. *Chem. Mater.*, 12, pp.3259–3263.
- Yang, Y. and Zhang, W., (2004). Preparation and photoluminescence of zinc sulphide nanowires. *Materials Letters*, 58, pp.3836–3838.
- Yordanov, G.G., Gicheva, G.D., Bochev, B.H., Dushkin, C.D., Adachi, E., (2006). The effects of temperature and carboxylic acid ligand on the growth of nanocrystalline CdSe in a hot paraffin matrix. *Colloids and Surfaces A: Physicochem. Eng. Aspects*, 273, pp.10–15.
- Yu, K., Hrdina, A., Zhang, X., Ouyang, J., Leek, D.M., Wu, X., Gong, M., Wilkinson, D., Li, C., (2011). Highly-photoluminescent ZnSe nanocrystals via a non-injection-based approach with precursor reactivity elevated by a secondary phosphine. *Chem. Commun.*, 47, pp.8811– 8813.
- Yu, W.W., Qu, L., Guo, W., Peng, X., (2003). Experimental determination of the extinction coefficient of CdTe, CdSe, and CdS nanocrystals. *Chem. Mater.*, 15(14), pp.2854–2860.
- Zaera, F., (2012). Nanostructured materials for applications in heterogeneous catalysis. *Chem Soc Rev*, pp.1–15.
- Zamiri, R., Zakaria, A., Abbastabar, H., Darroudi, M., Husin, M.S., Mahdi, M.A., (2011). Laserfabricated castor oil-capped silver nanoparticles. *International Journal of Nanomedicine*, 6(1), pp.565–568.
- Zhang, H., Hyun, B., Wise, F.W., Robinson, R.D., (2012). A generic method for rational scalable synthesis of monodisperse metal sulphide nanocrystals. *Nano Letters*, 12, pp.5856–5860.
- Zhang, H. and Banfield, J.F., (2009). Identification and growth mechanism of ZnS nanoparticles with mixed cubic and hexagonal stacking. *J. Phys. Chem. C*, 113, pp.9681–9687.

- Zhang, H., Banfield, J.F. and Hall, M., (2004). Aggregation, coarsening, and phase transformation in ZnS nanoparticles studied by molecular dynamics simulations. *Nano Letters*, 4(4), pp.713–718.
- Zhang, J., Huang, F. and Lin, Z., (2010). Progress of nanocrystalline growth kinetics based on oriented attachment. *Nanoscale*, 2, pp.18–34.
- Zhang, W., Li, Y., Zhang, H., Zhou, X., Zhong, X., (2011). Facile synthesis of highly luminescent Mn-doped ZnS nanocrystals. *Inorg. Chem.*, 50, pp.10432–10438.
- Zhang, X. V., Martin, S.T., Friend, C.M., Schoonen, M.A.A., Holland, H.D., (2004). Mineralassisted pathways in prebiotic synthesis: Photoelectrochemical reduction of carbon (+IV) by manganese sulphide. *J. Am. Chem. Soc.*, 126, pp.12503–12507.
- Zhang, Y., Li, X., Xu, W., Li, S., Wang, H., Li, L.S., (2012). The size controlled synthesis and self-assembled of monodisperse Cu<sub>2</sub>S nanocrystals. *Materials Letters*, 67(1), pp.117–120.
- Zhen, Z. and Xie, J., (2012). Development of manganese-based nanoparticles as contrast probes for magnetic resonance imaging. *Theranostics*, 2(1), pp.45-54
- Zheng, Y., Cheng, Y., Wang, Y., Zhou, L., Bao, F., Jia, C., (2006). Metastable  $\gamma$ -MnS hierarchical architectures: Synthesis, characterization, and growth mechanism. *J. Phys. Chem. B*, 110, pp.8284–8288.
- Zhou, G., Lu, M., Xiu, Z., Wang, S., Zhang, H., Zhou, Y., Wang, S., (2006). Controlled synthesis of high-quality PbS star-shaped dendrites, multipods, truncated nanocubes, and nanocubes and their shape evolution process. *J. Phys. Chem. B*, 110, pp.6543–6548.

Zhu, D., Li, W., Wen, H., Chen, Q., Hu, Y., (2014). Microwave-assisted aqueous synthesis of Mn-doped ZnS quantum dots and their room-temperature phosphorescence detection of indapamide. *Anal. Methods*, 6, pp.7489–7495.

Zhu, Y., Bando, Y. and Xue, D., (2003). Spontaneous growth and luminescence of zinc sulphide nanobelts. *Appl. Phys. Lett.*, 82(11), pp.1–4.

Zrazhevskiy, P., Sena, M. and Gao, X., (2010). Designing multifunctional quantum dots for bioimaging, detection, and drug delivery. *Chem. Soc. Rev.*, 39, pp.4326–4354.

## APPENDIX

### PUBLICATIONS (PAPERS UNDER REVIEW)

1. THE SYNTHESSES OF MANGANESE DOPED ZINC SULPHIDE ( $Mn_xZn_{1-x}S$ ) NANOCRYSTALS BY THE THERMAL DECOMPOSITION OF DIRICINOLEATE CARBOXYLATES IN OLEYLAMINE/DODECANETHIOL SOLVENT SYSTEM
2. THE SYNTHESSES OF MANGANESE DOPED ZINC SULPHIDE ( $Mn_xZn_{1-x}S$ ) NANOCRYSTALS BY THE THERMAL DECOMPOSITION OF HETEROCYCLIC

## DITHIOCARBAMATE SINGLE SOURCE PRECURSORS IN OLEYLAMINE

3. GROWTH KINETICS OF ZINC SULPHIDE NANOPARTICLES SYNTHESIZED IN OLEYLAMINE/ DODECANETHIOL SOLVENT SYSTEM
4. SYNTHESSES OF CADMIUM SULPHIDE NANOCCLUSERS AND LEAD SULPHIDE NANOBELTS VIA FACILE THERMOLYSIS OF ETHYLXANTHATE COMPLEXES IN CASTOR OIL
5. REVIEW PAPER ON „CASTOR OIL: A SUITABLE GREEN SOURCE OF CAPPING AGENT FOR NANOPARTICLES SYNTHESSES AND FACILE SURFACE FUNCTIONALIZATION“

